DIRK GRÜNDING

AN ARBITRARY LAGRANGIAN-EULERIAN METHOD FOR THE DIRECT NUMERICAL SIMULATION OF WETTING PROCESSES

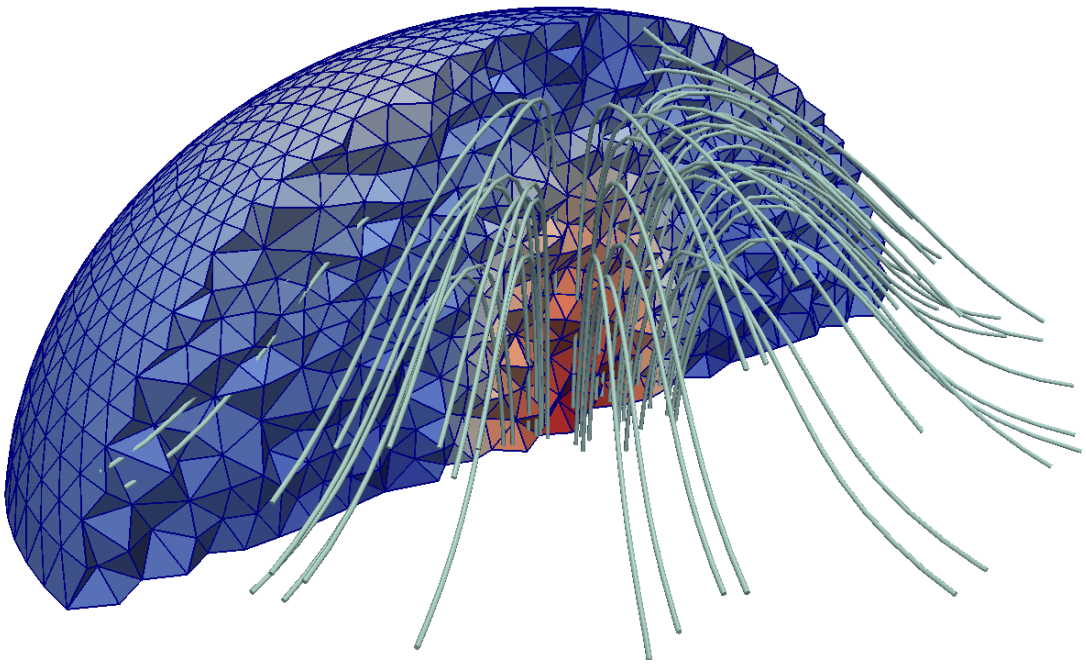

DISSERTATION

2019

On the cover: An application of the Arbitrary Lagrangian-Eulerian method developed in this work. The image shows a cross section of a droplet that is growing due to an inflow of liquid at the bottom. The colors illustrate the magnitude of the velocity field from lower (blue) to higher velocities (red). The lines originating at the center depict the streamlines of the flow.

AN ARBITRARY LAGRANGIAN-EULERIAN METHOD FOR THE DIRECT NUMERICAL SIMULATION OF WETTING PROCESSES

Am Fachbereich Maschinenbau
an der Technischen Universität Darmstadt
zur
Erlangung des akademischen Grades eines
Doktor-Ingenieurs (Dr.-Ing.)
genehmigte

DISSERTATION

vorgelegt von

DIRK GRÜNDING

aus Cloppenburg, Deutschland

Berichterstatter: Prof. Dr. rer. nat. Dieter Bothe
Mitberichterstatter: Prof. Dr. rer. nat. Michael Schäfer
Tag der Einreichung: 15.10.2019
Tag der mündlichen Prüfung: 10.12.2019

Darmstadt, 2019
D17

ABSTRACT

The process of wetting is present in virtually all technologies that involve liquids. Hence, the modeling and simulation of the involved physics is a key element in modern product design processes.

To investigate the wetting process, an Arbitrary Lagrangian-Eulerian (ALE) method is developed in OpenFOAM. The extension includes new Navier and a free slip boundary conditions that are introduced into the framework. Furthermore, a flexible contact angle library is provided. The implementation allows to combine heuristic models on arbitrary contact line topologies. Various test cases ranging from simple channel flows, over oscillating droplets and even local surface geometries provide a sound verification basis.

Special emphasis is given to the extension of available reference cases for moving contact lines, specifically, the case of a liquid rising in a capillary. For this purpose, an ordinary differential equation (ODE) is derived from the continuum mechanical description for free surface flows. This model incorporates a Navier slip boundary condition and outlines necessary assumptions for a comparison to a numerical solution of the associated continuum mechanical model. In addition, the derivation explains the origin of the singularity in the classical rise model that is closely related to a precise computation of the stationary height of the liquid column. Moreover, it is shown that a convective contribution is missing in standard rise models.

An extensive code to code comparison between the extended ALE-implementation, a geometric as well as an algebraic Volume of Fluid code, and a level-set approach has been executed in a collaborative effort. This provides novel benchmark data for the capillary rise test case that allows for a comprehensive comparison to the considered class of ODE rise models. Furthermore, the influence of numerical slip and Navier slip boundary condition on the rise behavior are analyzed.

Finally, an overview of different applications and a comparison to experimental results highlights the new capabilities of the implemented extensions.

ZUSAMMENFASSUNG

Benetzungprozesse sind allgegenwärtig in nahezu allen Technologien bei denen Flüssigkeiten eine Rolle spielen. Deshalb ist die Modellierung und Simulation der zugehörenden physikalischen Vorgänge ein zentraler Bestandteil in modernen Produktentwicklungsprozessen.

Für die Simulation von Benetzungsprozessen wird eine Arbitrary-Lagrangian-Eulerian-Methode (ALE-Methode) in OpenFOAM entwickelt, getested und validiert. Dabei wird die Implementierung mit Hilfe einer Versionskontrolle durch Git und Bitbucket umgesetzt. Die Erweiterungen beinhalten sowohl eine neue Navier- als auch eine Randbedingung mit freiem Schlupf, die in die Platform integriert werden. Ebenfalls wird eine flexible Kontaktwinkelbibliothek erstellt. Diese Implementierung erlaubt eine Kombination von heuristischen Kontaktwinkelmodellen auf beliebigen Kontaktlinientopologien. Diverse Testfälle, die von einfachen Kanalströmungen über oszillierende Tropfen bis hin zum Vergleich lokaler Oberflächengeometrien reichen, bilden eine solide Verifizierungsbasis.

Besondere Aufmerksamkeit wird auf die Erweiterung der verfügbaren Referenzfälle für bewegte Kontaktlinien gelegt, wobei insbesondere der Aufstieg von Flüssigkeiten in einer Kapillare untersucht wird. Zu diesem Zweck wird eine gewöhnliche Differentialgleichung (GDG) aus dem Zweiphasen-Kontinuumsmodell motiviert und bezüglich Navier Schlupf-Randbedingungen erweitert. Dabei zeigt die detaillierte Herleitung die Ursache der Singularität im klassischen Aufstiegsmodell, das in engem Zusammenhang zu einer präzisen Bestimmung der stationären Aufstiegshöhe steht. Darüber hinaus wird aufgezeigt, dass der Beitrag des Konvektionsterms im klassischen Modell nicht vorhanden ist.

Zur weiteren Verifizierung ist ein umfangreicher Code zu Code Vergleich zwischen der erweiterten ALE-Methode, einer geometrischen sowie einer algebraischen Volume of Fluid Methode und einem Level-Set Verfahren durchgeführt worden. Damit stehen neue Benchmark-Daten für den Flüssigkeitsaufstieg in einer Kapillaren zu Verfügung, die auch einen umfangreichen Vergleich zur untersuchten Klasse der GDG-Modelle erlaubt. Darüber hinaus wird der Einfluss von numerischem Schlupf und Navier-Schlupf-Randbedingungen auf die Dynamik des Flüssigkeitsaufstiegs untersucht.

Eine abschließende Übersicht unterschiedlicher Anwendungen und ein Vergleich zu experimentellen Ergebnissen zeigen die neuen Möglichkeiten der nun zur Verfügung stehenden Implementierung auf.

AWARDS

Best Poster Award for the poster entitled "Wetting processes with ALE interface tracking", 12th OpenFOAM Workshop 2017, Exeter.

PUBLICATIONS

Some ideas and figures used within this thesis have appeared previously in the following publications:

1. Gründing, D., Fleckenstein, S., and Bothe, D. „A subgrid-scale model for reactive concentration boundary layers for 3D mass transfer simulations with deformable fluid interfaces." In: *International Journal of Heat and Mass Transfer* 101 (Oct. 2016). doi: 10.1016/j.ijheatmasstransfer.2016.04.119, pp. 476–487

2. Gründing, D., Bothe, D., and Marschall, H. „Wetting phenomena with ALE interface tracking." In: *Proc. in Appl. Math. and Mech.* 18.1 (2018). doi: 10.1002/pamm.201800430, e201800430

3. Gründing, D. „An enhanced model for the capillary rise problem." In: *International Journal of Multiphase Flows* (2019). doi: 10.1016/j.ijmultiphaseflow.2020.103210

4. Gründing, D. et al. „A comparative study of transient capillary rise using direct numerical simulations." In: (2019). Submitted

5. Gründing, D., Fricke, M., and Bothe, D. „Capillary Rise - Jurin's Height vs Spherical Cap." In: *PAMM* 19.1 (2019). doi: 10.1002/pamm.201900336, e201900336

6. Hartmann, M. et al. „Breakup Dynamics of Capillary Bridges on Hydrophobic Stripes." In: (2019). Submitted

CONFERENCE AND WORKSHOP CONTRIBUTIONS

1. Gründing, D.: From the continuum mechanical description to the Washburn model. In: *Wetting on Soft or Microstructured Surfaces - 694. WE-Heraeus-Seminar*, April 11-13, 2019, Bad Honnef.

2. Gründing, D.; Marschall, Holger; Bothe, Dieter: The capillary rise as a benchmark for DNS wetting simulations. In: *GAMM 2019 - 90th Annual Meeting of the International Association of Applied Mathematics and Mechanics*, February 18-22, 2019, Vienna.

3. Gründing, D.; Marschall, Holger; Bothe, Dieter: Wetting phenomena with ALE interface tracking. In: *13th OpenFOAM Workshop*, June 24-29, 2018, Shanghai.

4. Gründing, D.; Marschall, Holger; Bothe, Dieter: Wetting with an ALE interface tracking method. In: *89th Annual Meeting of the International Association of Applied Mathematics and Mechanics*, March 19-23, 2018, München.

5. Gründing, D.; Marschall, Holger; Bothe, D.: Wetting processes with ALE interface tracking. In: *12th OpenFOAM Workshop*, July 24-27, 2017, Exeter.

6. Gründing, D.: Towards Wetting Processes with Interface Tracking. *NUMAP-FOAM School 2017*, August 21 - September 1 2017, Zagreb.

7. Gründing, D.; Marschall, H.; Bothe, D.: Moving contact line treatment using a finite volume ALE interface-tracking method. In: *ICNMMF-III International Conference on Numerical Methods in Multiphase Flows*, July 26-29, 2017, Tokyo.

8. Oberwolfach Seminar: *Compressible and Incompressible Multiphase Flows: Modelling, Analysis, Numerics*, June 4-10, 2017, Oberwolfach.

CO-SUPERVISED THESIS

[144] Waid, J. „Direct Numerical Simulation of Dynamic Wetting Processes by means of Arbitrary Lagrangian-Eulerian Interface-Tracking using OpenFOAM.“ MA thesis. TU Darmstadt, 2017

ACKNOWLEDGMENTS

I would like to express my deepest gratitude to my supervisor Prof. Dr. rer. nat. Dieter Bothe for his dedication, constructive criticism, helpful discussions and interest in my PhD work.

Writing this thesis would not have been possible without the support and countless discussions with my colleagues. These are specifically Chiara Pesci, Tobias Tolle, Andre Weiner, Matthias Niethammer, Holger Marschall and Dennis Hillenbrand. Furthermore, I have greatly benefited from the discussions of the intricate details of wetting models with Mathis Fricke. Moreover, the constant help and support by my friend and colleague Tomislav Maric, even in those times where his own work was pushing hard on him, will not be forgotten.

It was a great pleasure to be enrolled within the Collaborative Research Centre 1194 funded by the German Science Foundation (DFG). The opportunity to discuss especially experimental details has proven invaluable to my understanding of wetting processes. Special thanks go to Max Hartmann for providing most useful insights to experimental techniques. In addition, representing the more than 20 PhD students within the CRC1194 and organizing our yearly retreats together with Elisabeth Diehl has been a great pleasure. I could not have hoped for a better colleague to fill this position. Furthermore, the numerous visits of researchers within the SFB have been highly valuable to my understanding of various topics related to the simulation of wetting processes. I would like to thank Prof. Y. Shikhmurzaev and Prof. J. Sprittles for the interesting insights to the interface formation model. Furthermore, I would like to thank Prof. M. Perić to share his personal experience with control point algorithm. The experimental background given by Dr. Terry Blake especially in the context of coating flows were highly beneficial. Moreover, I would like to thank Prof. H. Jasak, Prof. and PhD V. Vukčević to share their detailed knowledge of OpenFOAM. Specifically, I am thankful to Prof. Ž. Tuković for his publication of the original version of the interTrackFoam solver on which I could base my work.

Bei meinen Eltern, Gisela und Willehard Gründing. Danke für Eure ausdauernde, emotionale und finanzielle Unterstützung auf meinem Weg und für einfach alles. Ohne das Einmaleins zu lernen, simuliert man keine Mehrphasenströmungen. Vielen Dank! A heartfelt thank you and great gratitude to Leonie Koch for her enduring support and patience even during the time where she had to deal with the challenges of her own PhD thesis.

This thesis would not have been possible without the countless open-source softwares I have used: Ubuntu (Linux), Paraview, Inkscape, neovim, jupyter notebooks, python and its countless modules, the C++ programming language, the various versions of OpenFOAM, latex, the latex classic thesis template, Kile. A big thank you to each and every person asking and answering questions on the various sites of stackoverflow and the contributors of the great website wikipedia, to only name a few.

Calculations for this research were conducted on the Lichtenberg high performance computer of the TU Darmstadt. The opportunity to use such large scale computational resources is gratefully acknowledged.

In this regard, I also kindly acknowledge the financial support by the German Research Foundation (DFG) within the Collaborative Research Centre 1194 “Interaction of Transport and Wetting Processes”, Project B02.

Interaction between
Transport and Wetting Processes

CONTENTS

LIST OF FIGURES

LIST OF TABLES

ACRONYMS

ALE	Arbitrary Lagrangian-Eulerian
AMR	adaptive mesh refinement
BC	boundary condition
BOSSS	bounded support spectral solver
CA	contact angle
CFD	computational fluid dynamics
CP	control point
FS3D	Free Surface 3D
FEM	Finite Element Method
FVM	Finite Volume Method
GDG	gewöhnliche Differentialgleichung
HDT	hydrodynamic theory
IFM	interface formation model
LS	least squares
MD	molecular dynamics
MKT	molecular kinetic theory
ODE	ordinary differential equation
PDE	partial differential equation
PLIC	piecewise linear interface reconstruction
TM-AFM	tapping mode atomic force microscope
TVD	total variation diminishing
VOF	volume of fluid
WENO	weighted essentially non-oscillating
xDG	extended discontinuous Galerkin

NOMENCLATURE

LATIN SYMBOLS

a	pertubation of sphere	m
$\mathbf{a}$	rotation axis at a contact line mesh point	$-$
A	amplitude	m^2
A	area	m^2
a	coefficient for the non-dimensional capillary rise equation	$s^2\,m^{-2}$
b	coefficient for the non-dimensional capillary rise equation	$s\,m^{-2}$
c	coefficient for the non-dimensional capillary rise equation	m^{-1}
Ca	capillary number	$-$
$\mathbf{d}$	displacement direction	$-$
D	integration depth	m
$\mathbf{D}$	rate of deformation or mesh-diffusivity tensor	s^{-1}
e_0	maximum height (low Eötvös number limit)	m
e_∞	maximum height of a droplet (large Eötvös number limit)	m
e^*	scaled maximum droplet height	$-$
e_{Jur}	relative error of Jurin's height	$-$
e_{corr}	relative error of corrected rise height	$-$
$\boldsymbol{e}$	normalized basis vector	$-$
$\boldsymbol{e}_{p_1,p_2}$	vector from point $\mathbf{x}_{p_1}$ to $\mathbf{x}_{p_2}$	m
$\boldsymbol{e}_e$	vector connecting the points (nodes) of edge e	m
E	total energy	J
Eo	Eötvös number	$-$
f	a general function typically $f : \mathbb{R} \to \mathbb{R}$	$-$
f_{Hoff}	function for the Hoffman contact angle model	$-$
g	coefficient gravitational acceleration	$m\,s^{-2}$
g	function for the Mathieu contact angle model	$-$
$\mathbf{g}$	vector of gravitational acceleration	$m\,s^{-2}$
G	constant pressure gradient	$N\,m^{-3}$
h	height function, or orthogonal distance to a face	m
$\tilde{h}$	rise correction for a spherical cap shaped interface	m
h_f^{r+1}	displacement height of a control point	m
$h(t)$	rise height of liquid in a capillary over time	m

$h(x)$	surface height in a graph representation	$-$
$h_{apex\,\infty}$	stationary apex height	m
$h_{Jur,2D}$	stationary Jurin's height in 2D	m
$H(x)$	surface height	m
H	mean curvature	m^{-1}
H	diameter of a 2D channel	m
I	identity	$-$
i_{max}	maximum number of iterations for the convection term	$-$
j_{max}	maximum number of pressure velocity iterations	$-$
k_{max}	maximum number of pressure correction loops	$-$
K	non-dimensional coefficient (extended capillary rise model)	$-$
L	slip length	m
L_{PeN}	discrete geodesic distance from	m
L_{cap}	capillary length, ratio of surface tension and gravity forces	m
n	mode of spherical harmonic	$-$
n_{max}	overall number of time steps	$-$
$\mathbf{n}$	normal vector	$-$
$\mathbf{n}_p$	point normal	$-$
$\mathbf{n}_f$	face normal	$-$
$\mathbf{n}_e$	edge normal of edge e	$-$
$\mathbf{n}_{LS,p}^{r+1}$	normal of the CP least square surface	$-$
N	degrees of freedom for a single discrete quantity	$-$
N_x	number of cells in x-direction	$-$
$\mathbf{N}$	surface bi-normal	$-$
p	pressure (field)	$N\,m^{-2}$
$\tilde{p}$	modified pressure	$N\,m^{-2}$
p_0	reference pressure	$N\,m^{-2}$
$\mathbf{p}_{LS,p}^{r+1}$	point on the CP least squared surface	m
$\mathbf{P}_{\partial\Omega}$	projector onto $\partial\Omega$	$-$
q	indicator: $q \in \{-1, 1\}$	$-$
Q	non-dimensional coefficient (extended capillary rise model)	$-$
r	radius, radial coordinate or residual	m
r_e	effective radius	m
R	halve of the diameter of a capillary, radius of a droplet	m
Re	Reynolds number	$-$
s	integration variable for a line integral	m

S	spreading parameter	$J\,m^{-2}$
S	energy function for a least square plane	J
S	non-dimensional slip length	$-$
S_e	edge length	m
S_f	face area	m^2
$\mathbf{S}$	Cauchy-stress tensor	$N\,m^{-2}$
$\mathbf{S}_f$	face area normal of face f	m^2
$\mathbf{S}^{visc}$	viscous stress tensor	$N\,m^{-2}$
SMALL	length used for regularization	m
t	time	s
$\mathbf{t}_\Sigma$	tangent to the interface Σ	$-$
U	velocity component	$m\,s^{-1}$
v	velocity component	$m\,s^{-1}$
$\overline{v}$	average velocity	$m\,s^{-1}$
v_Γ	contact line velocity (tangential to the solid)	$m\,s^{-1}$
$\mathbf{v}$	velocity vector (field)	$m\,s^{-1}$
$\mathbf{v}_w$	wall velocity	$m\,s^{-1}$
$\mathbf{v}_\Gamma$	normal velocity of the contact line (normal to Γ and Σ	$m\,s^{-1}$
V	velocity component	$m\,s^{-1}$
V	volume	m^3
V^n	volume of a cell at time step n	m^3
$\delta\dot{V}_f$	swept volume flux of face f	$m^3\,s^{-1}$
δV_f^{n+1}	swept volume of face f from time-step n to $n+1$	m^3
w_f	weight of face f	$-$
x^*	non-dimensional x-coordinate	$-$
$\mathbf{x}$	a point	m
$\mathbf{x}_e$	center of edge e	$-$
$\mathbf{x}_f$	center of face f	$-$
$\mathbf{x}_c$	center of cell c	$-$
$\mathbf{x}_f$	face center	m
$\mathbf{x}_{CP,f}^0$	initial location of the control point associated with face f	m
$\tilde{\mathbf{x}}_{CP,f}^{r+1}$	mirrored control point	m
x, y, z	cartesian coordinates	m
z	cartesian coordinate or transformed rise height	m^2
z_{Jur}	Jurin's height in transformed capillary rise height	m^2

GREEK SYMBOLS

α	correction factor for stationary height	$-$
$\alpha_{p,f}$	opening angle of face f at point p	$^\circ$
β	slip coefficient	$m^2\,s\,kg^{-1}$
Γ	contact line (mathematical set)	$-$
$\tilde{\Gamma}$	points and edges of the contact line mesh	$-$
δ	dampening constant of damped linear oscillator	s^{-1}
δt	time step	$-$
δ_e^r	orthogonal distance to the wall boundary	m
Δt	time step	s
Δx	cell width for an equidistant mesh	m
$\Delta h(x)$	distance between the apex height and the interface	m
$\epsilon(t)$	pertubation of transformed capillary rise height	$m^{1/2}$
ϵ_{micro}	microscopic length scale	m
ϵ_{macro}	macroscopic length scale	m
ζ	dampening ratio of damped linear oscillator	$-$
θ	contact angle	$^\circ$
θ_m	microscopic contact angle	$^\circ$
θ_{rot}	rotation angle	$^\circ$
κ	total curvature	m^{-1}
κ_f	curvature associated with a face	m^{-1}
κ_{cap}	curvature of spherical cap	m^{-1}
λ	inverse slip coefficient	$kg\,m^{-2}\,s^{-1}$
μ	dynamic viscosity	$N\,m^{-2}\,s$
ν	kinematic viscosity	$m^2\,s^{-1}$
π	ratio of a circles circumference to its diameter	$-$
ρ	density of the bulk domain	$kg\,m^{-3}$
ρ^Σ	surface density (interface formation model)	$kg\,m^{-2}$
σ	surface tension coefficient	$N\,m^{-1}$
σ_Σ	surface tension coefficient (interface formation model)	$N\,m^{-1}$
Σ	free surface or liquid-gas interface	$-$
$\tilde{\Sigma}$	discrete interface	$-$
$\tilde{\Sigma}_F$	faces of the discrete interface	$-$
τ	time integration variable	s
τ	dampening constant for droplet oscillation	s
$\mathcal{T}_c$	control volume with index c	m^3

φ_f^{n+1}	volume flux through face f at time step $n+1$	$m^3\,m^{-2}\,s^{-1}$
φ_f	, volume flux per face area	$m\,s^{-1}$
φ	, angular coordinate in polar coordinates	$^\circ$
φ	, phase shift for oscillation solution	$-$
ϕ	level-set function	$-$
ϕ	function, typically $\phi : \mathbb{R} \to \mathbb{R}$	$-$
ψ	stream function	$m^2\,s^{-1}$
Ψ	diffeomorphism for the deformation of the mesh	$-$
Ω	domain of integration or non-dimensional group	$-$
ω_0	angular frequency of damped linear oscillator	s^{-1}

MATHEMATICAL SYMBOLS

div	divergence	m^{-1}
div_Σ	surface divergence	m^{-1}
∇_Σ	surface gradient	m^{-1}
∇	gradient	m^{-1}
$\mathrm{ngb}_P(p)$	all vertices connected to vertex p by a single edge	
$\mathrm{ngb}_E(p)$	all edges that connect to the vertex p	
$\mathrm{ngb}_F(p)$	all faces that use the vertex p	
$\mathrm{ngb}_C(p)$	all cells that use the vertex p	
$\partial\Omega$	boundary of Ω	
$\mathcal{C}^1$	set of continuously differentiable functions	
$\mathcal{O}$	Landau-symbol "big-O"	
$[\![\cdot]\!]$	jump brackets	
$\lvert\Omega\rvert$	volume occupied by Ω	
$\langle\cdot\rangle$	arithmetic average	
$\lVert\cdot\rVert$	norm	
$\emptyset$	empty set	

SUB- AND SUPERSCRIPTS

0	initial or reference state/time
a	ambient
b	control volume boundary
c	index of a cell
d	dimension of the domain
e	index of an edge

f	index of a face
F	face
g	gas
i	index for different phases
l	liquid
n	index for the time step
r	iteration index of the control point algorithm
p	index of a point
P	point
T	transpose
w	wall
CP	control point
eq	equilibrium
in	inflow boundary
lg	liquid-gas
sl	solid-liquid
sg	solid-gas
adv	advancing
cap	capillary
Jur	Jurin
max	maximum
rec	receding
rot	rotation
apex	apex of the meniscus
Hoff	Hoffman
micro	microscopic
macro	macroscopic
visc	viscous
ϵ	extension to tubular neighborhood
Γ	used for a quantity defined on the contact line
Σ	liquid-gas interface
Σ	liquid-gas interface
Σ_l	liquid-solid interface
Σ_g	gas-solid interface
$\partial\Omega$	indicating a quantity defined on the boundary of Ω
H_2O	water
*	non-dimensional quantity

1

INTRODUCTION

The vast emptiness of space. It is the 16th July 2013 and protected by his space suit, ESA-astronaut Luca Parmitano is working outside of the International Space Station. While connecting cables to the station's external sockets he realizes that something is not quite right. He feels an unexpected sensation of water at the back of his neck - water, as should later be identified, that was leaking from the cooling system of his space suit. While immediately ordered to return to the inside of the space station, the liquid starts to creep over the inside of his helmet: "The water has also almost completely covered the front of my visor, sticking to it and obscuring my vision.„ the water covers my nose". Parmitano is moving towards the hatch of the space station, while the problem starts to become critical "[...] the upper part of the helmet is full of water and I can't even be sure that the next time I breathe I will fill my lungs with air and not liquid.".

Fortunately Parmitano remained calm. Due to his' and his colleagues' professionalism he could reach the inside of space station, open the space suit and save him from drowning in space [100]. Analyzing the incident, one can conclude that the liquid leaking from the cooling system was spontaneously spreading over the surfaces inside the helmet, including the face of the astronaut. The moment where the leakage occurred, the nature of the liquid flow changed. Not only did a liquid-gas interface form, but the interaction of this interface with the wall lead to the spreading of the liquid inside the space suit and over the astronaut's face.

The spreading of liquids on a solid surface is of course not exclusive to micro-gravity environments. Without exaggeration one can say that multiphase flows and their interaction with surfaces occur in virtually all cases where liquids are involved. However, on earth, surface tension dominated flows are typically limited to length scales below the capillary length which is in the case of pure water on the millimeter scale. Some of the forming surfaces can be observed in Figure 2, where water drops have formed on a leaf. For smaller liquid volumes, the surface tension shapes them into drops in the form of spherical caps. On the other hand, the larger liquid area in the lower part of the leaf is large enough to be influenced by gravity. Hence it wets a more flat and non-symmetric area instead of producing one symmetric, spherical drop. Other examples in nature include drops sliding down a

Figure 2: Water condensation from morning dew on a leaf.

window, the lotus effect, and the interesting properties of pitcher plants together with their interaction with insect feet. Yet, the process of wetting also plays a fundamental role in countless technologies - may it be during the production or performance phase: lab-on-a-chip blood tests, nozzles to form fine sprays for optimal fuel efficiency in car engines and air plane turbines, the liquid pool forming in welding and the casting of industrial products ranging from Lego bricks to five story sized ship engine blocks. Recently, the mass production of electronic circuits using printing technologies and the advent of 3D printing of polymers and metals in combination with meta materials promise unprecedented opportunities - and challenges for current and future engineers.

Parmitano's post ends with the lines "The skills of our engineers and the technology surrounding us make things appear simple when they are not, and perhaps we forget this sometimes. Better not to forget." An engineer is tasked with the formidable challenge to built the next generation 3D printing nozzle, optimized channels for blood flow in a-lab-on-chip or to predict the spreading of liquid in an astronaut helmet. Such tasks require a sound understanding of how a liquid wets a surface and in a modern design process usually involves computer simulations of the relevant physical effects.

Experimental investigations demonstrate that wetting is a multi-scale process by nature. If a plate is dipped into a pool, the interface shows curvature on the capillary length of millimeters. Approaching the solid wall, the liquid surface shows non-monotonic inclination angles on a length scale of about ten micrometers [111]. Even below this scale, the contact line may pin at objects on the nano-scale which may stop the movement of a macroscopic drop [47]. Another example is the dissipation of energy on all length scales between the macroscopic and the nanometer scale [128]. In addition, a direct observation

of the flow field close to the contact line is limited by the size of tracers and is influenced by Brownian motion below a certain limit. The shear number of material combinations and the typically small scales make a detailed experimental investigation extremely challenging in many cases. While one liquid such as silicon oil might perfectly spread on a planar surface, another such as mercury will form drops with extremely large contact angles. Furthermore, results can easily be obstructed by the influence of impurities of the liquid, evaporation effects, contamination by surfactants, temperature influences, the roughness of the solid surface (as with the leaf in Figure 2) or the presence of small particles that may cause a pinning of the contact line.

The basis for any computer simulation is a mathematical model of the physical system under investigation. Such descriptions range from the nano scale with molecular dynamic (MD) approaches, over kinetic theories on the mesoscopic to the continuum descriptions on the macroscopic scale. The latter can be considered the predominant model for solid body and fluid mechanical problems in engineering applications. Yet, the search for a suitable continuum model for wetting processes has not yet come to a fully agreed upon treatment that provides predictable results in arbitrary wetting scenarios [11].

While the solution of a molecular dynamics description requires large coupled systems of ordinary differential equations (ODE), the continuum mechanical description involves coupled partial differential equations (PDE). Given currently available computational capacities, MD and kinetic theory simulations are limited to systems on the nano-scale. But also the solution of the continuum mechanical model is extremely challenging, especially if strongly disparate length scales have to be resolved. The wide range of different physical processes has sparked a wide variety of different approaches to solve the PDE model. These descriptions mostly vary in their analytic description of the interface and the corresponding discrete interface representation as well as the discretization method.

Overall, the full cycle from experimental observation to creating a mathematical model, and solving the resulting equations that explain the experimental observation is extremely challenging in every step. While a successful partial description is often possible, a detailed prediction of the wetting on complex - possibly inhomogeneous or rough surface - still pushes the currently available models and the corresponding CFD capabilities beyond their limit.

2

STATE OF RESEARCH

The interaction of two fluids with a wall leads to the feature-rich, multi-scale process of wetting. The investigation of this process goes back to the onset of modern science and even beyond [57, 67, 150, 73]. Typical geometries to investigate wetting include rotational symmetric setups as they reduce the influence of the interface geometry and improve the control of certain details of the process. Hence, liquids moving in capillaries, drops moving on surfaces, film coating experiments, or liquid bridges are preferable for the experimental investigation of wetting. Such experiments are usually accompanied by additional physical effects that may influence the results. These may be for example soluto-capillary or thermo-capillary effects. Depending on the size of the free surface and the humidity of the gas phase, evaporation may also become important depending on the volatility of the fluid. In many cases surface roughness or particles in the liquid or on the surface may also become relevant. While these effects are *always* present, their influence has to be controlled in any experiment aiming to improve the understanding of wetting.

Hauksbee was an 18th century scientific instrument maker who was invited to the first session of the Royal society chaired by Isaac Newton

Laplace added a supplement "A la théorie de l'action capillaire" to the tenth volume of his "Traité de la mécanique céleste"

The following overview concentrates on the hydrodynamics of wetting processes. Specifically, the first section outlines flow features that can be observed experimentally. The subsequent section will give an overview over certain continuum mechanical models aiming to model the hydrodynamics of wetting. Note the available reviews [43, 69, 11, 124, 13, 128].

2.1 EXPERIMENTAL FEATURES OF WETTING

The various physical processes, the large variety of material combinations, and numerous influence factors often complicate a clear experimental observation [11]. Yet, some features of wetting are understood to be central to the process of wetting.

When a liquid wets a surface, the triple line between liquid gas and solid is called *three phase contact line*, *triple line* or, for short, *contact line*. At this line, the liquid-solid interface intersects the solid surface with a certain angle, referred to as the *contact angle*. This angle is usually measured through one of the involved liquids. While this model picture might seem reasonable, numerous factors may influence what is considered *the* contact angle and,

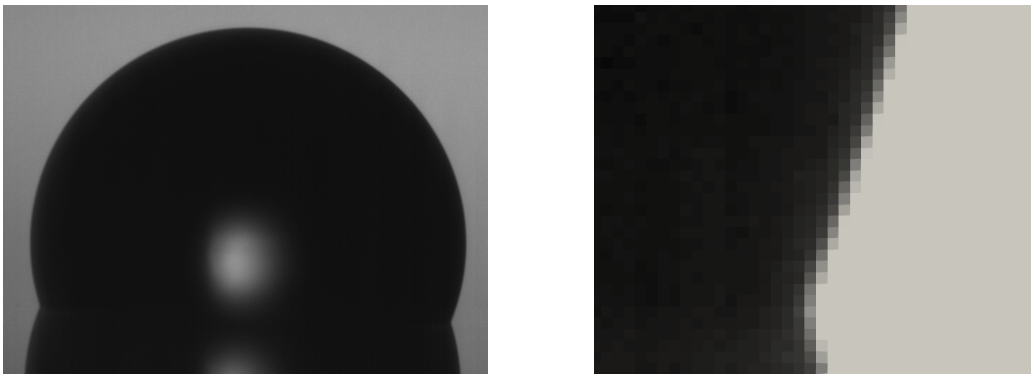

(a) Contact angle measurement. (b) Close-up at the contact line.

Figure 3: A typical contact angle measurement. Image of a droplet with a 1 µL volume at 25 °C and 25 % relative humidity. The left image was taken using a Photron SA-X2 with a Navitar 12X objectiv. Image on the left with courtesy of Max Hartmann, Institute for Nano- and Microfluidics, TU Darmstadt.

usually, this angle depends on the local composition of the solid surface and the distance from the solid surface at which it is measured. Depending on the liquid solid combination, some liquids tend to form a complete film over the surface, while others do not fully wet the surface. Hence, these two cases are called *complete* and *partial* wetting, respectively.

APPARENT CONTACT ANGLE A standard measurement technique to quantify a contact angle is to place a small amount of liquid onto a sample of the considered solid surface. This amount of liquid should be small enough, such that the shape of the interface is dominated by surface tension. This case can be observed in Figure 2, where the interface of the smaller liquid volumes form the shape of a spherical cap. To be precise, the relevant non-dimensional quantity is the ratio of droplet radius to the capillary length also known as the Bond or Eötvös number. For further details on the shape dependence on this non-dimensional quantity, compare Section 5.2.2. When the liquid drop is placed onto the surface, an image such as shown in Figure 3a is taken. Such images have a certain resolution that limits length scales that can be analyzed using this technique. A close-up of the contact line region of Figure 3a is shown in Figure 3b. Here, it is possible to distinguish single pixels which have the size of about 3 µm. In [11], a distance from the contact line, where a contact angle can be measured, is approximately 10 µm. Measurements in the dynamic setup are also able to measure the contact up to this distance to the wall [111]. This particular example of a dipping experiment is giving a good demonstration on how a dynamic contact angle can differ in close vicinity of the surface from the apparent contact angle observed on a larger length scale. To obtain a contact angle from such image data, a circular or an ellipsoidal section is typically fitted to the interface. Furthermore, to obtain information about a contact angle from this image data, a horizon has to be identified

the data sheet of dataphysics' CA measurement device reports a precision of 0.1° for CAs from 0° to 180°, [153]

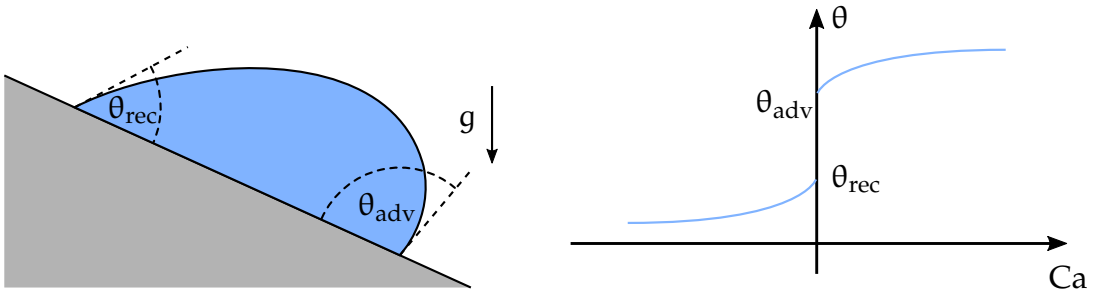

(a) A drop moving down an inclined wall under the influence of gravity.

(b) Dependency of the contact angle on the Ca number

Figure 4: Contact angle hysteresis for partially wetting liquids.

which is often done by hand. Hence, as the "actual" intersection of the interface with the solid surface is not resolved, whatever angle is measured on a macroscopic scale is referred to as *apparent contact angle*.

Another possible measurement techniques to obtain an estimate of the contact angle for a liquid-solid pairing is the conclusion from the stationary rise height of the liquid in a capillary [43]. Obviously, with this approach the contact angle is not measured directly. Therefore, the error depends on the model assumptions made for the particular situation. In the case of the capillary rise approach, Jurin's height is the formula at hand. See Chapter 5 for a derivation and an estimation of the involved errors.

HYSTERESIS, ADVANCING AND RECEDING CONTACT ANGLES While a drop is placed on a homogeneous horizontal surface as shown in Figure 3, the shape of the liquid volume is typically rotational symmetric and the contact angle is approximately constant along the contact line. However, when the plane is inclined with respect to the direction of gravity, the surface shape will change according to the influence of the volume force as illustrated in Figure 4a. The drop does not directly start to move as can be observed from rain drops sitting on a window glass or the droplets on the tilted parts of the leaf in Figure 2. Before the droplet starts to move, the contact angle changes until a certain threshold contact angle is reached. This threshold usually depends on whether the contact line will advance or recede with respect to the interface normal. The corresponding threshold angles are denoted as *advancing* and *receding* contact angles θ_{adv} and θ_{rec}, respectively, which are depicted in Figure 4a for a droplet moving down an inclined surface. Note that for such a physical droplet, the contact angle will of course vary along the contact line between the advancing and the receding region of the triple line. During the experimental observation of partially wetting liquids, it can be observed that the contact line starts to move when the advancing or receding contact angles are reached. This may e.g., be due to a movement or deformation of the interface. This situation is depicted in Figure 4b, where the contact angle is

shown over the Capillary number defined by $Ca := v_\Gamma \mu/\sigma$ with a contact line velocity v_Γ. For $Ca = 0$, the contact angle may change between the advancing and receding angle without a movement of the contact line. For a dynamic contact line the angle may also depend on the velocity of the dynamic contact line, which is typically expressed in a non-dimensional form, using the Ca-number. This behavior is also known as contact angle *hysteresis*.

As for the exact mechanism leading to this behavior, little compelling information is available. In [43] possible reasons for advancing receding behavior are listed: 1. surface roughness, 2. chemical contamination or inhomogenities in the surface and 3. solutes in the liquid. The author of [43] refers to [26], where the influence of surface roughness on the advancing and receding contact angle is analyzed using a surface that is coated with small pieces of wax. In general, basically all practical surfaces are rough to a certain degree as only few materials allow the production of surface that are smooth down to the molecular scale which are, e.g., mica or mono-crystalline silicon. Consequently, the behavior depicted in Figure 4 has to be expected on every technical surface.

CONTACT ANGLE DEPENDENCE ON CONTACT LINE VELOCITY For a water droplet moving over a surface due to gravitational forces, as depicted in Figure 4a, the contact line velocity and the Capillary number are rather small. In various applications, such as, e.g., curtain coating, a maximum contact line velocity is desirable to optimize production efficiency. Alternatively, the bulk phase can also be pushed or pulled to increase the contact line speed. A first observation that can be made in this case is the change of the dynamic contact angle related to the contact line velocity, as shown in Figure 4b. Various empirical models are available, attempting to capture this behavior [1, 149, 114, 119, 36, 120, 65, 17, 60, 138, 69, 66]. Usually, a monotonic behavior is reported, though anomalies have been found [9]. Furthermore, contact angle models motivated by hydrodynamic theory include those of [143, 89].

Somewhat more particular is the finding from [60, 65] which is the possibility to transform the experimental results for the dynamic contact angles from [60] to the master curve

$$\theta = f_{\text{Hoff}}\left(Ca + f_{\text{Hoff}}^{-1}(\theta_{eq})\right), \tag{1}$$

with the shift $f_{\text{Hoff}}^{-1}(\theta_{eq})$, giving a general relation for the contact angle. Note that this is only a heuristic model. Another popular relation is the one of [65, 17],

$$\frac{\cos(\theta) - \cos(\theta_{eq})}{\cos(\theta_{eq})} = f(Ca), \tag{2}$$

which is also known as the out-of-balance Young's force. The above relations are usually obtained from liquids that are pushed through cylindrical capillar-

ies, spreading drops or plates pulled from a pool of liquid. However, the existence of such master curves for general wetting processes has been doubted. In [10] it is demonstrated for water-glycerol solutions that the experimental data can not be transformed onto a master curve [124]. Furthermore, [96] mentions a possible influence of the test tube diameter on the relation.

A general limit for an advancing contact line is typically reached around $Ca \approx 1$, where air entrainment occurs. This phenomenon can for example be observed in coating applications, where the displacement of an air layer limits the coating speed.

HYDRODYNAMIC ASSIST In the applications of coating flows it has been observed that it is possible to reduce the contact angle by influencing the flow field in the contact line vicinity [12]. Hence, the term *hydrodynamic assist* was coined to emphasize the possibility to postpone air entrainment and allowing higher coating speeds [11]. These results suggest that the contact angle should in general depend on the flow field [124]. This experimental observation demonstrates that contact angle models of the type $\theta = f(Ca)$ is "at best, [...] incomplete" [11].

ROLLING MOTION In [33], the following intriguingly simple experiment can be found: A viscous drop of honey is placed on an initially planar and horizontal surface. To visualize the flow field on the interface, a small drop of food colorant is placed on the interface. On tilting the surface, the drop starts to move. The results of this experiment can be seen in the first row of Figure 5. Figure 5a shows the initial configuration with a dark dot which is the food colorant mark. In the subsequent Figures 5b to 5d, it can be seen that the dye mark moves towards the contact line. In the last figure, the dye mark has moved onto the plexiglas surface and below the bulk liquid. From this observation this flow feature has been termed *rolling motion*.

The second row in Figure 5 shows a recreation of the 1974 experiment. It was not possible to repeat the experiment using a water-based food colorant, as the colorant immediately spreads over the complete surface of the drop. The effect is presumably caused by the high water content of the food colorant. Instead, the food colorant has been resolved in water, mixed with a small amount of honey and heated in a microwave to reduce the water content of the honey dye mixture. The resulting colored honey had a viscosity slightly above the non-dyed honey. The pure honey drop is placed on a plexiglas surface with an inclination angle of approximately 30°. Analogously to the 1974 experiment, a rolling motion can be observed in Figures 5e to 5g, where the dye mark reaches the solid surface. In Figure 5h a top view is shown. Note that the blue dye mark is indeed located on the plexiglas surface. Interestingly, the dye mark has spread out significantly in contrast to the results of [33]. A diffusion effect of the food colorant can be excluded, as a colorant mark put on a stationary drop of honey did visually not change its shape during 5 min of

the material properties of the 1974 experiment were not reported

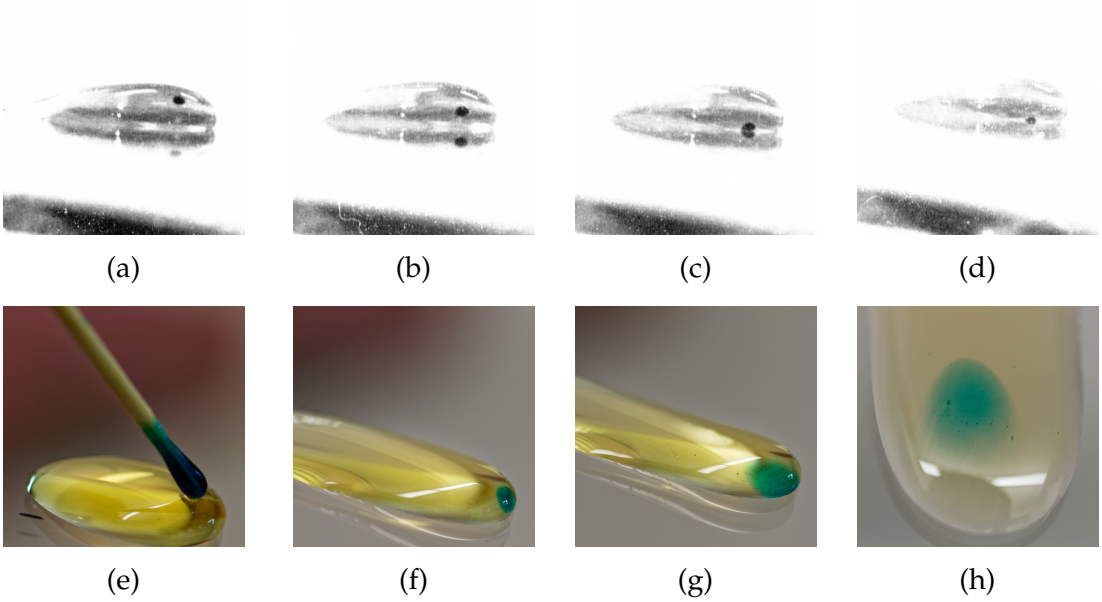

Figure 5: The first row shows the images from [33]. The second row shows a recreation of the rolling motion experiment. In contrast to the images from 1974, a significant spreading of the dye mark occurs.

observation. The time scale for the experiment in the second row of Figure 5 is approximately 30 s. Hence, a possibly reason for this effect seems to be the velocity field causing the creation of additional interface area.

Note that rolling motion is one of the features that has been subject to significant discussion concerning the interface formation model outlined in Section 2.2. The author of [124] refers to the experiments of [22] which show a velocity field in the bulk between $\pm 300\,\mu m$ around the contact line that is moving with $150\,\mu m\,s^{-1}$ to illustrate rolling motion. Indeed, a rolling motion can be observed in the bulk phase, but the same result holds true for any other approximate field if a particle is traced in the bulk phase [92, 32, 124, 40]. See Sections 2.2 for a more detailed discussion on the modeling aspect of this experimental observation.

PINNING When a liquid moves over a surface, the contact line may pin at certain locations on the substrate. This effect is suitably referred to as *pinning*. Various causes for the pinning of the contact line have been suggested. The contact line might be pinning at surface inhomogeneities or particles which can deposit from the liquid onto the substrate. Such effects can occur even after several purification cycles [99]. In general, especially surfaces with strong hysteresis tend to show pinning. Hence, in cases with strong hysteresis, low wetting speeds may not be accessible experimentally [11]. Nevertheless, such surface inhomogeneities are typically distributed randomly which makes a single pinning event hard to predict using continuum models.

PRECURSOR FILM When a small amount of liquid is placed on a surface, some liquid may spread ahead of the macroscopically observable contact line. This feature is accordingly referred to as *precursor film*. The length scale of such a precursor film is quantified in [124] to about 50-300 nm while referring to [3, 148, 7]. In [7], a profile for siloxane oil on glass is provided, where the thickness of the precursor film is below 250 nm. After 180 min the film extends by approximately 0.4 mm away from the contact line. In [43], the typical thickness of a precursor film is given to be below 100 Å, though no references or experimental justification is provided. The influence of the precursor film is typically considered negligible at least for industrial relevant processes [11, 124].

Note that in some experiments, the surface is *prewetted* by the liquid under investigation in combination with the assumption that the contact angle is zero. This approach is followed for example in [88], where the pressure dependence of the surface tension coefficient is investigated. While the apparent macroscopic contact angle may indeed be 0°, the situation is fundamentally different from a liquid advancing on a dry surface. The actual contact line may be stationary in such a case and the thin film left from the prewetting procedure is typically on the micro meter scale in contrast to an actual precursor film. While a precursor film may be present in various combinations of a liquid wetting a solid, it will be neglected in the remaining part of this work as no significant influence on the macroscopic behavior of the three phase system is to be expected [11, 124].

MULTI-SCALE NATURE OF WETTING Certainly, liquid surfaces can extend over large length scales of thousands of kilometres (that also wet, e.g., a ship hull) while single air bubbles may sit on surfaces that have radii down to the micro or even nano-meter scale [79]. However, it is not this feature of multiphase flows that is typically meant to when referring to "multiscale" in the context of wetting. It is rather the processes occurring at scales smaller than the capillary length and in close vicinity of a moving contact line. For example, in [111] a dipping plate experiment is performed where a planar plate is dipped into a pool of water. The reported surface shape shows significant curvature changes on a length smaller than 100 µm. Extrapolating from the measured interface data, the value of the apparent dynamic contact angle changes by more than 20° between a distance of 1 mm to 10 µm from the solid surface.

A similar observation has been made in [21], where a tapping mode atomic force microscope (TM-AFM) is used to give surface shapes of liquid moving over a mica surface. However, in this case surface shapes on a much smaller length scale than those measured in [111] are reported. The surface measured by the TM-AFM show significant curvature of the interface on length scales of 10-200 nm for contact line velocities of $V_\Gamma \approx 5\,\mathrm{nm\,s^{-1}}$. Obviously, such small variations are impossible to detect by an optical measurement, such as

along with mono-crystalline silicon, mica is one the the few materials that can give nearly smooth surfaces on the atomic scale

the one used to obtain the results shown in Figure 3, which are the standard method to quantify static and dynamic contact angles. This demonstrates that most available experimental results on contact angles can only be considered "apparent".

The next section gives an overview over different approaches to model wetting processes. Some of these models predict for example significant energy dissipation on every length scale between the macroscopic and microscopic scales [11, 128]. Hence, they give another example of the multiscale nature of wetting - in this case arising from the corresponding mathematical model.

2.2 CONTINUUM MODELS FOR WETTING

As outlined in the last section, experimental observations demonstrate that wetting is a multiscale process. Various models ranging from molecular dynamics on the smaller scales to density functional analysis and Boltzmann equations on the intermediate to continuum mechanical models can be applied on the various scales. However, numerous wetting processes relevant for engineering applications take place far above the nanometer length scale. Hence, a continuum mechanical model is suitable for the description of wetting and typically applicable above the nanometer scale for a wide range of parameters. Furthermore, this modeling approach is virtually standard for macroscopic fluid dynamic problems. Moreover, given the current development of computational processing power, the solution of molecular dynamics or even Boltzmann equations on a macroscopic scale is out of reach for the foreseeable future.

Ideally, a continuum model would be able to capture or even predict all relevant experimental observations and fulfill certain mathematical requirements, e.g. well-posedness or the ABC-criteria listed in [124]. In addition, following Occam's razor, the model should only use a minimal number of quantities that are necessary to characterize the wetting process. Besides, the model should be as simple as possible and require as little computational resources to solve it. The following section gives an overview over some modeling aspects as well as corresponding analytical results for different modeling approaches.

YOUNG'S EQUATION One of the first models for the wetting process goes back to [150, 30]. It considers a force balance at the contact line in a *stationary state* as depicted in Figure 6. A wedge-shaped region around the contact line is shown with a gas (g) and a liquid domain (l). Here, a liquid-gas, liquid-solid, and solid-gas surface tension coefficient σ_{lg}, σ_{ls}, and σ_{sg}, respectively, are considered. These quantify the contributing forces of the three interfaces. A force balance tangential to the surface yields

$$\sigma_{sg} = \sigma_{sl} + \sigma_{lg} \cos\theta, \tag{3}$$

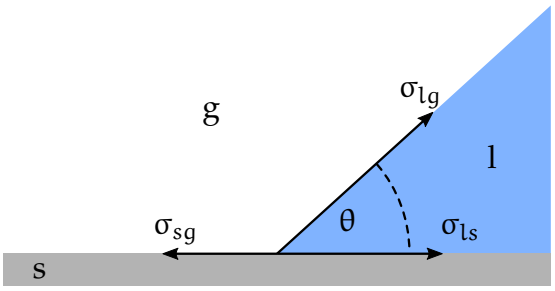

Figure 6: Illustration of the Young-Dupré equation.

where the contact angle θ is used. While the liquid-gas surface tension coefficient can be obtained using standard measurement equipment and the contact angle can be quantified using the standard methods associated with Figure 3, the two remaining surface tension coefficient are rather hard to measure. However, rearranging (3) shows that $\sigma_{sg} - \sigma_{sl}$ can be quantified. Using the surface tension coefficients, the *spreading parameter* is defined by

$$S = \sigma_{sg} - (\sigma_{sl} + \sigma_{lg}). \tag{4}$$

In experimental observations, this parameter is often used to distinguish whether a liquid completely ($S > 0$) or partially ($S < 0$) wets a solid. These cases correspond to contact angles $\theta = 0$ and $\theta > 0$, respectively, compare [43].

BOUNDARY CONDITIONS In a standard continuum mechanical model, boundary conditions (BC) are needed at the boundaries of each fluid domain. For this case, the change of total energy can be computed, yielding

$$\frac{dE}{dt} = -2\int_{\Omega\setminus\Sigma} \mu\mathbf{D} : \mathbf{D}\, dV + \int_{\partial\Omega} \langle \boldsymbol{v}, \mathbf{S}\mathbf{n}_{\partial\Omega}\rangle\, dA + \sigma\int_{\Gamma} (\cos\theta - \cos\theta_e) V_\Gamma\, ds, \tag{5}$$

where Ω is the fluid domain, Σ is the fluid-fluid interface, Γ is the contact line, E is the total energy of the system, $\boldsymbol{v}$ is the velocity of the fluid, $\mathbf{D} = (\nabla\boldsymbol{v} + \nabla\boldsymbol{v}^T)/2$ is the rate-of-deformation tensor, $\mathbf{S}$ is the Cauchy stress tensor, θ is an equilibrium contact angle and $\mathbf{n}_{\partial\Omega}$ is the outer normal to the domain boundary [39]. In order to satisfy the second law of thermodynamics in the considered isothermal case, the closures for $\mathbf{S}\mathbf{n}_{\partial\Omega}$ and θ have to be chosen such that $dE/dt \leqslant 0$. Note that the choice of boundary condition for the velocity field is directly related to $\mathbf{S}\mathbf{n}_{\partial\Omega}$ on $\partial\Omega$ which in parts may represent a wetted surface. Furthermore, the requirement may also yield a condition on the model for the contact angle which is often assumed to have the form $\theta = f(\theta_e, Ca, \dots)$ based on empirical relations such as listed in Section 2.1.

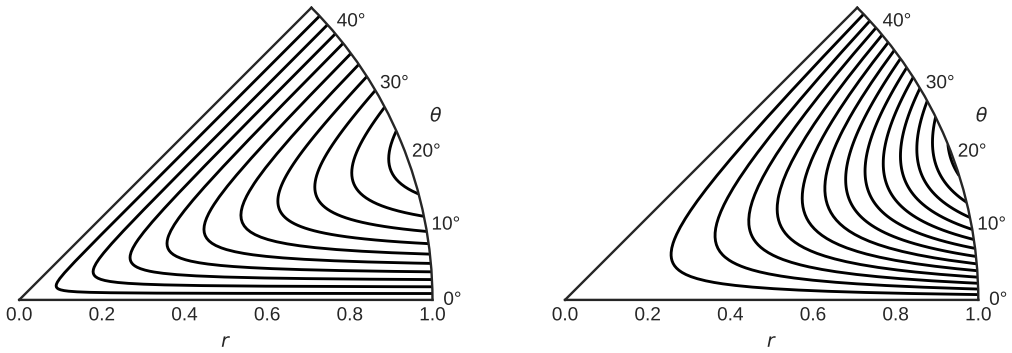

(a) No-slip. (b) Navier slip.

Figure 7: Comparison of contour plots for stream function solutions of Stokes flow in a wedge. The choice of boundary condition has a significant influence on the shape of the velocity field for $r \to 0$.

note that in [92] the given relations for general stream functions are inconsistent and the solution for no-slip boundary conditions is incorrect

NO-SLIP AT THE CONTACT LINE The no-slip boundary condition is a standard boundary conditions to model fluid wall interaction for single phase flows [5]. Hence, the combination of this boundary condition with a suitable contact angle model, also known as the *classical model*, is a first (naive) candidate to yield a well-posed model for wetting processes [124]. Yet, this is not the case. Considering the flow in a wedge and a description by stationary Stokes equations, it is possible to obtain a stream function solution [92] shown in Figure 7a. Using the same stream function approach, an extension of the analysis is provided in [62]. There, the interaction of a two-phase system with a wall boundary is considered, i.e., the gas phase is not neglected in contrast to [92]. The contributions of Moffatt, and Huh and Scriven have lead to what has become to be known has as the *moving contact line paradoxon*. In both contributions, the velocity field is multi-valued at the contact line [33]. Furthermore, the pressure is non-integrably singular at the contact line. It has to be noted that the stream functions from [92] as well as from [62] do only consider the flow field in a fixed wedge domain. It can even be shown that the solution to the classical model does not exist in a "physical-relevant class of smooth bounded functions", see [123, 124]. The argument is based on an asymptotic expansion of the two-dimensional flow in a wedge, which is considered in the leading order of the Reynolds number Re for $\mathrm{Re} \to 0$. The first expansion in this approach yields the velocity field presented in [92]. The subsequent correction of the interface shows that with the obtained diverging pressure field towards the contact line, the interface does not reach the wall. Nevertheless, if the normal stress condition is dropped, a solution of the problem seems to exists. However, the asymptotic expansion in this case shows that the bulk pressure as well as the stress acting on the solid surface are both non-integrably singular. Consequently, using this model, no finite

force would be able to submerge a solid object into a pool of liquid. Due to the non-existence of a solution and the strong unphysical properties, the no-slip boundary condition is not a viable choice to model wetting processes [124].

AVOIDING THE SINGULARITY Various authors have chosen to avoid an actual contact line. For example, in [84] it is assumed that the surface is prewetted by the spreading fluid. This approach is motivated by observations in [3] where a thin primary film of approximately 10 nm thickness is spreading ahead of a thick precursor film with a thickness of about 1 µm. Others assume long-range molecular forces [80] or ignore a region around the contact line up to some length scale l_m and apply a boundary condition to the outer surface. A somewhat similar approach is taken in [143], resulting in a model for the interface shape in the case of a moving contact line, namely

$$\frac{\partial^3 h}{\partial x^3} = -q\frac{3Ca}{h^2}, \qquad q \in \{-1, 1\}, \tag{6}$$

where q is $+1$ for advancing and -1 for receding contact lines [128]. To derive this equation, cut-off lengths for a large and a small length scale have been introduced. Furthermore, it should be emphasized that this approach assumes the surface to be wetted to some extend. This assumption is somewhat peculiar as this would mean that a significant liquid film is *always* present ahead of the macroscopically observable contact line. In addition, it also contradicts experimental observations regarding the spreading time scales of precursor films on much smaller length scales, cf. Section 2.1. However, as mentioned before, this approach leads to the Voinov contact angle model. While avoiding the singularity may yield useful results in certain setups, the usefulness of contact angle models in a general continuum model remains hard to evaluate and is most likely limited.

KINEMATIC CONSIDERATIONS Considering the findings in [92] and [62] the feature of rolling motion is analyzed in [33] with purely kinematic considerations. This line of argument demonstrates that the flow near the contact line indeed differs from the velocity field of a stagnation point. In this investigation, it is shown that even if only a kinematic description is used, the velocity field is multi-valued at the contact line. It is concluded that due to a purely kinematic reasoning an "emitted surface" must leave the contact line. Note that stream function solutions of [62] as well as a numerical solution with a slip boundary condition (see e.g. [135]) do also give a velocity field with a dividing stream line which further support this argument.

NAVIER SLIP AT THE CONTACT LINE As the no-slip boundary condition gives rise to non-integrable singularities, the use of a Navier slip boundary condition (going back to [95]) has been suggested in [62]. This boundary con-

dition reduces to a no-slip and a perfect slip boundary condition for vanishing and diverging slip length, respectively.

Again, asymptotic expansions and subsequent application of the stream function method are used to evaluate the properties. A constant slip coefficient on the solid surface allows to find the stream function solution [124] shown in Figure 7b. It can be seen that the stream lines for the Navier slip boundary condition are significantly less curved than those for the the no-slip case shown in Figure 7a. Hence, the streamline connecting the largest with the smallest angle for $r = 1$ will give a larger maximum velocity (close to the contact line) for the no-slip BC than the one for the Navier slip BC. The shapes of the stream functions are independent of the used length scale, while of course the contour values will change.

Similar to the no-slip case, the velocity field is not differentiable at the contact line. However, while the pressure is still singular, it is integrable in this case. Even though unique solutions to the ODE for path lines into the contact line exist if the velocity field is locally Lipschitz continuous, a particle may not reach the wall in finite time. Hence, the rolling motion that can be seen in experiments in Figure 5 can not be described using this particular choice of slip length distribution.

the logarithmic spiral has diverging curvature, yet a finite length and a finite contact angle

For a non-vanishing slip length the specific properties of this model depend on the choice of slip length distribution on the wall. The influence of slip length variation has been considered in [32]. The study is based on an asymptotic analysis for small Re, Ca and small deviations from a stationary contact angle. The second order terms give a problem that is solved with a stream function solution involving a Mellin transformation instead of the Bi-Laplace equation used in [92, 124] and [40]. Two of the velocity fields give a bounded limit for the radial derivative of the velocity field, i.e. $\lim_{r\to 0} \partial U/\partial r < \infty$. Hence, for these slip length distributions, the model can not describe a rolling motion of the interface. The third distribution gives a velocity field for which $\partial U/\partial r$ is unbounded. This field allows for a rolling motion of the interface. It is noteworthy that this velocity field allows for a non-divergent pressure at the contact line. Furthermore, the solution has a well behaved interface shape which is also computed using asymptotic analysis for $Eo \ll 1$. This demonstrates that it is possible to obtain a rolling or non-rolling interface depending on the distribution of the slip length. It should be noted that this distinction may be important in cases, where surfactants are present on the interface. Only a rolling motion can cause the surfactants to move from the interface to the wall boundary. More generally, if an impermeability condition is used at the solid wall boundary, then rolling motion of the interface is only possible if the velocity gradient $\|\nabla v\|$ is unbounded at the contact line. This is the case for both, the no-slip and the Navier slip boundary condition [33].

It is important to note that a motion that could be considered to be of "rolling type" can be found in any of the stream function solutions if a point however close to (but not on) the interface is considered. However, the discus-

sion of rolling motion for a point on the interface involves the well-posedness of the problem [124, 40].

Using a Navier slip boundary condition, e.g., for the simulation of a moving drop, the slip length of the Navier slip boundary condition has to be quantified. Utilizing molecular dynamics (MD) simulations, this slip length is typically quantified in the nano-meter range 1-100 nm, where systems with approximately 10^5 molecules [107] are used. A short overview of some slip lengths used in the literature is given in Table 5. A wide range of different slip lengths can be found, originating from various approaches and arguments. Regarding the modeling aspect, using a slip length significantly improves the model as it becomes at least weakly solvable. However, it also introduces a significant problem for the solution of the overall continuum model. If for example a liquid drop as shown in Figure 2 is to be simulated using a slip length in the nanometer range, this requires a significant mesh resolution which is necessary to resolve the different length scales. Furthermore, it should be noted that MD simulations usually consider surfaces that are perfectly smooth down to the molecular scale even though technical surfaces typically show roughness on and above the micro meter length scale.

Table 5: Literature values for the slip length, where R is the radius of a capillary.

reference	L in m
[61]	0.45-14.4 μm
[61]	10^{-9} m
[135]	0.02 R
[132]	10^{-9} m
[133]	10^{-6} m
[75]	10^{-9} m
[151]	2.8×10^{-10} m

One main tool to obtain the properties of a certain continuum model towards the contact line is an asymptotic expansion for small values of, e.g., Re, Ca, and Eo. This approach leads to a Bi-Laplace equation. An available solution to such an equation has been used in [92, 74] and can be forced to be continuous at the contact line in contrast to, e.g. the velocity field arising from such stream functions. Note the significant influence of the boundary condition on the shape of the velocity field as depicted in Figure 7. However, with the continuity-requirement and a finite slip length at the contact line it is possible to derive an evolution equation for the contact angle [40]. This means that, given a velocity field, the contact angle evolution can directly be computed from this information even in the more general case with a varying

surface tension coefficient. Hence, it is not possible to satisfy a contact angle model and obtain a differentiable solution at the contact line with this model.

INTERFACE FORMATION Changing the no-slip boundary condition to a Navier slip boundary condition allows for the existence of a solution and removes the (non-integrable) singularities at the contact line. However, the pressure field is still singular. Even though an integrable singularity (such as for the pressure) may be manageable in some settings, it is still unphysical.

A possible alternative, aiming to fully avoid the disadvantages of a model that uses a no-slip or Navier slip boundary conditions in combination with a no penetration condition at the wall may be the interface formation model (IFM) introduced in [122]. This model employs additional balance equations on each interface between liquid, solid, and gas and relaxes the no penetration boundary condition $\boldsymbol{v} \cdot \boldsymbol{n} = 0$ at the solid surfaces. Introducing these surface balance equations is motivated by relaxation time scales for liquid or gas molecules that reach the phase boundaries. For each of these domains, mass and momentum balances are incorporated. The surface tension for each of these domains depends, among others, on the associated surface mass density. To some extend, this can be interpreted as relieving the no penetration condition at the solid surface. The surface tension coefficient for each of the interface requires an additional constitutive equation. This introduces a variety of physical parameters that are not straight forward to quantify with macroscopic experiments or to interpret physically. However, the model comprises a possibly mathematically well-posed problem without the occurrence of any singularities at the contact line. In addition, a rolling motion is also inherent to the model. Moreover, one of the most promising features of the IFM is that it can possibly provide a contact angle as model output. Currently, the IFM is the only model that is capable to provide such an information [124].

Extending the mathematical model in the form of the IFM significantly increases the problem complexity considering its solution by a numerical approach as additional surface equations need to be solved. Furthermore, introducing surface balances requires a closure for the surface tensions $\sigma(\rho^{\Sigma})$, $\sigma_{\Sigma_l}(\rho^{\Sigma_l})$, and $\sigma_{\Sigma_g}(\rho^{\Sigma_g})$, which are the surface tension relations of the liquid-gas, liquid-solid, and gas-solid interfaces, respectively. The quantification of the corresponding coefficients is not straight forward in contrast to well understood coefficients such as those for surface tension, density or dynamic viscosity. In addition, the range of applicability for the IFM model may be limited to length scales below the micrometer range.

Recent approaches include reduced IFM models that have been used for quasi-stationary flow without change in contact angle [124, 85]. These models maintain the preferable properties of a bounded curvature and pressure at the contact line, while the surface conservation equations are reduced to ordinary differential equations for the surface densities. Furthermore, a tracer that starts on the interface reaches the wall in finite time. Possibly similar models

may yield a compromise between the full complexity of the IFM that can proof useful for standard engineering applications on a macroscopic scale. While the IFM offers various promising features, it has attracted opposition that the conventional hydrodynamic model is sufficient (accepting the divergent quantities) and the aforementioned relaxation time scales are too small to be relevant. See [35] and [125] for the response. Among others, the IFM has been implemented to simulate impact of rotationally symmetric drops onto planar surface, e.g. [70], or to handle general rotationally symmetric geometries such as capillaries, e.g. [132].

However, as of today, there is no fully agreed treatment of the wetting process that provides predictable results [11].

2.3 MOTIVATION AND AIM OF THIS WORK

As outlined in Section 1, wetting processes are essential to the effectiveness and efficiency of countless technologies. But not only is the simulation of the involved physical processes relevant to an industrial product optimization. Sections 2.1 and 2.2 outline that there is currently no agreed upon treatment of the wetting process itself. Furthermore, the influence of surfactants on the wetting process has been widely neglected.

The Collaborative Research Center 1194 (CRC1194), currently and in future funding periods aims at the investigation of the interaction between wetting and and additional transport phenomena. To cover the simulation demand within the various conducted experiments, a numerical tool that is capable to provide sharp interface representation to precisely represent the contact line vicinity is required. As future investigations also aim to consider the influence of surfactants on the wetting process, an Arbitrary Lagrangian-Eulerian (ALE) approach is chosen. This method represents the interface using the computational mesh, which can also be used to consistently discretize surface transport equations for the description of surfactant influences. Furthermore, the method should apply to non-trivial geometrical setups.

To fulfill the above requirements, the open-source software library OpenFOAM is employed. Specifically, an ALE approach that is under development at the Institute for Mathematical Modeling and Analysis (MMA) is to be extended. The basic version of this implementation is available in the OpenFOAM extend solver family and is known as ”interTrackFoam“. In its original form it goes back to [141, 140]. In the following, the approach extended at the MMA will also be referred to as the “ALE implementation“. OpenFOAM is a general numerical framework with an emphasize on the numerical solution of continuum mechanical problems using the finite volume method (FVM). This requirement also determines the discretization method to be FVM. Furthermore, OpenFOAM allows to utilize meshes with arbitrary polyhedral cells. Hence, the corresponding extension of the available ALE

method has to account for arbitrary polyhedral cell shapes and has to utilize the existing capabilities such as the available linear solvers.

To summarize, to be able to simulate wetting processes using the available implementation, the following additional developments and extensions are necessary

- a flexible contact angle library is to be implemented that integrates within the OpenFOAM platform and allows a flexible combination of contact angle models
- as a first implementation, Navier slip and free slip boundary conditions are to be implemented as `fvPatchFields`
- extend the control point algorithm on arbitrary contact line topologies
- suitable reference solutions to test the extension are to be identified and compared to the developed numerical approach

It should be emphasized that one of the major challenges is the seamless integration of the required functionality into the existing OpenFOAM library, which is a parallelized numerical framework written in templated C++ code. To verify the considered extensions, test cases have to be identified. While several stationary reference cases for multiphase flows without wetting effects are available, well understood solutions with moving contact lines are rather scarce. Therefore, providing detailed understanding of generally applicable test cases in, e.g., rotationally symmetric geometries, is desirable.

As generally applicable numerical implementations are long time investments far beyond the time scale of a PhD study, this work aims a development processes using the versioning tool *git* based on the online platform Bitbucket provided within the CRC1194. A corresponding workflow has to be developed and implemented.

The thesis proceeds as follows: Chapter 3 gives a short introduction to the standard continuum mechanical model for two-phase flows for a sharp interface representation. The relevant numerical background for the OpenFOAM ALE implementation and its extensions for wetting processes is described in Chapter 4. Building on the continuum mechanical description, an extended model for the case of a liquid rising in a capillary is derived in Chapter 5. The ALE implementation is tested against various verification cases with analytic solutions in Chapter 6. Special emphasize is given to the capillary rise test case. For this purpose, an overview over four fundamentally different numerical methods for multiphase flows is given at the beginning of Chapter 7. Furthermore, in a collaborative effort, the four methods are tested for the capillary rise benchmark providing publicly available reference data. These benchmark computations are presented towards the end of Chapter 7. In Chapter 8 some sample applications are presented that can be simulated with the developed solver. Finally, Chapter 9 gives a short summary of this

work and an outlook to possible future developments. The Appendix provides a list of inconsistencies that have been found in literature cited within this work, a full derivation of the oscillating pertubation solution of the capillary rise equation considered in Chapter 5, and additional scalings of the benchmark results presented in Chapter 7.

3

CONTINUUM MECHANICAL DESCRIPTION

In the case of two phase flows, the region separating the two phases, e.g. a liquid and a gas, is called *interface*. For physical systems away from the critical point a liquid-gas interface has a thickness on the scale of $10\,\mathrm{nm}$ and is modeled as a *sharp interface*, i.e., a mathematical hypersurface. No mass on this interface will be considered. In some limit cases for the ratios of liquid to gas densities, and dynamic viscosities, the influence of gas on the liquid phase may be neglected. In this case, the interface is referred to as a *free surface*.

3.1 CONSERVATION EQUATIONS

The following description of two-phase flows is restricted to incompressible isothermal flow of Newtonian fluids with constant density, which are immiscible on the molecular scale. For a constant density, such flows can be described by the incompressible Navier–Stokes equations. Such an approximation is typically suitable for liquids and for gases in the case of low Mach number flows. The bulk phases Ω_l and Ω_g are considered as subsets of a domain $\Omega \subset \mathbb{R}^d$ with $d \in \{1, 2, 3\}$ for times $t \in [t_0, t_{\mathrm{end}}) \subset \mathbb{R}$. The different domains are illustrated in Figure 8 for the case of a droplet sitting on a surface. Inside each of the phases, mass and momentum balances yield

$$\nabla \cdot \boldsymbol{v} = 0 \tag{7}$$

$$\partial_t(\rho \boldsymbol{v}) + \nabla \cdot (\rho \boldsymbol{v} \otimes \boldsymbol{v}) = \nabla \cdot \boldsymbol{S} + \rho \boldsymbol{g} \tag{8}$$

in $\Omega(t) \setminus \Sigma(t)$. Here, $\boldsymbol{v}$ is the continuum mechanical velocity, ρ is the density, and $\boldsymbol{g}$ is the gravitational acceleration. Furthermore, the stress tensor of the Newtonian fluid is given by

$$\boldsymbol{S} = -pI + \boldsymbol{S}^{\mathrm{visc}} \tag{9}$$

with $\boldsymbol{S}^{\mathrm{visc}} := \mu(\nabla \boldsymbol{v} + \nabla \boldsymbol{v}^T)$, where p is the pressure, $\boldsymbol{S}^{\mathrm{visc}}$ is the viscous stress

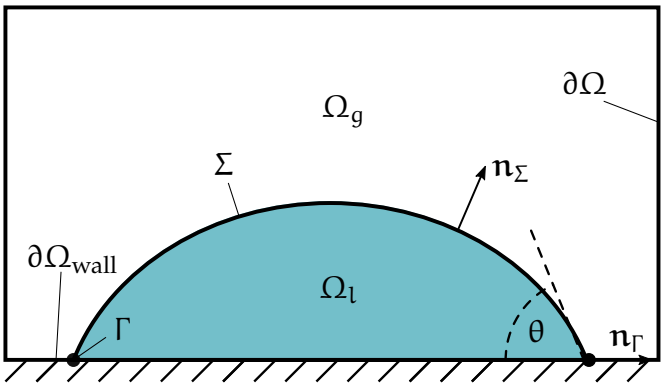

Figure 8: The different domains of the continuum mechanical model for a liquid (l) drop on surface $\partial\Omega_{\text{wall}}$ surrounded by a gaseous phase (g).

tensor and μ is the dynamic viscosity. The bulk equations are complemented by the transmission conditions

$$[\![\boldsymbol{v}]\!] = 0, \tag{10}$$

$$[\![p\mathbf{I} - \mathbf{S}^{\text{visc}}]\!]\mathbf{n}_\Sigma = \sigma\kappa\mathbf{n}_\Sigma + \nabla_\Sigma\sigma \tag{11}$$

at the interface Σ. The surface tension coefficient is denoted by σ and the total curvature is defined by $\kappa = -\nabla_\Sigma \cdot \mathbf{n}_\Sigma$ where $\mathbf{n}_\Sigma$ is the interface normal. In this case $\nabla_\Sigma \cdot \mathbf{f} := \operatorname{tr}(\nabla_\Sigma \mathbf{f})$ and $\nabla_\Sigma \mathbf{f} = (\mathbf{I} - \mathbf{n}_\Sigma \otimes \mathbf{n}_\Sigma)\nabla \mathbf{f}^e$, where $\mathbf{f}^e$ is a continuous differentiable extension of $\mathbf{f}$ from the interface to a tubular neighborhood $\mathcal{U}_\epsilon(\Sigma) \supset \Sigma$. This definition of curvature can be related to the mean curvature by $\kappa = (d-1)H$ where H is the mean curvature of the interface, [15]. For a function $\phi : \Omega \setminus \Sigma \to \mathbb{R}$, the jump brackets $[\![\cdot]\!]$ are defined by

$$[\![\phi]\!](\boldsymbol{x}_\Sigma) := \lim_{h \downarrow 0} (\phi(\boldsymbol{x}_\Sigma + h\mathbf{n}_\Sigma) - \phi(\boldsymbol{x}_\Sigma - h\mathbf{n}_\Sigma)). \tag{12}$$

The two conditions (10) and (11) not only couple the two sets of mass and momentum equations with each other, but also with the shape of the interface itself, as they involve the interface curvature κ. Furthermore, note that (10) gives a unique velocity $\boldsymbol{v}$ at the interface in contrast to cases with, e.g., phase change where the velocity field may be multi-valued on Σ.

KINEMATIC CONDITION In the general case, the interface Σ may deform over time. Let $\boldsymbol{x}_\Sigma(t)$ be a path through $\boldsymbol{x}_{\Sigma,0} \in \Sigma(t_0)$ that remains inside Σ for all $t > t_0$. At time t_0, the normal velocity at $\boldsymbol{x}_{\Sigma,0}$ is defined by

$$V_\Sigma(t_0, \boldsymbol{x}_{\Sigma,0}) = \lim_{t \to t_0} \frac{\langle \boldsymbol{x}_\Sigma(t) - \boldsymbol{x}_{\Sigma,0}, \mathbf{n}_\Sigma(t_0, \boldsymbol{x}_{\Sigma,0})\rangle}{t - t_0} \tag{13}$$

and is called *speed of normal displacement*. This leads to the *kinematic condition*

$$V_\Sigma = \boldsymbol{v} \cdot \mathbf{n}_\Sigma \tag{14}$$

for the displacement of the interface, which is actually a consequence of mass conservation in the absence of phase change. Note that the case considered here is the special case without considering mass on the interface and without phase change, i.e. $\dot{m} = 0$ across the interface. Also note that (14) guarantees that points in Σ remain on the interface while advected with $\boldsymbol{v}$. Any velocity field $\boldsymbol{v}$ that satisfies the kinematic condition for a given V_Σ is called a *consistent* velocity field [15].

BOUNDARY CONDITIONS One of the basic properties that can be attributed to a wall boundary is that no liquid should pass through it. This property is modeled by the so called *no penetration* or *impermeability condition*, i.e.

$$(\boldsymbol{v} - \boldsymbol{v}_w) \cdot \boldsymbol{n}_{\partial\Omega} = 0, \tag{15}$$

where $\boldsymbol{v}_w$ is the velocity of the wall. For single phase flows, the no penetration condition for the normal component of the velocity is typically combined with the *no-slip* boundary condition

$$\mathbf{P}_{\partial\Omega}(\boldsymbol{v} - \boldsymbol{v}_w) = 0, \tag{16}$$

where $\mathbf{P}_{\partial\Omega} := I - \boldsymbol{n}_{\partial\Omega} \otimes \boldsymbol{n}_{\partial\Omega}$ is the projector onto the local tangent space of the domain boundary and I is the unit tensor. This combination yields $\boldsymbol{v} = \boldsymbol{v}_w$. This model for the liquid wall interaction is a well established standard boundary condition for single phase flows [5, 31, 37]. A generalization of the no-slip boundary condition is the Navier boundary condition

$$\mathbf{P}_{\partial\Omega}(\boldsymbol{v} - \boldsymbol{v}_w) + \beta \mathbf{P}_{\partial\Omega} \mathbf{S}^{visc} \boldsymbol{n}_{\partial\Omega} = 0, \tag{17}$$

which goes back to [95]. Here, β is the *slip coefficient*. For $\beta > 0$ the inverse slip coefficient is $\lambda := 1/\beta$. This boundary condition allows a tangential velocity at the wall itself. The so-called slip length is defined by $L = \beta\mu$ as $[\beta\mu] = m$ which give for the unit of the slip coefficient $[\beta] = m^2\,s\,kg^{-1}$. Note that for $\beta = 0$ it follows that $L = 0$. Hence, (17) reduces to the usual no slip condition resulting in a homogeneous Dirichlet condition for the velocity $\boldsymbol{v} = 0$. For $\beta > 0$, multiplication of (17) by λ and taking the limit $\lambda \to 0$ gives the *free slip* boundary condition

$$\mathbf{P}_{\partial\Omega} \mathbf{S}^{visc} \boldsymbol{n}_{\partial\Omega} = 0. \tag{18}$$

The three phase *contact line* is the intersection between the two fluid phases and the solid surface, defined by $\Gamma(t) = \partial\Omega \cap \overline{\Omega_l}(t) \cap \overline{\Omega_g}(t)$, see Figure 8. At $\Gamma(t)$, a contact angle θ can be defined using

$$\cos\theta = -\langle \boldsymbol{n}_\Sigma, \boldsymbol{n}_{\partial\Omega} \rangle. \tag{19}$$

In the case of a liquid gas interface this angle is measured through the liquid from the solid surface to the liquid-gas interface. For the considered continuum mechanical model, an additional boundary condition for the contact

angle has to be specified. Such boundary conditions have been listed in Section 2.2 and are usually based on experimental results or are motivated by theoretical considerations. A general form of this type of boundary condition is given by

$$\theta = f(\theta_{eq}, Ca, \dots), \qquad \text{on } \Gamma, \tag{20}$$

where θ_{eq} is the equilibrium contact angle obtained from experiments as discussed in Chapter 2. Using the contact line normal

$$\mathbf{n}_\Gamma := \mathbf{P}_{\partial\Omega}\mathbf{n}_\Sigma / \left\|\mathbf{P}_{\partial\Omega}\mathbf{n}_\Sigma\right\|, \quad \text{at } \Gamma, \text{ for } 0 < \theta < \pi, \tag{21}$$

the contact line velocity is defined by $\boldsymbol{v}_\Gamma = V_\Gamma \mathbf{n}_\Gamma$, where $V_\Gamma = \boldsymbol{v} \cdot \mathbf{n}_\Gamma$. A local Capillary number is defined in terms of the contact line velocity V_Γ. This velocity enters the empirical contact angle models via the Capillary number which is defined as $Ca = \mu V_\Gamma / \sigma$. Note that the velocity V_Γ and thereby also the local Ca number may vary along the contact line.

As the pressure only occurs as derivative within the bulk equation, a reference pressure has to be specified. A possible choice is to specify a reference pressure at some boundary. Another possibility often used for theoretical considerations is to specify the average pressure p_0 as

$$\frac{1}{|\Omega|}\int_\Omega p \, dV = p_0. \tag{22}$$

THE FREE SURFACE APPROXIMATION Numerous applications involve the interaction of a liquid and a gas. In this case a free surface description may be sufficient which corresponds to $\rho_g/\rho_l \ll 1$, and $\mu_g/\mu_l \ll 1$, where subscripts l and g denote the liquid and gas phase, respectively. In this *free surface* limit, the model is restricted to the denser and more viscous phase for which the mass and momentum conservation equations (7) and (8) apply. The transmission conditions reduce to the free surface boundary conditions

$$-p\mathbf{n}_\Sigma + \mathbf{S}^{visc}\mathbf{n}_\Sigma = \sigma\kappa\mathbf{n}_\Sigma. \qquad \text{on } \Sigma. \tag{23}$$

In this case, the pressure reference p_a is often chosen as the ambient pressure.

For convenience, the list of all equations of the continuum mechanical model considered here is

$$\begin{aligned}
\nabla \cdot \boldsymbol{v} &= 0 && \text{in } \Omega \setminus \Sigma && (24)\\
\rho \partial_t \boldsymbol{v} + \rho \nabla \cdot (\boldsymbol{v} \otimes \boldsymbol{v}) &= \nabla \cdot \mathbf{S} + \rho \mathbf{g} && \text{in } \Omega \setminus \Sigma && (25)\\
\mathbf{S} &= -pI + \mu(\nabla \boldsymbol{v} + \nabla \boldsymbol{v}^T) && \text{in } \Omega && (26)\\
[\![\boldsymbol{v}]\!] &= 0, && \text{on } \Sigma && (27)\\
-[\![\mathbf{S}\mathbf{n}_\Sigma]\!] &= \sigma\kappa\mathbf{n}_\Sigma + \nabla_\Sigma \sigma && \text{on } \Sigma && (28)\\
V_\Sigma &= \boldsymbol{v} \cdot \mathbf{n}_\Sigma && \text{on } \Sigma && (29)\\
(\boldsymbol{v} - \boldsymbol{v}_w) \cdot \mathbf{n}_{\partial\Omega} &= 0 && \text{on } \partial\Omega_{\text{wall}} && (30)\\
\mathbf{P}_{\partial\Omega}(\boldsymbol{v} - \boldsymbol{v}_w) + \beta \mathbf{P}_{\partial\Omega} \mathbf{S}^{\text{visc}} \mathbf{n}_{\partial\Omega} &= 0 && \text{on } \partial\Omega_{\text{wall}} && (31)\\
\theta &= f(\theta_{eq}, Ca, \dots) && \text{on } \Gamma && (32)
\end{aligned}$$

where in the case of two-phase flows, the reference pressure is defined by

$$\frac{1}{|\Omega|} \int_\Omega p \, dV = p_0. \tag{33}$$

If a free surface problem is considered, the ambient pressure $p_a \in \mathbb{R}$ in the gas phase is usually used as reference. Furthermore, initial conditions for the velocity and the pressure field are required in Ω. In addition, boundary conditions may be required on $\partial\Omega \setminus (\partial\Omega_{\text{wall}} \cup \Gamma)$ which are chosen depending on a particular problem.

A more detailed derivation of the continuum mechanical model outlined above can be found in, e.g., [34, 127, 63, 106].

4

ARBITRARY LAGRANGIAN-EULERIAN INTERFACE TRACKING

The name Arbitrary Lagrangian-Eulerian approach is based on the flexibility of the involved description to arbitrarily, vary between a Lagrangian (also known as co-moving) and an Eulerian description. This allows to locally use a description to resolve physical effects such as steep gradients or moving domain boundaries. Even though it is also possible to consider volume of fluid approaches as ALE methods, cf. [4], the following considerations concentrate on a more specific approach.

The ALE method considered in this work represents the boundaries of a certain domain, e.g. liquid, solid, or gas, by a surface mesh. Hereby, the mass and momentum conservation equations are solved using the bulk mesh. This means, that if the domain boundaries deform, the mesh will have to follow this movement, which is, why the ALE approach as considered here, is also known as a *moving mesh method*.

One of the first applications of an ALE method go back to [97] and [59], where, among others, the flow of gas over a deforming sphere and the flow of an incompressible liquid in a deforming channel have been considered. While for instance the in- and outflow boundaries in a channel flow remain stationary (Eulerian part), the outer boundaries may deform over time (Lagrangian part). Hence, the location where boundary conditions need to be applied does change as well. The deforming mesh provides a suitable representation to apply boundary conditions if part of the mesh coincides with the domain boundary. Due to this property, the ALE method has grown to become a standard discretization method for solving fluid-structure-interaction problems. An introduction can be found in [27] and a formal introduction involving the analysis on manifolds is given in [2]. Due to the capability to adequately follow geometric deformations or resolve changing regions of interest, the approach is successfully applied in, e.g., soil mechanics [118, 130], impact problems [8], and Fluid Structure Interaction (FSI) [4].

The property to precisely resolve the movement of a domain boundary and a readily available surface mesh to compute surface properties such as curvature make the ALE method an interesting approach for the simulation of multiphase flows. Here, the deformation of a single (free surface) or two interacting fluid domains (e.g. two phase flows) are to be computed. The free

surface or transmission conditions can in these cases be applied using the available surface mesh. Embedded approaches, where for example a phase fraction field or tracer points are moved over a background mesh, can lead to ill-conditioned intersections with the background mesh. Such problems do not occur with ALE methods as long as an appropriate mesh motion method is applied. In addition, the ALE approach is less prone to the problematic effects of numerical diffusion or dispersion, which are for example present in algebraic VOF and phase field methods. This allows for a suitable context to, e.g., enforce a dynamic contact angle in wetting processes[49]. Beyond the benefit of a sharp interface representation, the boundary meshes can be used to capture additional physics. This makes the ALE approach particularly suitable when the influence of surfactants is of interest [102, 103]. Among others, the ALE approach has been applied in multiphase flows in [115, 116, 117]. Here, finite difference discretization is developed and applied in an extensive study of free rising and deforming bubbles. In [129], a stabilization method and preconditioning approach are introduced. The resulting algorithm is applied to liquid sloshing in a tank, a low resolved flow around a harbor installation and a vortex in a cylinder. The ALE approach is used to investigate magneto-hydrodynamic problems in [45, 46]. The same authors introduce a generalized Navier-boundary condition and apply it to the Couette flow benchmark for two fluids [44]. In addition, an explicit and implicit interface treatment is considered. Based on a finite element method a curvature discretization based on a variational formulation is introduced in [19]. The method is applied to the oscillating drop test case [72] and the reorientation of a liquid-gas surface after a gravity step reduction [91]. The ALE approach is often used for setups involving rotationally symmetric geometries. Here, one direction of motion for the interface mesh can be prescribed avoiding possibly fatal mesh deformation. Such applications can be found in [82, 6, 132, 133] where the influence of the Navier slip length on the shapes of quasi-stationary interface shapes is investigated. In addition, a detailed description of the FEM implementation can be found in [132] where also a special meshing approach is used to resolve the slip region near the contact line. The approach is applied to resolve the quasi-stationary flow in a rotationally symmetric capillary, where the coordinate system is co-moving with the contact line. A discussion of ALE approaches in comparison to various other numerical approaches for multiphase flows can be found in Chapter 7.

For the present work, an ALE implementation based on the OpenFOAM framework is used. The original implementation is due to [141] and available in OpenFOAM extend version 3.1. This version has been extended at the Institute of Mathematical Modeling and Analysis and is used as the basis for the present work.

This chapter proceeds as follows. First, the local conservation equations from Chapter 3 are converted into an integral formulation using arbitrarily moving control volumes. Then, an overview of the overall algorithmic ap-

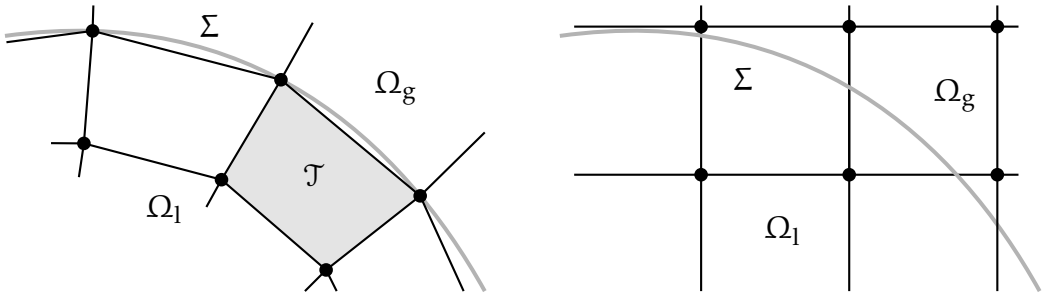

(a) ALE mesh. (b) Background mesh.

Figure 9: Comparison of ALE- and background meshes around the interface Σ illustrated by a gray continuous line.

proach is given. This outlines the method that couples the movement of the interface with the solution of the pressure-velocity system within each fluid phase. The following section describes the mesh motion approach with an emphasize on the control point (CP) algorithm which is used for the movement of the interface. Based on this control point algorithm, the chapter concludes with a description of the implemented extension of the CP-algorithm to simulate wetting processes.

4.1 FORMULATION FOR MOVING CONTROL VOLUMES

The computational domain $\Omega = \Omega_1(t_0) \cup \Omega_2(t_0) \cup \Sigma(t_0)$ is tessellated by non-intersecting control volumes $\mathcal{T}_c$, which are also known as cells. This tessellation is chosen such that part of the boundary of the discretized bulk phase is an approximation of the interface as illustrated in Figure 9a. The analytic interface is illustrated by a gray line. Note that the mesh points (black dots) are located on this interface. This allows to represent the interface by a surface mesh formed by a boundary of the bulk mesh. While for two-phase flows, this boundary is an internal boundary, where the transmission conditions are applied, it represents the boundary of the overall domain in the case of a free surface. Various other methods such as level-set, front-tracking, phase field, and algebraic as well as geometric volume of fluid methods chose a different representation of the interface that is moving over a background mesh. This approach is depicted in Figure 9b. Within this approach an additional representation of the interface is required, e.g. a phase fraction in a VOF approach or tracer points in a front tracking approach. However, using a regular or octree meshes offers potentially faster algorithms as no changing cell volumes, or face areas have to be recomputed. However, such methods may have to deal with ill-condition intersection of the respective interface representation with the background mesh. For a more detailed comparison between various approaches see Chapter 7.

4.1.1 *The Mesh Motion Map*

The description given in this section is based on the definition of the diffeomorphism Ψ. This is in contrast to, e.g., [27, 141, 140], where the mesh motion velocity is introduced on an ad hoc basis and usually arises from using an integral balance over an arbitrarily moving control volume.

The deformation of the ALE mesh is described for $\Omega \subset \mathbb{R}^d$ by a family of diffeomorphisms

$$\Psi^t : \Omega \to \Omega,\ t \in [t_0, t_{end}) \text{ with } \Psi^{t_0} = \mathrm{id}, \tag{34}$$

which are defined on Ω. Here $(t, \mathbf{x}) \to \Psi^t(\mathbf{x})$ is at least $\mathcal{C}^1$. As this map is used to describe the deformation of the mesh, it is called *mesh motion map*. This map generates trajectories starting at $\mathbf{x}_0 \in \Omega$ by

$$\Psi^t(\mathbf{x}_0) =: \mathbf{x}(t; t_0, \mathbf{x}_0). \tag{35}$$

Note that it is also possible to consider the discrete analog of 34. Using this trajectory and taking the time derivative, defines the *mesh velocity* $\boldsymbol{v}_b$ as

$$\boldsymbol{v}_b := \frac{d}{dt}\mathbf{x} = \dot{\mathbf{x}}. \tag{36}$$

So far, the mesh motion map is not related to any motion of the two-phase flow system. To provide such a coupling, (36) is integrated such that the mesh motion map can be expressed via

$$\Psi^t(\mathbf{x}_0) = \mathbf{x}_0 + \int_{t_0}^{t} \boldsymbol{v}_b(\tau, \Psi^\tau(\mathbf{x}_0))\, d\tau. \tag{37}$$

Note that defining the mesh motion map by (37) requires $\boldsymbol{v}_b$ to be integrable, while providing a mesh motion map Ψ^t has to be a diffeomorphism in order to define the mesh velocity in (36). For a general ALE approach, the movement of the mesh does not require many restrictions to follow the deformation - it is indeed arbitrary, except for the domain boundaries. In order to follow the interface in a multiphase flow, the interface mesh has to follow the deformations of the actual interface. Hence, it is desirable to follow the interface with a subset of the mesh in a partially Lagrangian way. The minimal requirement to follow the deformation of the interface is for the normal part of the mesh motion velocity to agree with the normal part of the interface velocity. This means restricting the mesh motion map by a coupling to the interface motion via

$$\boldsymbol{v}_b \cdot \mathbf{n}_\Sigma = V_\Sigma \quad \text{on } \Sigma, \tag{38}$$

where the speed of normal displacement V_Σ is defined in (13). In general, no additional coupling to the hydrodynamic solution is necessary to maintain a

mesh motion velocity that is consistent with the deformation of the solution domains. It is possible to also couple the tangential component of the mesh velocity on the interface to the interface velocity in a fully Lagrangian manner, leading to $\boldsymbol{v}_b = \boldsymbol{v}_\Sigma$ on Σ. However, such an approach may yield undesirable properties: Consider the Stokes flow regime for a gas bubble rising in a liquid corresponding to the reference solution of Hadamard–Rybczynski [55]. The flow is, in the most part of the interface, tangential to it and directed from the top to the bottom of the bubble. If the points would follow the flow in a fully Lagrangian manner, the mesh resolution would continue to decrease at the top and an increases at the bottom of the bubble. An alternative choice for the tangential component of the surface mesh velocity is to set $\mathbf{P}_\Sigma \boldsymbol{v}_b = 0$. This yields

$$\boldsymbol{v}_b = V_\Sigma \boldsymbol{n}_\Sigma \quad \text{on } \Sigma, \tag{39}$$

which is the choice of movement that the basic form of the control point algorithm derived in Chapter 4 is aiming at. As long as the deformations and the change of the center of mass of, e.g., a bubble or an oscillating droplet are small, condition (39) is sufficient to maintain an acceptable mesh quality at the interface.

While (39) is used to define $\boldsymbol{v}_b$ on Σ, the mesh motion in the bulk phases has to follow the deformations of the interface. The choice of a suitable algorithm to move the bulk mesh is subject to additional requirements: When the interface deforms, such cells in close vicinity should remain almost unchanged to maintain the initial mesh quality. On the other hand, the mesh resolution may need to maintain or change in regions where, e.g., strong gradients have to be resolved. This can, for example, be a strong shear flow or a concentration boundary layer near a boundary. In addition, the bulk mesh motion should require as little resources as possible, which is the reason why some authors refer to spring models [141]. One rather general approach to maintain a sufficient mesh quality for a wider range of interesting applications is to use a diffusion equation for the bulk mesh,

$$\nabla \cdot (\mathbf{D} \nabla \boldsymbol{v}_b) = 0 \quad \text{in } \Omega, \tag{40}$$

where the diffusivity tensor $\mathbf{D}$ can be used to steer the mesh as needed. Hence, the diffusivity tensor is in general inhomogeneous and anisotropic. Note that this is a diffusion equation that is defined based on the mesh motion velocity. As boundary conditions for this diffusion equation, the definition of the coupling condition (39) is used to ensure a consistent mesh velocity field.

In addition, boundary conditions are required at the domain boundaries. These may be chosen such that the boundary mesh does not move or such that it slides along the boundary. The latter may be required for example in wetting simulation such that the mesh representing the wall boundary can

follow the movement of the contact line. Hence, as boundary conditions on non-interface boundaries

$$\mathbf{P}_{\partial\Omega}\boldsymbol{v}_b = 0, \quad \text{or} \quad \mathbf{P}_{\partial\Omega}\boldsymbol{v}_b = \mathbf{P}_{\partial\Omega}\boldsymbol{v}, \quad \text{on } \partial\Omega \setminus \Sigma \tag{41}$$

is used. The set $\partial\Omega \setminus \Sigma$ may consist of, e.g., wall and inflow boundaries with $\boldsymbol{n}$ as its outer normal. Altogether, the flow map Ψ is defined by (34), (37), (40), (39) and one of the conditions from (41).

The initial mesh tessellates the initial simulation domain $\Omega(t_0)$ with cells $\mathcal{T}_0$ at time t_0. This tessellation is such that the interface is represented by a subset of mesh faces. Let $\mathcal{T}_0$ be the set of points of such a cell at the initial time t_0. Then, the evolution of this set is defined using the mesh motion map by

$$\mathcal{T}(t) := \Psi^t(\mathcal{T}_0). \tag{42}$$

4.1.2 *Mass Conservation*

As described above, the conservation equations are solved on the evolving incompressible sub-domains $\Omega_l(t)$ and $\Omega_g(t)$. To discretize the bulk equations, they are integrated over a moving control volume $\mathcal{T}$ such as shown in Figure 9a. Integrating the mass conservation equation (7) gives

$$\int_{\mathcal{T}(t)} \nabla \cdot \boldsymbol{v} \, dV = \int_{\partial\mathcal{T}(t)} \boldsymbol{v} \cdot \boldsymbol{n} \, do = 0. \tag{43}$$

Adding $\int_{\partial\Omega} \boldsymbol{v}_b \cdot \boldsymbol{n} \, do$ on both sides and applying the Reynolds Transport Theorem gives

$$\frac{d}{dt}|\mathcal{T}(t)| = \int_{\partial\mathcal{T}(t)} (\boldsymbol{v}_b - \boldsymbol{v}) \cdot \boldsymbol{n} \, do, \tag{44}$$

where $|\mathcal{T}(t)|$ denotes the volume of the control volume $\mathcal{T}(t)$. The summation over all control volumes that tessellate Ω_i (for phase $i \in \{l, g\}$) gives

$$\frac{d}{dt}|\Omega_i(t)| = \int_{\partial\Omega_i(t)} (\boldsymbol{v}_b - \boldsymbol{v}) \cdot \boldsymbol{n} \, do. \tag{45}$$

When the boundaries are closed, i.e., if no-penetration boundary conditions are used, it follows from (38) that

$$\frac{d}{dt}|\Omega_i(t)| = 0 \tag{46}$$

which is the volume conservation of phase i. Hence, global volume conservation follows from local volume conservation. For

$$\int_{\partial\Omega} \boldsymbol{v} \cdot \boldsymbol{n} \, do = 0, \tag{47}$$

(45) reduces to an equation also known as the *space conservation law* [139, 25], i.e.,

$$\frac{\mathrm{d}}{\mathrm{dt}} \int_{\Omega_i(t)} 1 \,\mathrm{dV} = \int_{\partial\Omega_i(t)} \boldsymbol{v}_b \cdot \boldsymbol{n} \,\mathrm{do}. \tag{48}$$

Note that this relation is a consequence of the mass conservation of a certain "volume" if the flow is incompressible.

4.1.3 *Momentum Conservation*

Integrating the momentum conservation equation (8) over a moving control volume $\mathring{\mathcal{T}}(t) \cap \Sigma(t) = \emptyset$ gives

$$\int_{\mathcal{T}(t)} \partial_t(\rho \boldsymbol{v}) \,\mathrm{dV} + \int_{\mathcal{T}(t)} \nabla \cdot (\rho \boldsymbol{v} \otimes \boldsymbol{v}) \,\mathrm{dv} = \int_{\mathcal{T}(t)} \operatorname{div} \boldsymbol{S} \,\mathrm{dV} + \int_{\mathcal{T}(t)} \rho \boldsymbol{g} \,\mathrm{dV}. \tag{49}$$

Adding $\int_{\partial V(t)} \rho \boldsymbol{v} \otimes \boldsymbol{v}_b \cdot \boldsymbol{n} \,\mathrm{dV}$ on both sides and applying the Reynolds Transport Theorem for arbitrarily moving control volumes yields

$$\begin{aligned} \frac{\mathrm{d}}{\mathrm{dt}} \int_{\mathcal{T}(t)} \rho \boldsymbol{v} \,\mathrm{dV} = &\int_{\partial\mathcal{T}(t)} \rho \boldsymbol{v} \otimes \boldsymbol{v}_b \cdot \boldsymbol{n} \,\mathrm{dV} \\ &- \int_{\mathcal{T}(t)} \nabla \cdot (\rho \boldsymbol{v} \otimes \boldsymbol{v}) \,\mathrm{dV} + \int_{\mathcal{T}(t)} \operatorname{div} \boldsymbol{S} \,\mathrm{dV} + \int_{\mathcal{T}(t)} \rho \boldsymbol{g} \,\mathrm{dV}. \end{aligned} \tag{50}$$

Using the divergence theorem to combine the integrals over the convective terms results in

$$\frac{\mathrm{d}}{\mathrm{dt}} \int_{\mathcal{T}(t)} \rho \boldsymbol{v} \,\mathrm{dV} = \int_{\partial\mathcal{T}(t)} \rho \boldsymbol{v} \otimes (\boldsymbol{v}_b - \boldsymbol{v}) \cdot \boldsymbol{n} \,\mathrm{dV} + \int_{\mathcal{T}(t)} \operatorname{div} \boldsymbol{S} \,\mathrm{dV} + \int_{\mathcal{T}(t)} \rho \boldsymbol{g} \,\mathrm{dV}. \tag{51}$$

This equation is referred to as the *integral momentum conservation equation*. For the implementation in OpenFOAM , a *modified pressure* defined as

$$\tilde{p} = p - \rho \langle \boldsymbol{g}, \boldsymbol{x} \rangle \tag{52}$$

is used. With the model for the Cauchy stress tensor (9) the gravity term can be combined with the pressure term yielding

$$\int_{\mathcal{T}(t)} \operatorname{div} \boldsymbol{S} \,\mathrm{dV} + \int_{\mathcal{T}(t)} \rho \boldsymbol{g} \,\mathrm{dV} = -\int_{\mathcal{T}(t)} \nabla \tilde{p} \,\mathrm{dV} + \mu \int_{\mathcal{T}(t)} \Delta \boldsymbol{v} \,\mathrm{dV}. \tag{53}$$

This allows to combine and thereby reduce the number of terms that have to be discretized. However, using (52) the boundary and transmission conditions have to be adapted accordingly. Reformulating (11), using the modified pressure $\tilde{p}$, gives

$$[\![\tilde{p} \boldsymbol{n}_\Sigma + \rho \langle \boldsymbol{g}, \boldsymbol{x} \rangle \boldsymbol{n}_\Sigma - \boldsymbol{S}^{\mathrm{visc}} \boldsymbol{n}_\Sigma]\!] = \sigma \kappa \boldsymbol{n}_\Sigma + \nabla_\Sigma \sigma \qquad \text{on } \Sigma. \tag{54}$$

With the definition of the jump brackets, the free surface boundary conditions are

$$-\tilde{p}\mathbf{n}_\Sigma - \rho\langle \mathbf{g}, \mathbf{x}\rangle \mathbf{n}_\Sigma + \mathbf{S}^{\text{visc}}\mathbf{n}_\Sigma = \sigma\kappa\mathbf{n}_\Sigma + \nabla_\Sigma\sigma \qquad \text{on } \Sigma. \tag{55}$$

From here on the tilde will be dropped and the modfied pressure will be denoted by p in the context of the ALE implementation.

4.1.4 *Transmission Conditions using Surface Operators*

The transmission conditions at the interface are reformulated to simplify the implementation within the OpenFOAM framework. This reformulation aims to utilize surface and normal derivatives. This allows to use the finite area implementation of OpenFOAM, which can be considered an analog of the finite volume discretization applied to a curved surface. The available framework provides a flexible implementation of discrete surface differential operators for the surface gradient, the surface divergence and the surface Laplacian. To obtain this formulation, a relation for deformable slip surfaces from [20] is used:

$$\mathbf{n}_\Sigma \otimes \mathbf{n}_\Sigma : \mathbf{D} = -\nabla_\Sigma \cdot \boldsymbol{\nu} \quad \text{at } \Sigma. \tag{56}$$

where $\mathbf{D} = (\nabla\boldsymbol{\nu} + \nabla\boldsymbol{\nu}^T)/2$ is the rate of strain tensor. Projecting the momentum transmission conditions (54) into the surface normal direction and applying (56) gives

$$[\![p]\!] = \sigma\kappa - [\![\rho]\!]\langle \mathbf{g}, \mathbf{x}\rangle - 2[\![\mu]\!]\nabla_\Sigma \cdot \boldsymbol{\nu}, \tag{57}$$

where the contribution of the gravity term results from the use of the modified pressure (52).

Projecting (54), onto the tangential space of the interface and applying certain relations for the projection of the velocity gradient and (56), the author of [141] arrives at

$$\mathbf{n}_\Sigma \cdot [\![\mu\nabla\boldsymbol{\nu}]\!] = -\nabla_\Sigma\sigma - \mathbf{n}_\Sigma[\![\mu]\!]\nabla_\Sigma \cdot \boldsymbol{\nu} - [\![\mu]\!](\nabla_\Sigma\boldsymbol{\nu})\mathbf{n}_\Sigma \tag{58}$$

as a reformulation of the tangential part of 54. With this formulation of the momentum transmission conditions, the right side of (58) is formulated using surface derivatives of the velocity field. These operators are discretized using the surface operators within the OpenFOAM framework. For more details on this discretization see [141].

4.2 OVERALL ALGORITHMIC APPROACH

The integral formulation derived in Section 4.1 has to be discretized and linearized to obtain a system of equations that can subsequently be solved using

linear iterative solvers. For the discretization of the bulk equations, a collocated finite Volume Method (FVM) is used [58, 101]. The momentum transmission condition (11) has been reformulated to use surface operators giving (58) and (57). This discretization is enforced within each loop of the pressure velocity coupling. To provide the context in which the surface movement algorithm is used, Figure 10 shows an overview of the general algorithm for the interface tracking approach.

After the initialization step, the time loop is started. This loop is repeated until n_{max} iterations are reached, where $n_{max} := \lceil (t_0 - t_{end})/\Delta t \rceil$. As a first step the bulk mesh is moved to follow the interface deformation computed in the former time step. The bulk mesh movement is skipped in the first time step as no interface deformation has taken place yet.

When the momentum equation is solved in the previous non-linear iteration, a new velocity field is obtained. This velocity is then extrapolated to the interface mesh and yields a volume flux for each face of the interface mesh, which is called *face volume flux*. To ensure that interface mesh represents the actual interface, it has to be moved in order to compensate for the face volume flux for each face of the interface mesh. To obtain a phase volume conserving movement of the interface mesh, the control point (CP) algorithm (colored in dark gray) is applied. This algorithm is aiming to compensate the face volume flux at the interface and is described in detail in Section 4.3.3. Note that this step corresponds to finding an interface location that satisfies the constraint (39). Hence, it aims to find a consistent mesh motion velocity for the interface mesh. As the CP-algorithm may introduce high frequency oscillation of the interface it is possible to apply a surface smoothing step. However, it should be noted that this smoothing step is optional. The CP-algorithm is derived in detail for a surface without boundary in Section 4.3.3. In Section 4.4 an extension for a surface with a boundary is presented. Following the initial movement of the interface, a loop to for the solution of the non-linear terms is started. These are on the one hand side the convection term in the momentum conservation equations (8). On the other hand, obtaining the discrete interface for the next time step involves the computation of flux volumes and the computation of curvature. This loop is executed i_{max} times. The number of maximum iterations can either be preset to a fixed integer or can be based on the residuals of the linear solver for the discrete momentum equation. The non-linear iteration starts with enforcing the transmission conditions. For this purpose, the discretized transmission conditions (58) and (57) are used. In the next step, the discrete momentum conservation equation is solved using a pressure predictor. This means that to solve the momentum conservation equation for the velocity of the current iteration, the pressure field from the previous non-linear iteration is used. The initial step is using the pressure field from the former time step.

In the next sub-algorithm an iteration process also known as PISO (pressure implicit with splitting of operators) going back to [64] is executed. This

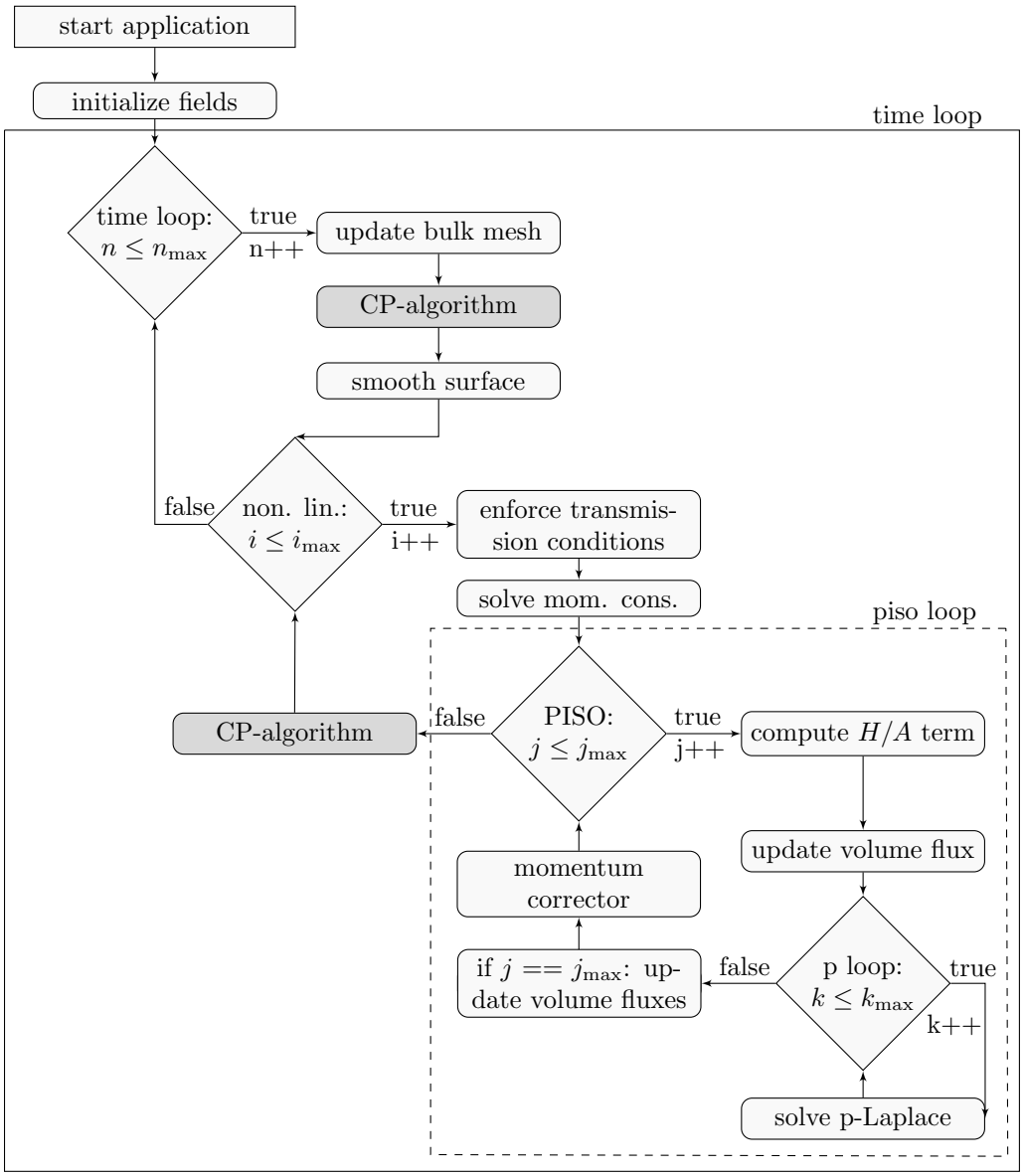

Figure 10: Top level algorithmic overview.

approach is an iterative procedure to find the velocity and pressure fields that solve the equation system that arises from the discrete mass and momentum conservation equations on a fixed domain. As for the loops before, the maximum number of PISO-iterations j_{max}, can be chosen as a fixed number or may be based on the residual of the linear solver of the discrete pressure-Laplace equation.

The first steps of the PISO loop involve computation of an approximate solution of the right hand side of the pressure Laplace equation denoted by the H/A-term. Note that the interpolation of this term from the face centers to the cell centers has been adapted in [140] aiming to reduce a time step dependence of the overall algorithm. A first (partial) update of the volume flux field is computed before solving the pressure-Laplace equation. The pressure-Laplace equation can be solved several times to reduce the error on non-orthogonal meshes, see e.g. [24, 93]. The pressure loop ends with updating the face volume fluxes and the velocity field using the results of the latest solution of the pressure-Laplace equation.

Note that for a maximum number r_{max} of iterations of the CP-algorithm, the interface is moved $r_{max}(i_{max}+1)$-times. Moreover, the pressure Laplace equation is solved $i_{max}j_{max}k_{max}$-times which is typically the most time-consuming part of the overall algorithm. For more details on the implementation of the pressure velocity coupling see [141, 140].

STABILITY In [140], a restriction on the time step is given

$$\Delta t < \sqrt{\frac{\rho \min(L_{PeN})}{2\pi\sigma}} \tag{59}$$

with an argument that this time step limit is smaller than the shortest period for capillary waves with a reference to [16]. While many numerical approaches refer to this reference, it should be noted that such a time step limit is based on a heuristic argument that involves the velocity of capillary waves on the interface. This line of argument arrives at

$$\Delta t < \sqrt{\frac{\langle\rho\rangle(\Delta x)^3}{2\pi\sigma}} \tag{60}$$

as restriction on the time step. Here, the average density is $\langle\rho\rangle := 1/2(\rho_l + \rho_g)$. Note that this restriction contains the mesh width Δx *cubed*, where Δx is the mesh width of the homogeneous background mesh of an algebraic volume of fluid (VOF) approach used in [16]. It is surprising that relation (59) from [140] does not contain this exponent and indeed the extend 3.1 implementation is based on $\Delta t < \sqrt{\rho \min(L_{PeN})^3/(2\pi\sigma)}$. Note that this is a significant difference for choice of a time step. See Appendix A for a list of similar inconsistencies.

4.3 MESH MOTION

Within the overall algorithm outlined in the previous chapter, the surface mesh has to be moved to follow the deformations of the interface. The CP-algorithm, which is used for this purpose, requires various discrete properties of the interface mesh. These mesh properties, together with the CP-algorithm for closed surfaces, are described in the following. In addition, an extension of the CP-algorithm to surfaces with boundaries is described and applied for the simulation of wetting processes.

4.3.1 *Mesh Properties in OpenFOAM*

One of the distinguishing features of OpenFOAM is the capability to deal with unstructured meshes that can consist of combinations of arbitrary polyhedral cells. In the following, a few mesh quantities are defined to simplify the description of the algorithms outlined below. While some of the formula below may seem redundant in some cases, the definitions attempt to reflect the OpenFOAM implementation as close as possible. For an outline of the corresponding data-structures see e.g. [48, 93].

To describe certain neighborhood relations between vertices, edges, faces and cells of the computational mesh, the following sets are defined:

$$\mathrm{ngb}_P(p) := \{\text{all vertices connected with vertex } p \text{ (by an edge)}\} \tag{61}$$

$$\mathrm{ngb}_E(p) := \{\text{all edges that use } p\} \tag{62}$$

$$\mathrm{ngb}_F(p) := \{\text{all faces that use } p\} \tag{63}$$

$$\mathrm{ngb}_C(p) := \{\text{all cells that use } p\} \tag{64}$$

These definitions easily extend to other cases, e.g., $\mathrm{ngb}_F(f)$ is the set of faces that share an edge with the face f and $\mathrm{ngb}_C(c)$ is the set of cells that share a face with the cell c.

Furthermore, to define different types of boundary conditions, the boundary of Ω is split into various subsets. The different parts of the discrete mesh are split accordingly. To denote the set of points, edges, or faces for such *patches* of the domain boundary, a tilde is used, e.g. $\tilde{\Sigma}$ denotes the discrete interface. Furthermore, the set of vertices of the interface mesh is denoted by $\tilde{\Sigma}_P$, while $\tilde{\Sigma}_F$ is the set of faces that is used to approximate Σ.

The definitions and derivations below make use of an abuse of notation in the following sense: If an entity is associated with a certain geometric quantity, a corresponding index is used. That is, p is used for a vertex, e for an edge, f for a face and c for a cell c. For example, the location of a mesh point is denoted by x_p, while an edge center is referred to as x_e. Accordingly, x_f is a face center and x_c a cell center, as illustrated in Figure 11.

FACE NORMALS For the computation of a *face normal*, the face is triangulated with respect to the face center, which is defined by

$$\boldsymbol{x}_f = \frac{1}{|\mathrm{ngb}_P(f)|} \sum_{p \in \mathrm{ngb}_P(f)} \boldsymbol{x}_p, \tag{65}$$

where $|\mathrm{ngb}_P(f)|$ denotes the cardinality of $\mathrm{ngb}_P(f)$. The connection vector between two vertices p_1 and p_2 with $p_1 \neq p_2$ is denoted by

$$\boldsymbol{e}_{p_1,p_2} := \boldsymbol{x}_{p_2} - \boldsymbol{x}_{p_1}. \tag{66}$$

Note that the edge vector may also be written as $\boldsymbol{e}_e$. The normal of a single triangle $\tilde{f}$ in the triangulation process of the face f is computed by

$$\boldsymbol{n}_{\tilde{f}} = \frac{\boldsymbol{e}_{f,p} \times \boldsymbol{e}_{f,p+1}}{\|\boldsymbol{e}_{f,p} \times \boldsymbol{e}_{f,p+1}\|_2 + \mathtt{SMALL}} \tag{67}$$

where $\tilde{f}$ denotes one of the triangles used to triangulate the face f. The connection vector between the face center $\boldsymbol{x}_f$ and a point $\boldsymbol{x}_p$, $p \in \mathrm{ngb}_P(f)$ is denoted by $\boldsymbol{e}_{f,p}$. To dampen the influence in cases where $\|\boldsymbol{e}_{f,p} \times \boldsymbol{e}_{f,p+1}\|_2$ is small, the value SMALL is added. This value is 10^{-15} in OpenFOAM standard settings. Using (67) the face normal for face f is computed by

$$\boldsymbol{n}_f = \sum_{\tilde{f}} \boldsymbol{n}_{\tilde{f}} / \Big|\Big| \sum_{\tilde{f}} \boldsymbol{n}_{\tilde{f}} \Big|\Big|_2, \tag{68}$$

where $\tilde{f}$ refers to the triangles used in the triangulation of face f. The normal is always oriented, such that it points out of the domain to which the boundary patch is associated. The face normals are illustrated by arrows with a black tip in Figure 11.

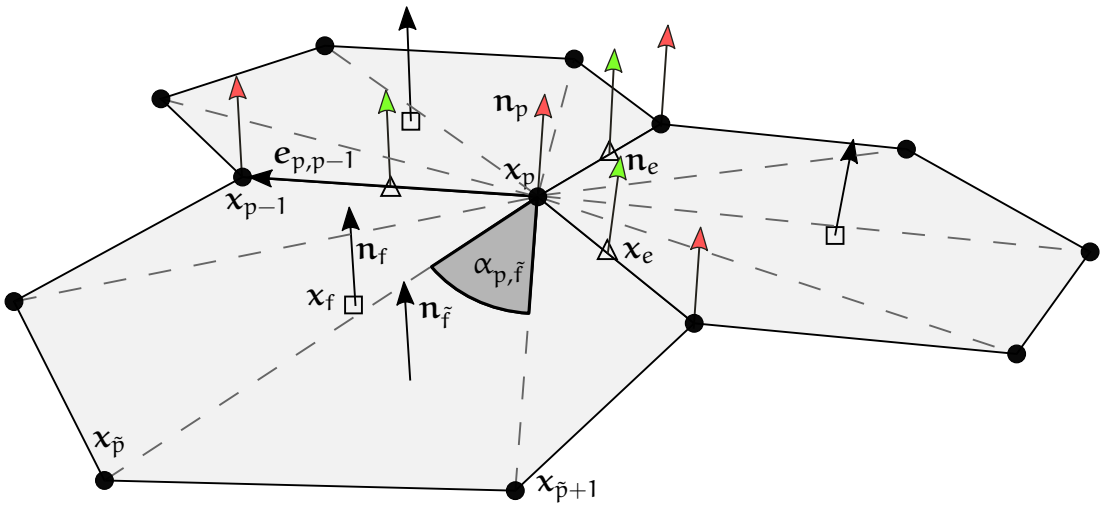

Figure 11: Geometrical quantities of the polyhedral surface mesh in OpenFOAM .

POINT NORMALS A surface *point normal* $\mathbf{n}_p$ is associated with each surface mesh point $\mathbf{x}_p$. The computation of this point normal uses a triangulation similar to the approach that is used for the face normals. However, this triangulation is centered around $\mathbf{x}_p$, as illustrated in Figure 11 by the gray dashed lines. With this approach, the faces on the surface mesh using $\mathbf{x}_p$ are split into triangles such that $\mathbf{x}_p$ and two additional points form a triangle. For example, in Figure 11, the points $\mathbf{x}_p$, $\mathbf{x}_{\tilde{p}}$, and $\mathbf{x}_{\tilde{p}+1}$ form such a triangle. Each of these triangles has an opening angle $\sin \alpha_{p,\tilde{f}}$ at the point $\mathbf{x}_p$, defined by

$$\sin \alpha_{p,\tilde{f}} = \frac{\|\boldsymbol{e}_{p,\tilde{p}} \times \boldsymbol{e}_{p,\tilde{p}+1}\|_2}{\|\boldsymbol{e}_{p,\tilde{p}}\|_2 \|\boldsymbol{e}_{p,\tilde{p}+1}\|_2}. \tag{69}$$

The face normal of each triangle is computed by

$$\mathbf{n}_{\tilde{f}} = \frac{\boldsymbol{e}_{p,\tilde{p}} \times \boldsymbol{e}_{p,\tilde{p}+1}}{\left\|\boldsymbol{e}_{p,\tilde{p}} \times \boldsymbol{e}_{p,\tilde{p}+1}\right\|_2 + \texttt{SMALL}}. \tag{70}$$

which is weighted by

$$w_{\tilde{f}} = \frac{\sin \alpha_{p,\tilde{f}}}{\|\boldsymbol{e}_{p,\tilde{p}}\|_2 \|\boldsymbol{e}_{p,\tilde{p}+1}\|_2}, \tag{71}$$

yielding the weighted sum

$$\tilde{\mathbf{n}}_p := \sum_{\tilde{f}} w_{\tilde{f}} \mathbf{n}_{\tilde{f}}. \tag{72}$$

The weighting of each normal by (71) has been introduced to the OpenFOAM ALE-method by Tukovic [141], while the weighting itself goes back to Max [90]. Finally, the point normals are obtained by a normalization of (72), yielding

$$\mathbf{n}_p := \tilde{\mathbf{n}}_p / \left\|\tilde{\mathbf{n}}_p\right\|_2. \tag{73}$$

The corresponding point normal field is illustrated in Figure 11, by arrows with a red tip.

EDGE NORMALS While the point normal vectors are associated with the surface mesh points, an *edge normal* is defined on each surface edge that connects, e.g., a point p_1 and p_2. This edge vector is computed by

$$\tilde{\mathbf{n}}_e = (\mathrm{I} - \boldsymbol{e}_{p_1,p_2} \otimes \boldsymbol{e}_{p_1,p_2}) \tilde{\mathbf{n}}_e (\mathbf{n}_{p_1} + \mathbf{n}_{p_2}). \tag{74}$$

The projection ensures that the edge normal is orthogonal to the edge vector $\boldsymbol{e}_{p_1,p_2}$. The edge vector is obtained by normalization of (74), giving

$$\mathbf{n}_e := \tilde{\mathbf{n}}_e / \left\|\tilde{\mathbf{n}}_e\right\|_2. \tag{75}$$

The edge normal field is illustrated by arrows with a green tip in Figure 11.

CURVATURE The discretization of the total curvature κ is based on the divergence theorem for curved surfaces

$$\int_{\partial\Sigma} \mathbf{f}^{\Sigma} \cdot \mathbf{N}\, ds = \int_{\Sigma} \operatorname{div}_{\Sigma} \mathbf{f}^{\Sigma}\, do + \int_{\Sigma} \kappa_{\Sigma} \mathbf{f}^{\Sigma} \cdot \mathbf{n}_{\Sigma}\, do, \tag{76}$$

where Σ is a surface with boundary $\partial\Sigma$, see [146, p. 239]. Here, $\mathbf{N}$ is the bi-normal, which is tangent to Σ and normal to $\partial\Sigma$. Using $\mathbf{f}^{\Sigma} = \boldsymbol{e}_i$ with $i \in \{1, 2, 3\}$, it follows from (76) that

$$\int_{\Sigma} \kappa_{\Sigma} \mathbf{n}_{\Sigma}\, do = \int_{\partial\Sigma} \mathbf{N}\, ds. \tag{77}$$

This equation motivates the computation of the total curvature that is based on the sum of a discretized bi-normal over the boundary of a face of the surface mesh. For this purpose, the bi-normal $\mathbf{N}$ is approximated by

$$\tilde{\mathbf{t}}_e = \mathbf{n}_e \times \boldsymbol{e}_e \tag{78}$$

at each edge of the surface mesh, where $\mathbf{n}_e$ is the edge normal vector defined in (75), and $\boldsymbol{e}_e$ is the vector between the start and end point of the edge e. For a face that "owns" the edge, the tangent vector is defined by

$$\mathbf{t}_e = -\operatorname{sign}(\tilde{\mathbf{t}}_e, \mathbf{x}_f - \mathbf{x}_e)\tilde{\mathbf{t}}_e. \tag{79}$$

With this definition, $\mathbf{t}_e$ is defined such that it points out of the face that "owns" the edge. For a general description of "owner" and "neighbor" relations in OpenFOAM see [48]. A weighted sum of the tangent vectors approximates the integral on the right hand side of (77), yielding

$$\tilde{\mathbf{n}}_f = \sum_{e \in \mathrm{ngb}_E(f)} S_e \cos(\alpha_e/2)\mathbf{t}_e, \tag{80}$$

where the contribution of each tangent vector is weighted based on the angle between two point normal vectors at points p_1 and p_2. This angle is defined by

$$\sin(\alpha_e) = \|\mathbf{n}_{p_1} \times \mathbf{n}_{p_2}\|_2 . \tag{81}$$

Finally, the curvature associated with a face f is computed by

$$\kappa_{\Sigma,f} = \operatorname{sign}(\langle \tilde{\mathbf{n}}_f, \mathbf{n}_f \rangle)\, \|\tilde{\mathbf{n}}_f\|_2 . \tag{82}$$

Note that the "sign"-factor ensures that the curvature is positive if the surface Σ is curved into the direction of the face normal $\mathbf{n}_f$.

SWEPT VOLUME When the interface is moved, a certain area is swept. The swept volume flux is defined by

$$\delta\dot{V}_f(t) = \int_{S_f(t)} \boldsymbol{v}_b(t) \cdot \boldsymbol{n}(t)\, do \tag{83}$$

Integration of (83) in time gives

$$\delta V_f^{n+1} := \int_{t^n}^{t^{n+1}} \int_{S_f(t)} \boldsymbol{v}_b(t) \cdot \boldsymbol{n}(t)\, do\, dt \tag{84}$$

which is the volume δV_f^n that is swept from t^0 to t^n by the face f. An approximation of 84 is computed by triangulating the swept volume using tetrahedral volumes. For this purpose, the moving face is decomposed using the same approach as for the computation of the face normal field. Then, the volume that is swept by each triangle is computed by the sum of three tetrahedral volumes. The volume of a tetrahedron between the points $\boldsymbol{x}_{p_1}, \boldsymbol{x}_{p_2}, \boldsymbol{x}_{p_3}, \boldsymbol{x}_{p_4} \in \mathbb{R}^3$ is computed by

$$V(\boldsymbol{x}_{p_1}, \boldsymbol{x}_{p_2}, \boldsymbol{x}_{p_3}, \boldsymbol{x}_{p_4}) := \frac{|(\boldsymbol{x}_{p_1} - \boldsymbol{x}_{p_4}) \cdot (\boldsymbol{x}_{p_2} - \boldsymbol{x}_{p_4}) \times (\boldsymbol{x}_{p_3} - \boldsymbol{x}_{p_4})|}{6} \tag{85}$$

Let $\boldsymbol{x}_{p_1}, \boldsymbol{x}_{p_2}, \boldsymbol{x}_{p_3} \in \mathrm{ngb}_P(\tilde{f})$ be the points of the triangle $\tilde{f}$ before and $\tilde{\boldsymbol{x}}_{p_1}, \tilde{\boldsymbol{x}}_{p_2}, \tilde{\boldsymbol{x}}_{p_3} \in \mathrm{ngb}_P(\tilde{f})$ after a displacement of the original face f. Then the swept volume is approximated by

$$\delta V_n^f \approx \frac{1}{2}(V_1 + V_2) \tag{86}$$

where

$$V_1 = V(\tilde{\boldsymbol{x}}_{p_1}, \boldsymbol{x}_{p_2}, \boldsymbol{x}_{p_3}, \boldsymbol{x}_{p_1}) + V(\tilde{\boldsymbol{x}}_{p_2}, \boldsymbol{x}_{p_3}, \tilde{\boldsymbol{x}}_{p_1}, \boldsymbol{x}_{p_2}) + V(\boldsymbol{x}_{p_3}, \tilde{\boldsymbol{x}}_{p_2}, \tilde{\boldsymbol{x}}_{p_1}, \tilde{\boldsymbol{x}}_{p_3}) \tag{87}$$

$$V_2 = V(\tilde{\boldsymbol{x}}_{p_1}, \boldsymbol{x}_{p_2}, \boldsymbol{x}_{p_3}, \boldsymbol{x}_{p_1}) + V(\boldsymbol{x}_{p_2}, \tilde{\boldsymbol{x}}_{p_1}, \tilde{\boldsymbol{x}}_{p_3}, \tilde{\boldsymbol{x}}_{p_2}) + V(\boldsymbol{x}_{p_3}, \boldsymbol{x}_{p_2}, \tilde{\boldsymbol{x}}_{p_1}, \tilde{\boldsymbol{x}}_{p_3}) \tag{88}$$

The volumes V_1 and V_2 can be interpreted as two different tetrahedron-based approximations of the swept volume δV_f. Note that this is in contrast to [141].

4.3.2 *Discretization of the Space Conservation Law*

As illustrated in Figure 10, the interface location is update before and after the PISO algorithm. A basis for the movement of the interface movement is (48) as derived above for a phase volume $\Omega_i(t)$. The same derivation can be applied to the arbitrarily moving control volume $\mathcal{T}$ (a cell with index c):

$$\frac{d}{dt} \int_{\mathcal{T}(t)} 1\, dV = \int_{\partial\mathcal{T}(t)} \boldsymbol{v}_b \cdot \boldsymbol{n}\, do. \tag{89}$$

Note that these cells are chosen such that a subset of the mesh faces represent the interface. The temporal derivative is discretized using a second order backward differentiation scheme in time. The right hand side integral is approximated by a mid-point rule yielding

$$\frac{3V^{n+1} - 4V^n + V^{n-1}}{2\Delta t} = \sum_{f \in \mathrm{ngb}_F(c)} \boldsymbol{v}_{b,f}^{n+1} \cdot \mathbf{S}_f^{n+1} = \sum_{f \in \mathrm{ngb}_F(c)} \delta \dot{V}_f^{n+1} \tag{90}$$

where $V^n := |\mathcal{T}^n|$ has been used. Furthermore, $\mathbf{S}_f^{n+1} := S_f^{n+1} \mathbf{n}_f^{n+1}$ and S_f^n is the area of the face f at time step $n+1$. The right hand side of (90) can be reinterpreted by defining the *swept volume flux* for a face f by $\delta \dot{V}_f^{n+1} := \boldsymbol{v}_{b,f}^{n+1} \cdot \mathbf{S}_f^{n+1}$. However, integrating (89) from t^n to t^{n+1} and t^{n-1} to t^n, respectively, allows to express the change in volume of a mesh cell by the swept volumes for consecutive time steps by

$$V^{n+1} - V^n \approx \sum_{f \in \mathrm{ngb}_F(c)} \delta V_f^{n+1} \tag{91}$$

$$V^n - V^{n-1} \approx \sum_{f \in \mathrm{ngb}_F(c)} \delta V_f^{n}. \tag{92}$$

Inserting these two expressions for the volume differences between two consecutive time steps into (90) gives

$$\frac{3 \sum_{f \in \mathrm{ngb}_F(c)} \delta V_f^{n+1} - \sum_{f \in \mathrm{ngb}_F(c)} \delta V_f^{n}}{2\Delta t} = \sum_{f \in \mathrm{ngb}_F(c)} \delta \dot{V}_f^{n+1}. \tag{93}$$

Now, the task is as follows: Find locations $\mathbf{x}_p^{n+1}$ for all points on the discrete interface to minimize

$$\varphi_f^{n+1} - \delta \dot{V}_f^{n+1} \tag{94}$$

for all faces $f \in \tilde{\Sigma}$. Here, $\varphi_f^{n+1} := \boldsymbol{v}_f^{n+1} \cdot \mathbf{S}_f^{n+1}$ is the *volume flux* through the face f with face area S_f^{n+1}, which is part of the interface mesh at time step $n+1$. For this purpose, the movement of a single cell-face is considered, specifically the movement of a face of the discrete interface. The interface at two subsequent iterations r and $r+1$ is shown in Figure 12. In this case, only a single face $\tilde{f}$ is moved and the right hand side of (93) can be approximated by the swept volume flux of this face. The volume $\Delta t \varphi_f$ that is flowing through face f is illustrated in blue. The swept volume δV_f^r is in this case formed by the points $\mathbf{x}_p^r, \mathbf{x}_{p+1}^r, \mathbf{x}_p^{r+1}, \mathbf{x}_{p+1}^{r+1}$.

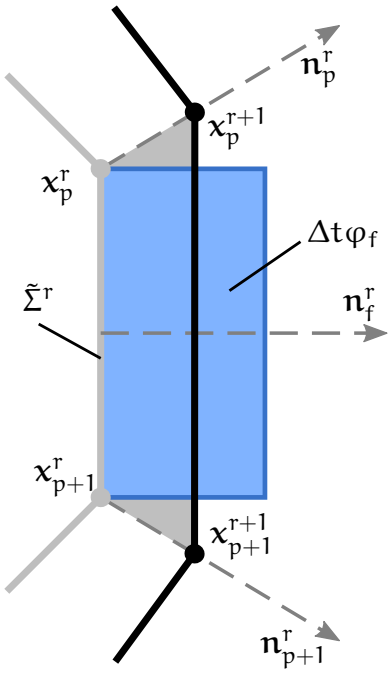

Figure 12: Difference between volume fluxes and swept volumes.

This consideration motivates to approximate (93) by

$$\delta \dot{V}_f^{n+1} \approx \frac{3}{2} \frac{\delta V_f^{n+1}}{\Delta t} - \frac{1}{2} \frac{\delta V_f^n}{\Delta t} \tag{95}$$

for the backward differencing scheme. An analog computation for the implicit Euler scheme gives

$$\delta \dot{V}_f^{n+1} \approx \frac{\delta V_f^{n+1}}{\Delta t}. \tag{96}$$

which is also used as startup for the backward differencing scheme. These two approximation are suitable in the case where the flux volume is mostly cause by the displacement of a single face. The CP-algorithm presented in the next section is taking advantage of this particular property. For this iterative search, r is used as index for the subsequent iterations.

4.3.3 *The CP-Algorithm for Surfaces without Boundaries*

A possible approach for the movement of the interface is the *control point algorithm* (CP-algorithm) going back to [94]. While the original version is provided for 2D flows, the algorithm has been extended in [141] for 3D flows. The algorithm aims to minimize (94) and thereby to find a consistent velocity field for the mesh points of the interface. If (94) equals zero for every interface face then the phase volume is also conserved. The CP-algorithm is applied in an iterative procedure - possibly serveral times per time step - to minimize (94)

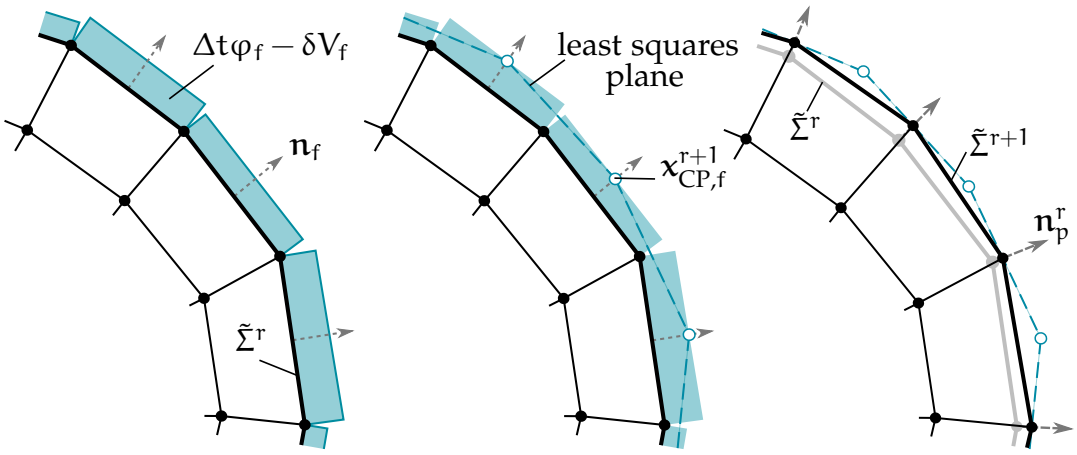

(a) Face flux volumes. (b) Control points. (c) Point displacement.

Figure 13: Control point algorithm at the interface.

locally. The following description explains the CP-algorithm which is used in the overall algorithm, cf. Figure 10. The CP-algorithm itself consists of various steps illustrated in Figure 13. The index for the subsequent iterations of the CP-algorithm is $r \in \mathbb{N}$. For surfaces without boundaries, the CP-algorithm consists of the following steps:

1. **Definition of control points**
   A *control point* $\mathbf{x}_{CP,f} \in \mathbb{R}^d$ is associated with every face (with index f) of the interface mesh. Each control point is initialized at the center $\mathbf{x}_f$ of its associated face, hence

   $$\mathbf{x}_{CP,f}^0 = \mathbf{x}_f. \tag{97}$$

   Note that the interface changes with consecutive iterations of the CP-algorithm. Hence, the face center is not necessarily the face center of the last time step, c.f. Figure 10.

2. **Define displacement directions**
   The *face* and *point displacement directions* $\mathbf{d}_f \in S^{d-1}$ and $\mathbf{d}_p \in S^{d-1}$, respectively, are computed. The face displacement directions are typically chosen in face normal direction defined by (68), i.e.

   $$\mathbf{d}_f = \mathbf{n}_f. \tag{98}$$

   Such a displacement can for example be suitable for the simulation of an oscillating droplet.

   The *point displacement directions* $\mathbf{d}_p$ are defined by the point normals (73), i.e.

   $$\mathbf{d}_p = \mathbf{n}_p^n. \tag{99}$$

In cases where a predominated displacement direction can be expected the displacement directions can also be set to a common arbitrary direction. For more general volume displacements, the above choice of displacement direction may be insufficient.

3. **Computation of the control point displacement**
The distance by which the control points are moved is computed by

$$h_f^{r+1} = \frac{\Delta t \varphi_f - \delta V_f^r}{\mathbf{S}_f^r \cdot \mathbf{d}_f} \tag{100}$$

This formula is based on the assumption that the complete volume flux is flowing in orthogonal direction through the face f. The problem is illustrated for the 2D case in Figure 12 and similarly in Figure ref-fig:cpAlgorithm1 as starting point of the CP-algorithm . In the considered case, (100) is only an approximation, as the flux volume (blue area) is to be compensated by the swept volume which is the quadrilateral formed by $\mathbf{x}_p^r, \mathbf{x}_{p+1}^r, \mathbf{x}_p^{r+1}, \mathbf{x}_{p+1}^{r+1}$. In a general 3D problem, the situation becomes even more challenging as the boundaries of the swept volume are not necessarily planar in contrast to the 2D case. This motivates the repetitive application of the CP-algorithm to minimize (94).

4. **Update the control point locations**
The location of the control points is updated by

$$\mathbf{x}_{CP,f}^{r+1} = \mathbf{x}_{CP,f}^r + h_f^{r+1} \mathbf{d}_f. \tag{101}$$

This step is illustrated in Figure 13b. The control points are depicted by white circles with a blue boundary. Updating the CP location corresponds to placing them onto the boundary of the of the blue flux flux volumes. Note that the displacement direction does not change during the various CP-iterations.

5. **Compute weighted least square (LS) plane**
A weighted least squares (LS) plane is computed for each surface point. The LS plane is based on such control points that are associated with those faces that use the interface mesh point $\mathbf{x}_p^r$. The index for those control points is $l \in \{1, \ldots, |ngb_F(p)|\}$. The distance of a control point $\mathbf{x}_{CP,l}^{r+1}$ to the least square surface of the interface point $\mathbf{x}_p^r$ is given by

$$d_l = (\mathbf{x}_{CP,l}^{r+1} - \mathbf{p}_{LS,p}^{r+1}) \cdot \mathbf{n}_{LS,p}^{r+1}. \tag{102}$$

where $\mathbf{p}_{LS,p}^{r+1}$ is a point on and $\mathbf{n}_{LS,p}^{r+1}$ the normal of the least square plane that is associated with $\mathbf{x}_p^r$. The placement of the least square plane is computed using the weights

$$w_l = \frac{1}{||\mathbf{x}_{CP,l}^{r+1} - \mathbf{x}_p^r||_2 + \texttt{SMALL}}. \tag{103}$$

for the influence of a certain control point the least square plane. The closer a control point is located to the surface point $\mathbf{x}_p$, the more influence the control point has on the motion of the surface point. Here, the CP-iteration index for d_l and w_l has been omitted.

The energy function for the least square plane is defined by

$$S = \sum_l w_l d_l^2 \tag{104}$$

where the weights w_l are governing the influence of a data point on the orientation and location of the least square plane. To obtain the least square plane,

$$\nabla S = 0 \tag{105}$$

has to be solved, giving the coefficients for $\mathbf{p}_{LS,p}^{r+1}$ and $\mathbf{n}_{LS,p}^{r+1}$. The orientation of the least square plane is illustrated in Figure 13b by dashed lines that form a connection between the control points in 2D. Note that in a 3D computation, the control points are not necessarily located on the least square plane.

6. **Update surface points**
   After computation of the associated LS plane, the interface points are projected onto this plane by

$$\mathbf{x}_p^{r+1} = \mathbf{x}_p^r + \frac{(\mathbf{p}_{LS,p}^{r+1} - \mathbf{x}_p^r) \cdot \mathbf{n}_{LS,p}^{r+1}}{\mathbf{d}_p \cdot \mathbf{n}_{LS,p}^{r+1}} \mathbf{d}_p. \tag{106}$$

   where $\mathbf{d}_p$ is the point displacement direction which has been set in step 2. Note that the displacement distance is also weighted by the the point displacement direction.

   For subsequent iterations the algorithm continues with step three to further decrease (94).

Considering that zero tangential velocity has been prescribed above, it has to be noted that this condition is not exactly guaranteed by the CP-algorithm, as the surface points are projected onto the associated LS planes. Choosing $\mathbf{d}_p$ allows to set a prescribed movement direction for the interface mesh in addition to the kinematic condition. This introduces indirectly a motion velocity that is tangential to the interface. Thereby, a suitable interface mesh motion can be achieved in cases with a predominant direction of motion, e.g. the capillary rise case considered in Section 6.3.3.

While the algorithm has been applied successfully in various applications, e.g., [94, 102, 147, 140], general conditions for the convergence of the scheme are not available. Hence, the usage of this approach requires constant monitoring of its results, especially if the discrete velocity field contains high frequency oscillations. Alternative approaches are available in the context of a

FEM discretization, see e.g. [38] for an approach that is based on an constraint optimization problem.

4.4 WETTING

The description of the continuum model for wetting as given in Chapter 3 consists of a Navier slip boundary condition at the solid surface and a model for the contact angle that depends, in particular on the Ca number. Hence, the CP-algorithm described in the last section has to be extended to deal with boundaries of an interface. Furthermore, the contact angle has to be enforced according to the results of a contact angle model. Moreover, the OpenFOAM platform and more specifically the available ALE-implementation only consider pseudo-2D meshes. This means that even though a 2D problem is considered, the mesh used in OpenFOAM has to be a full 3D mesh with a single layer of cells where two domain boundaries consist of co-planar faces. This peculiarity has to be taken into account. The following sections outline how these aspects are realized.

4.4.1 *The CP-Algorithm for Surfaces with Boundaries*

In Section 4.3.3 the CP-algorithm has been derived for cases where the interface comprises a closed surface. This method can for example be applied to an oscillating droplet or a bubble rising in water. However, for the consideration of wetting processes the situation is different as the fluid-fluid interface forms a contact line at the wall. Hence, the interface is not a closed surface. Consequently, the CP-algorithm for the internal part of the interface has to be adapted at the surface boundaries to facilitate a moving contact line. This extension is illustrated in Figure 14.

As for the close surface, the algorithm consists of three stages. In the initial step, the flux volumes through the faces of the discrete interface are computed analog to the approach for the internal part of the interface. This initial step is depicted in Figure 14a with a contact angle θ^r which is measured between a face of a wall mesh and the face of the discrete interface that is sharing an edge with the discrete contact line. A mesh point $\mathbf{x}_p$ that represents the discrete contact line is used by at least two faces and hence is associated with two regular control points. To orient a least square plane in 3D, at least three points are required. For this reason, and to somewhat balance the influence of the internal control points on $\mathbf{x}_p$, so called *mirrored* control points $\tilde{\mathbf{x}}_{CP,f}$ are introduced. Such a mirrored control point is associated with each face f that shares an edge with the discrete interface boundary. While internal control points are update using (101), the mirrored control points are placed - as the

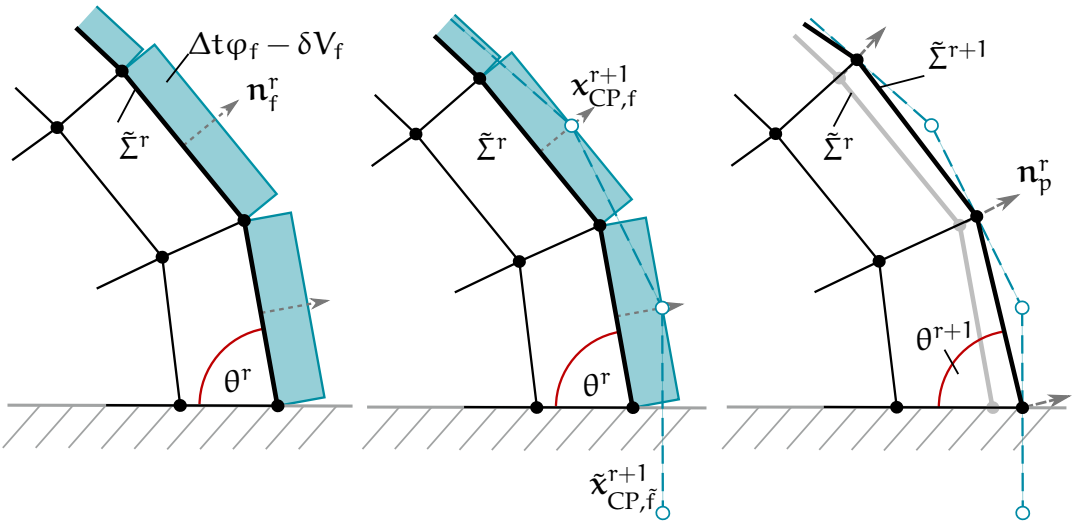

(a) Face flux volumes. (b) Control points. (c) Point displacement.

Figure 14: Control point algorithm at the contact line.

name says - by mirroring the associated internal control point at the wall boundary using

$$\tilde{x}_{CP,f}^{r+1} = x_e^r + (I - 2n_{\partial\Omega,f}^r \otimes n_{\partial\Omega,f}^r)\delta_e^r, \quad \delta_e^r := x_{CP,f}^r - x_e^r. \tag{107}$$

Here, δ_e^r is the distance of the internal control point $x_{CP,f}^r$ to the center x_e of the edge e that face f shares with the discrete boundary. This placement is illustrated in Figure 14b. The mirrored control point $\tilde{x}_{CP,f}^{r+1}$ is placed at an *orthogonal* distance δ_e^r from the wall boundary.

After placing the mirrored control points, a least square plane is computed analogously to the movement of internal mesh points. However, for each mesh point on the contact line there are two additional mirror control points that have to be taken into account for the computation of the least square plane. This step is illustrated in Figure 14c where the least square plane connects an internal control point and a mirror control point. This case occurs in both, the 2D as well as the 3D case, as in the 2D case each of the four contact line mesh points is associated with two control points. An example of a pseudo-2D mesh is given in Figure 15. In Figure 15a a pseudo-2D mesh of a droplet on a surface is shown. The corresponding close-up of the right contact line of the droplet is depicted in Figure 15b. As can be seen, the "contact line" consists of two mesh points.

As for the internal movement of the mesh, the points on the contact line are projected onto the associated LS-plane. In the 3D case, the LS-plane is not necessarily perpendicular to the wall boundary. Hence, projecting the contact line mesh point onto the LS-plane might lift the contact line point away from the wall. Hence, an additional projection onto the wall boundary is applied.

For additional iterations, the CP-algorithm continues with step 3 analog to the approach for the internal control points, see 4.3.3.

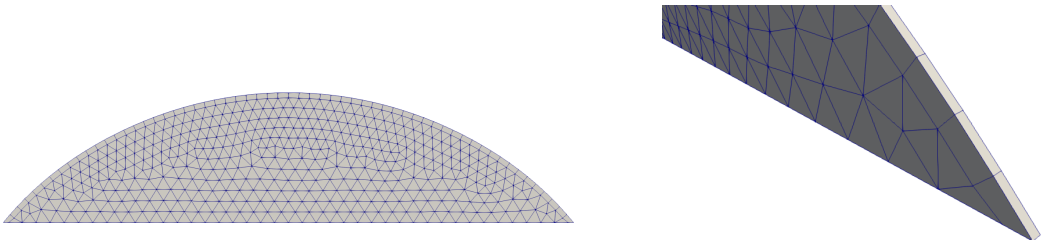

(a) 2D mesh of a droplet. (b) Contact line close up.

Figure 15: Pseudo-2D meshes in OpenFOAM.

4.4.2 *Contact Angle Library*

As pointed out in Chapter 2, there is no generally agreed on model for wetting processes. This includes the contact angle behavior for varying contact line velocities. Therefore, a wide variety of different models has been implemented. These are now readily available within a contact angle library that is fully compatible with the OpenFOAM framework. The library includes empirical contact angle models such as [17, 65, 60, 69] and those motivated by hydrodynamic theory e.g. [143, 89, 138]. The details of these models are listed in Table 6. In addition, a constant contact angle model is available which can for example be used to compare to analytic models or in cases with extremely small contact line velocities.

though technically imprecise, the advancing-receding behavior is also called hysteresis

The implemented library allows to combine different models for advancing and receding behavior. In this case, one model is used for contact angles larger than the advancing and the other for contact angles smaller than the receding contact angle θ_{adv} and θ_{rec}, respectively. Such models are for example used in [126] for the simulation of engineering problems, where a certain advancing-receding behavior of the macroscopic contact can be observed.

The contact angle models considered here, require the local Capillary number. Moving the contact line, e.g., by using the CP-algorithm outlined in Sections 4.3.3 and 4.4.1 indirectly gives the contact line velocity $\boldsymbol{v}_\Gamma$. To approximate this velocity, a standard explicit Euler time differencing scheme is used, i.e. $\boldsymbol{v}_p^n \approx (\boldsymbol{x}_p^{n+1} - \boldsymbol{x}_p^n)/\Delta t$. When a second-order time differencing scheme is used for the temporal discretization of (8), a second order backward differencing scheme $(3\boldsymbol{x}_p^{n+1} - 4\boldsymbol{x}_p^n + \boldsymbol{x}_p^{n-1})/(2\Delta t)$ for the computation of $\boldsymbol{v}_\Gamma$ is suitable. Here, $\boldsymbol{v}_p^n$ is the velocity of the mesh point p. This velocity is used to compute the local Ca number as $Ca = \mu v_\Gamma/\sigma$, which is then inserted into one of the contact angle models illustrated in Section 4.4.2, i.e. $v_\Gamma^n = \boldsymbol{v}_p^n \cdot \boldsymbol{n}_\Gamma$. The obtained angle is then enforced by adapting the point normal field of the contact line points analogously to [78, 112, 126]. The interface location is adjusted twice during the overall algorithm as outlined in Section 4.2. After each of the applications of the iterated CP-algorithm, the point normal field is adjusted using the latest location of the contact line, i.e. $\boldsymbol{x}_p^{r_{max}}$.

Table 6: Contact angle models.

name	model
Voinov	$\theta^3 = \theta_m^3 + 9\mathrm{Ca}\ln\left(\frac{\epsilon_{macro}}{\epsilon_{micro}}\right) \quad \text{for } \theta < 135°$ $(\pi-\theta)^3 + 2.25\pi\ln\left(\frac{1-\cos(\theta)}{1+\cos(\theta)}\right) = \theta_m^3 + 9\mathrm{Ca}\ln\left(\frac{\epsilon_{macro}}{\epsilon_{micro}}\right)$
Hoffmann-Voinov-Tanner	$\theta = (\theta_m^3 + 72\mathrm{Ca})^{1/3}$
Mathieu	$\theta = g^{-1}\left(g(\theta_{macro,sta}) + \mathrm{Ca}\ln\left(\frac{\epsilon_{macro}}{\epsilon_{micro}}\right)\right)$ $g(x) := \frac{x^3}{9} - 0.00183985x^{4.5} + 1.845829\cdot 10^{-6}x^{12.258487}$ $g^{-1}(x) = (9x)^{1/3} + 0.0727387x - 0.0515388x^2 + 0.00341336x^3$
Kistler	$\theta = f_{Hoff}(\mathrm{Ca} + f_{Hoff}^{-1}(\theta_e),$ where $f_{Hoff}(\mathrm{Ca}) := \arccos\left(1 - 2\tanh\left(5.16\left(\frac{\mathrm{Ca}}{1+1.31\mathrm{Ca}^{0.99}}\right)^{0.706}\right)\right)$
Jiang	$\frac{\cos\theta_e - \cos(\theta)}{\cos\theta_e + 1} = \tanh\left(4.96\mathrm{Ca}^{0.702}\right)$
Bracke	$\frac{\cos\theta_e - \cos\theta}{\cos\theta_e + 1} = 2\sqrt{\mathrm{Ca}}$

A plot of the different contact angle models from Table 6 is given in Figure 16. The collection of contact angle models has been adapted from [78]. As parameters, a microscopic length scale $\epsilon_{micro} = 0.01\,\mu m$ and a macroscopic length scale of $\epsilon_{macro} = 10\,\mu m$ have been used. The equilibrium contact angle is set to $\theta_e = 45°$. The microscopic contact angle has been set equal to the equilibrium contact angle, i.e. $\theta_m = \theta_e$. Air inclusions typically start to occur above $\mathrm{Ca} = 1$. The different models show the same qualitative behavior up to $\mathrm{Ca} \approx 0.2$, where the contact angle increases for all models. For higher Ca numbers, the predictions start to differ. The model from Bracke et al. does not give any predictions above this Ca value, the models of Hoffman-Voinov-Tanner, and the Voniov-model gives an unrealistic contact angle of more than 180°. The remaining contact angle models are at least bounded by 180°. The overall quantitative difference is up to 20° which can, in general, have a significant influence on both, the evolution of the contact line and overall dynamics.

4.4.3 *Enforcing the Contact Angle*

For most numerical methods such as geometric or algebraic VOF as well as front tracking approaches, the typical approach to set the contact angle is to adapt the interface normal field close to the contact line. For some approaches this corresponds to adjusting the inclination angle of a reconstructed PLIC sur-

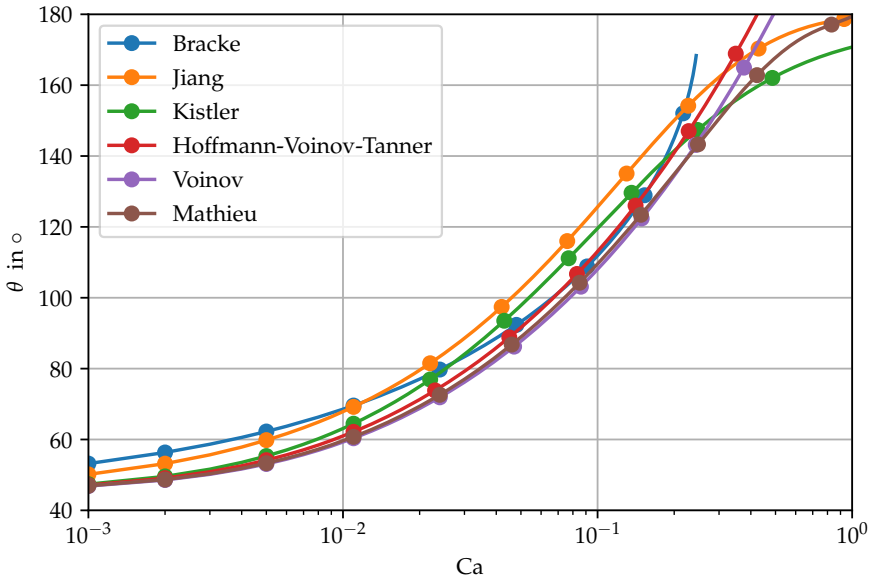

Figure 16: Comparison of contact angle models.

face within a cell see, e.g. [78]. This changes the value of the curvature in cells close to the contact line. As the curvature influences the velocity field through the transmission conditions, the interface then starts to move. This method is for example used in the context of a geometric Volume of Fluid method in [78] and for the algebraic volume of fluid implementation interFoam in [112, 54]. A similar approach for a level-set method with front reconstruction in [126]. The orientation of the reconstructed interface is prescribed, which moves the full interface through its influence on curvature computation.

In the context of FEM, a more rigorous approach is possible. Typically, boundary conditions are enforced using either a "natural" or an "essential" approach. In [132], a FEM implementation for a rotationally symmetric quasi-stationary setup in a co-moving reference frame is considered for a liquid rising in a tube. The authors consider both, an essential and a natural discretization.

To enforce a contact angle using the ALE approach, the interface mesh of the ALE method has to be moved. For this purpose, the approach that corresponds to the correction of the normal field at the contact line is chosen. The computations have to be independent from the orientation of the domain boundary within the OpenFOAM coordinate system. Hence, the adapted normal vectors are computed based on the mesh normal fields. Specifically, the point normal field of the wall boundary mesh is utilized. As general convection, the wall boundary is oriented such that the wall normal vectors are pointing outside of the domain. By rotation of this normal field, the desired normal field with a desired inclination angle is obtained. The necessary computations are outlined in the following.

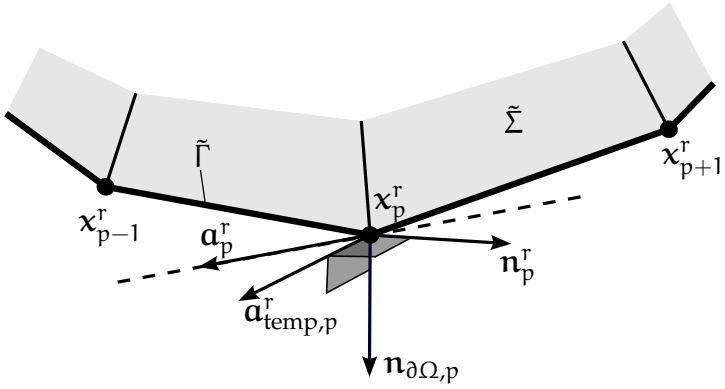

Figure 17: Computation of rotation axis at x^r_p.

ROTATION AXIS To obtain a surface normal field that has the desired orientation, a temporary axis is established at each mesh point of the discrete contact line by

$$a^r_{temp,p} := \frac{1}{\|n^r_{\partial\Omega,p} \times n^r_p\|_2 + \texttt{SMALL}} n^r_{\partial\Omega,p} \times n^r_p, \tag{108}$$

where n^r_p is the point normal field of the interface and $n^r_{\partial\Omega,p}$ is the point normal field of the solid surface. The situation is illustrated in Figure 17. It shows a part of the surface mesh $\tilde{\Sigma}$ around the discrete contact line $\tilde{\Gamma}$ centered at the point x^r_p. Next, the normalized edge vectors are computed by

$$e_L := \frac{e^n_{p,p-1}}{\left\|e^n_{p,p-1}\right\|_2}, \qquad e_R := \frac{e^n_{p,p+1}}{\left\|e^n_{p,p+1}\right\|_2} \tag{109}$$

While Figure 17 implies an ordering of the contact line points $p-1, p, p+1$, the available list of contact line mesh points in OpenFOAM does not provide such an ordering. Hence, it is necessary to ensure the orientation of the edge vectors by

$$\tilde{e}^r_L := \frac{\langle e^n_L, a^r_{temp}\rangle}{\left\|\langle e^n_L, a^r_{temp}\rangle\right\|_2} e^n_L, \qquad \tilde{e}^r_R := \frac{\langle e^n_R, a^r_{temp}\rangle}{\left\|\langle e^n_R, a^r_{temp}\rangle\right\|_2} e^n_R \tag{110}$$

where the edge vectors are renormalized. This gives the rotation axis of interface mesh point x^r_p by

$$a^r_p = \frac{\tilde{e}^r_L + \tilde{e}^r_R}{\left\|\tilde{e}^r_L + \tilde{e}^r_R\right\|_2 + \texttt{SMALL}} \tag{111}$$

This rotation axis is shown in Figure 17 by the dashed line.

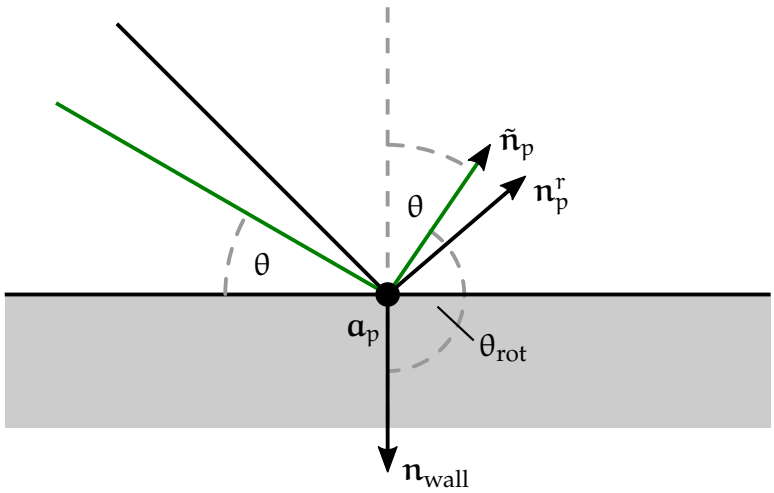

Figure 18: Utilization of the wall normal field to obtain adapted interface point normals.

ROTATION OF CONTACT LINE POINT NORMALS The point normal of the solid surface is rotated around $\mathbf{a}_p^r$ to obtain a point normal field at the contact line (a different patch) that is oriented according to the contact angle from one of the contact angle models in Section 4.4.2. This rotated point normal is then used for the computation of the interface curvature.

The rotation of a wall point normal at the point $\mathbf{x}_p$ is illustrated in Figure 16. The rotation axis $\mathbf{a}_p$ is perpendicular to the paper plane. The current interface together with the current point normal is illustrated in black and generally has an inclination angle $\theta \neq 0$. Here θ is the result of one of the contact angle models considered in Section 4.4.2. The green line and arrow are the interface and the contact line point normal $\tilde{\mathbf{n}}_p$ with the desired inclination angle θ. To obtain the desired point normal orientation, the wall point normal $\mathbf{n}_{wall}$ is rotated by $\theta_{rot} = \pi - \theta$ around the rotation axis $\mathbf{a}_p$. The rotation of the wall normal is implemented using the Rodrigues rotation formula which gives

$$\tilde{\mathbf{n}}_p = \mathbf{n}^n_{\partial\Omega,p} \cos\theta_{rot} + (1 - \cos\theta_{rot})\mathbf{a}^r_p \otimes \mathbf{a}^r_p \mathbf{n}^n_{\partial\Omega,p} + \mathbf{a}^r_p \times \mathbf{n}^n_{\partial\Omega,p} \sin\theta_{rot} \quad (112)$$

for the adjusted contact line point normal. Note that adjusting the normal vector field in vicinity of the contact line has to take into account the different parts of the contact line as illustrated in the next section.

4.4.4 *Surface Boundaries in OpenFOAM*

In general, all OpenFOAM versions, and in particular OpenFOAM extend 3.1 which is used here, are built to handle 3D meshes only. This means that even in cases where the problem is 2D, a full 3D mesh has to be provided. This design decision has lead to so called pseudo-2D meshes. Such a case for a spreading droplet is shown in Figure 15. While the 2D spreading drop may have the same contact angle at both sides, other problems may require

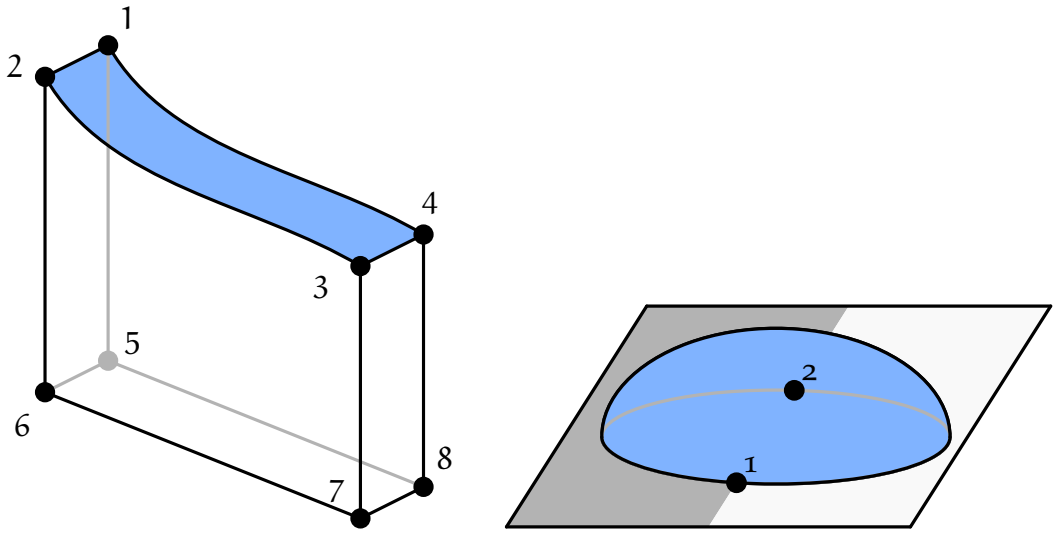

(a) 2D problem - meniscus at a wall. (b) 3D drop on an inhomogeneous surface.

Figure 19: Contact line patches for 2D and 3D applications in OpenFOAM.

significantly more flexibility. For instance, the 2D problem of a liquid rising up a wall is such a problem. This case is illustrated in Figure 19a, where a liquid meniscus at a wall boundary is depicted.

The interface, which is colored in blue, has four boundary parts: The contact line is the connection between points 1 and 2. Here, a contact angle model has to be applied. The curve between points 3 and 4 is the boundary to the open water where a 90° contact angle is suitable in the stationary case. While a 2D mesh in the 1,5,4-plane would be sufficient for this problem, the OpenFOAM platform requires a 3D mesh consisting of one cell orthogonal to this plane. Hence, the two curves between points 1 and 4 as well as points 2 and 3 represent "empty" boundaries in terms of OpenFOAM . The deformation of the pseudo-2D mesh also requires that the interface remains orthogonal

The rotational symmetric 3D droplet on a homogeneous surface requires only a single contact line instance. However, when considering the spreading of a drop on a patterned surface, a similar treatment for the different regions of the contact line are required. This is illustrated in Figure 19b where the contact line of such a drop is split into two regions by the points 1 and 2. For the two regions there might for example be a different stationary contact angle that needs to be enforced.

Hence, even seemingly simple cases demand a significant flexibility from the implementation of the contact line treatment. These aspects have to be taken into account for the implementation of the numerical treatment of the wetting models.

For this purpose, contact line patches are introduced that represent a subset of edges of the contact line. For each contact line patch, a different treatment

of the inclination angle can be enforced. This allows to fulfill the different structural requirements arising from cases such as shown in 19.

The following listing shows how boundary conditions can be chosen for the 2D meniscus problem:

Listing 1: Specification of contact line boundary conditions.

```
contactLine
{
    type                hoffman;
    staticContactAngle  45;
}
openWater
{
    type                constant;
    staticContactAngle  90;
}
```

The patch `contactLine` represents the subset of the surface boundary between points 1 and 2 in 19a. The `openWater` patch corresponds to the connection between points 3 and 4. At the contact line boundary the empirical contact angle model from Table 6 is specified using a static contact angle of 45°. At the open water boundary, a constant angle of 90° is used. The empty parts of the surface boundaries are identified automatically and do not have to be specified explicitly. In this way, the choice of different contact angle models for a part of a contact line can be achieved in the same way as for any other boundary condition. Hence, the contact line functionality integrates smoothly into the existing OpenFOAM platform and corresponding workflows.

5

CAPILLARY RISE MODELS

5.1 LITERATURE OVERVIEW

In various occurrences in nature and technology, the intrusion of liquid into small cavities plays an important role. These application may e.g.be the liquid infiltrating into a sponge, capillary pumps, or the extraction of crude oil from porous rock. A prototypical problem for such phenomena is the rise of a liquid in a capillary. It can be summarized as follows: A liquid of density ρ and dynamic viscosity μ, rises in a narrow cylinder with radius R against the direction of gravitation with gravitational acceleration g. The liquid is rising due to the interaction of surface tension forces with the capillary walls. The surface tension is quantified by the coefficient σ and the liquid-gas-interface is enclosing an angle θ with the wall, also known as the contact angle. For this setup, the approximate rise height h_{Jur} of a liquid in the case of a cylindrical capillary can be computed by

$$h_{Jur} = \frac{2\sigma\cos\theta}{R\rho g} \tag{113}$$

and is also known as *Jurin's height* [68]. In Ref. [83, 145] the rise height of liquid over time has been modeled considering a one-dimensional ad hoc force balance of inertia, viscous and capillary forces. Both authors provide an approximate solution to their model and validate against experiments for various liquids rising in a porous medium and a single cylindrical capillary. In [14], this model is enhanced adding an additional term for inertia, yielding

$$\rho\frac{d h\dot{h}}{dt} + \frac{8\mu h}{R^2}\dot{h} + \rho g h = \sigma\frac{2\cos\theta}{R}, \quad \dot{h}(t_0) = \dot{h}_0,\, h(t_0) = h_0 > 0 \tag{114}$$

as a model of the rise height of the liquid over time. This nonlinear ordinary differential equation will be referred to as the *classical model*. While (114) is the description for the rise of liquid in a cylindrical capillary, an analogous description can be derived for liquid rising between two planar plates. Depending on the parameters of the setup, it is possible to neglect the inertia and gravitational term for small t. Then, an integration in time yields the approximate *Lucas-Washburn-solution* $h(t) = \sqrt{R\sigma\cos\theta t/2\mu}$ for the rise of a liquid in a cylindrical capillary. Even though this approximate solution does

not yield a finite rise height, it is still a popular choice in a comparison with experiments for the initial stage of the rise. The classical model, on the other hand, is consistent with Jurin's height, i.e. $\lim_{t\to\infty} h(t) = h_{Jur}$.

Various extensions to the classical model have been suggested, aiming to incorporate additional physical effects or adapting the classical model to the specific setup of an experiment. In [137], the classical model is extended by including an infinite reservoir of liquid below the inlet of the capillary. This removes the singularity of the classical model for $t \to 0$ and formally allows to use $h(0) = 0$ as initial condition. While referring to [81], it is stated in [42] that the quadratic term in the classical model should be neglected for decreasing h. It is argued that this adaptation is necessary due to the singular pressure loss at the inlet of the capillary caused by the change of diameter between the reservoir and the capillary. In [66], the contact angle θ is assumed to depend on the rise velocity by including an empirical contact angle model $\theta(Ca)$ with capillary number $Ca = \mu\dot{h}/\sigma$. To include the influence of surfactants on the rise height of the liquid over time, [152] is enhancing the model with a varying surface tension coefficient. This model includes a simple sorption mechanism using a Langmuir isotherm. In [134] the classical model is enhanced by incorporating the reservoir with the approach from [137]. Furthermore, the contact angle is assumed to follow the Hoffman model. Additional influences of the free surface of the reservoir, and damped oscillation of the surface itself are incorporated.

A dimensional analysis of the classical model is given in [42]. Different scalings are analyzed and related to limiting regimes where known analytic solutions for the classical model are applicable. This comparison includes the approximate analytic solutions from [83, 145, 14, 108, 41].

As the liquid in the capillary wets the capillary walls, it is subject to the problem of how the contact line behavior should be modeled. A standard boundary condition for solid surfaces in single phase flows is the no-slip boundary condition. In the case of a moving contact line this model leads to the moving contact line paradox [62]. This problem has been addressed in the context of the capillary rise by various authors: In [61], an approximation of the velocity field locally at the contact line is derived for a quasi-stationary rise, where a Navier slip boundary condition is used on the capillary walls near the contact line. Various interface shapes are computed for different quasi-stationary rise velocities in [82] using an axis-symmetric finite element (FEM) implementation. A similar setup within a reference frame co-moving with the quasi-static interface is provided by a FEM implementation in [132]. In addition to local velocity fields, the rise height over time is considered and compared to the classical model.

In [77] models for the rise of liquid between two parallel plates and within a cylindrical tube are derived. The models assume a meniscus of fixed shape, a quasi steady-state acceleration and that non-linear terms are negligible. Two regions are considered: one comprises the main part of the capillary walls

where the no-slip boundary condition is applied, while the second region contains the immediate vicinity around the contact line, where a Navier slip boundary condition is used. The two regions are combined using asymptotic matching.

The rise of a liquid in a capillary is also interesting as a reference case for the numerical solution of the full continuum mechanical free surface problem. The geometric setup is rather simple and can even be reduced to a 2D problem for the rise of a liquid between two plates. Furthermore, away from the inflow and the interface, a standard Poiseuille flow profile can be expected. To obtain integrable pressure and dissipation fields near the contact line, it is necessary to replace the no-slip/no penetration boundary condition by e.g., a Navier slip boundary condition [61]. Such an approach is necessary to at least partially circumvent the aforementioned moving contact line paradox and the associated singularities. This, however, introduces an additional scale that needs to be resolved. Computations based on molecular dynamics yield slip lengths in the nanometer range or even below [107]. A lab experiment of liquid rising in a capillary is typically on the scale of Jurin's height which is usually a few centimeters. In order to compute the experimental setup, both length scales need to be resolved requiring significant mesh resolution in contact line vicinity. While the motivation for the extension of the classical model is usually to incorporate more physical effects or to adapt to a given experimental setup, a more simple test case for a comparison with the numerical solution of the continuum mechanical description of the capillary rise problem is desirable. This provides a reference solution that includes the influence of slip, also allowing to choose the slip length on the scale of the capillary radius. In the following section, the classical model is motivated from a full continuum mechanical description given in Chapter 3. This includes the use of Navier slip boundary conditions on the capillary walls. In parts, the derivation follows the approach from [28] using the mass and momentum conservation balance over arbitrarily moving control volumes.

5.2 DERIVATION OF AN EXTENDED MODEL

For the rise of liquid in a capillary a free surface flow is assumed, cf. Chapter 3. This model corresponds to the case where $\rho_g/\rho_l \ll 1$, and $\mu_g/\mu_l \ll 1$ where subscripts l and g denote the liquid and gas phase, respectively. The general setup for the rise of a liquid between two plates is illustrated in Figure 20. The liquid domain $\Omega(t) \subset \mathbb{R}^3$ is changing over time and hence, the liquid gas interface $\Sigma(t)$ rises in y-direction while liquid flows through $\partial\Omega_{in}$ into the capillary. Due to the inflow, an increasing area on the capillary walls $\partial\Omega_{wall}(t)$ is wetted over time.

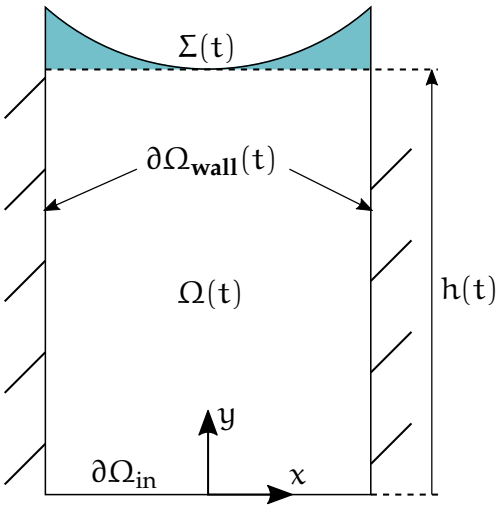

Figure 20: Domain and boundary names for a liquid rising in a capillary.

5.2.1 *Free Surface Approximation*

Integrating the mass and momentum conservation equations (7) and (8), respectively, for the liquid phase over an arbitrarily moving control volume $\Omega(t)$ as illustrated in Figure 20 gives

$$\frac{d}{dt}\int_{\Omega(t)} \rho \, dV = \int_{\partial\Omega(t)} \rho(\boldsymbol{v}_b - \boldsymbol{v}) \cdot \boldsymbol{n} \, do \tag{115}$$

$$\frac{d}{dt}\int_{\Omega(t)} \rho\boldsymbol{v} \, dV = \int_{\partial\Omega(t)} \boldsymbol{S}\boldsymbol{n} \, do + \int_{\partial\Omega(t)} \rho\boldsymbol{v} \otimes (\boldsymbol{v}_b - \boldsymbol{v}) \cdot \boldsymbol{n} \, do + \int_{\Omega(t)} \rho\boldsymbol{g} \, dV. \tag{116}$$

Here, ρ is the density of the liquid. The surface tension coefficient of the liquid-gas interface $\Sigma(t)$ is denoted by σ. The gravitational acceleration points in negative y-direction and its coefficient is $\boldsymbol{g}$. Since the control volume $\Omega(t)$ changes over time, so does its boundary with the velocity $\boldsymbol{v}_b$. The normal to the moving control volume is denoted by $\boldsymbol{n}$ and coincides with the interface normal $\boldsymbol{n}_\Sigma$ on $\Sigma(t)$. The orientation of the interface is such that $\boldsymbol{n}_\Sigma = \boldsymbol{e}_2$ at $x = 0$.

The boundary conditions are applied such that the resulting ODE model can be reduced to the classical rise model. For this purpose, homogeneous Neumann boundary conditions for the velocity are applied on the inflow boundary. This choice is discussed below in more detail. On the capillary walls a combination of no penetration and Navier slip boundary condition with slip length L is used. At the interface standard free surface boundary conditions are applied. For the contact angle, a constant contact angle is used. A discussion whether these boundary conditions are suitable is given below.

Hence, the following boundary conditions are used on different subsets of $\partial\Omega$:

$$\partial_n \boldsymbol{v} = 0 \qquad \text{on } \partial\Omega_{\text{in}} \tag{117}$$

$$\langle \boldsymbol{v}, \boldsymbol{n} \rangle = 0 \qquad \text{on } \partial\Omega_{\text{wall}}(t) \tag{118}$$

$$L\partial_n \boldsymbol{P}_{\partial\Omega} \boldsymbol{v} = P_{\partial\Omega} \boldsymbol{v} \qquad \text{on } \partial\Omega_{\text{wall}}(t) \tag{119}$$

$$p\boldsymbol{n}_\Sigma - \boldsymbol{S}^{\text{visc}} \boldsymbol{n}_\Sigma = \sigma\kappa \boldsymbol{n}_\Sigma \qquad \text{on } \Sigma(t) \tag{120}$$

$$\theta = \text{const} \qquad \text{at } \partial\Sigma(t). \tag{121}$$

The velocity $\boldsymbol{v}_b$ of the control volume boundary is chosen to track the fluid inside the capillary. This means that the control volume boundary will consist of the interface, the capillary walls and the inflow boundary. Furthermore, the inflow boundary will not co-move with the fluid, but remain at the inflow of the capillary. These assumptions couple the movement of the control volume to the fluid velocity by

$$\boldsymbol{v}_b \cdot \boldsymbol{n} = \boldsymbol{v} \cdot \boldsymbol{n} \qquad \text{on } \Sigma(t) \cup \partial\Omega_{\text{wall}}(t) \tag{122}$$

$$\boldsymbol{v}_b = 0 \qquad \text{on } \partial\Omega_{\text{in}} \tag{123}$$

The contact angle is assumed to be constant. This is in contrast to the application of, e.g., empirical contact angle models which have also been used in this context [66].

5.2.2 *Consistent Inflow Boundary Conditions*

In the stationary state, the liquid in a capillary, formed by two planar plates with distance $2R$, is at rest, i.e. $\boldsymbol{v} = 0$. Using the free surface approximation described in the last section with outer pressure $p_a = 0$ gives

$$\nabla p = -\rho g \boldsymbol{e}_y \qquad \text{in } \Omega \tag{124}$$

$$-p = \sigma\kappa \qquad \text{in } \Sigma \tag{125}$$

$$\boldsymbol{n}_\Sigma \cdot \boldsymbol{n}_{\partial\Omega} = -\cos\theta \qquad \text{in } \Gamma \tag{126}$$

where Ω, Σ and Γ are the liquid domain, the interface, and the contact line in the stationary state, respectively. The outward pointing normal of the domain boundary is denoted by $\boldsymbol{n}_{\partial\Omega}$. Assuming symmetry, it can be deduced from (124) that $\partial_x p = 0$ in Ω concluding that the pressure p_0 at the inflow/outflow boundary of the liquid domain is constant. This allows to integrate the bulk equation in y-direction and combine the result with the transmission condition at the interface yielding

$$\rho g H(x) = \sigma\kappa(x) + p_0. \tag{127}$$

Here, $H(x)$ is the distance between $\partial\Omega_{\text{in}}$ and the interface, where the coordinate system is located on the symmetry plane of the capillary. Evaluating

a spherical cap shaped interface is only an approximation

(127) at $x = 0$ and assuming that the interface has the shape of a circular section (constant curvature) implies $\kappa = \cos\theta/R$ and hence $H = \sigma\cos\theta/(\rho g R)$. This is the stationary rise height also known as Jurin's height. However, this implies that $H(x)$ is constant, which is a contradiction (for $0 < \theta < \pi/2$) if the interface is curved (as $H(x) > H(0)$ for $0 < x \leqslant R$ in this case). Hence, there exists no stationary solution where the interface has the shape of a spherical cap. Evaluating (127) at the symmetry axis gives

$$\rho g H(0) = \sigma\kappa(0) + p_0, \tag{128}$$

where $H(0)$ is the height of the apex which is denoted as the rise height. As all remaining parameters and the pressure p_0 are constants the curvature at the interface can not be constant. In the following, the curvature of the interface is computed at the symmetry axis.

FREE SURFACE SHAPES Inserting the free surface boundary conditions and expressing the curvature term with a graph representation yields the nonlinear boundary value problem

$$h'' = (1 + h'^2)^{\frac{3}{2}}\left(\mathrm{Eo}h - p_0^*\right), \quad h'(0) = 0,\ h'(1) = \cot\theta \tag{129}$$

where the radius as well as the rise height have been scaled using the radius of the capillary. Furthermore, $h := H(x)/R$ is the scaled height, $\mathrm{Eo} = \rho g R^2/\sigma$ is the Eötvös number, and $p_0^* := pR/\sigma$ is the non-dimensional (capillary) pressure. Note that it is possible to obtain a general form where p^* does not occur, using the transformation $\tilde{h} := h - p_0^*/(\mathrm{Eo})$. Also note that (129) is a singularly perturbed problem regarding the Eo number.

The boundary value problem (129) has been solved numerically using python, version 3.6.5, in combination with the numpy package, version 1.14.3. The results of the computations are shown in Figure 21 a) - c) for different contact angles $\theta = 1°, 45°, 80°$. For each contact angle, the free surface profiles are shown for $\mathrm{Eo} = 10^{-2}, \ldots, 10^4$. The profiles are shown between the symmetry plane at $x^* = 0$ and the wall boundary at $x^* = 1$. The surfaces are aligned by adjusting their apex height in order to compare their shapes. The plot is scaled equally on both axis. As a reference, a circular section with the corresponding contact angle is illustrated by black markers. It can be seen that for vanishing Eo numbers, the surface shapes approach the circular reference curve.

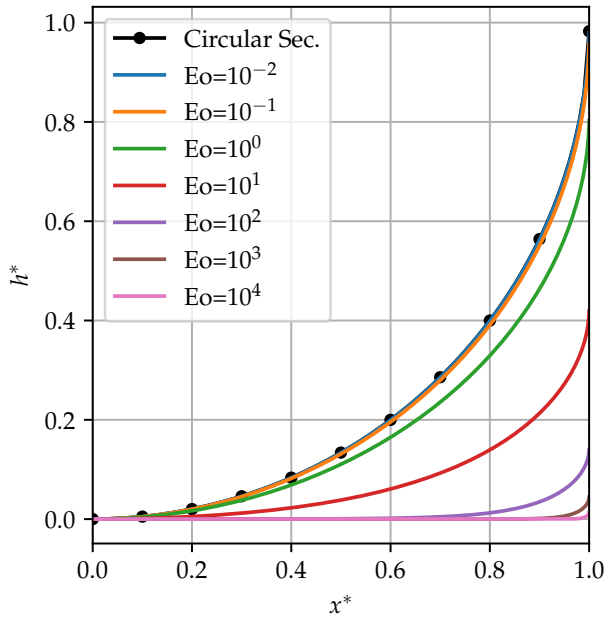

(a) Contact angle $\theta = 1°$.

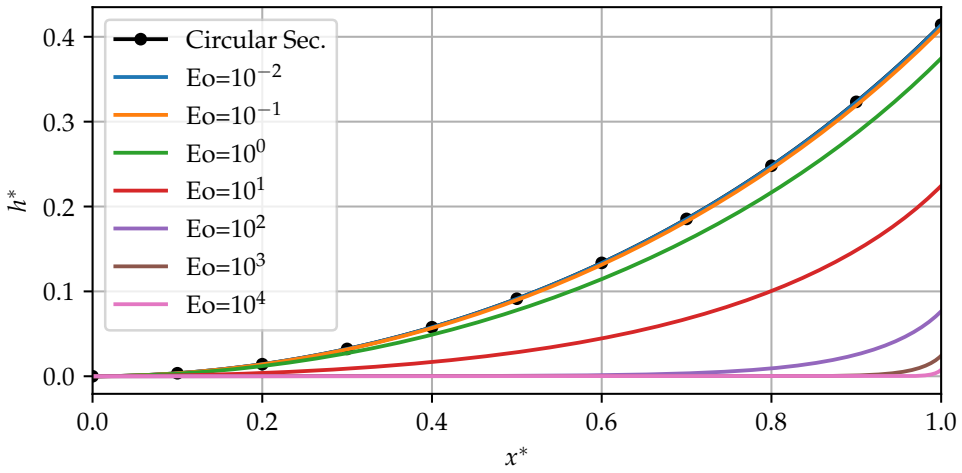

(b) Contact angle $\theta = 45°$.

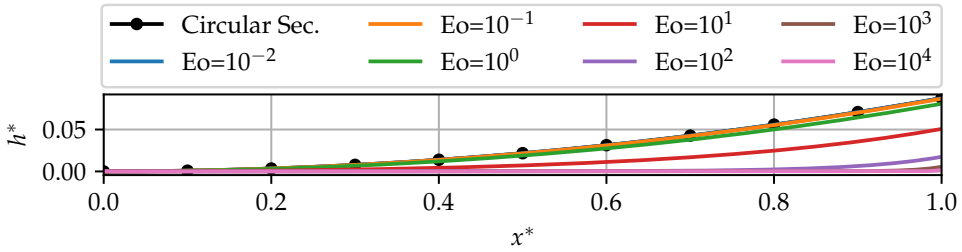

(c) Contact angle $\theta = 80°$.

Figure 21: Comparison of stationary free surfaces between two planar plates. The surfaces have been adjusted by a constant offset for each surface to compare the different shapes.

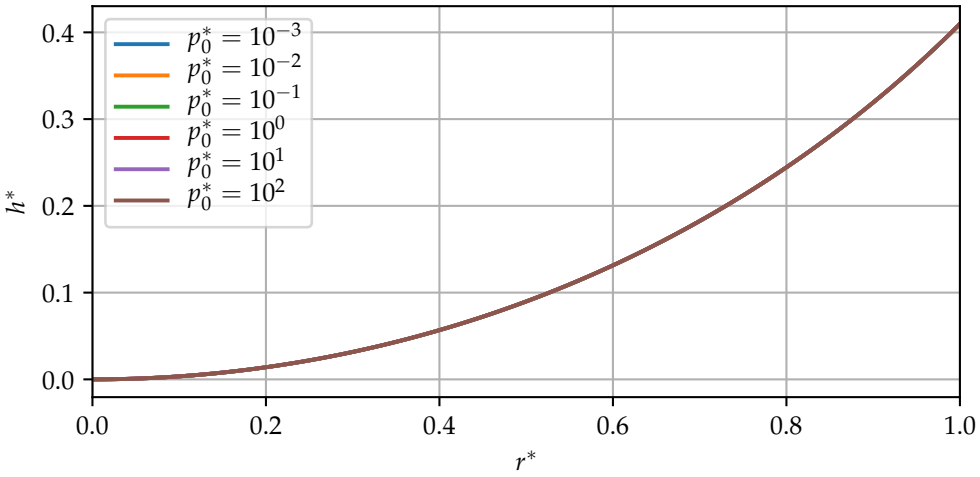

Figure 22: Influence of the pressure value on the surface shape for Eo = 0.1 and $\theta = 45°$.

For increasing Eo-numbers the interface shape becomes increasingly flat and the region where the interface is curved is more and more restricted close to the contact line. Equation (127) can be non-dimensionalized giving

$$H^*(0) = \frac{\kappa^*_{cap}}{Eo} - \alpha + \tilde{p}_0, \quad \alpha := \frac{\kappa^*_{cap} - \kappa^*(0)}{Eo} \tag{130}$$

where $\kappa^*_{cap} = \cos\theta$ is the non-dimensional constant curvature of a spherical cap shaped interface and $\tilde{p}_0 = p_0/(R\rho g)$. Here, the first term corresponds to a non-dimensional Jurin's height and the second term gives a correction listed in Table 7 for the surfaces in Figure 21b. The upper limit on α can be computed from the case with circular interface yielding $\alpha_{Eo\to\infty} \approx 0.1288$.

Table 7: Non-dimensional curvature corrections.

Eo	10^{-2}	10^{-1}	10^{0}
α	$1.286 \cdot 10^{-1}$	$1.269 \cdot 10^{-1}$	$1.125 \cdot 10^{-1}$

Eo	10^{1}	10^{2}	10^{3}
α	$5.236 \cdot 10^{-2}$	$7.065 \cdot 10^{-3}$	$7.071 \cdot 10^{-4}$

Figure 22 shows the solution of (132) for a fixed Eo = 0.1 and various pressure values at the inflow boundary. All curves for pressure values $p_0^* = 10^{-3}, \ldots, 10^2$ coincide. This demonstrates that the shape of the interface is independent of the value of the pressure at the inflow boundary in the stationary state.

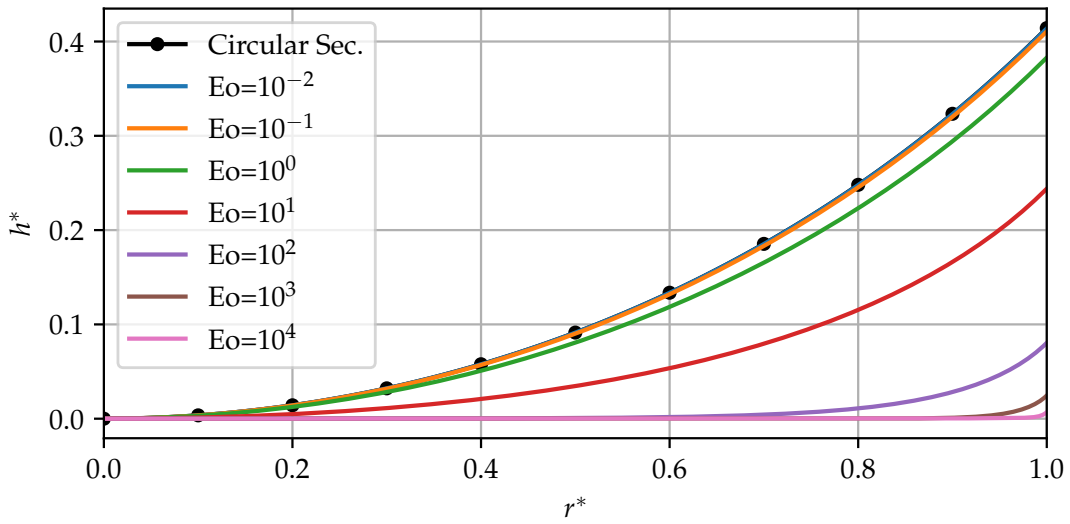

Figure 23: Free surface profiles in a cylindrical capillary for a contact angle of $\theta = 45°$.

3D RISE IN A CYLINDER Similar to the approach for the 2D case, a boundary value problem for the rotational symmetric interface in a 3D cylinder can be derived giving

$$h'' = (1 + h'^2)^{3/2} \left(\frac{\rho g}{\sigma} h - \frac{p_0}{\sigma} - \frac{h'}{r\sqrt{1 + h'^2}} \right). \tag{131}$$

Scaling the rise height with the radius of the capillary and using the capillary pressure results in

$$h^{*\prime\prime} = (1 + h^{*\prime 2})^{\frac{3}{2}} \left(\mathrm{Eo} h^* - p_0^* - \frac{h^{*\prime}}{r^*\sqrt{1 + h^{*\prime 2}}} \right) \tag{132}$$

with boundary conditions $h^{*\prime}(0) = 0$ and $h^{*\prime}(1) = \cot\theta$. Here, the non-dimensional quantities are defined as in the 2D case. Using the same procedure as outlined above, the boundary value problem (132) for the 3D case has been solved. The surfaces for various Eo-numbers for a contact angle of $\theta = 45°$ are shown in Figure 23. A qualitatively similar picture as for the 2D case in Figure 21b can be seen. Again, the circular section with a contact angle of $\theta = 45°$ is shown by the black dotted line as a reference. The surface shapes approach this reference for decreasing Eo-numbers. For the scaled surface shapes, the distance between apex and contact line is slightly larger than in the 3D case as can be seen by comparing the red curves for $\mathrm{Eo} = 10$.

5.2.3 *Stationary Rise Height*

It has been shown in the last section that for small Eo numbers a circular section or a spherical cap in 2D and 3D, respectively, are an excellent approximation for the shape of the free surface. Figure 24 shows an illustration of

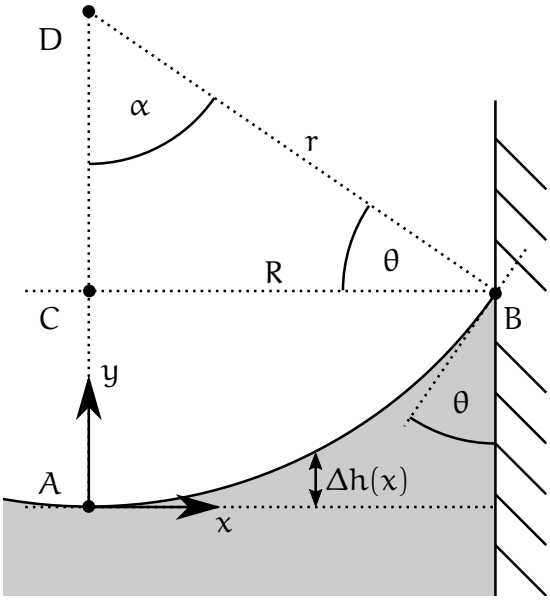

Figure 24: Surface geometry in vicinity of the contact line.

this free surface approximation near the contact line for the 2D case. The distance between point A and C is the height of the spherical cap denoted by Δh. From geometrical considerations it is clear that the contact angle θ is the same as $\angle(\overline{BD}, \overline{BC})$. The distance $\overline{CB}$ is half the diameter (radius) of the capillary and denoted by R. The full capillary diameter is denoted by W, i.e. $2R = W$. From Figure 24 it can be taken that $r = R/\cos\theta$. In order to compute the full mass in the capillary under the assumption of a spherical cap shaped free surface, the distance from the inflow to the interface can be written as

$$\tilde{h}(t, x) = h_{apex}(t) + \Delta h(x) \tag{133}$$

where $h_{apex}(t)$ is the distance from the inflow boundary to the interface at $x = 0$, also known as the apex. The distance between the base of the spherical cap (dotted line at height $y = 0$) to the interface depends on the distance from the symmetry plane (axis) and is denoted by $\Delta h(x)$. With $\Delta h(x) = r - \sqrt{r^2 - x^2}$ the liquid volume in the capillary is given by

$$|\Omega(t)| = 2D \int_0^R h_{apex}(t) + r\left(1 - \sqrt{1 - \left(\frac{x}{r}\right)}\right) \, dx \tag{134}$$

The integral can be solved analytically to the result

$$|\Omega(t)| = 2DR(h_{apex}(t) + \hat{h}) \tag{135}$$

$$\hat{h} := \frac{R}{2\cos\theta}\left(2 - \sin\theta - \frac{\arcsin\cos\theta}{\cos\theta}\right). \tag{136}$$

Note that for both equations, the volume is split into two contributions. The first part is the volume between the cross section at apex height and the inflow

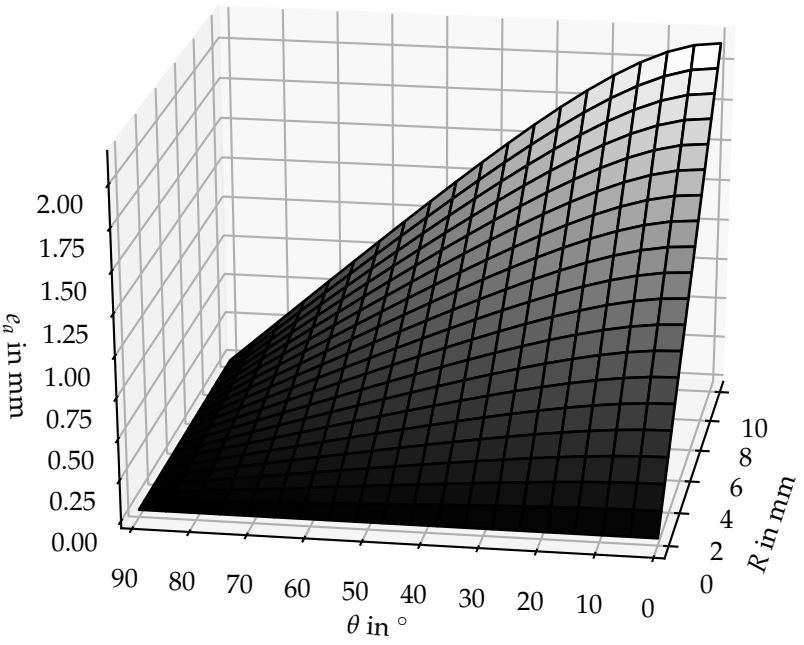

Figure 25: Absolute error for the stationary height using Jurin's height for $\mathrm{Eo} \to 0$.

and the second contribution is the volume between this cross section and the interface. In the stationary state, the acting forces are the gravitational and capillary forces in y-direction. A force balance yields the corrected stationary height

$$h_{\mathrm{apex}\,\infty} = \frac{\sigma \cos\theta}{R\rho g} - \hat{h}. \tag{137}$$

The first term in (137) is Jurin's height $h_{\mathrm{Jur,2D}}$ for the liquid height between two planar plates. The second term is a correction due to incorporation of the liquid in between the horizontal cross section at apex height and the interface. Hence, Jurin's height is an approximate solution for the stationary rise height that does only consider the volume between the inflow $\partial\Omega_{\mathrm{in}}$ and the cross section at apex height.

Note that the classical model for the cylindrical capillary (114) is consistent with Jurin's height (113), i.e. $\lim_{t\to\infty} h(t) = h_{\mathrm{Jur}}$. Hence, the classical model does not reach the stationary height as predicted by (137). A possible approach for the measurement of a contact angle is the capillary rise method described in e.g. [43]. With this approach, the stationary rise height of the liquid in the capillary is measured and the contact angle is computed using Jurin's height. This introduces in addition to the measurement errors the errors comprised in the model. Figure 25 gives an overview of the absolute error where the spherical cap approximation is used as interface shape,

i.e. the limit $Eo \to 0$. It can be seen that the error is small for small capillary radii. The error increase is more significant for smaller contact angles. Note that for standard conditions with $g \approx 9.81\,m\,s^{-1}$ and water in a capillary the error is rather small, as the spherical cap assumption only holds for $R < L_{cap,H_2O} \approx 2.7\,mm$. A situation where this situation changes due to the change is volume force is e.g. a drop tower or space craft applications. The influence of the correction on the stationary state is considered in in Chapter 6 by a comparison to a numerical solution of the corresponding full continuum mechanical problem.

5.3 DERIVATION FROM CONSERVATION EQUATIONS

In the following, it is assumed that the bulk velocity field does in the major part of the capillary not depend on the vertical coordinate, and is symmetric with respect to the y-z-plane, i.e.

$$\boldsymbol{v} = \begin{pmatrix} 0 \\ v(t,x) \\ 0 \end{pmatrix} \quad \text{with} \quad v(t,-x) = v(t,x). \tag{138}$$

It is clear, that the former assumption does not apply close to the interface. Hence, it is to be expected that the viscous dissipation caused by the horizontal component of the velocity field in the cap region is not contained within the model based on (138). [61] reports that the influence of the interface extends up to one tube diameter away from the interface. This estimate is confirmed in [82, p.21], where it is shown that a Poiseuille flow profile establishes at roughly one capillary diameter away from the interface for the case of liquid rising in a cylindrical capillary. However, in both cases the quasi-stationary regime is considered.

MASS CONSERVATION Assuming a constant density in the liquid phase, allows to reduce the mass conservation equation (115) to a condition for the change of liquid volume in the capillary

$$\frac{d}{dt}\int_{\Omega(t)} 1\,dV = \int_{\partial\Omega(t)} (\boldsymbol{v}_b - \boldsymbol{v}) \cdot \boldsymbol{n}\,do. \tag{139}$$

The integral over the boundary of the liquid control volume is split into $\partial\Omega(t) = \partial\Omega_{wall}(t) \cup \Sigma(t) \cup \partial\Omega_{in}$. In combination with the boundary conditions for the control volume velocity, (122) and (123), the flux integral on the right-hand side of (139) reduces to

$$\int_{\partial\Omega(t)} (\boldsymbol{v}_b - \boldsymbol{v}) \cdot \boldsymbol{n}\,do = -\int_{\partial\Omega_{in}} \boldsymbol{v} \cdot \boldsymbol{n}\,do, \tag{140}$$

where the normal of $\partial\Omega_{in}$ points to the outside of $\Omega(t)$, i.e. $\mathbf{n} = (0, -1, 0)^T$. The combination of the assumption for the velocity field (138), the expression for the liquid volume (135) and the volume conservation (139) gives

$$\frac{d}{dt}|\Omega(t)| = HD\dot{h}(t) \tag{141}$$

Combining (141), (138), and (140) with (139) gives

$$HD\dot{h}(t) = \int_{\partial\Omega_{in}} v(t, x)\, do. \tag{142}$$

where v is the velocity component in y-direction and h is the apex height. Defining the x-average of v by

$$\bar{v}_y(t) := \frac{1}{H}\int_{-H/2}^{H/2} v(t, x)\, dx \tag{143}$$

allows to write the apex velocity as

$$\dot{h}(t) = \bar{v}_y(t). \tag{144}$$

In the following, each term of the integral momentum conservation equation will be considered separately. If a coordinate system is necessary, the origin is located at the inflow while the orientation will be the same as in Figure 20.

INERTIA TERM Using assumption (138) allows to take the velocity out of the integral in y-direction. The definition of the distance between inflow and interface (133) allows to split the inertia term into two contributions

$$\begin{aligned}\rho D\frac{d}{dt}\int_{-H/2}^{H/2} \tilde{h}(t, x)v(t, x)\boldsymbol{e}_y\, dx = \\ \rho D\frac{d}{dt}\left(\int_{-H/2}^{H/2} hv(t, x)\boldsymbol{e}_y\, dx + \int_{-H/2}^{H/2} \Delta\tilde{h}(x)v(t, x)\boldsymbol{e}_y\, dx\right).\end{aligned} \tag{145}$$

Subsequent application of (143) and (144) gives

$$\rho D\frac{d}{dt}\int_{-H/2}^{H/2} hv(t, x)\boldsymbol{e}_y\, dx = \rho DH\frac{d}{dt}(h\dot{h})\boldsymbol{e}_y. \tag{146}$$

Neglecting

$$\frac{1}{H}\int_{-H/2}^{H/2} \tilde{h}(x)v(t, x)\boldsymbol{e}_y\, dx, \tag{147}$$

gives in combination with (144) the following approximation for the inertia term:

$$\frac{d}{dt}\int_{\Omega(t)} \rho\boldsymbol{v}\, dV \approx \rho DH\frac{dh\dot{h}}{dt}\boldsymbol{e}_y. \tag{148}$$

This approximation is reasonable as for increasing t, $\tilde{h}(x) \ll h(t)$ and yields the inertia term on left-hand side of the 2D version of the classical capillary rise equation. Nevertheless, it is possible to approximate the second term in the brackets of (145). The interface rises with velocity $\dot{h}_{\text{apex}}(t)$. Hence, the velocity $v(t,x)$ is in the order of $\dot{h}$ in interface vicinity. Thus, $v(t,x)$ should be of the order of $\dot{h}(t)$, i.e. $v(t,x) \approx \dot{h}(t)$. This allows to include the cap volume via

$$\frac{1}{H}\int_{-H/2}^{H/2} \tilde{h}(x)v(t,x)\boldsymbol{e}_y \,dx \approx \frac{1}{H}\int_{-H/2}^{H/2} \tilde{h}(x)\dot{h}\boldsymbol{e}_y \,dx \overset{(136)}{=} \dot{h}\hat{h}\boldsymbol{e}_y \tag{149}$$

Thus, the resulting approximation for the inertia term that includes a contribution from the liquid volume above the apex height, amounts to

$$\frac{d}{dt}\int_{\Omega(t)} \rho\boldsymbol{v}\,dV \approx \rho DH\frac{d}{dt}(\dot{h}(h+\hat{h}))\boldsymbol{e}_y. \tag{150}$$

Note that including the cap volume in this way has significant implications on the behavior of the model in the case with initial conditions $h(t_0) = 0$. As mentioned above, the classical model becomes singular for this initial height. This issue is addressed in [137], where similar term is the result of incorporating liquid volume in the reservoir that needs to be accelerated. The improvement of [137] puts a term of $7/6R$ (for a cylindrical capillary) at the exact same position as the $\hat{h}$ in (150). The same argument is followed in [86]. In [76], the additional term is $37/36R$, while in [134] it is $73/60R$. The term $0.916r_e$ is used for the regularization in [28] where the rise between two parallel, and planar plates is modeled. The effective radius r_e is defined by $r_e = 2\sqrt{cd/\pi}$ with gap width $2c$ and gap length $2d$. All these authors argue that for their additional term, liquid from a reservoir below the capillary needs to be accelerated. The argument leading to (150) however, illustrates why the singularity of the classical model occurs in the first place: Consider the situation as illustrated in Figure 20. With the classical model only the volume between the inflow and the apex height is considered, i.e. the volume of $\Omega(t)$ without the volume of the blue region. If the initial height is chosen to be zero, this corresponds to zero mass in the capillary, i.e. zero mass for viscous and capillary forces to act on and hence yielding the singular problem. A zero initial height corresponds to the case where the apex is touching the inflow boundary. With the assumption of a spherical cap shaped interface, there should still be some mass left in the capillary. This mass corresponds to the blue region in Figure 20 and the regularization in (150) corresponds to this mass. Also note that the regularization given in 150, is compatible with arguments accounting for an acceleration of liquid in the reservoir. In this regard, regularizing the rise equation with the mass in the cap region is self-consistent with the assumption of a spherical cap shaped interface.

CONVECTION TERM The convection term is split into contributions from the wall $\partial\Omega_{\text{wall}}$, the inflow boundary $\partial\Omega_{\text{in}}$, and the interface Σ. On the inter-

face $\Sigma(t)$ and on the wall $\partial\Omega_{\text{wall}}(t)$ the control volume moves with the normal velocity of the liquid. Hence

$$\int_{\Sigma(t)\cup\partial\Omega_{\text{wall}}(t)} \rho \boldsymbol{v} \otimes (\boldsymbol{v}_b - \boldsymbol{v}) \cdot \boldsymbol{n} \, do = 0. \tag{151}$$

On the inflow boundary $\partial\Omega_{\text{in}}$, the control volume does not move, i.e. $\boldsymbol{v}_b = 0$ on $\partial\Omega_{\text{in}}$. This gives in combination with assumption (138) for the velocity

$$\int_{\partial\Omega_{\text{in}}} \rho \boldsymbol{v} \otimes (\boldsymbol{v}_b - \boldsymbol{v}) \cdot \boldsymbol{n} \, do = \rho D \int_{-R}^{R} v^2(t,x) \boldsymbol{e}_y \, dx \tag{152}$$

as $\boldsymbol{n} = -\boldsymbol{e}_y$ on $\partial\Omega_{\text{in}}$. Using the Cauchy-Schwartz inequality for integrals on a bounded domain gives

$$\int_{-R}^{R} v^2(t,x) \, dx \geqslant \frac{1}{H} \left(\int_{-R}^{R} v(t,x) \, dx \right)^2 = H\dot{h}^2. \tag{153}$$

For equality, the velocity field would need to be constant in x-direction, i.e. $v(t,x) = \alpha(t)$, $\alpha \in L_2$, which would require a free slip boundary condition on the capillary walls. Hence, the above considerations give

$$\frac{1}{\rho D H} \int_{\partial\Omega(t)} \rho \boldsymbol{v} \otimes (\boldsymbol{v}_b - \boldsymbol{v}) \cdot \boldsymbol{n} \, do \geqslant \dot{h}^2 \boldsymbol{e}_y \tag{154}$$

for the convective momentum flux into the capillary. With increasing distance of the interface from the inflow, the inflow velocity profile approaches a Poiseuille flow profile. In [61, 82] approximately two radii of the capillary are sufficient for a Poiseuille flow profile to establish. Such a velocity profile can be used to evaluate the integral over the convection term explicitly. Here, a Poiseuille flow with a Navier slip boundary condition on the capillary walls is used. With this boundary condition, the stationary Poiseuille-flow velocity field is

$$v = \frac{3}{2} \left(\frac{R + 2L}{R + 3L} - \frac{x^2}{R(R + 3L)} \right) \dot{h}. \tag{155}$$

Evaluating (152) using (155) gives

$$\int_{-H/2}^{H/2} v^2(x) \, dx = \dot{h}^2 \frac{6R(15L^2 + 10LR + 2R^2)}{5(R + 3L)^2} \tag{156}$$

which evaluates for $L = R$ to $81/80 H\dot{h}^2$. For the no slip limit $L = 0$, (156) reduces to $6/5 H\dot{h}^2$. Expanding the inertia term gives $\ddot{h}(h + \hat{h}) + \dot{h}^2$. The combination of this $\dot{h}^2$ term with any other $\dot{h}^2$-contribution arising from e.g. (151) or other reasoning (such as the reservoir) is denoted *combined square term* in the following. For the classical model, the combined square-term is

$\dot{h}^2$. In the classical model, no convection is considered at all. However, for the extended model above, e.g., with $L = 0$, the combined square-term is $-1/5\dot{h}^2$.

In [18], a model based on the assumption of forces acting on the liquid in the transient rise are the same as in a steady state, is derived. The combined square-term is $5/4\dot{h}^2$. A pressure field in the inflow region of a cylindrical capillary is modeled in [137]. This approach considers volume from the reservoir that needs to be accelerated which gives a combined square-term of $1.225\dot{h}^2$. This approach is refined in [76] resulting in an overall contribution of $7/6\dot{h}^2$. In [28] the pressure field in the reservoir is considered giving $(0.959 + \mathrm{Re}/4)\dot{h}^2$ as combined square-term. It should be noted that Re is defined by using h which in general does not yield a constant non-dimensional group. In [81] the rise of liquid in a cylinder driven by hydrostatic forces is considered. It is suggested that the combined square-term in the classical model should be $\dot{h}^2$ for $\dot{h} > 0$ and zero otherwise. The same idea is followed in [42] and applied to the classical model. Similar to the regularization derived in above, all authors argue for their model with the influence of the liquid reservoir.

incorporating h into the Re-number is not admissible

GRAVITATION TERM In the following, the capillary axis is assumed to be aligned with the direction of gravity, i.e. $\mathbf{g} = -g\boldsymbol{e}_y$. This gives for the gravitational contribution

$$\int_{\Omega(t)} \rho \mathbf{g} \, dV = \rho \mathbf{g} \int_{\Omega(t)} 1 \, dV \overset{(135)}{=} -\rho g 2RD(h + \hat{h})\boldsymbol{e}_y. \tag{157}$$

As shown in Figure 25 Jurin's height can be a good approximation to the stationary rise height of the liquid in capillary. Note that this introduces $\hat{h}$ which corrects the stationary height of the rise model.

THE STRESS TERM As for the convection term, the integral over the viscous stress is split into contributions from the wall, the inflow boundary, and the interface. Using the symmetry assumption, this gives for the viscous forces on the inflow boundary and on the wall

$$\int_{\partial\Omega_{in}} \mathbf{S}^{visc}\mathbf{n} \, do = -\mu \int_{\partial\Omega_{in}} \partial_x v_y \boldsymbol{e}_x \, do = 0, \quad \text{and} \tag{158}$$

$$\int_{\partial\Omega_{wall}(t)} \mathbf{S}^{visc}\mathbf{n} \, do = 2\mu \int_{\partial\Omega_{wall,R}(t)} \partial_x v_y|_{x=R} \, \boldsymbol{e}_y \, do. \tag{159}$$

With (138), the velocity field and thereby the x-derivative of v_y does not depend on y, yielding

$$\int_{\partial\Omega_{wall}(t)} \mathbf{S}^{visc}\mathbf{n} \, do = 2\mu D(h + \Delta h(R))\partial_x v_y|_{x=R}\boldsymbol{e}_y, \tag{160}$$

with $\Delta h(R) \approx \hat{h}$. On the interface, the free surface boundary condition is plugged into the integral over the viscous stress yielding

$$\int_{\Sigma(t)} \mathbf{S}^{visc}\mathbf{n}_\Sigma \, do = \int_{\Sigma(t)} p\mathbf{n}_\Sigma \, do - \int_{\Sigma(t)} \sigma\kappa\mathbf{n}_\Sigma \, do. \tag{161}$$

Applying the surface transport theorem to the surface tension term allows to use the contact line bi-normal, which can be expressed using the contact angle. This gives for the viscous forces on the free surface

$$\int_{\Sigma(t)} \boldsymbol{S}^{\text{visc}} \boldsymbol{n}_\Sigma = \int_{\Sigma(t)} p \boldsymbol{n}_\Sigma \, do + 2D\sigma \cos\theta \boldsymbol{e}_y. \tag{162}$$

The pressure integral is split in the same way as the viscous forces, resulting in

$$\int_{\partial\Omega} p\boldsymbol{n} \, do = -\int_{\partial\Omega_{\text{in}}} p\boldsymbol{e}_y \, do + \int_{\Sigma(t)} p\boldsymbol{n}_\Sigma \, do. \tag{163}$$

As the problem is assumed to be symmetric, so is the pressure field. Hence, the pressure integrals over the wall cancel. Combining (163), (162), (160), and (158) gives

$$\int_{\partial\Omega(t)} \boldsymbol{S}\boldsymbol{n} \, do = 2\mu D(h + \hat{h})\partial_x v_y|_{x=R} \boldsymbol{e}_y + 2D\sigma \cos\theta \boldsymbol{e}_y. \tag{164}$$

The reduced stress integral (164) allows to model the x-derivative of the y-velocity at the capillary walls. For this purpose, the stationary Poiseuille flow field with Navier slip boundary conditions can be used. Using (155) leads to

$$\partial_x v_y|_R = -\frac{3\dot{h}}{R + 3L}. \tag{165}$$

In the wedge close to the contact line, the gradient at the wall can be modeled using a stream function solution for a Stokes flow in a wedge with Navier slip boundary conditions. An asymptotic expansion around the contact line gives the stream function solution, see Ref. [124]

$$\psi(r, \varphi) = \frac{r^2 U}{4L} \left(\frac{\varphi}{\theta} - 1 - \frac{\sin(2\varphi)}{\tan(2\theta)} + \cos(2\varphi) \right). \tag{166}$$

With $v_r = \frac{1}{r}\partial_\theta \psi$ and $v_\theta = -\partial_r \psi$, this stream function leads to the velocity components

$$v_x = \frac{U}{2L} \left(\frac{x}{2\theta} + \frac{y \arctan(y/x)}{\theta} - 2y - \frac{x}{\tan(2\theta)} \right) \tag{167}$$

$$v_y = \frac{U}{2L} \left(\frac{y}{2\theta} - \frac{x \arctan(y/x)}{\theta} + \frac{y}{\tan(2\theta)} \right) \tag{168}$$

in a cartesian coordinate system centered at the contact line. This gives an approximation of the forces at the wall in the vicinity of the contact line. For $y < h$, the wall stresses are approximated using (165). Furthermore, in a region $\overline{h}$ around the contact line, the wall stresses are modelled based on the wedge velocity field (167) and (168). This yields

$$\frac{1}{\rho 2DR} \int_{\partial\Omega_{\text{wall}}} \langle \boldsymbol{S}^{\text{visc}} \boldsymbol{n}, \boldsymbol{e}_y \rangle \, do \approx -\frac{3\mu}{\rho R(R + 3L)} \dot{h} h - \frac{\mu \overline{h}}{\rho R L} \dot{h}, \tag{169}$$

where the first term results from the Poiseuille flow approximation and the second term from the wedge flow near the contact line. The integration height $\overline{h}$ is estimated by a comparison to solutions of the corresponding continuum mechanical problem presented in Chapter 6. This leads to a reasonable integration height of $\overline{h} \approx 0.14\Delta h(R)$.

THE EXTENDED MODEL Equations (150), (156), (157), and (164) are combined with the momentum conservation equation (116). If further (165) is used to model the viscous forces on the capillary wall, one arrives at

$$\rho\frac{d}{dt}(\dot{h}(h+\hat{h})) = -\frac{3\mu\dot{h}}{R(R+3L)}(h+\hat{h}) + \frac{\sigma\cos\theta}{R} - \rho g(h+\hat{h}) + \rho\dot{h}^2\frac{3(15L^2+10LR+2R^2)}{5(R+3L)^2}. \quad (170)$$

If the velocity field near the contact line is incorporated by using (169), the overall model is

$$\rho\frac{d}{dt}(\dot{h}(h+\hat{h})) = -\frac{3\mu}{\rho R(R+3L)}\dot{h}h - \frac{\mu\overline{h}}{\rho RL}\dot{h} + \frac{\sigma\cos\theta}{R} - \rho g(h+\hat{h}) + \rho\dot{h}^2\frac{3(15L^2+10LR+2R^2)}{5(R+3L)^2}. \quad (171)$$

The classical model adapted for liquid rising between two planar plates can be obtained from (170) or (171) by setting $\hat{h} = 0$, $L = 0$, and ignoring the convection term and the wedge velocity field, respectively. This results in

$$\rho\frac{d(h\dot{h})}{dt} = -\frac{3\mu\dot{h}h}{R^2} - \rho g h + \sigma\frac{\cos\theta}{R}, \quad (172)$$

which is the 2D version of the classical rise equation (114).

5.4 OSCILLATION THRESHOLD

In [110] it is stated that the rise height oscillations in a cylindrical capillary occur for $\Omega < 2$ though no derivation of this criterion is given. In [121], an equation for a damped oscillator is given, though the result is incomplete and the derivation seems inconsistent, cf. Appendix A. Furthermore, no oscillation criterion is motivated. Hence, the following a general first order pertubation solution for the capillary rise model is derived in the following section. This solution covers in contrast to literature, the 2D and 3D case, and gives a general criterion for the occurrence of rise height oscillations.

Both, the 2D and the 3D model can be cast into

$$a(\ddot{h}h + \dot{h}^2) + b\dot{h}h + ch = 1, \quad h(t_0) = h_0. \quad \dot{h}(t_0) = \dot{h}_0 \quad (173)$$

with coefficients given in Table 8. The coefficient Ω in the last column has been identified as suitable non-dimensional group of the capillary rise problem in numerous works, among others in [110, 152, 41]. It can be expressed using the coefficients in Table 8, giving

$$\Omega = \sqrt{\frac{b^2}{ac^2}}. \tag{174}$$

In [42] it is derived as the single non-dimensional group arising in three different scalings of (173), see Section 5.5. To find a pertubation solution, the ODE (173) is first transformed using $\sqrt{z} := h$. Note that it is important not to take $h^2 = z$ as this would lead to an incorrect stationary height.

Table 8: Scaling coefficients for 2D and 3D cases.

	a	b	c	Ω
2D	$\rho R/(\sigma\cos\theta)$	$3\mu/(R\sigma\cos\theta)$	$\rho g R/(\sigma\cos\theta)$	$\sqrt{9\sigma\cos\theta\mu^2/(\rho^3 g^2 R^5)}$
3D	$\rho R/(2\sigma\cos\theta)$	$4\mu/(R\sigma\cos\theta)$	$\rho g R/(2\sigma\cos\theta)$	$\sqrt{128\sigma\cos\theta\mu^2/(\rho^3 g^2 R^5)}$

This gives for $h > 0$

$$\sqrt{z_{Jur}} := h_{Jur} = 1/c, \quad \sqrt{z} = h, \quad \dot{z} = 2h\dot{h}, \quad \ddot{z} = 2(\dot{h}^2 + h\ddot{h}).$$

which is used to transform (173) to

$$\frac{a}{2}\ddot{z} + \frac{b}{2}\dot{z} + c\sqrt{z} = 1, \quad z(t_0) = h_0^2. \tag{175}$$

A pertubation solution around the stationary height z_{Jur} in the form $z = z_{Jur} + \epsilon(t)$ is considered. This gives

$$\frac{a}{2}\ddot{\epsilon} + \frac{b}{2}\dot{\epsilon} + c\sqrt{z_{Jur} + \epsilon} = 1 \tag{176}$$

with

$$z(t_0) = z_{Jur} + \epsilon(t_0) = h_0^2, \qquad \epsilon(t_0) = h_0^2 - z_{Jur}. \tag{177}$$

Considering the Taylor-series of $\sqrt{z_{Jur} + \epsilon}$ around $\epsilon = 0$ and truncating after the second order term yields

$$\sqrt{z_{Jur} + \epsilon} = \sqrt{z_{Jur}} + \frac{1}{2\sqrt{z_{Jur}}}\epsilon + \mathcal{O}(\epsilon^2) \approx \frac{1}{c} + \frac{c}{2}\epsilon. \tag{178}$$

Plugging this approximation into the transformed equation for $\sqrt{z_{Jur} + \epsilon}$ results in

$$a\ddot{\epsilon} + b\dot{\epsilon} + c^2\epsilon = 0 \tag{179}$$

with

$$\epsilon(t_0) = \epsilon_0 := h_0^2 - z_{Jur}, \quad \dot{\epsilon}(t_0) =: \dot{\epsilon}_0 = 2h_0\dot{h}_0 \text{ for } h_0 > 0. \tag{180}$$

This is the the equation for a linear damped oscillator

$$\ddot{\epsilon} + 2\delta\dot{\epsilon} + \omega_0^2\epsilon = 0, \quad \epsilon(t_0) = h_0^2 - 1/c^2, \ \dot{\epsilon}(t_0) = 2h_0\dot{h}_0 \tag{181}$$

from which the dampening constant $\delta = b/(2a)$, the angular frequency $\omega_0 = c/\sqrt{a} = 1/\sqrt{az_{Jur}}$ and the damping ratio $\zeta = \delta/\omega_0 = b/(2c\sqrt{a})$ is obtained. From the theory of damped linear oscillators it is known that the behavior of the solution of (181) depends on the damping ratio ζ:

1. $\zeta > 1$ overdamped exponential decay to steady state
2. $\zeta = 1$ critically damped, fastest return to equilibrium
3. $\zeta < 1$ underdamped, oscillations occur

Hence, rise height oscillations can be expected to occur for $\zeta = b/(2c\sqrt{a}) < 1$. In [108] it is stated that oscillations do occur when the time scale to reach the stationary height is much smaller than the viscous time scale. This argument seems sufficient for the explanation of experimental results which gives for a cylindrical capillary

$$\mu \ll g\rho^{3/2}R^{5/2}\sigma^{-1/2}, \tag{182}$$

as condition for the occurrence of rise height oscillations. Using the definition of Ω, this condition can be written as

$$\text{2D}: \quad \Omega \ll \sqrt{9} = 3 \qquad \text{3D}: \quad \Omega \ll \sqrt{128} \approx 11 \tag{183}$$

where the same procedure from [108] has been applied to obtain the estimate for the 2D case. Using the linear oscillator approximation gives for the oscillating case ($\zeta < 1$)

$$\zeta = \frac{1}{2}\sqrt{\frac{b^2}{ac^2}} = \frac{\Omega}{2} < 1 \tag{184}$$

as an improved condition for oscillations to occur for 2D as well as the 3D setups. For completeness, the full pertubation solution for $\Omega < 2$ is given by

$$h(t) \approx \sqrt{h_{Jur}^2 + A\exp(-\zeta\omega_0 t)\cos(\sqrt{1-\zeta^2}\omega_0 t + \varphi)} \tag{185}$$

$$A = (h_0^2 - h_{Jur}^2)\exp(\zeta\omega_0 t_0)\sqrt{1 + \frac{(2h_0\dot{h}_0 + \zeta\omega_0(h_0^2 - h_{Jur}^2))^2}{(h_0^2 - h_{Jur}^2)^2(1-\zeta)\omega_0^2}} \tag{186}$$

$$\varphi = \tan^{-1}\left(\frac{-(2h_0\dot{h}_0 + \zeta\omega_0(h_0^2 - h_{Jur}^2))}{\omega_0(h_0^2 - h_{Jur}^2)\sqrt{1-\zeta^2}}\right) - \sqrt{1-\zeta^2}\omega_0 t_0. \tag{187}$$

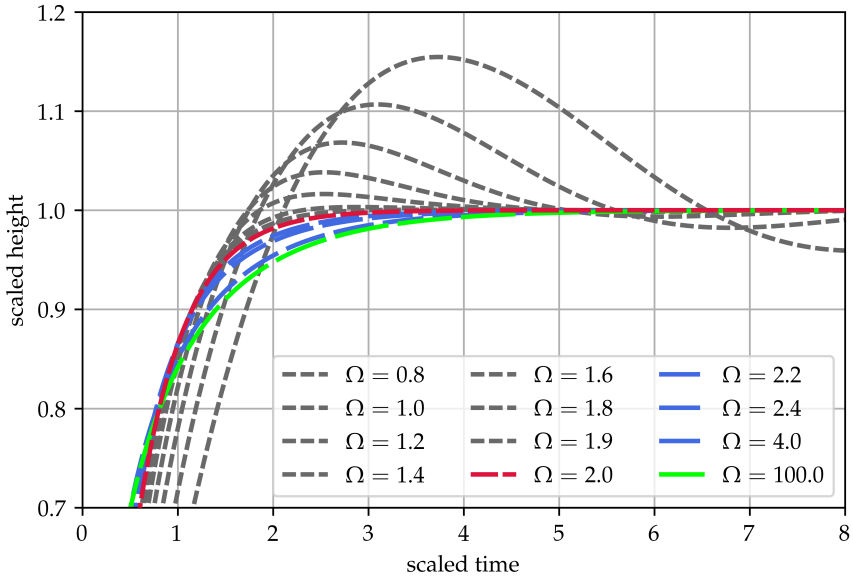

Figure 26: Numerical solution of (173) for $h_0 = 10^{-6}$, $\dot{h}_0 = 0$ and various values for Ω around the critical value of $\Omega = 2$. Results are scaled using scaling I from Table 9.

with initial conditions $h_0, \dot{h}_0$ at t_0 and parameters

$$\omega_0 = c/\sqrt{a}, \qquad \zeta = b/(2c\sqrt{a}), \qquad h_{Jur} = 1/c. \tag{188}$$

See Appendix B for a derivation. This gives the viscous time scale $\tau = \zeta\omega_0 = b/(2a)$ as time scale for the dampening of oscillations. Equation (173) has been solved numerically for various values of Ω between 0.8 and 100. For this purpose, the `odeint` function of numpy version 1.14.3 with python version 3.6.5 has been used. The results are depicted in Figure 26. To allow a suitable comparison, the time and rise height have been non-dimensionalized using scaling I in Table 9. The length scale with this scaling is Jurin's height. Thus, the stationary height of all curves is one. As initial values, $h_0^* = 10^{-6}$ and $\dot{h}_0^* = 0$ are used. The plots are color coded as follows: Curves with $\Omega < 2$ are illustrated by a gray dashed line with shorter dashes. Plots with $\Omega > 2$ are depicted by blue dashed lines with longer dashes. The result for the critical $\Omega = 2$ curve is colored in red. The curve for $\Omega = 100$ is illustrated by a green curve with the longest dashes.

Clearly all curves for $0.8 < \Omega < 1.9$ do show significant to mild oscillation around the stationary height $h_{Jur}^* = 1$. The curve $\Omega = 2$ corresponds to the case with critical dampening and does not show any oscillations. The results for $\Omega > 2$ do also not show any oscillatory behavior and require an increasing time to reach the stationary height h_{Jur}^*. This illustrates that the condition obtain from the pertubation solution of the classical model does give an excellent and sharp criterion for rise height oscillations to occur.

strong Ω-dependence for Ω > 2 makes this a challenging test case

Note that the solutions for $\Omega > 2$ are barely influenced by a change of Ω. For $\Omega < 2$ however, the quantitative influence of a change in Ω on the rise height behavior is significant. E.g., the change of $h^*(t)$ for changing Ω from 1.0 to 0.8 is significantly larger than the difference between for a change of Ω from 2 to 100. Further increase of Ω above 100 has little influence on the scaled rise height over time. This robustness to changes in Ω might indicate why this model has been successfully applied in experimental comparison in the $\Omega > 2$ regime.

5.5 SCALING FOR THE ENHANCED MODEL

For the classical capillary rise model in a cylinder, 114, a dimensional analysis is given in [42]. The authors consider three different scalings where

I. viscous and gravity effects

II. inertia and gravity effects

III. viscous and inertia effects

are used as scaling forces. Furthermore, the *same* non-dimensional group Ω has been identified as a single relevant dimensional group Ω for each of the scalings. The various limits for Ω correspond the special cases for which analytic solutions are available. An analog non-dimensionalization has been performed for the model (170). The coefficients for the 2D case have been defined analog to the 3D case from [42] and can be found in Table 8.

Table 9: Time and length scales

	I	II	III
t	c^2/b	$\sqrt{c^2/a}$	b/a
h	c	c	$b/\sqrt{2a}$

The time and length scales as well as the non-dimensional group Ω can be expressed using the coefficients a, b and c as in Table 8. This gives rise to three different scalings denoted by I, II, and III with scales given in Table 9. For example, considering scaling I, the dimensionless time is defined by $t^* = c^2/bt$ and the dimensionless rise height is $h^* = ch$. The scales have been chosen in accordance with [42]. From here on dimensionless quantities are used where applicable and the "*" is dropped. Using the three different scalings listed in Table 8, the extended rise model (170) is non-dimensionalized. The scaled extended models for all three scalings are listed in Table 10. where the following coefficients have been used.

$$S := \frac{L}{R}, \quad K := \frac{1}{1+3S}, \quad Q := \frac{3(15S^2+10S+2)}{5(1+3S)^2}. \tag{189}$$

Note that for $L = 0$ it follows that $K = 1$. Hence, the scaling for the model with Navier slip is consistent with the scaling for the model with no slip boundary conditions [42, 50] if the additional volume is neglected $\hat{h} = 0$ and the convection contribution is set to zero ($Q = 0$).

Table 10: Scaled extended model with Navier slip boundary conditions

Scaling	Scaled Equation
I	$1/\Omega^2 \partial_t(\dot{h}(h+\hat{h})) + K\dot{h}(h+\hat{h}) + h + \hat{h} = 1 + Q/\Omega^2 \dot{h}^2$
II	$\partial_t(\dot{h}(h+\hat{h})) + K\Omega(h+\hat{h})\dot{h} + h + \hat{h} = 1 + Q\dot{h}^2$
III	$2\partial_t(\dot{h}(h+\hat{h})) + 2K\dot{h}(h+\hat{h}) + \sqrt{2}/\Omega(h+\hat{h}) = 1 + 2Q\dot{h}^2$

5.6 CONCLUSIONS FOR THE CAPILLARY RISE MODEL

CONCLUSION To obtain a unique stationary solution for the capillary rise problem, it is sufficient to assume a constant pressure boundary condition at the inflow boundary. While rise models for liquid in capillary assume an interface with the shape of a spherical cap, this condition is satisfied in the limit of a vanishing Eötvös number. While an interface with the shape of a spherical cap is not a stationary solution of the capillary rise problem, it does provide an excellent approximation in the limit case. Computations show that for the stationary state Eötvös numbers smaller than 0.1 are a sufficient criterion to assume a spherical cap, yet the error in the rise height quantified by Jurin's height is maximal in this limit. The detailed derivation of the extended capillary rise model reveals that the actual cause of the singularity for vanishing initial heights is the neglected volume between apex level and the interface. This allows to regularize the model without considering the influence of a reservoir. Furthermore, incorporating the same volume to the gravity term corrects the stationary rise height. The derivation shows that the inflow of momentum into the capillary results in a term proportional to $\dot{h}^2$ if the reservoir is not modelled explicitly. The derivation allows to incorporate various models for the viscous dissipation in the bulk and shows that no specific influence of the flow field in contact line vicinity and its dissipation is considered in the considered class of ode models. Overall, the derivation outlines the assumptions necessary for the applicability of this model and a comparison to full continuum simulations in a benchmark case.

OUTLOOK In general, experimental results for the parameter regime $\Omega > 2$ are scarce. One of the few results can be found in [108, 109]. These results have been extracted from the publication using Engauge Digitizer. A few comments on the experimental results are of order. This experimental results seems to have been used in [108] and [109] as identical parameters for the setups are listed in those publications. Surprisingly, different stationary heights

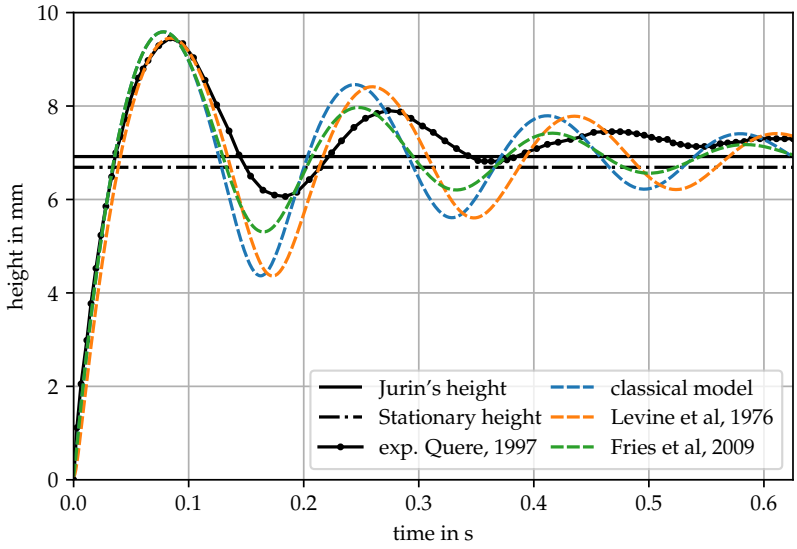

Figure 27: Comparison of models from [145, 76, 42] to experimental data from [108, 109] for the rise of a liquid in a cylindrical capillary.

the quality of the experimental results is often not sufficient for model validation

are reported: [108] gives 7.1 mm while [109] gives 7.3 mm - neither of them agrees with Jurin's height which is in this case $h_{Jur} = 6.9\,\text{mm}$ (based on the given parameters). Hence one can conclude that the stationary rise height has been obtained from experimental results and that the measurement error is at least 0.2 mm. In addition, no statistics or error bars for the experiment are available. As no local data for this experiment is available, a speculation on the cause of these discrepancies is not purposeful. Hence, the experimental data is not suitable for a detailed validation of theoretical models but can at least provide a good reference. Figure 27 shows a comparison between the experimental data from [108, 109] together with the models from [145, 76, 28, 42]. As an outlook, the approach developed in this chapter should be extended to a rotational symmetric capillary to allow for an experimental comparison. The ALE method presented in Chapter 4 can also be used to provide reference data for a detailed comparison to experimental observations.

6

VERIFICATION AND VALIDATION

6.1 BOUNDARY CONDITIONS

For the simulation of wetting processes, new boundary conditions have been implemented in OpenFOAM. These include a Navier slip boundary condition and a free slip boundary condition. A Navier slip boundary condition is required for the wetting model outlined in Chapter 3 in the vicinity of the contact line. A free slip boundary condition can be used in cases with stationary interface shapes. These implementations are to be verified. For this purpose, the case of a flow in a channel is used. This corresponds to an extended setup for Poiseuille flow in a channel, as here a Navier slip boundary condition is used on the channel walls.

6.1.1 *Reference Solutions - Channel Flows*

In the following, the one-dimensional stationary incompressible flow in a channel for $Re \to 0$ is used as reference case. For these assumptions, the momentum conservation equation (8) reduces to

$$\mu \partial_{yy} v_x = \partial_x p. \tag{190}$$

Applying the boundary conditions

$$v_x = L \partial_y v_x \quad \text{at} \quad y = 0, \tag{191}$$
$$v_x = U \quad \text{at} \quad y = H \tag{192}$$
$$v_y = 0 \quad \text{at} \quad y = 0, H \tag{193}$$

yields for the solution of the boundary value problem (190), (191), (192), and (193)

$$v_x(y) = \frac{G}{2\mu}\left(\frac{H^2}{H+L}(L+y) - y^2\right) + U\frac{y+L}{H+L}, \tag{194}$$

where the coordinate system is located on the same boundary on which the Navier slip boundary condition is applied. Here, H is the channel height, L is the slip length and G is the linear pressure gradient in flow direction. The

cross section of the channel coincides with the y-axis. For $y = 0, G = 0$ the slip velocity at the walls is given by

$$v_x(0) = U\frac{L}{H+L}. \tag{195}$$

Note that for $L = 0$, the solution (194) reduces to the well-known solution for Couette flow in a channel

$$v_x(y) = \frac{G}{2\mu}\left(Hy - y^2\right) + U\frac{y}{H}, \tag{196}$$

see, e.g., [5, 31].

In the following, the analytic reference solutions are used for a comprehensive verification of the implemented boundary conditions. To quantify the obtained errors, the following norms for $\mathbf{x} \in R^N$ are applied:

$$\text{1-norm} \qquad \|\mathbf{x}\|_1 := \frac{1}{N}\sum_{i=1}^{N}|x_i| \tag{197}$$

$$\text{2-norm} \qquad \|\mathbf{x}\|_2 := \sqrt{\frac{1}{N}\sum_{i=1}^{N}x_i^2} \tag{198}$$

$$\text{maximum-norm} \qquad \|\mathbf{x}\|_\infty := \max_i |x_i|. \tag{199}$$

Let $\tilde{\mathbf{v}}_x$ be the discrete solution obtained from using one of the implemented boundary conditions and $\mathbf{v}_x = (v_x(y_1), \ldots, v_x(y_N))^T$ the vector with the exact solution based on (194). Using these quantities, the residuals are defined by

$$r = \|\tilde{\mathbf{v}}_x - \mathbf{v}_x\| \tag{200}$$

where $\|\cdot\|$ is one of the norms (197), (198), or (199). The boundary conditions have been implemented as a general `fvPatchField` in OpenFOAM . This allows a general usage of the these boundary conditions with any other utility or solver that is available in OpenFOAM given that the discretization is suitable for the particular type of application. Hence, the single phase Navier-Stokes solver `icoFoam` from OpenFOAM extend 3.1 can be used to validate the implementation. The parameters for the channel flow test case are listed in Table 11 and Table 12. To achieve the same pressure gradient for test cases on a regular mesh, the domain size is adapted accordingly. As the inflow pressure level $p_{in} = 0$ has been used.

Table 11: Parameters for the channel flow test cases.

ρ in kg m^{-3}	μ in kg m^{-1} s^{-1}	U in m s^{-1}	H in m	Re
1	1	1	1	1

Table 12: Geometric parameters for the channel flow test cases.

Ny	5	10	20	40	80	160
L in m	0.6	0.3	0.15	0.075	0.0375	0.01875
D in m	0.2	0.1	0.05	0.025	0.0125	0.00625
p_{out} in Pa	-0.6	-0.3	-0.15	-0.075	-0.0375	-0.01875

6.1.2 *Navier Slip*

To use a Navier slip boundary condition in OpenFOAM extend version 3.1, a new boundary condition is implemented. This boundary condition can be used analog to any other boundary condition available in OpenFOAM . For a boundary patch `boundaryPatchName` of the bulk mesh, a Navier slip boundary condition can be used by placing

Listing 2: Usage of the Navier slip boundary patch in OpenFOAM.

```
boundaryPatchName
{
    type navierSlip;
    value uniform (0 0 0);
    slipLength uniform 0.001;
    wallVelocity uniform (0 0 0);
}
```

into the corresponding file for the bulk velocity. The `value` entry allows to prescribe the initial velocity distribution on the patch. In addition, the specification of the `slipLength` entry facilitates to prescribe an arbitrary distribution of a slip length across the patch. Moreover, the `wallVelocity` can be used to incorporate a moving wall boundary. Note that the boundary condition combines a no penetration condition in normal direction with the Navier slip boundary condition is applied in tangential direction.

VERIFICATION WITH REFERENCE SOLUTIONS As a first validation, the numerical solution is compared to (194) with $G = 0$. This provides a linear velocity profile in y-direction that shows a slip at the non-moving wall boundary and is given by (195). The test case has been solved for $L \in \{0, 0.001, 0.01, 0.1, 1, 10\}$. The results of this convergence study is shown in Figure 28.

It can be seen that the residuals vary around 10^{-12} for the $\|\cdot\|_1$ and the $\|\cdot\|_2$ norms and below 10^{-11} for the $\|\cdot\|_\infty$ norm. Note that the error is only slightly varying for all norms and increasing mesh resolutions. These results can be explained as follows: The discretization used for the solution of the Navier-Stokes equation is second order convergent such that a linear solution can be

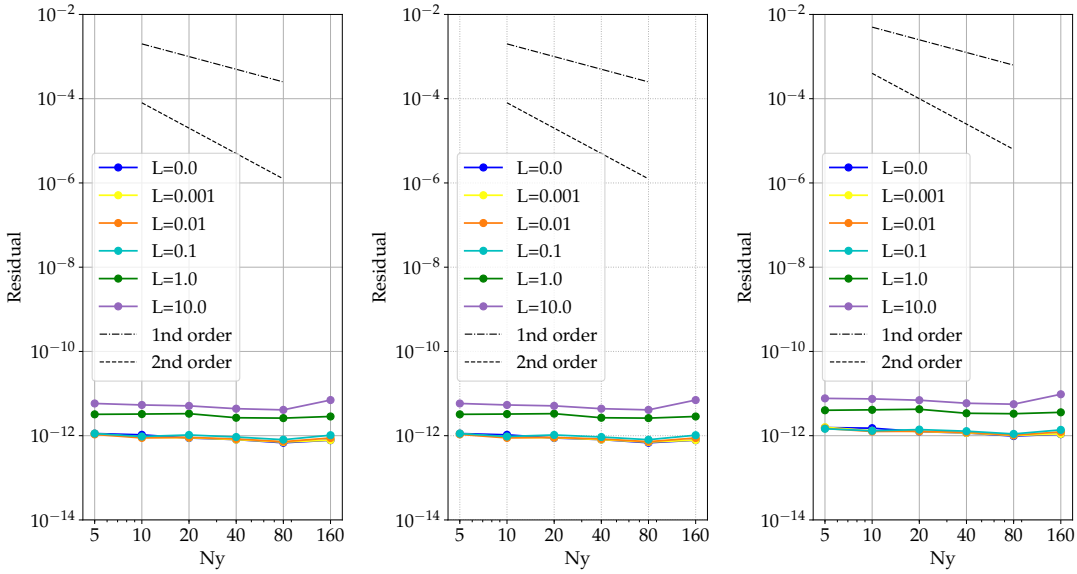

(a) Residuals for $\|\cdot\|_1$. (b) Residuals for $\|\cdot\|_2$. (c) Residuals for $\|\cdot\|_\infty$.

Figure 28: Convergence study for a Couette flow with Navier slip boundary conditions.

computed exactly. However, all involved equation systems and the non-linear convection term are solved with iterative matrix solvers and a Picard iteration respectively.

The above calculations have been repeated for the channel flow, using $G = 1\,\mathrm{Pa\,m^{-1}}$ and the same set of slip lengths. The results for this test case are depicted in Figure 29. All convergence studies for the different slip lengths show excellent agreement. A comparison to the dotted reference curve also shows that the results are second order convergent in all considered norms. Note that the actual values of residuals differ between the different norms.

CONSISTENCY WITH NO SLIP The discretization and implementation of the Navier slip boundary condition should reduce to a no slip boundary condition in the limit $L \to 0$. To demonstrate that the implemented Navier slip boundary condition is in this sense consistent with the corresponding available boundary condition in OpenFOAM, the test setup is executed using the `fixedValue` boundary condition with `value uniform (0 0 0)`. This corresponds to $\nu = 0$ on the wall boundary. For this test case, the Poiseuille flow solution (196) is used as a reference solution. The results the calculations are depicted in Figure 30. Both, the `fixedValue` boundary conditions as well as the `navierSlip` boundary condition show the same residuals with equal convergence orders as both curves coincide for all considered residual-norms. Hence, the implemented Navier slip boundary condition is for vanishing slip length consistent with the available no slip boundary condition.

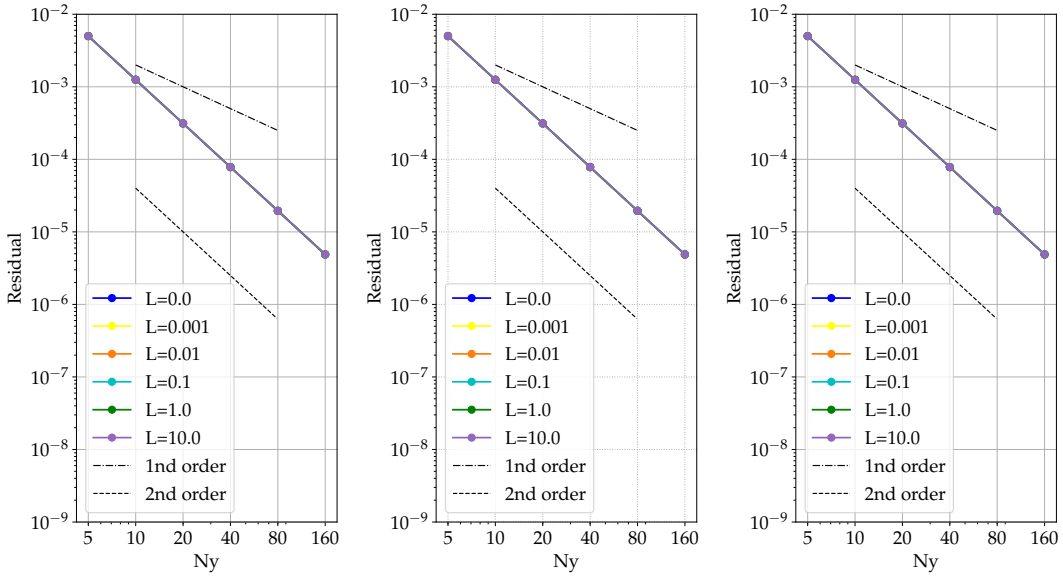

(a) Residuals for $\|\cdot\|_1$. (b) Residuals for $\|\cdot\|_2$. (c) Residuals for $\|\cdot\|_\infty$.

Figure 29: Convergence study for a Poiseuille flow with Navier slip boundary conditions.

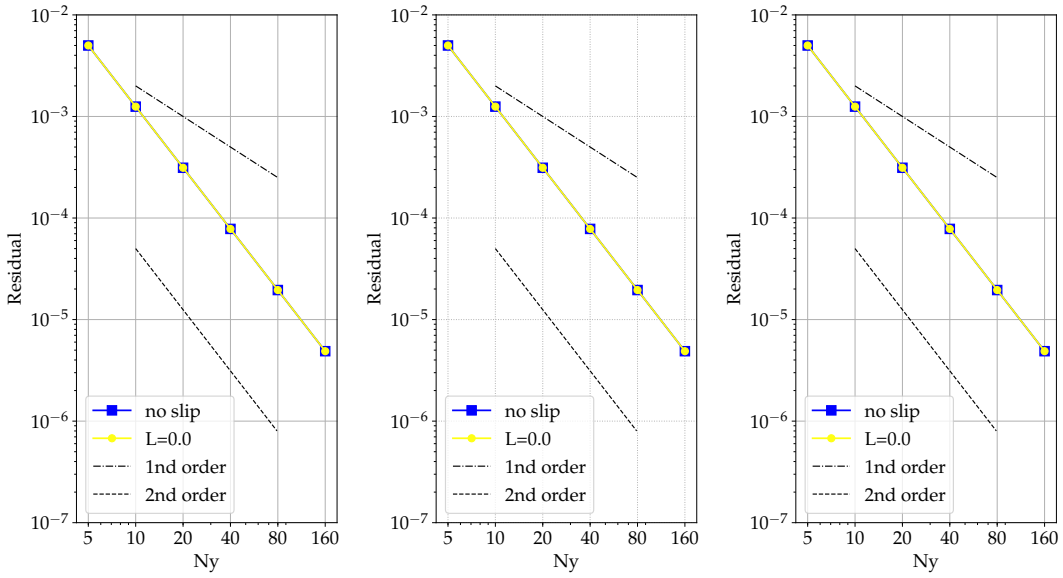

(a) Residuals for $\|\cdot\|_1$. (b) Residuals for $\|\cdot\|_2$. (c) Residuals for $\|\cdot\|_\infty$.

Figure 30: Consistency between the implementation of the Navier slip and the no slip boundary condition.

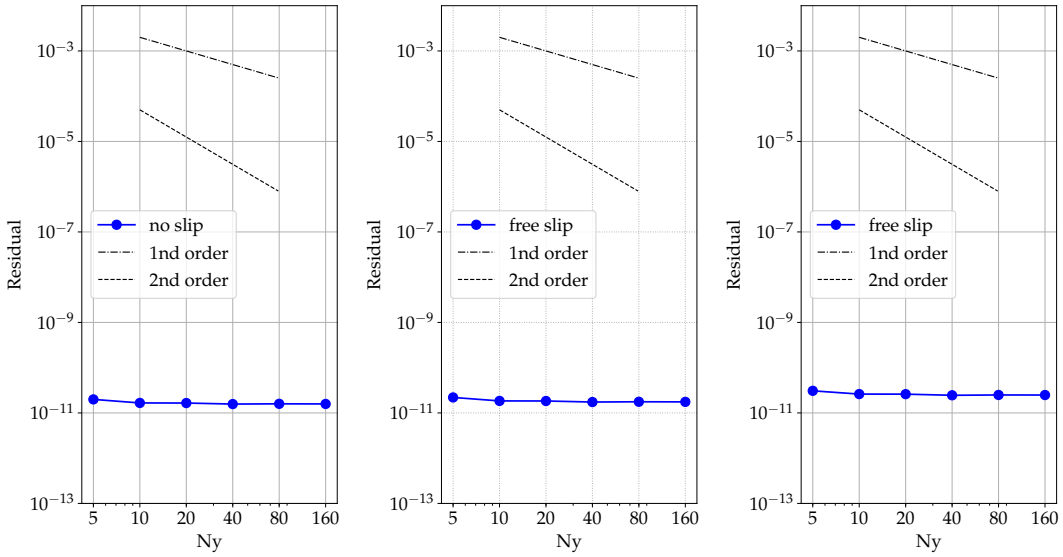

(a) Residuals for $\|\cdot\|_1$. (b) Residuals for $\|\cdot\|_2$. (c) Residuals for $\|\cdot\|_\infty$.

Figure 31: Convergence study for the Couette flow with a free slip boundary condition.

6.1.3 *Free Slip*

The Navier slip boundary condition (17) reduces to a free slip boundary condition for the limit $L \to \infty$. For an implementation of this boundary condition it is possible to approximate the behavior for large values of the slip length L. However, an exact implementation of the free slip boundary condition requires a separate implementation of

$$\frac{\partial \boldsymbol{v}}{\partial \boldsymbol{n}} = 0. \tag{201}$$

For the purpose of verification, the channel flow (194) with boundary conditions

$$\mathbf{P}_{\partial\Omega}\mathbf{S}\boldsymbol{n} = 0 \quad \text{at} \quad y = 0, \tag{202}$$

$$v_x = U \quad \text{at} \quad y = H \tag{203}$$

$$v_y = 0 \quad \text{at} \quad y = 0, H \tag{204}$$

is used. Note that 201 follows from 202. In this context, the analytic solution for the laminar flow in the channel is given by

$$v_x(y) = \frac{G}{2\mu}\left(H^2 - y^2\right) + U. \tag{205}$$

The results for the Couette flow case with free slip boundary condition in Figure 31 show similar results as for the no slip and Navier slip boundary condition analyzed above. The errors for all norms are well below 10^{-11} as can

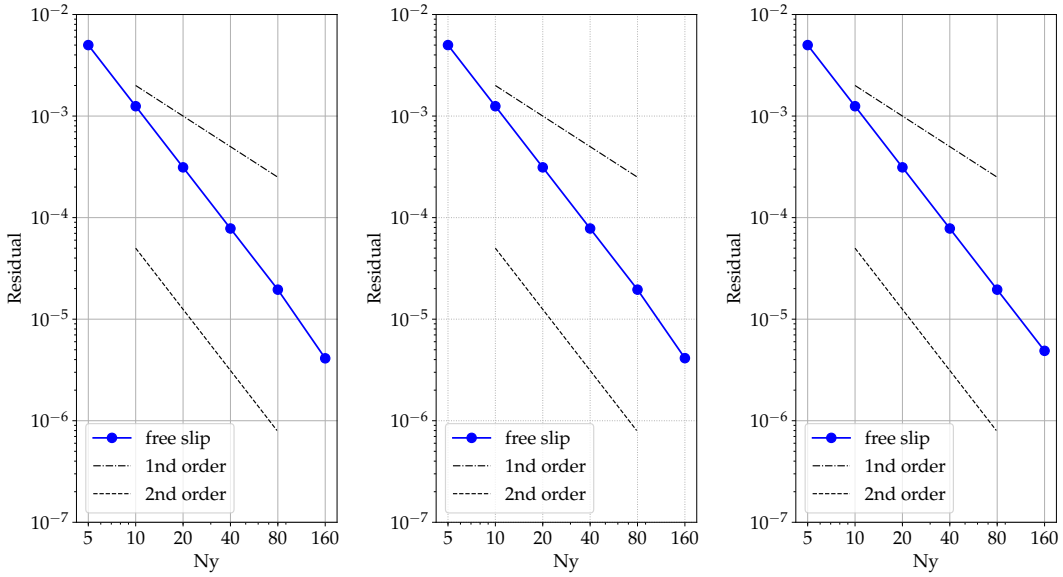

(a) Residuals for $\|\cdot\|_1$. (b) Residuals for $\|\cdot\|_2$. (c) Residuals for $\|\cdot\|_\infty$.

Figure 32: Convergence study for a Poiseuille flow with a free slip boundary conditions.

be expected for a constant velocity solution (see discussion for the Navier slip boundary condition above). Figure 32 shows the mesh convergence study for $G = 1\,Pa\,m^{-1}$. Analog to the convergence study for the Navier slip boundary condition, a second order convergence can be seen for all considered norms.

6.2 FREE SURFACE FLOWS

6.2.1 *Curvature*

The momentum transmission conditions (11) require the curvature of the interface. How this geometric quantity is computed from a surface mesh is derived in Section 4.3. The implementation is verified in the following. For this purpose, a sphere with radius $R = 1$ is used. In this case, the exact value of the total curvature is $\kappa = -2$. The sphere is discretized with a mesh that consists exclusively of triangular faces. Examples for these meshes are shown in Figure 33.

For each of the shown meshes, the curvature field associated with the surface faces is evaluated. The corresponding error norms are computed using $\mathbf{r} = (r_0, \ldots, r_f, \ldots, r_{N_F-1})^T$ with $r_f := \kappa_f - \kappa$. Applying (197), (198), and (199) to $\mathbf{r}$ gives the convergence plot in Figure 34. The tessellation of the spheres are mostly homogeneous, such that a comparison to the first and second order reference lines reveals a first order convergence. Note that the convergence in the infinity norm is linear above 714 surface faces. The curve for the one-norm

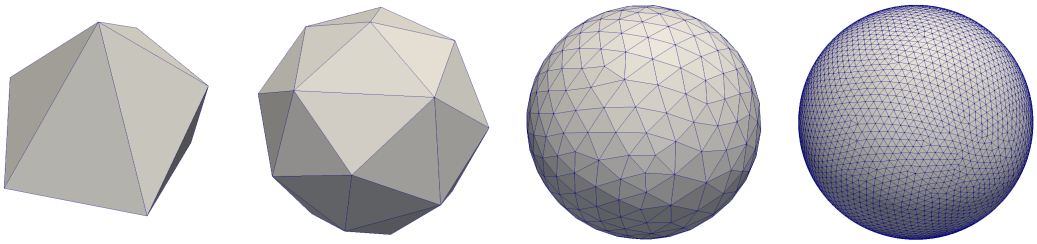

(a) 14 faces. (b) 40 faces. (c) 714 faces. (d) 9020 faces.

Figure 33: Meshes for the curvature mesh convergence study.

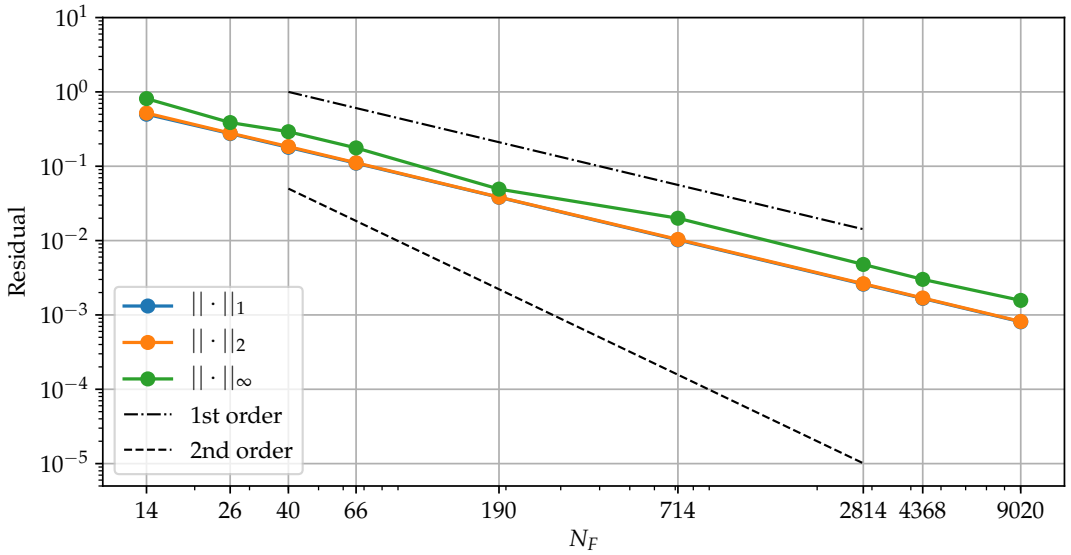

Figure 34: Residuals for the curvature computation for a sphere with radius $R = 1$ for increasing mesh resolutions using (80) without the factor $\cos(\alpha_e/2)$.

is nearly coinciding with the results from the two-norm, though they are not identical.

6.2.2 *Oscillating Drop*

The oscillating droplet is a suitable dynamic test for a multiphase flow solver, where a slightly perturbed disk or a rotational symmetric ellipsoid is used as initial condition in 2D or 3D, respectively. After the simulation is started, the droplet begins to oscillate due to surface tension forces. The oscillation amplitude follows an exponential decay. The equilibrium shapes for the 2D and the 3D cases are a disk and a sphere, respectively.

For the 3D case an analytical reference solution is available, see, e.g., [72]. The reference solution gives a damped oscillation with dampening constant

$$\tau = \frac{R^2}{\nu(n-1)(2n+1)}. \tag{206}$$

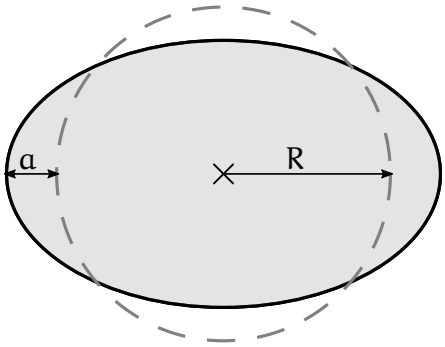

Figure 35: Droplet deformation for the oscillating droplet case.

Table 13: Parameters for the oscillating droplet case.

ρ in $kg\,m^{-3}$	μ in $kg\,m^{-1}\,s^{-1}$	σ in $N\,m^{-1}$	R in m	a in m
1	10^{-2}	1	0.2	0.01

Here, $\nu = \mu/\rho$ is the kinematic viscosity and n is the mode of the spherical harmonic, which is used in the derivation of the approximate solution. Typically the ellipsoidal mode is considered, which corresponds to $n = 2$. The envelop of the damped oscillation is given by

$$r(t) = R \pm a \exp(-t/\tau) \tag{207}$$

An illustration of the coefficients in shown in Figure 35. The disk or spherical droplet with radius R is scaled to obtain an ellipsoid or an ellipsoidal droplet, where the larger major axis has the length $R + a$. The second major axis is chosen such that the deformed droplet has the same volume as the original sphere. The physical parameters have to be chosen according to the assumptions for the reference solution and are given in Table 13. These physical parameters are used for both, the 2D and the 3D case.

OSCILLATING ELLIPSE The oscillating droplet case has been setup for a 2D case. For this purpose, a slightly ellipsoidal droplet is initialized. A selection of the used meshes for the 2D study is shown in Figure 36. The used meshes consist of 44, 122, 542, 2062, and 8124 cells. All meshes have at least one boundary layer consisting of quadrilateral cells, while the remainder of the mesh exclusively consists of triangular cells. The simulation is run for 1 s and the major axis sizes are evaluated using a bounding box of the mesh vertices. The results from all considered meshes for the length of one of the major axis over time is shown in Figure 37. The results from all meshes are barely distinguishable. Even the smaller meshes with 44 and 122 hardly differ from those with a higher resolutions. The results from three fine meshes perfectly agree on this scale of observation and hence are considered sufficiently resolved for the considered problem.

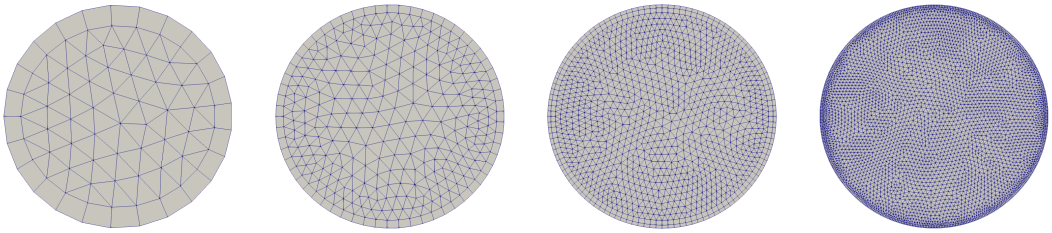

(a) 44 cells. (b) 542 cells. (c) 2062 cells. (d) 8124 cells.

Figure 36: Meshes for the 2D oscillating droplet test case.

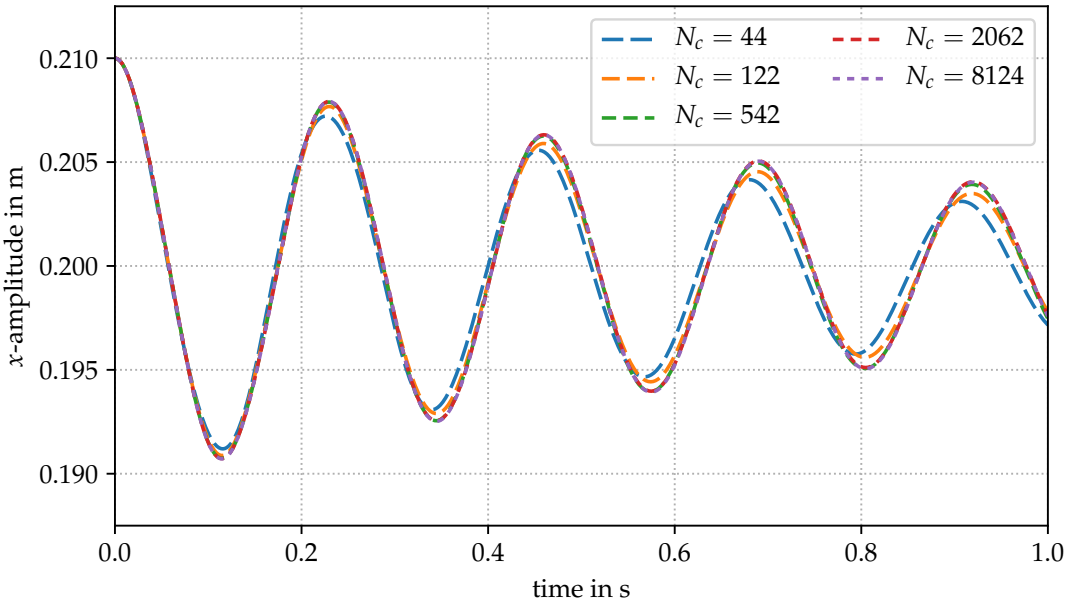

Figure 37: Ellipse radius in direction of the rotation axis (z-axis).

OSCILLATING ELLIPSOID A mesh study for the oscillating droplet case has also been executed for a 3D case. Analog to the 2D case, meshes with increasing mesh resolution have been tested. These are shown in Figure 38, where the color represents the pressure distribution on the droplet surface. The mesh resolution increases from 508 cells to 69074 cells. The more coarse meshes with 508 and 882 cells do not fully match the geometric setup given in Table 13. This can be seen in Figure 39, where the oscillation amplitude of the x-axis over time is depicted. It can be seen that the two less resolved meshes, depicted by a blue and an orange dashed line, do not start at 0.21 m. These curves do not stay within the reference envelop (207), which is illustrated by the black continuous line. The finer resolved meshes do match the initial amplitude and fit the . The mesh with 8321 cells shows good agreement with the finest mesh up to roughly 0.5 s. After this time, the 8321-cell mesh shows a slight drift with respect to the envelop. The finest mesh shows

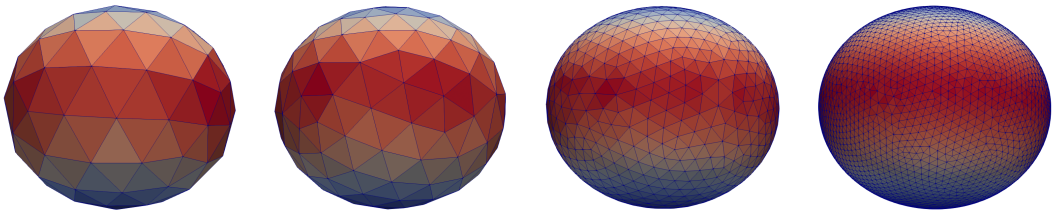

(a) 508 cells. (b) 882 cells. (c) 8321 cells. (d) 69074 cells.

Figure 38: Initial distribution of the modified pressure for the 3D oscillating droplet case. The color shows the pressure distribution over the interface. Red indicates a high and blue a low pressure.

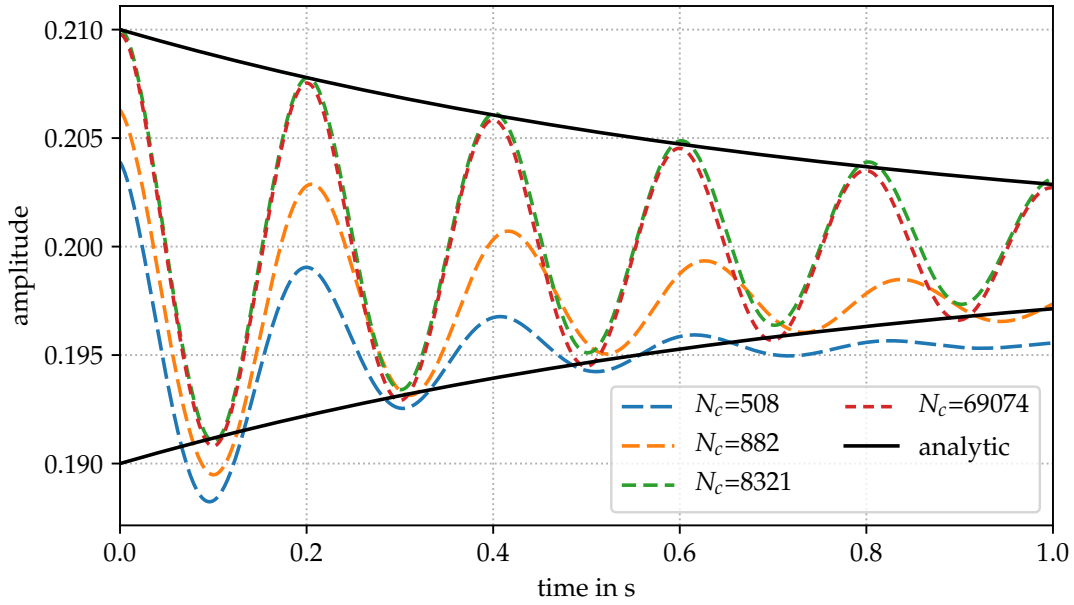

Figure 39: Ellipsoidal radius in the direction of the rotation axis (x-axis).

excellent agreement with the envelop for the full simulation time. The above simulations have been obtained with the application that has been extended for the simulation of wetting processes. The above results confirm that the implemented extensions do not affect the results for free surface flows. The following test cases verify the extension to wetting processes.

6.3 WETTING

6.3.1 *Gravity Drop Spreading*

In Chapter 4, a numerical approach to obtain a prescribed contact angle using the CP-algorithm is described. The corresponding implementation is to be tested to verify that the approach indeed enforces a prescribed contact an-

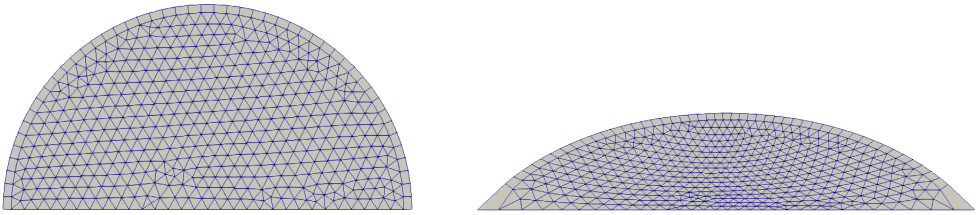

(a) Initial mesh. (b) Stationary state.

Figure 40: Comparison between the initial and the final mesh for Eo = 1.

gle. For this purpose a droplet spreading on a planar surface is considered, following [29].

The test case proceeds as follows: A drop of liquid is initialized as a hemisphere on a flat surface. As contact angle, $\theta = 50°$ is used. When an equilibrium state is obtained (evaluated by the movement of interface points) the surface shape is evaluated. An example of such a deformation is shown in Figure 40. The initial configuration is shown in 40a and the corresponding stationary shape with a contact angle of $\theta = 50°$ is shown in Figure 40b. In the following, different drop heights obtained by varying the Eo number are compared. For the limiting cases $Eo \to 0$ and $Eo \to \infty$ reference solutions are available [29]. In the small Eo limit, the surface tension dominates the gravitational forces and the drop has the shape of a spherical cap. In this case, the radius of the spherical can be computed by

$$R = R_0 \sqrt{\frac{\pi}{2(\theta - \sin\theta\cos\theta)}}, \tag{208}$$

where R_0 is the radius of the initial hemisphere and θ is the prescribed contact angle. The maximum height of the deformed droplet is found at the symmetry plane and given by

$$e_0 = R_0(1 - \cos\theta)\sqrt{\frac{\pi}{2(\theta - \sin\theta\cos\theta)}}. \tag{209}$$

In the large Eo limit, the drop forms a puddle with the height

$$e_\infty = 2\sqrt{\frac{\sigma}{\rho_l g}}\sin\frac{\theta}{2}, \tag{210}$$

which is directly proportional to the capillary length [29]. This limit corresponds to the case where gravitational forces dominate over surface tension forces.

While the above references are applicable in the limit of small and large Eötvös numbers, the transition region around $Eo \approx 1$ is not covered by these approximations. However, it is possible to compute the exact shape and therefore, also the exact height of the stationary droplet at the symmetry plane/axis. For this purpose, the interface is represented as a graph

Table 14: Physical parameters for the gravity drop spreading test case.

ρ in $kg\,m^{-3}$	μ in $kg\,m^{-1}\,s^{-1}$	σ in $N\,m^{-1}$	R_0 in m	θ in $^\circ$
10^3	10^{-2}	0.072	10^{-3}	50

Table 15: Variation of the Eo number for the gravity drop spreading test case.

Eo	0.001	0.01	0.1	0.5	1	2	5	10
g in $m\,s^{-2}$	0.072	0.72	7.2	36	72	144	360	720

$h : (-r_{cl}, r_{cl}) \to \mathbb{R}$. Then the interface is given via the height of its points $\Sigma = \{(r, h(r)) : r \in (-r_{cl}, r_{cl})\}$. Note that this parameterisation is possible for $\theta < \pi/2$. Using this graph representation, the interface shape is the solution of the boundary value problem

$$\sigma h'' = (1 + h'^2)^{3/2}(\rho g h - p_0) \qquad \text{in } (0, 2r_{cl}), \tag{211}$$

$$h(0) = 0, \quad h'(0) = \tan\theta. \tag{212}$$

Furthermore, the interface height h needs to satisfy the integral condition

$$A = \int_0^{2r_{cl}} h \, d\xi. \tag{213}$$

where, A is the area of the 2D drop. Note that this integral condition makes the boundary value problem an integro-differential equation. Furthermore, in contrast to the problem for the interface shape in a capillary, which has been considered in Chapter 5, neither the pressure inside the liquid p_0, nor the radius of the domain r_{cl} are known a priori. Hence, an inverse problem for the the unknown parameters are p_0 and r_{cl} has to be solved in order to obtain the interface h. In this context, the integro-differential equation (211) and (212) is the underlying problem from which p_0 and r_{cl} have to be computed. The algorithm to solve the inverse problem is described in Appendix D.

The test case described in [29] has been executed using the parameters from Table 14. The results are presented in a non-dimensional form by varying the Eötvös number. This is achieved by adjusting the gravitational acceleration as listed in Table 15. A comparison between the obtained numerical results, numerical results from a Geometric Volume of Fluid (VOF) method from [29], and the reference solutions given above is shown in Figure 41. The data has been scaled using the drop height in the small Eo number limit, i.e., $e^* := h/e_0$. Hence, the drop height is unity for the small Eo number limit. This reference height is indicated by the black horizontal line. The large Eo limit based on (210) is indicated by the dotted line and is also scaled using (209). The reference solution based on the inverse problem above is given by the green continuous line. For each Eötvös number, an inverse problem as described above

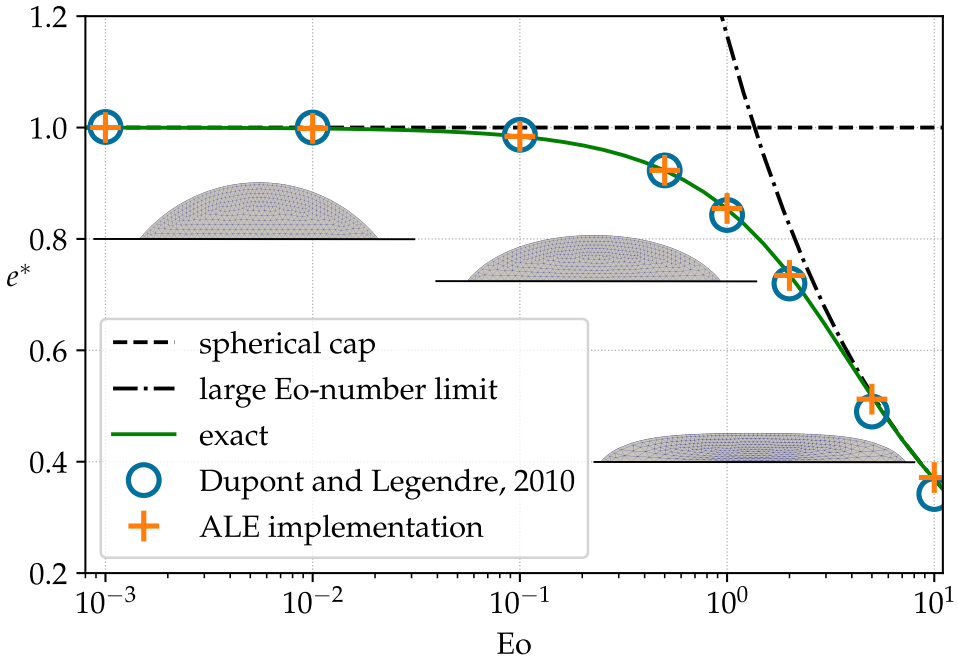

Figure 41: Non-dimensional drop height for varying Eo number and $\theta = 50°$.

has been solved. The numerical approach used for the solution of the inverse problem is described in Appendix D. Note that the exact solution agrees with the available reference solution for both limiting cases of the Eötvös number. The results from [29, Figure 9] have been extracted using engauge digitizer version 10.4. The data from [29] is indicated by blue circles, while the test results from the ALE interface tracking method are given by red crosses. The results from both methods show good agreement with both limiting cases of the Eötvös number. The agreement between the VOF results from [29] and the stationary results of the ALE method coincide for $Eo < 1$. For $Eo \geqslant 1$ the agreement is still good with minor deviations for increasing Eo numbers. A comparison with the exact reference solution shows excellent agreement with the numerical results that have been obtained with the extended ALE method for the full range of Eötvös numbers. The results from the geometric VOF method from [29] also show excellent agreement with the exact solution for $Eo < 1$, while the stationary drop height is increasingly underestimated for increasing Eötvös numbers.

Overall, the test case confirms that the algorithm described in Chapter 4 has been successfully implemented into the existing ALE approach and agrees well with the reference solution provided in [29]. Moreover, the available reference has been significantly improved by formulating and solving an inverse problem for the full shape of the free surface.

6.3.2 *Stationary Surface*

In Chapter 5 interface shapes between two plates and within a cylindrical capillary are computed. In that regard, the 1D boundary value problem 129 is solved numerically. These surfaces provide local information that can be used as reference data to verify the ALE implementation presented in Chapter 4.

For the solution of the full continuum mechanical problem the physical parameters in Table 16 are used. Though these values approximately correspond to the properties of water, the Eo is the only relevant non-dimensional group for the shape of the stationary interface. The simulation is started from a square and cylindrical domain, respectively, and is run for 0.3 s. This time has shown to be sufficient to reach a stationary interface in all considered cases. To vary the Eo number, the gravitational acceleration is varied, while all other parameters in Table 16 remain constant. For the given choice of parameters this means that the value of g is set to the same value as the considered Eo number. Six different surfaces are computed, which corresponds to the different values of the Eo numbers. To illustrate and compare the obtained numerical results, the surface shape is scaled using the same method as outlined in Section 5.2.2. This includes the alignment at the symmetry plane and the symmetry axis in the 2D and 3D case, respectively.

Table 16: Parameters for the verification of the stationary capillary surface.

ρ in kg m^{-3}	μ in kg m^{-1} s^{-1}	σ in N m^{-1}	θ in $^\circ$	R in mm
1000	10^{-2}	10^{-3}	45	1

2D CASE STUDY For the 2D verification case, the domain has been resolved with N_x cells per radius, which leads to a mesh with 80×80 cells. The initial and the stationary state of this mesh are shown in Figure 42 for Eo $= 0.01$.

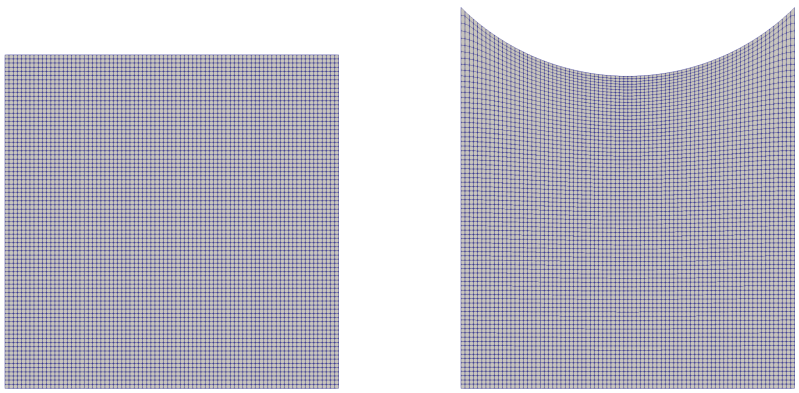

(a) Initial shape. (b) Final shape.

Figure 42: Initial and final meshes (80×80 cells) for Eo $= 0.01$.

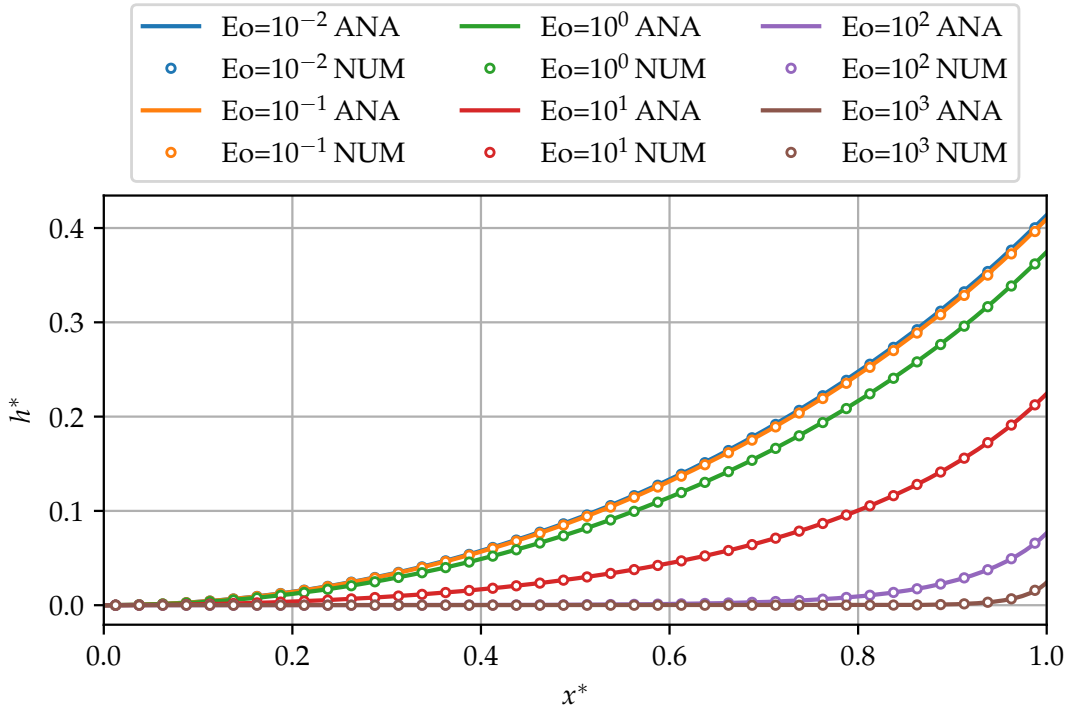

Figure 43: Comparison of 2D results between the numerical solution of (129) and the results from the ALE implementation outlined in Chapter 4.

The results of the 2D verification study are shown in Figure 43. The continuous lines show the numerical solution of the boundary value problem (129) similar to Figure 21b and are labeled "ANA". The circular markers represent the stationary surface shape obtained from ALE results from meshes as shown in Figure 42b and are labeled "NUM". It can be seen that the results from the ALE implementation and the solution of (129) show excellent agreement for all Eo numbers. Note that the results for $\mathrm{Eo} = 10^{-2}$ and $\mathrm{Eo} = 10^{-1}$ nearly coincide. This case represents a successful verification of the presented method concerning the extension of the CP-algorithm to wetting scenarios. Furthermore, the contact angle is correctly set such that the reference solution can be accurately reproduced. Moreover, the 2D test case verifies a correct implementation of the contact line patch implementation. Note that in this case, the equidistant distribution of the ALE-results is caused by the regular mesh used for the 2D cases.

3D CASE STUDY For the 3D verification case a cylindrical capillary is used. An example of the initial and the deformed mesh is given in Figure 44 for $\mathrm{Eo} = 0.01$. To illustrate the cell distribution inside the capillary, a cross section of the volume mesh is shown. The results of the 3D verification case are given in Figure 45. As above, results from the numerical solution of (132) are labeled "ANA", while results from the ALE implementation are labeled "NUM". The

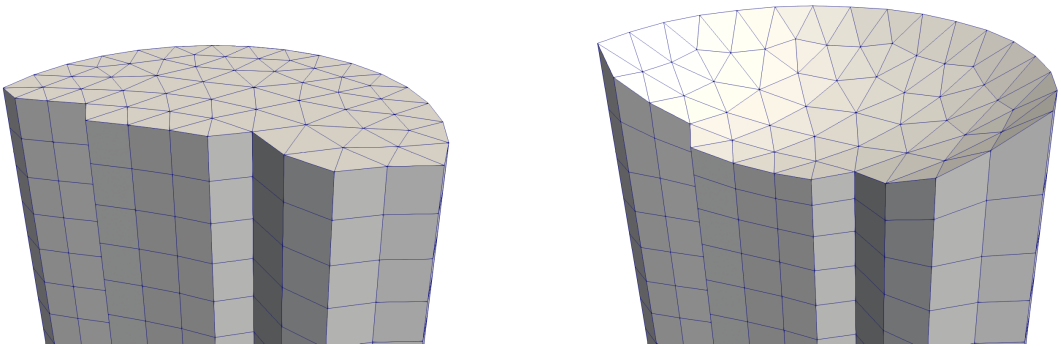

(a) Initial shape. (b) Final shape.

Figure 44: Cross section of a cylinder for initial and final meshes with Eo = 0.01.

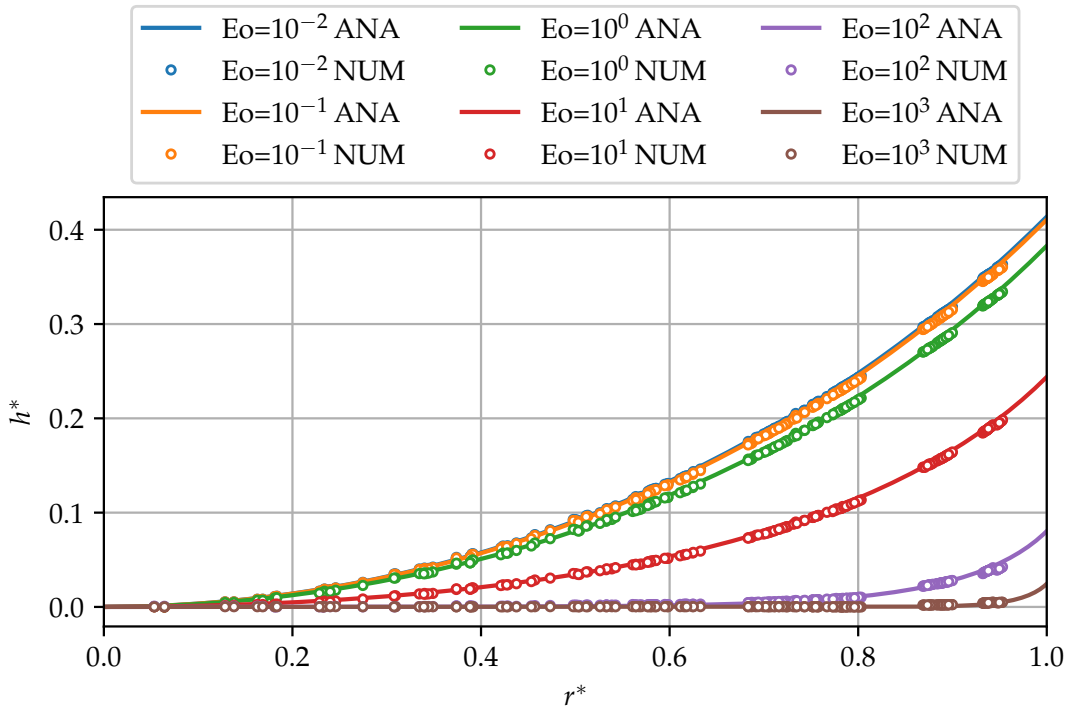

Figure 45: Comparison of 3D results between the numerical solution of (132) and the results from the ALE implementation outlined in Chapter 4.

circular markers represent the cell centers of the surface mesh which have been extracted and scaled as before. As for the 2D case, the results are in excellent agreement with the reference solution for all Eo numbers. Note that the non-equidistant distribution of the ALE-results results from the triangular interface mesh shown in Figure 44.

6.3.3 *Capillary Rise*

As outlined in Chapter 2, using a no slip boundary condition for the simulation of wetting processes does not yield a solvable mathematical problem. Nevertheless, enforcing this condition on the solid surface while advecting the interface with an extrapolated velocity is a frequently occurring approach to obtain a "moving contact line". To analyze this approach, the capillary rise benchmark case is used.

CHOICE OF PARAMETERS The parameters for this test case are chosen in order to obtain an oscillating rise behavior. A condition for such damped rise oscillations to occur for a liquid rising between two plates has already been derived in Section 5.4:

$$\Omega < 2, \quad \text{with } \Omega = \sqrt{9\sigma\cos\theta\mu^2/(\rho^3 g^2 R^5)}. \tag{214}$$

Furthermore, the parameters have to be chosen such that the interface remains a spherical cap during the rise. Another important aspect is the time to reach the final rise height and a stationary state should be small in order to minimize simulation time. Following these requirements, the parameters have been chosen as listed in Table 17. For a more detailed discussion of the parameter selection, see Chapter 7.

Table 17: Parameters for the capillary rise mesh convergence study.

ρ in $kg\,m^{-3}$	μ in $kg\,m^{-1}\,s^{-1}$	σ in $N\,m^{-1}$	g in $m\,s^{-2}$	θ in $^\circ$	R in mm
83.14	10^{-2}	0.04	4.17	30	5

These parameters give $\Omega \approx 1$ such that an oscillating rise behavior can be expected. The rise height h is measured from the inflow boundary to the apex as illustrated in Figure 20.

NUMERICAL SLIP VS NAVIER SLIP For the comparison to the ODE models, the interface must have the shape of a spherical section. This shape is obtained analog to the procedure which has been used for the computation of the stationary interfaces in Section 6.3.2. As a start mesh, a regular, equidistant mesh is used. Subsequently, the simulation is started and run until an equilibrium state is obtained. This approach gives the mes shapes shown in

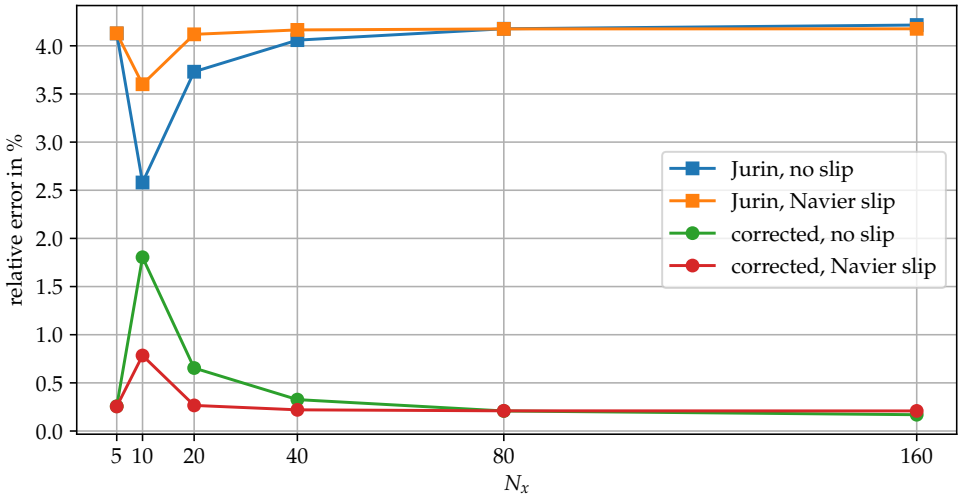

Figure 46: Error comparison between Jurin's height and the corrected height (137)

Figure 40. The mesh is than used as initial condition for the liquid distribution in the capillary.

The initialization process is executed for meshes with resolutions from 5 to 160 cells per diameter. After a successful equilibration procedure, the boundary conditions on the inflow boundary $\partial\Omega_{in}$ are changed from $\boldsymbol{v} = 0$ to $\partial_n \boldsymbol{v} = 0$ and the apex height over time is recorded.

Generally, two different boundary conditions are compared. A first parameter study is executed using no slip no penetration boundary conditions on the capillary walls, i.e. $\boldsymbol{v} = 0$ on $\partial\Omega_{wall}$. To obtain a moving contact line with the classical model, the contact line points are moved using the velocity from the mesh cell which is closest to the contact line. For this purpose the velocity is projected onto the solid surface. The approach is also referred to as *numerical slip*. The second mesh convergence study is executed with a Navier slip boundary condition of the form (17). The slip length used for this study is $L = 1\,mm$ which can be resolved by meshes with reasonable sizes.

The stationary apex height for both boundary conditions and all meshes are shown in 46. The plot depicts the relative errors

$$e_{Jur} := \frac{h_{num} - h_{Jur}}{h_{Jur}}, \qquad e_{corr} := \frac{h_{num} - h_{apex\,\infty}}{h_{apex\,\infty}}. \tag{215}$$

The results show that for increasing mesh resolution the errors for no slip and Navier slip boundary conditions stabilize at the same value. Furthermore, while a comparison to Jurin's height shows an error of more than 4 %, the error for the corrected stationary height is below 0.25 %. Hence, the corrected stationary height improves the rise height prediction by Jurin's height.

The rise height over time for the mesh convergence study using the numerical slip boundary conditions are shown in Figure 47. It can be seen that the curves for all meshes start at the same initial height $h(t_0) = 9.2\,mm$. While the

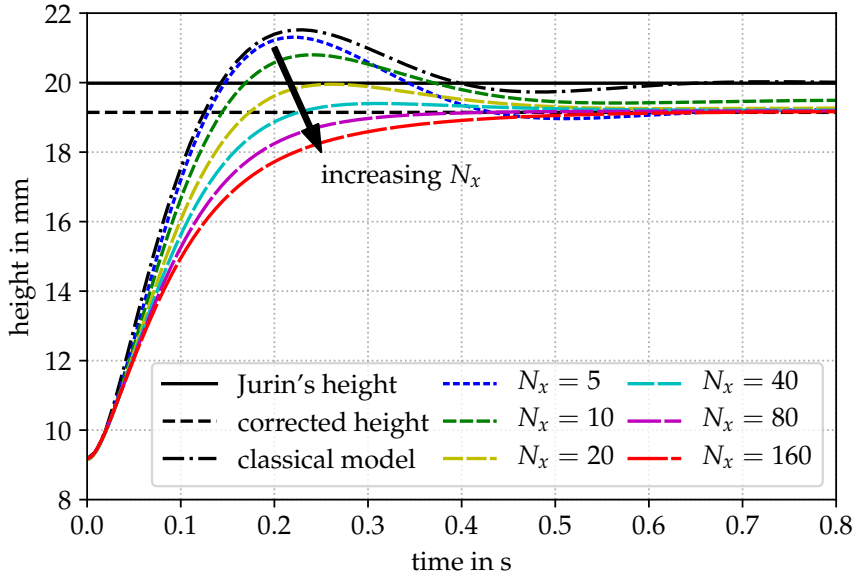

Figure 47: Influence of numerical slip on the mesh convergence.

less resolved meshes show a clearly visible maximum between 0.2 s and 0.3 s, the finer meshes approach the stationary height asymptotically. Together with the numerical results, the classical model is shown by a dashed-dotted line that levels at Jurin's height, which is in turn, depicted by a continuous line at $h_{Jur} \approx 20\,mm$. However, *all* numerical solutions except for the two lowest resolved meshes level at the corrected stationary rise height given by (137).

The stationary height predicted by meshes with $N_x = 20$ and higher resolutions agree well with each other and the corrected stationary rise height. Obviously, no mesh convergence can be observed for the dynamic rise using the numerical slip approach. This observation alone does not proof that there is no mesh convergence in general. However, it is questionable if any mesh convergence can be achieved using the available OpenFOAM implementation, as no solution exists and both, the pressure and the dissipation at the wall, are non-integrable singular. In the considered test case the influence is so severe that the results do not only change quantitatively but also qualitatively with increasing mesh resolution. Hence, while the lower resolved meshes do indeed predict an oscillatory rise behavior, the finer meshes do not. Consequently, it is questionable whether it is possible to obtain predictable results from an approach that utilizes numerical slip to obtain a moving contact line. The situation is different for the Navier slip boundary condition as illustrated in Figure 48. While the curves for the rise height differ around $t = 0.2\,s$ for meshes that are lower resolved than $N_x = 40$ the rise heights for meshes with a resolution of 40 and more cells per diameter coincide for the full simulation time. Furthermore, the stationary rise heights of all simulations show an excellent agreement with the stationary height predicted by the corrected rise height.

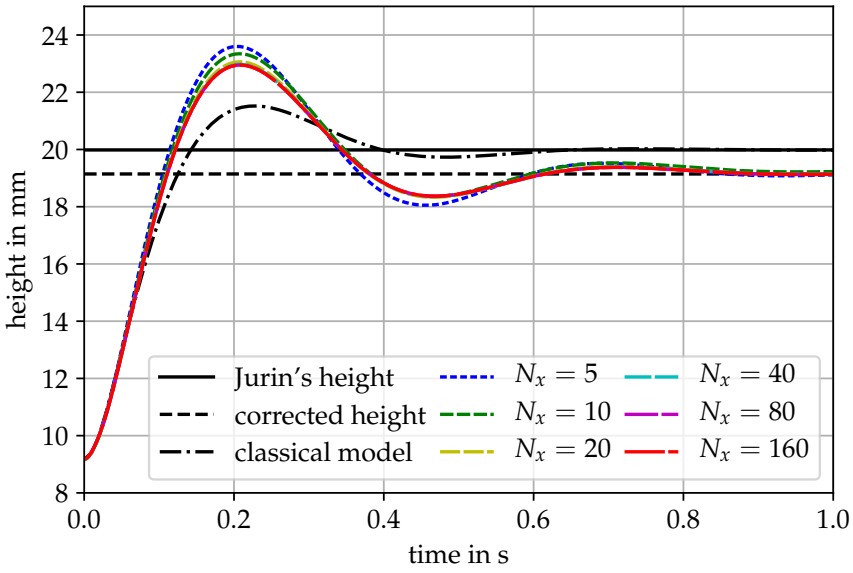

Figure 48: Influence of the Navier slip boundary condition on the mesh convergence.

The agreement with the reference solution is reasonable. In comparison to the classical rise model larger maxima and minima can be observed from the results of the numerical simulation. However, a certain deviation between the rise height curves has to be expected: Firstly, the reference solution makes numerous assumptions about the velocity field as outlined in Chapter 5. Secondly, to be able to resolve the slip length with the same mesh that is able to resolve the occurring Poiseuille flow and the interface, a significant slip length on the scale of the capillary is used. Hence, the viscous dissipation is reduced in contrast to the ODE model.

Changing the boundary condition from no slip to Navier slip allows for a solution to exist as outlined in Chapter 2. Furthermore, pressure and local dissipation remain integrable up to the contact line. Hence, a solution can be found using a finite volume approach which has been utilized here.

VALIDATION OF THE EXTENDED MODEL A detailed comparison between the classical model (classical), the extended model (extended), the extended model with a 30 % increased viscosity (adjusted), and a solution of the continuum mechanical description (continuum) is shown in Figure 49. The numerical solution of the continuum mechanical problem has been obtained with the ALE approach as described above. The capillary rise problem has been solved using the physical parameters from Table 18 and an initial apex height of $h_0 = 1.6 \times 10^{-3}\,\mathrm{m}$. The results are presented in a non-dimensional form, using a scaling that emphasizes the influence of inertia, while viscous effects

Table 18: Parameters for the validation of the extended rise model.

Ω	ρ in $kg\,m^{-3}$	μ in $Pa\,s$	σ in $N\,m^{-1}$	g in $m\,s^{-2}$	R in m	θ
0.1	1000	1.4×10^{-3}	5×10^{-2}	10	800×10^{-6}	45°
0.97	500	5.5×10^{-3}	2×10^{-2}	10	800×10^{-6}	45°
4.5	915	50×10^{-3}	3.2×10^{-2}	10	800×10^{-6}	45°

are used as scaling forces. In this case, the non-dimensional quantities are defined by

$$t^* = \frac{t}{\tilde{t}} \quad \text{and} \quad h^* = \frac{h - h_0}{\tilde{h} - h_0}, \tag{216}$$

with time and length scales

$$\tilde{t} = \sqrt{\frac{a}{c^2}} = \sqrt{\frac{\sigma \cos\theta}{g^2 \rho R}}, \qquad \tilde{h} = \frac{1}{c} = \frac{\sigma \cos\theta}{\rho g R}, \tag{217}$$

analogously to [42]. Note that this scaling removes the influence of the initial height and leads to the non-dimensional groups

$$\Omega = \sqrt{\frac{9\sigma \cos\theta \mu^2}{\rho^3 g^2 R^5}} \quad \text{and} \quad S = \frac{L}{R}. \tag{218}$$

Based on these parameters, the results in Figure 49 are arranged such that the rows correspond to $\Omega = 0.1, 0.97, 4.5$, while the columns correspond to $S = 0.2, 0.01$. Overall, the parameter Ω describes the dynamics of the system. For the classical solution $\Omega < 2$ yields rise height oscillations and $\Omega > 2$ results in an overdamped asymptotic rise. Hence, the results vary between the overdamped regime in the first to strong oscillations in the last row. On comparing the columns in Figure 49, it can be seen that decreasing S further decreases the dynamic of the system, as this influences the slip at the wall and hence increases the amount of viscous dissipation at the wall and in the vicinity of the contact line. Comparing the results regarding the stationary height, the classical model overestimates the stationary rise height in general. In contrast, the stationary height of the extended and the adjusted model coincide with the reference solution obtained from the continuum description. Furthermore, the extended model shows a good agreement with the continuum solution, which becomes more apparent for an increasing value of Ω. Specifically, the extended solutions show a good agreement regarding the oscillation amplitude in contrast to the classical model. In addition, the extended models successfully incorporate the influence of a decreasing slip length, which can be seen by comparing the left and right columns. Nevertheless, the extended model does not include the additional dissipation occurring due to

the transition from a Poiseuille flow to the velocity field that is tangential to the free surface. Hence, it is reasonable to consider an increased viscosity contribution to the rise model. An increase of 30 % in the viscous term leads to the adjusted model and an additional improvement in comparison to the extended model. Overall, the extended models significantly improve the classical model. However, for the most challenging rise regimes with strong oscillations, the extended model is slightly overestimating the oscillation amplitude and shows a phase shift in comparison to the continuum solution.

For an in-depth comparison to other numerical approaches, which are used for the simulation of wetting processes and the corresponding analysis regarding the numerical and Navier slip boundary conditions, see Chapter 7.

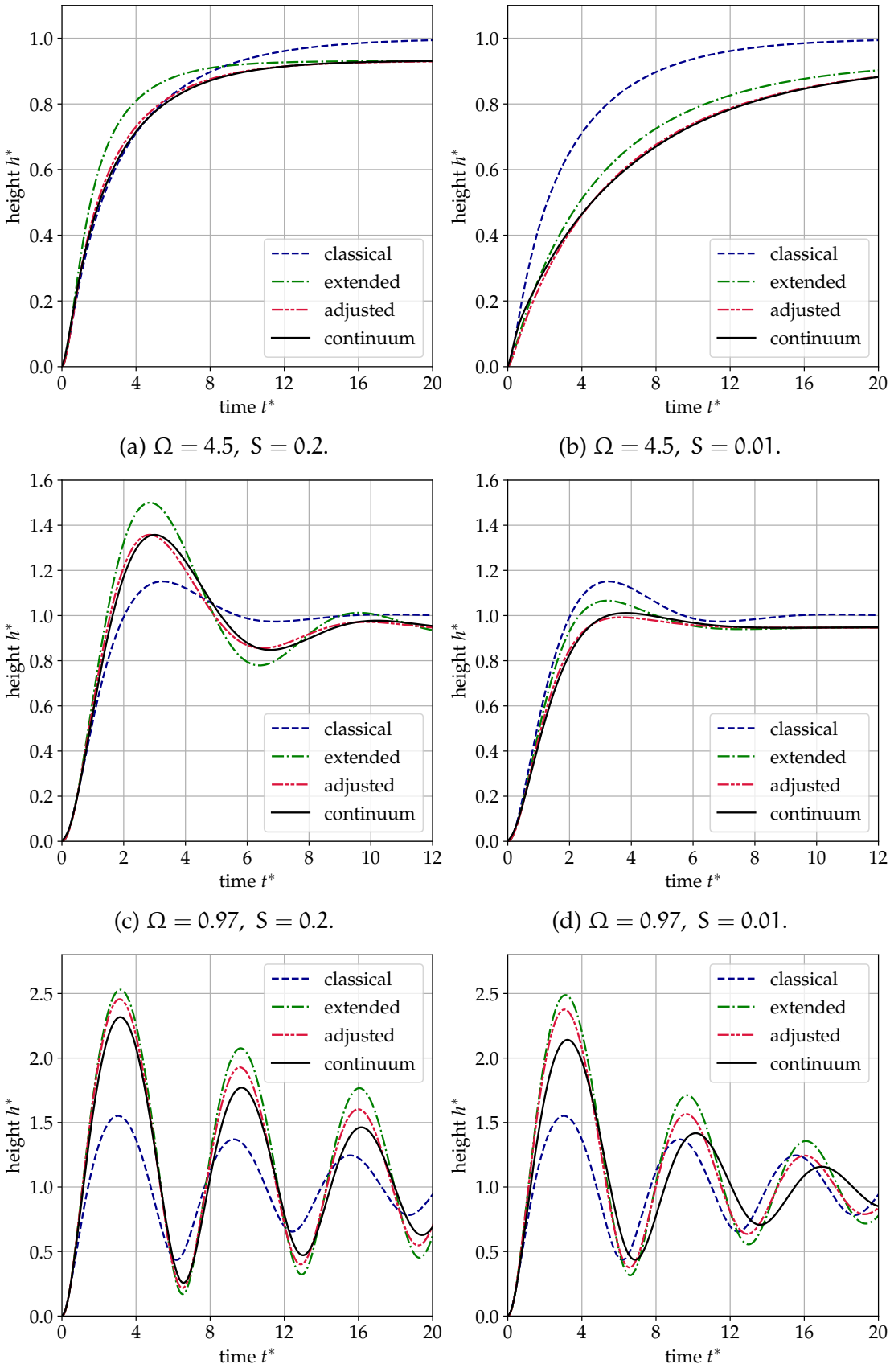

(a) $\Omega = 4.5,\ S = 0.2.$ (b) $\Omega = 4.5,\ S = 0.01.$

(c) $\Omega = 0.97,\ S = 0.2.$ (d) $\Omega = 0.97,\ S = 0.01.$

(e) $\Omega = 0.14,\ S = 0.2.$ (f) $\Omega = 0.14,\ S = 0.01.$

Figure 49: Comparison between the classical rise model (172), the extended model (171), the extended model with a 30 % increased viscosity, and the reference results from numerical solution of the continuum description.

7

CAPILLARY RISE - A BENCHMARK FOR WETTING PROCESSES

Since the first approaches to simulate multiphase flows in the 1960s, various fundamentally different methods have emerged. These can be roughly distinguished by their discrete representation of the fluid-fluid interface. Sharp interface models described the interface as a mathematically perfectly thin surface, while smooth interface models adopt a transition region. As for the human eye, a phase interface is typically perceived as a surface or in mathematical terms as a submanifold of $\mathbb{R}^3$. However, practitioners of smooth interface models argue that a physical fluid-fluid interface represents a transition region where the fluid properties change continuously, e.g., the change of density from a liquid to the gas phase. An advantage of the latter approach is that the smooth fields represent a mathematically more benign problem than a sharp interface representation. However, the typical physical diameter of a liquid-gas interface is (away from the critical point) on the order of $10\,\mathrm{nm}$ - a range of resolution that is typically out of reach for simulations of macroscopic phenomena. Nevertheless, while sharp interface models do not have to consider the aspect of interface width, the sharp surface gives rise to properties that are discontinuous at the interface.

The following section gives an overview of four different approaches that are based on the sharp interface model for multiphase flows. Four corresponding implementations are thoroughly compared using the capillary rise test case investigated in Chapter 5. The results provide novel benchmark data for wetting processes available in [49].

7.1 METHOD OVERVIEW

COMMON PROPERTIES The following section gives an overview of different numerical methods for multiphase flows based on a sharp interface model. The choice of interface representation has far-reaching consequences.

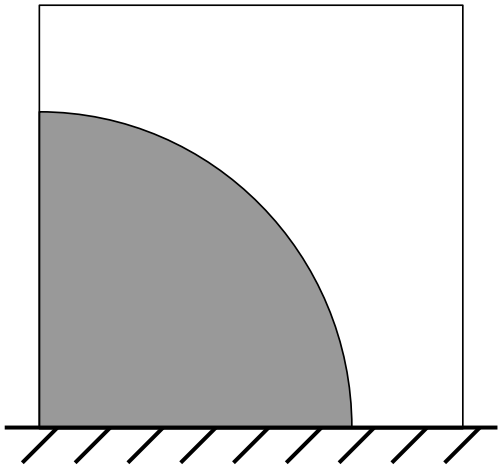

Figure 50: A drop wetting a surface.

Firstly, the choice of interface representation directly influences the required advection algorithm and consequently the volume conservation properties of the overall approach. Secondly, while some approaches represent the interface by a smoothed indicator function, others require special data structures to store subgrid data which directly affects performance and parallelization of the advection algorithm. Thirdly, an intersection with a background mesh may become necessary in order to couple the interaction of the interface with the solution of the mass and momentum conservation equations in the bulk phase. Depending on the interface orientation this may become an ill-conditioned problem. Fourthly, the coupling between interface movement and Navier-Stokes equations involves the curvature of the interface which is to be computed from the current shape of the interface, where different interface representations allow for varying precision of the curvature computation. However, one major common property is the time-explicit treatment of the interface evolution.

For a conceptual comparison, an illustration of the discrete representation of the droplet depicted in Figure 50 is given for each numerical approach.

7.1.1 *Level-Set*

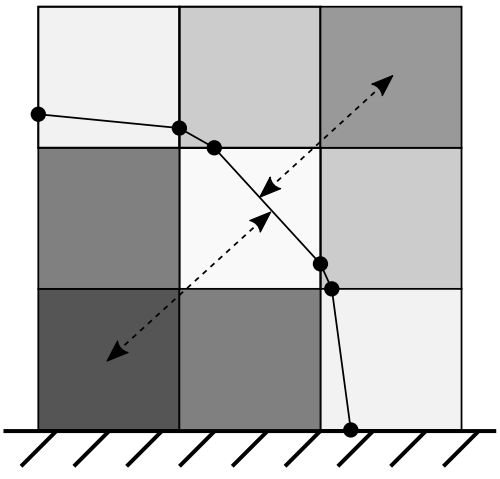

Figure 51: Level-set representation.

The level-set approach represents the interface as the level-set of a function $\phi : \mathbb{R}^d \to \mathbb{R}$ where typically the zero level-set is used. The discrete level-set function depicted in Figure 51 is often transported algebraically. Even though total variation diminishing (TVD) schemes, such as higher order weighted essentially non-oscillating (WENO) schemes, are often used, the discrete transport deteriorates the initially sharp interface. This effect accumulates with longer simulation times and can impair the curvature computation. To alleviate this influence, the level-set function is reinitialized or amended with a distance information to improve the curvature computation. The interface representation is usually coupled to the level-set via cut-cell approaches where, cells are intersected as illustrated

in Figure 51. Other approaches involve, cell averaging (one-field formulation) and a local smoothing of the discrete level-set. However, the interface can intersect a cell of the background mesh with a disadvantageous orientation leading to extremely large or small phase ratios.

Applications of the level-set approach include applications to curvature driven flows, an implementation for unstructured meshes in OpenFOAM , and such developed specifically for the investigation of wetting processes [136, 87, 131]. For a more general overview on level-set methods see [98]. The approach considered within the computational benchmark is based on an extended discontinuous Galerkin (xDG) discretization and is going back to [71].

7.1.2 *Arbitrary Lagrangian Eulerian*

The unique feature of the ALE approach, is that the domain is discretized with a mesh, such that edges in 2D or faces in 3D represent the discretized interface, see Figure 52. This means that the computational mesh has to follow the deformation of the interface. During this movement, the mesh has to maintain a sufficient quality for the solution of the mass and momentum conservation equations.

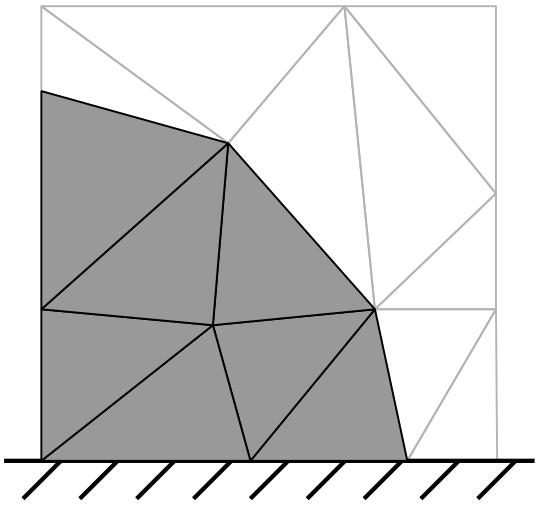

Figure 52: Arbitrary Lagrangian-Eulerian.

Representing the interface by a surface mesh, allows to compute a high quality estimate of the surface curvature. Furthermore, the interface mesh allows to discretize the free surface or transmission conditions analog to a usual domain boundary, e.g. a solid wall. On the downside, the frequent movement of the mesh requires recomputation of mesh data such as face areas and cell volumes, which can significantly increase the simulation time. Although a remeshing of the computational mesh can be used to improve the mesh quality and handle larger deformations, such an approach has to take into account the shape of all solid boundaries and the fluid-fluid interface, while providing a volume conserving new mesh. This is in general a highly non-trivial task and complicates the automization of this procedure. However, as long as the mesh is only moved and not remeshed, no topological information has to be recomputed. The closed interface mesh can also be used to add additional physics e.g. in the form of soluable or thermocapillary Marangoni effects. Examples of the ALE approach are a FEM based implementation for magneto-hydrodynamic

flows [46], multiphase flows [140], ground water problems [118] and impact problems [130].

7.1.3 *Algebraic Volume of Fluid*

Integrating the indicator function for the phase fraction over a cell and dividing by the cell volume gives a volume fraction field between 0 and 1, as illustrated in Figure 53. The corresponding evolution equation is typically discretized and advected using numerical schemes for shock problems, such as higher order TVD-schemes. These schemes are sometimes combined with anti-diffusion terms, aiming to reduce the numerical diffusion arising from the algebraic transport. As typically no sub-cell information of the interface is computed, a one field-formulation is suitable to couple the interface location with the mass and momentum conservation equations. Due to the smearing of the interface, the computation of the curvature term is often challenging and can be improved by additional reconstruction steps. A known issue for algebraic VOF approaches are strong spurious currents which may significantly impair simulation results. In contrast to Geometric VOF methods outlined in the next section, algebraic VOF approaches do not require extensive computations for the advection of the phase fraction field. Hence, the method is in principle suitable for large scale problems, e.g. Tsunami simulations with meshes that consist of more than 10^9 cells, see [104].

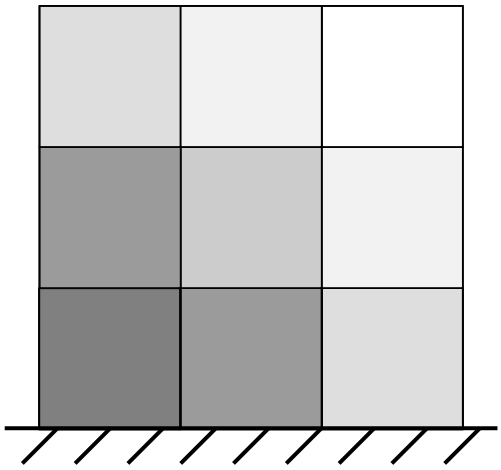

Figure 53: Algebraic Volume of Fluid.

Though the algebraic VOF approach may have some similarities with smooth interface descriptions, such as phase field methods, the underlying sharp interface model for the indicator function is fundamentally different from the Cahn-Hilliard equation, used within the context of phase field methods. OpenFOAM provides an algebraic VOF approach, developed in [142], and is primarily used for general engineering applications. An alternative approach for the application to surface tension governed multiphase flows has been proposed in [16].

7.1.4 *Geometric Volume of Fluid*

For algebraic VOF methods, the increased smearing of the phase fraction field can become problematic for longer simulation times and stronger

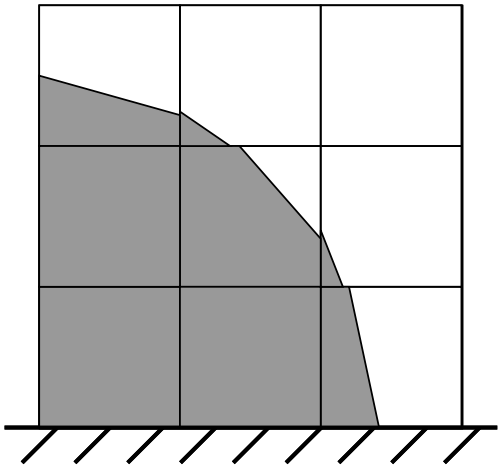

Figure 54: Geometric Volume of Fluid.

deformations. This motivates a cell-based reconstruction of the interface as illustrated in Figure 54, which goes back to [59]. If the phase fraction field is also advected geometrically, the approach allows for excellent mass conservation properties, while maintaining a sharp interface. Combined with a regular background mesh, the approach is favourable for problems with complex geometries that require a precise evolution of the interface. Typically, piecewise linear interface constructions (PLIC) are used that do not necessarily form a closed interface. While this allows to maintain a sharp surface in the discrete sense, inhomogeneously sized interface sections in combination with a non-closed surface often complicate the computation of the curvature contribution. Furthermore, the interface can intersect a cell of the background mesh, yielding extremely large or small phase ratios leading to ill-conditioned intersection problems. Cut-cell or cell averaged approaches are often used to couple the interface advection to the mass and momentum conservation equations.

Geometric VOF methods are applied mostly within the context of multiphase flows. Application examples include droplet splashing capillary instabilities and gas bubble [113, 105].

In the following, four implementations are compared that are based on the different approaches outlined above. The implementations are compared using the capillary rise test case and provide extensive benchmark data.

7.2 BENCHMARK SETUP

As outlined above, various fundamentally different numerical approaches for multiphase flows are available. It is often not clear how such methods perform in comparison, especially not for wetting problems. Four different implementations of the general approaches outlined above are available within the CRC1194, which offers a unique opportunity for an in depth comparison. This leads to the following benchmark, which aims to compare the results from the different implementations of the four numerical approaches described in Section 7.1.

As level-set implementation, the code “Bosss” is used, which is described in [71]. The solver employs an extended discontinous Galerkin approach (DG) for the discretization of the bulk equations. The ALE approach described in Chapter 4 is used, which is implemented in OpenFOAM and is based on a finite volume discretization. As a representative from the class of geometric VOF solvers FS3D is used which is going back to [113]. From the class of

algebraic VOF methods, an extended version the interFoam solver based on OpenFOAM extend 3.1 is applied [142]. For a more detailed information on the different implementations and their extensions, see [49] and the literature referred to therein. The following results have been obtained in collaboration within the Technische Universität Darmstadt. These are namely Daniel Rettenmaier (Graduate School of Computation Engineering, interFoam), Thomas Antritter (Institute for Technical Thermodynamics, interFoam), Mathis Fricke (Institute for Mathematical Modeling and Analysis, FS3D), and Martin Smuda (Institute for Fluid Dynamics, BOSSS).

Using such a large variety of different approaches requires specific and careful preparation of the corresponding initial conditions. The choice of physical parameters is described in the following.

7.2.1 *Physical parameters*

To be able to compare to the classical model and the extended solution derived in Chapter 5, the assumptions used to derive these models must be equally satisfied by the numerical solutions. Furthermore, following [42], a set of physical parameters (see Table 19) is chosen to vary the non-dimensional group

$$\Omega = \sqrt{\frac{9\sigma\cos\theta\mu^2}{\rho^3 g^2 R^5}} \tag{219}$$

to obtain the values $0.1, 0.5, 1, 10$ and 100. This choice covers the full range of different rise behaviors from strong oscillations $\Omega = 0.1$ to highly damped asymptotic rise $\Omega = 100$. In addition, the physical parameters are chosen to satisfy the following requirements:

- The interface has to maintain its circular shape during the rise (requirement to compare to the ODE model, see Chapter 5).
- The setup must yield a rise height that differs significantly from its initial height. This way, various rise behaviors for the different values of Ω can form.
- The simulation domain should be small to reduce computational costs.
- In order to reduce simulation time, the physical parameters should be chosen such that the necessary number of time steps is as small as possible.
- For two-phase flow solvers, the influence of the gas phase is to be minimized to allow, comparability with the reference model.

The contact angle is chosen at $\theta = 30°$ for all simulations. This avoids not only ill-conditioned intersection problems for small contact angles, but also leads

to a sufficient overall rise height in combination with the remaining physical parameters. The assumption of the spherical cap yields a geometric condition on the initial height of the capillary rise model, h_{apex} in the following form

$$h_{apex}(t_0) = h_{cl}(t_0) - \Delta h(R) \geqslant 0. \tag{220}$$

To limit the simulation time and the mesh deformation for the ALE approach, the final rise height is estimated using Jurin's height to four times the radius of the capillary

$$h_{Jur} = 4R \quad \Leftrightarrow \quad 4 = \frac{h_{Jur}}{R} = \frac{\cos\theta}{Eo}. \tag{221}$$

Hence, the initial height is chosen to be $h_0 = 2R = h_{Jur}/2$ to ensure a spherical cap shaped interface. To allow for oscillation with amplitudes larger than Jurin's height, the extend of the computational domain in y-direction is chosen to be $h_D = 2h_{Jur} = 8R$ for all implementations following a two phase approach. In addition, the density and viscosity ratios are set to $\frac{\rho}{\rho_g} = 1000$ and $\frac{\mu}{\mu_g} = 1000$ for these approaches to ensure that the influence of the gas phase is negligible. Choosing $R \ll L_{cap}$ allows to fulfill the first requirement (see [23] and Figure 43), i.e.

$$\frac{R}{L_{cap}} = \sqrt{\frac{\rho g R^2}{\sigma}} = \sqrt{Eo} \ll 1. \tag{222}$$

Using (221) and the chosen contact angle, the Eo number is fixed to $Eo = \cos(30°)/4 \approx 0.217$. During the dynamic rise, a circular shape of the interface can be expected for a sufficiently small Capillary number

$$Ca = \frac{\mu v_\Gamma}{\sigma}, \tag{223}$$

where the maximum Ca number is obtained using the maximal contact line velocity. However, this quantity is not available a priori and has to be evaluated from the contact line velocity of the performed simulations.

Several time step restrictions apply for the various approaches. A common restriction is due to the explicit movement of the interface, from which the strongest restrictions for the different approaches is

$$(\Delta t)_\sigma < \sqrt{\frac{\rho \Delta x^3}{4\pi\sigma}}, \tag{224}$$

which is the restriction for FS3D. Due to the common time-explicit discretization of the interface movement, a CFL condition has to be satisfied for all approaches. Furthermore, the FS3D solver uses an explicit time integration scheme and therefore has to satisfy an additional viscous stability criterion given by

$$\Delta t < \min\{(\Delta t)_\sigma, (\Delta t)_\mu, (\Delta t)_\nu\} \tag{225}$$

Table 19: Physical parameters for the Ω-study.

Ω	R	ρ	μ	g	σ	θ_e	Ca_{max}	Eo
-	m	$kg\,m^{-3}$	$Pa\,s$	$m\,s^{-2}$	$N\,m^{-1}$	°	-	-
0.1	0.005	1663.8	0.01	1.04	0.2	30	0.003	0.217
0.5	0.005	133.0	0.01	6.51	0.1	30	0.015	0.217
1	0.005	83.1	0.01	4.17	0.04	30	0.029	0.217
10	0.005	3.3255	0.01	26.042	0.01	30	0.106	0.217
100	0.005	0.33255	0.01	26.042	0.001	30	0.110	0.217

with

$$(\Delta t)_\mu = \frac{\rho \Delta x^2}{6\mu}, \qquad (\Delta t)_\nu = \frac{\Delta x}{\|\boldsymbol{\nu}\|_\infty} \tag{226}$$

for the time discretization. For more details on these limitations see [113, 50] and the literature referred to therein.

The above considerations lead to the physical parameters in Table 19. The left column shows the different values of Ω analog to the selection in [42]. The values of the Ca number have been extracted from the results of the parameter study described in Section 7.3.2. The remaining parameters do not necessarily correspond to actual material combinations as they are chosen to satisfy the requirements above for a comparison to the reference models.

The derivation of the extended ODE model in Chapter 5 shows that the shape of the interface is a spherical cap during the complete rise. Hence, the initial condition must also satisfy this requirement. In principle, it is possible to obtain the initial distribution by a direct computation. For the ALE approach a standard meshing tools can be used. However, an exact initialization of the phase fraction field for both VOF approaches is more involved as a curved surface has to be intersected with each control volume.

For the VOF approaches every cell of the background mesh has to be intersected with the curved spherical interface. This approach requires a suitable initialization tool. While this direct initialization is in principle possible, an indirect approach is sufficient in this case: First, a square volume of liquid is initialized. Then, the simulation is started with a "closed" inflow boundary by using a homogeneous Dirichlet boundary condition. To obtain the initial distribution of the liquid, the simulation is run until an equilibrium has been established. The resulting initial conditions for all approaches are shown in Figure 55. A low resolved mesh is depicted for the ALE approach to illustrate the initial mesh structure. Instead, for the geometric VOF and algebraic VOF approaches an initial distribution of the indicator function is illustrated. For the initial configuration the interface thickness remains within a few cells for both approaches. While the geometric VOF approach is able to maintain such a small interface width, this thickness increases for interFoam with longer

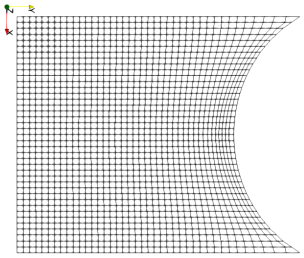

(a) Initial 40×40 mesh for the ALE implementation.

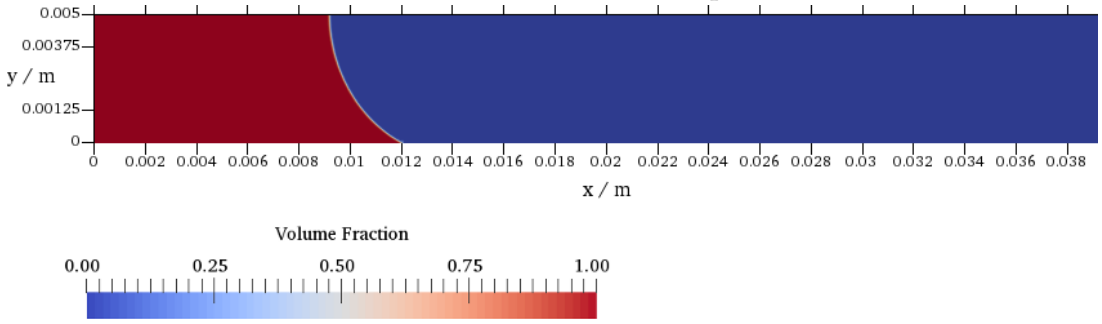

(b) Initial indicator field for interFoam.

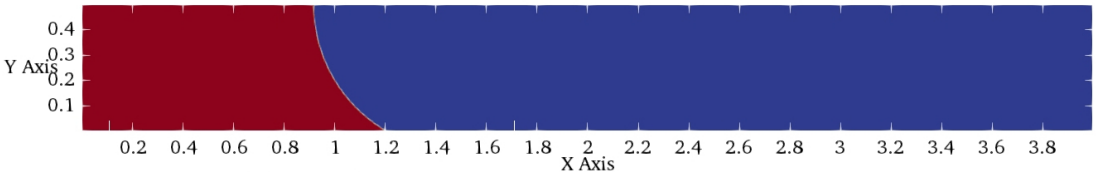

(c) Initial indicator field for FS3D, same scale as for interFoam.

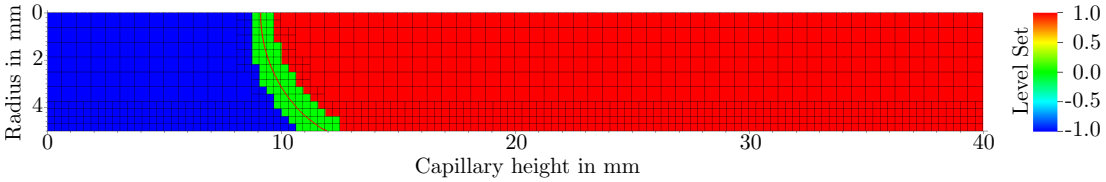

(d) Initial level set for BOSSS.

Figure 55: Initial conditions for the capillary rise benchmark.

simulation times. The BOSSS approach shows an octree-mesh that is locally refined to resolve the wall boundary layer and the interface region. The green cells illustrate a region of rapid change of the level-set function and the corresponding interface.

7.3 RESULTS

7.3.1 *Numerical vs Navier Slip*

As discussed in Chapters 2 and 5, the no slip boundary condition is basically the standard wall boundary condition in single phase flow models. Despite the strong arguments given in [124] that no physically relevant solution exists

in this case, it is still used in the context of wetting simulations. This leads to the following question: If the analytic description does not have a solution, how are the overall results influenced by using numerical slip as boundary conditions?

The analytic description with a no slip boundary condition on the wall yields the contact line paradox: While the no slip condition should prevent any tangential movement of the discrete contact line, the interface should move over the surface in experimental observations going back to [62]. Nevertheless, to obtain a "moving contact line" in this case the velocity field close to the contact is extrapolated to the contact line. For the ALE method this means that the velocity of the cell adjacent to the contact line is extrapolated to the mesh point (a constant extrapolation in the simplest case) and projected onto the wall to move the boundary mesh. The interFoam and FS3D approaches use the velocity in the cells that is adjacent to the contact line for the advection of the discrete phase fraction field. This kind of "discretization" is referred to as *numerical slip* in the following. The numerical slip approach has been implemented for the ALE, FS3D and interFoam approach. The BOSSS implementation adapts the slip length of the Navier slip boundary condition, depending on the mesh resolution near the contact line to imitate the behavior of the numerical slip in the other three approaches.

The behavior of the numerical slip boundary condition is evaluated using a mesh convergence study for the capillary rise test case setup given in 7.2.1. As a comparison, a Navier slip boundary condition with a constant slip length on the capillary walls is also computed using the same mesh resolutions. The slip length for this convergence study is set to $L = R/5$, to be able to resolve the problem with "small" meshes. It should be noted that each of the approaches has a time step restriction analog to (224). The results for this study are shown in Figures 56, 57, 58, and 59 for ALE, FS3D, interFoam, and BOSSS results. For each Figure, the left sub-figure shows the results using numerical slip as described above. In turn, the right sub-figure depicts the results using the Navier slip boundary condition on the walls.

The results for the numerical slip boundary conditions show minor to distinct oscillations for the lowest mesh resolution. With increasing mesh resolution the oscillations are completely damped and the rise height behavior changes into the overdamped regime, which is expected only for $\Omega > 2$. Furthermore, no mesh convergence could be obtained for the considered resolutions and any of the considered methods.

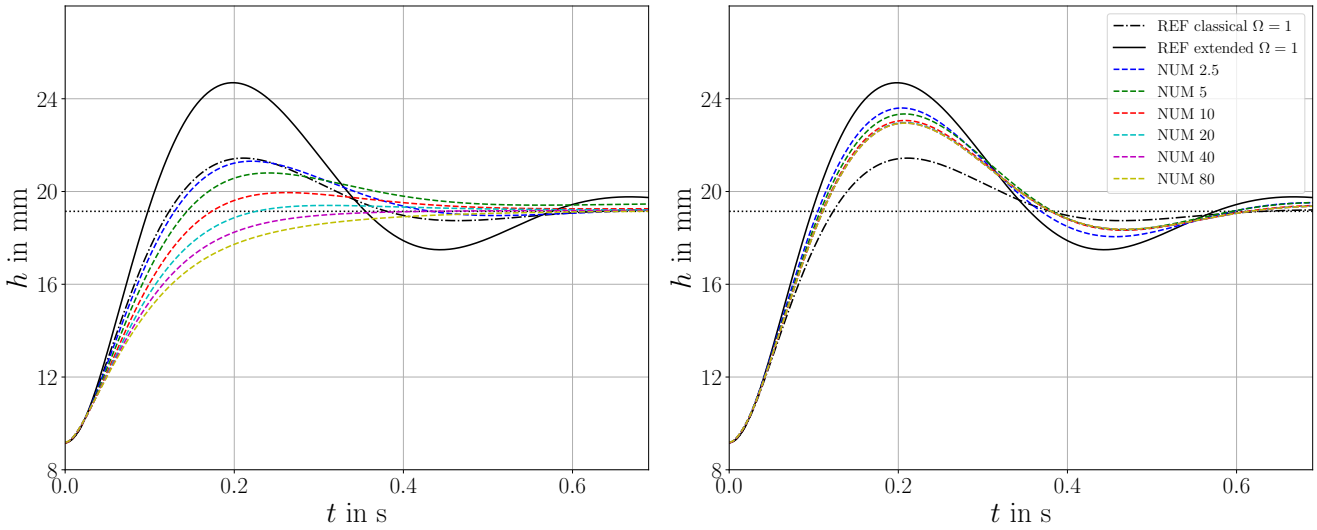

(a) Numerical slip.

(b) Navier slip.

Figure 56: ALE convergence study.

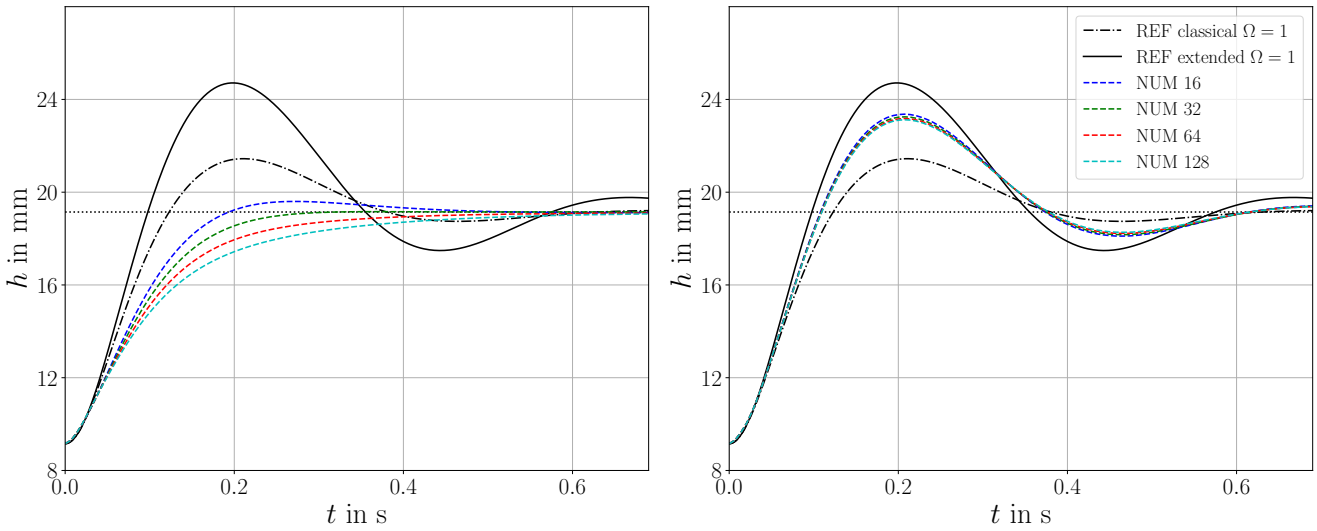

(a) Numerical slip.

(b) Navier slip.

Figure 57: FS3D convergence study.

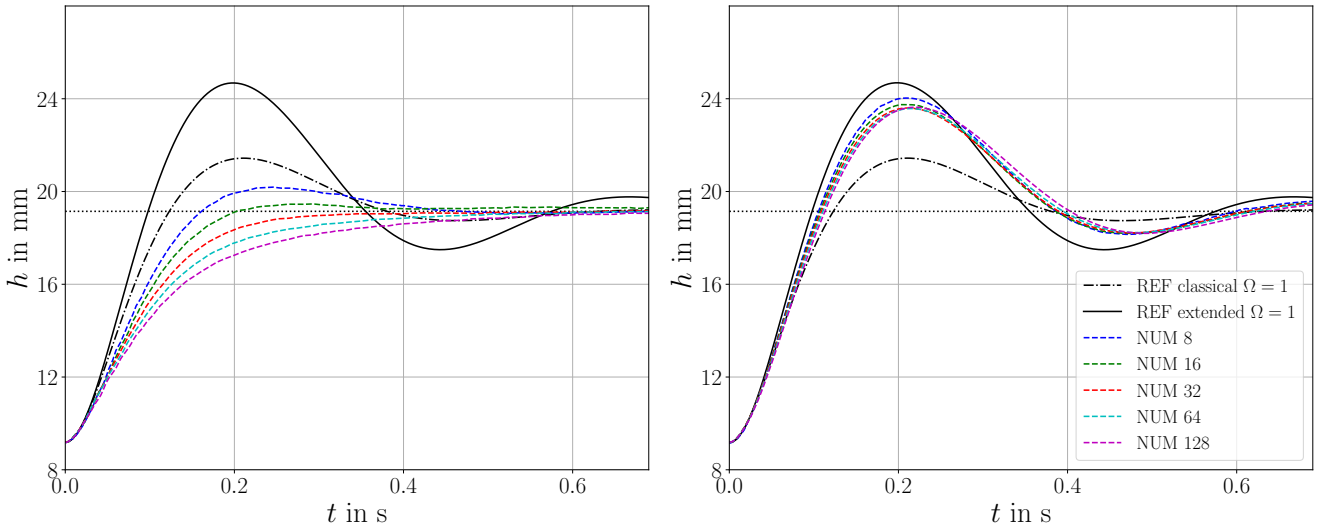

(a) Numerical slip. (b) Navier slip.

Figure 58: Convergence study for interFoam.

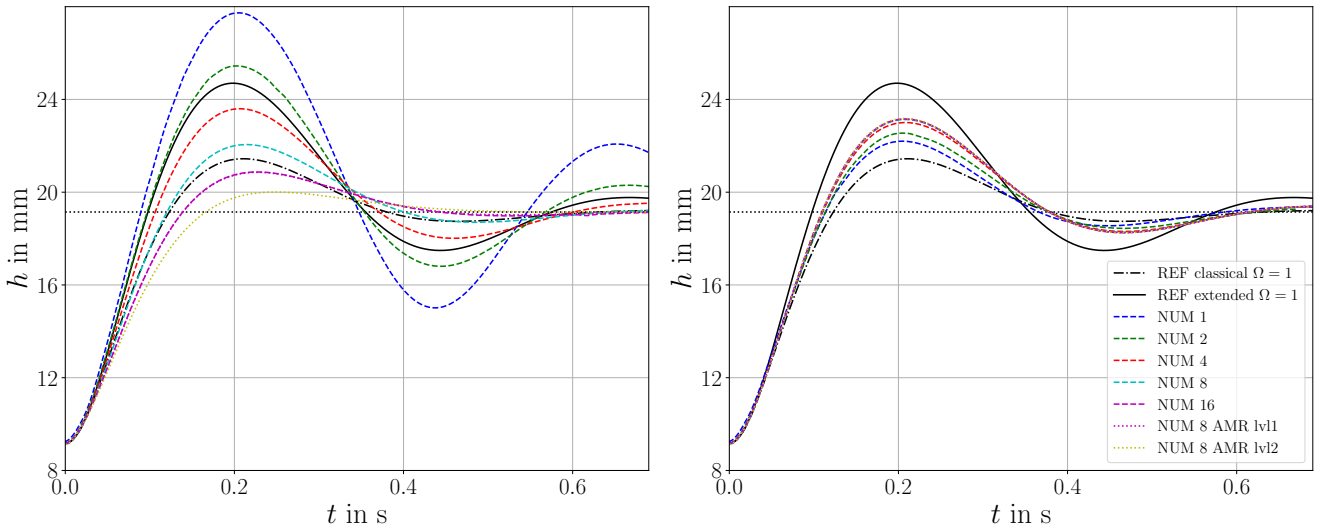

(a) Numerical slip. (b) Navier slip.

Figure 59: BOSSS convergence study.

The Navier slip boundary condition tested in Chapter 6 has been implemented as a general OpenFOAM boundary condition. Hence, no changes in the implementation were necessary to reuse the boundary condition for the interFoam solver. All methods except for the interFoam solver show results where the rise curves for subsequent mesh resolutions coincide. Even though no mesh convergence in the dynamic case could be obtained for the numerical slip boundary condition, the stationary results are mesh convergent for all considered cases and approaches, except for the interFoam approach.

Overall, no mesh convergent results could be obtained for any of the considered methods using numerical slip boundary conditions. The results from the BOSSS solution indicate that the behavior corresponds to reducing the slip length. This observation can be explained as follows: The point from which a velocity is extrapolated to the contact line moves moves closer to the no slip wall for increasing mesh resolution and hence towards a zero velocity. Generally, this suggests that no predictive results can be obtained using a numerical slip boundary condition, since the solution depends on the mesh resolution.

A comparison between the results from Figures 56b 57b, 58b, and 59b is given in Figure 60. It shows the rise height over time from the four numerical implementations and the corresponding maximum mesh resolution. A comparison between the results from the ALE, BOSSS and FS3D implementations shows an excellent agreement, while stronger dynamics and a higher first maximum can be observed in the curves generated with the interFoam solver. However, the deviations are smaller than the deviations to the reference curves. The rise behavior from the the numerical solutions are more dynamic than the classical model and less dynamic than the extended solution derived in Chapter 5.

To consider the influence of the slip length, the setup given in Table 19 has also been computed for $\Omega = 1$ and a slip length of $L = R/50$. The results for the finest meshes with $L = R/50$ are shown in Figure 61. Again, the ALE, BOSSS and FS3D results are consistent. In both cases, the rise curves obtained with the interFoam solver deviates from the results of the other three approaches. This effect is more noticeable for the larger slip length. However, all numerical results do show significantly reduced dynamics for the smaller slip length in Figure 61. An oscillation can barely be observed and the rise behavior is more similar to the overdamped case. Note that the reference solution is far more sensitive to changes in Ω for values above the threshold for critical dampening than below, cf. Figure 26. In this case, reducing the value of the slip length has a significant influence of the qualitative behavior of the solution for all considered solvers, such that it is comparable to the effect of numerical slip. Nevertheless, it is a converged solution that is changing due to the value of the slip length. Hence, it has to be doubted that a nano-meter slip length can be used to model the capillary rise (at least) in the oscillatory regime.

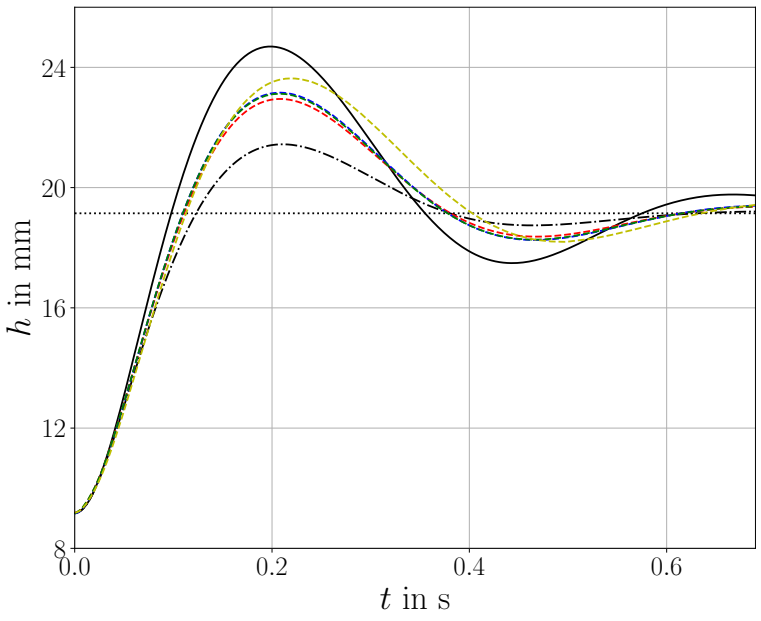

Figure 60: Comparison of the convergence study for $\Omega = 1$ and a slip length $L = R/5$.

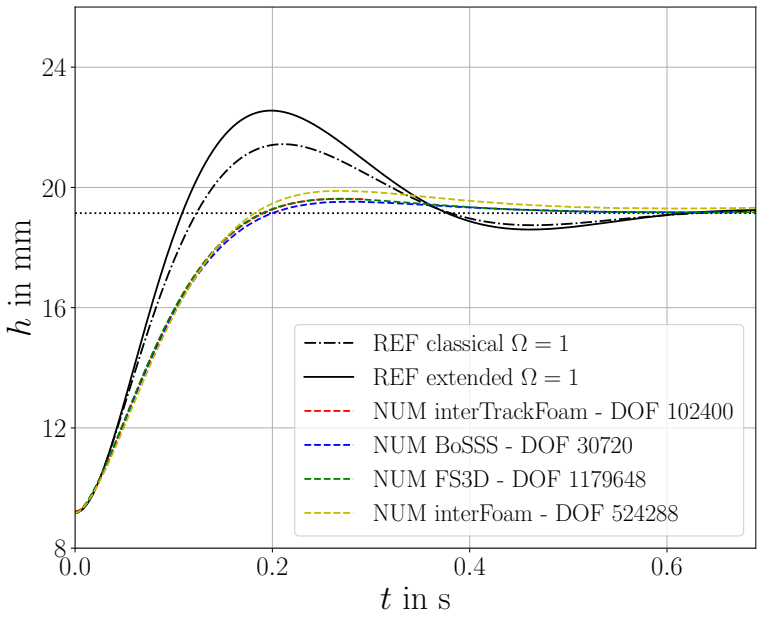

Figure 61: Comparison of the convergence study for $\Omega = 1$ with slip length $L = R/50$.

7.3.2 *Parameter Study*

To provide general benchmark data a comprehensive parameter study for the non-dimensional group Ω and the parameter given in Table 19 has been performed. For this analysis, the same values of Ω as in [42] are used, i.e. $\Omega \in \{0.1, 0.5, 1, 10, 100\}$. These are three values above and two values below the case of critical dampening at $\Omega = 2$ (see Section 5.4 for a derivation). The results from all four numerical approaches in comparison to the two approximate reference solutions are shown in Figure 62. All sub-figures display the rise height over time of the apex of the liquid gas interface. It can be seen that the rise height oscillations decrease with increase values of Ω from the top left to the bottom right sub-figure for both approximate reference solutions as well as the numerical solutions. Hence, all numerical solutions do show a good qualitative agreement with the behavior of the approximate reference solutions. Furthermore, the quantitative accordance between the four different numerical solutions is excellent for all considered cases. Minor deviations can be observed for the interFoam solver. While results qualitatively conforms with the reference solutions, the quantitative agreement between the numerical results and the two approximate reference models is reasonable at most. A somewhat general trend is that the numerical results are located inbetween the extended and the classical rise models (114) and (170), respectively. The largest deviations between numerical results and approximate references can be observed for $\Omega = 0.1$ in the top left sub-figure, where the agreement between the numerical results and the extended solution is good, while the classical model underestimates the maximal amplitude of oscillation by roughly 50 %. This behavior changes with time, such that the oscillations show good agreement with the classical model after approximately 3 s. A similar but less prone effect can be seen for the cases with $\Omega = 0.1, 0.5, 1$. A possible explanation for this behavior might be that neither of the approximate models captures the viscous dissipation in the wedge near the contact angle.

To provide general benchmark results for the capillary rise test case, the data from Figure 62 has been non-dimensionalized using the scaling II from [42], for which the coefficients in the 2D and 3D case are given in Table 9. The scaled results are shown in Figures 63 and 64.

This scaling uses inertia and gravity as scaling parameters and an increasing value of Ω can be interpreted as an increasing influence of viscosity. Analog to the results in [42], the increasing value of Ω yields a more damped solution. However, the overall qualitative and quantitative behavior is the same as for the unscaled results. No particular trend for deviations between the approximate reference models and the results from the four numerical approaches can be extracted from this scaling. Similar results were found by applying scalings I and III, which can be found in the Appendix C.

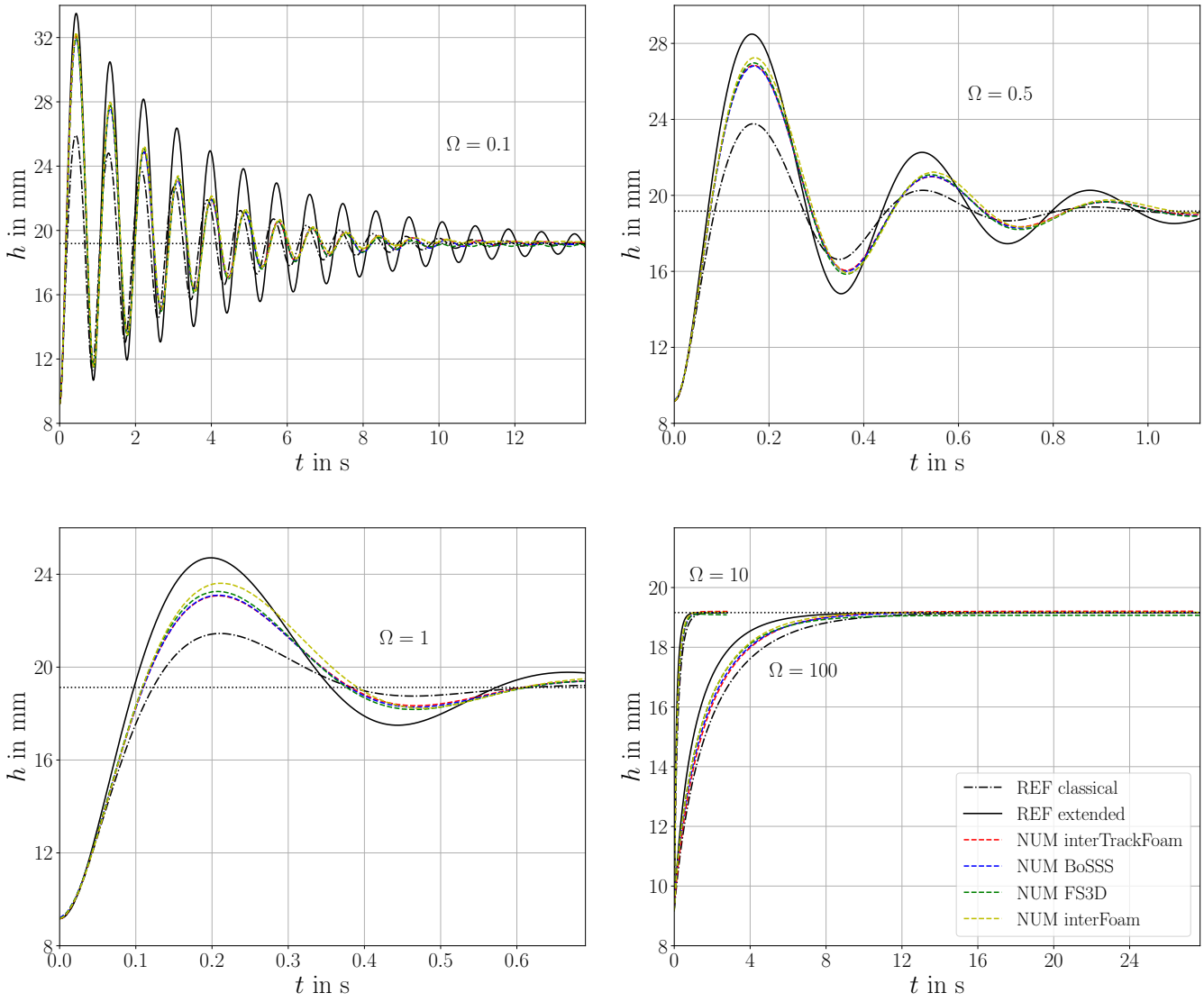

Figure 62: Unscaled solutions of all numerical methods and reference models for the Ω-study: $\Omega = 0.1$ (top left), $\Omega = 0.5$ (top right), $\Omega = 1$ (bottom left), $\Omega = 10, 100$ (bottom right).

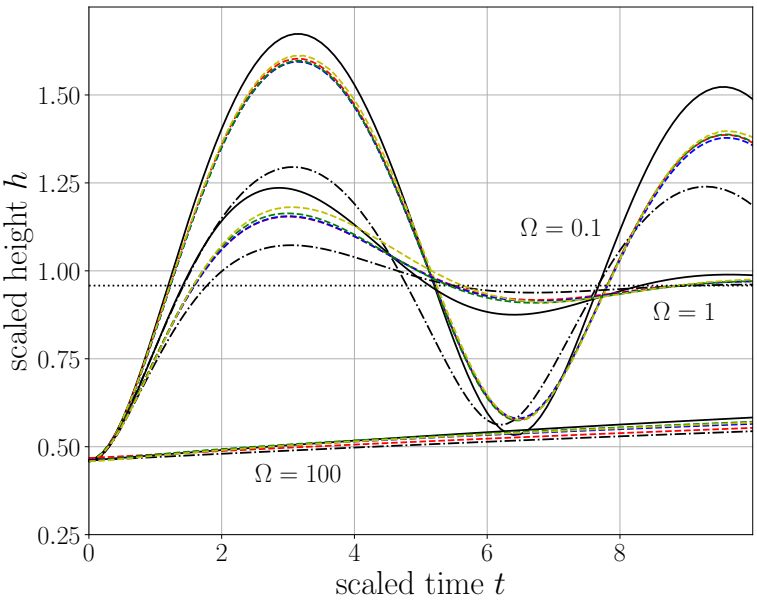

Figure 63: Scaled solutions of all numerical methods and reference models for $\Omega = 0.1, 1, 100$.

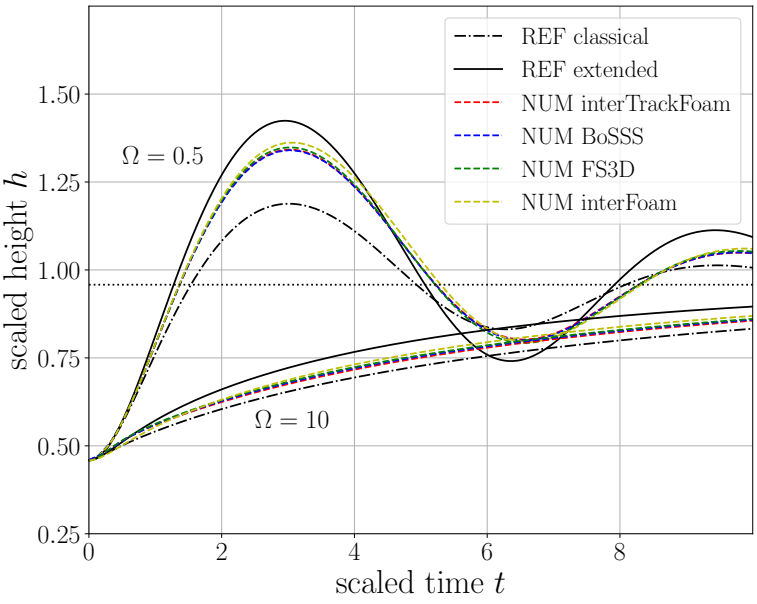

Figure 64: Scaled solutions of all numerical methods and reference models for $\Omega = 0.5, 100$.

7.4 CONCLUSION

The capillary rise test case has been used to perform a cross code verification for a level set xDG method, an algebraic as well as a geometric VOF approach, and the implementation of the ALE approach described in Chapter 4. No mesh convergent results could be obtained for any of the considered numerical approaches using numerical slip boundary conditions. This indicates that numerical slip is not a viable approach for the simulation of wetting processes, as an increasing mesh resolution does not only yield a quantitative but also a qualitative change in the solution. Mesh convergent results for all approaches, except for interFoam could be obtained using a Navier slip boundary condition. However, while literature values typically give a slip length on the nanometer scale, a rise height behavior that agrees with the reference solution could only be obtained for slip on the scale of the capillary diameter. Using this larger slip length, a comprehensive parameter study for all four codes has been performed. Excellent agreement between the results of the four numerical approaches, with minor deviations for interFoam solver, could be obtained. Results show good qualitative agreement with the approximate reference models from Ref. [145] and the extended version from Ref. [50], which has been derived in Chapter 5. Quantitative deviations between the numerical solutions and the approximate reference models increase with a decreasing value of the non-dimensional parameter Ω, which can be interpreted as a measure of the influence of inertia. To provide general code to code verification data, the data for Figures 56 to 64 have been made available online, cf. [49].

Detailed experimental results that are capable to provide an error estimate for a suitable validation are generally scarce and not available in the 2D case. Results for liquid rising in a 3D capillary from Ref. [108] and Ref. [109] do not agree for the stationary height and not with the predicted Jurin's height. More precise reference data is required for a detailed validation in the $\Omega < 2$ parameter range.

8

APPLICATIONS

CYLINDRICAL CAPILLARIES The rise of a liquid in a 2D model domain has been studied in Chapters 5 and 7. The implementation presented in Chapter 4 allows to consider 3D cylindrical capillaries as shown in Figure 65 and thereby a detailed analysis of ODE models and a corresponding experimental validation.

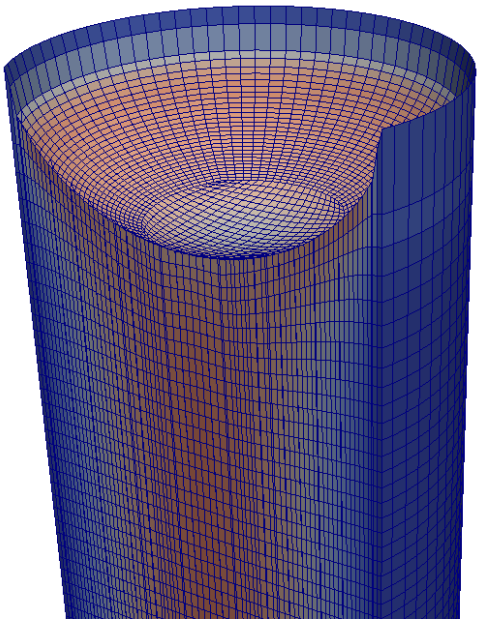

Figure 65: Cross section of a cylindrical capillary. Colors illustrate the magnitude of the velocity between a high (red) and and low velocity (blue).

Hence, the extensions now allow to study the interaction of the wetting process with additional physical influences, such as surfactants or mass transfer.

THIN CAPILLARIES The implementation has been used to predict the contact angle inside a thin capillary, as illustrated in Figure 66. The measurements of the physical cross section are shown in Figure 66a. The cross section has a width of 4 mm, a height of 200 µm and a corner radius of 50 µm. The mesh used for the computation of a stationary surface is shown in Figure 66b.

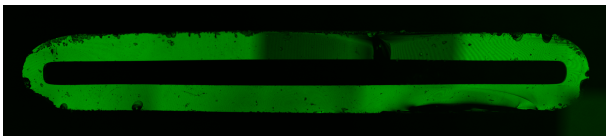

(a) Cross section of the physical capillary.

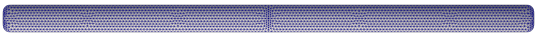

(b) Computational mesh (top view).

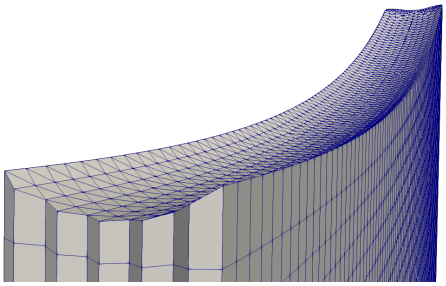

(c) Capillary surface.

Figure 66: Geometry of the thin capillary. Experimental observation at the physical capillary with courtesy of the Institute for Technical and Macromolecular Chemistry, TU Darmstadt.

The contact angle measurement on the surface inside the capillary is not possible by a standard contact angle measurement using the droplet method. Contact angle measurements for planar glass surfaces yield a contact angle around 54°. To obtain an estimate of the contact angle inside the capillary, it has been dipped into purified water. The resulting interface has been overlayed by simulation results and is shown in Figure 67.

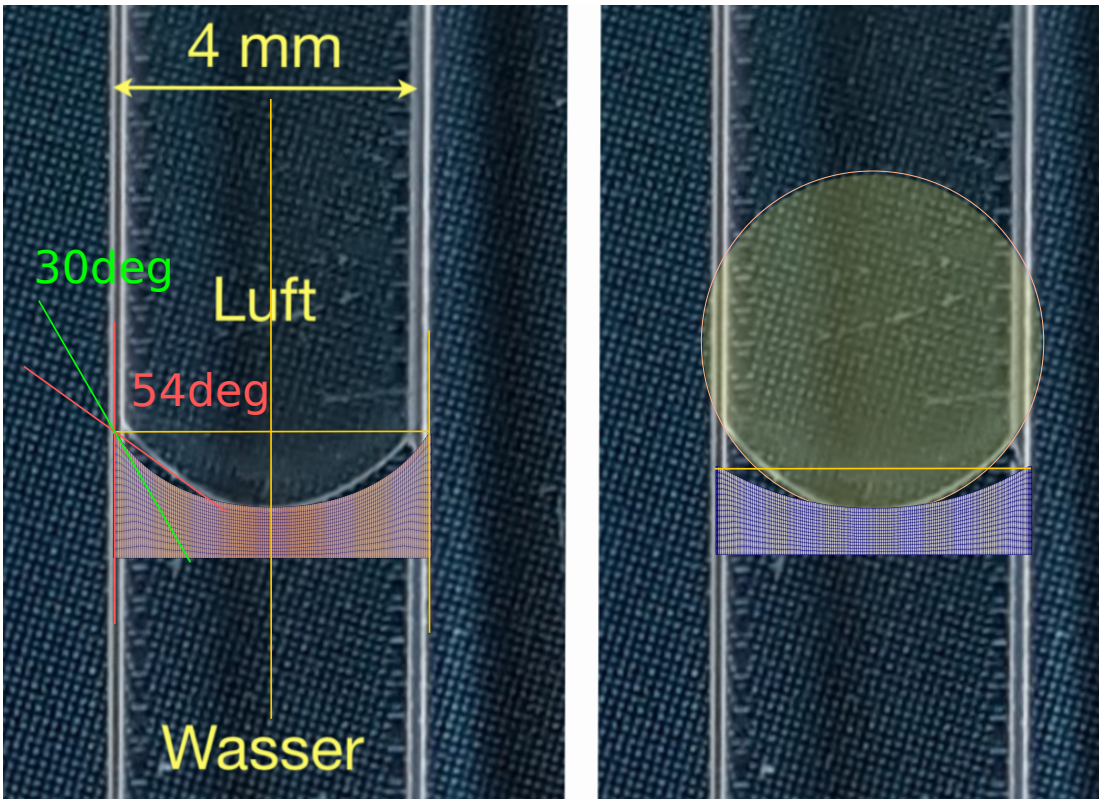

Figure 67: Comparison between experimental observations and interface shapes from ALE simulations, using a 30° (left) and a 54° contact angle (right).

The simulation results for a contact angle of 54° and 30° are shown on the right and left, respectively. It can be seen that for a contact angle of 54° the contact angle height from the simulation is significantly below the one observed in the experiment. For a 30° contact angle the distance between the apex of the interface and the contact line shows good agreement. This suggests that the surface inside the capillary has a smaller contact angle than that measured on a planar glass surface.

This comparison to preliminary experimental results shows a first application of the implemented methods. While the reason for a different contact angle may be possibly be caused by the fabrication process or impurities on the surface, a more detailed investigation is necessary to explain the experimental observations.

GROWING DROPLET Figure 68 shows a cross section of a hemispherical droplet, which is placed on a planar surface. The droplet volume is increasing due to an inflow of liquid through a circular orifice on the solid surface. The influence of the inlet is displayed in Figure 68, which is evident from red region around the center of the droplet base. The tubes originating from the inlet boundary illustrate the velocity field in the droplet.

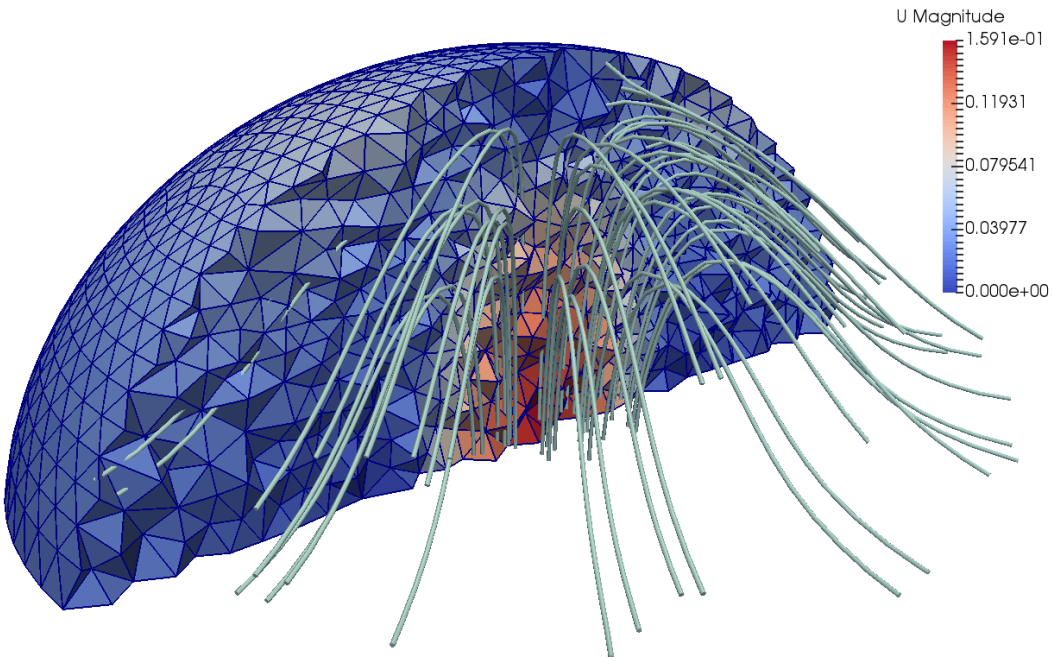

Figure 68: Cross section of a drop growing due to an inflow of liquid at the bottom.

9

CONCLUSION AND OUTLOOK

9.1 CONCLUSION

A new solver for the investigation of wetting processes using the Arbitrary Lagrangian-Eulerian approach has been developed in OpenFOAM. For this purpose, the control point algorithm used for the movement of the interface mesh has been extended to incorporate the three phase contact line. The newly implemented Navier slip and a free slip boundary condition allow to model moving contact lines. These have been implemented to seamlessly integrate with any OpenFOAM solver. To model a dynamic contact angle, a contact angle library has been introduced that provides an easily extendable and combinable selection of contact angle models. Moreover, the implementation allows for arbitrary contact line topologies in two and three dimensional domains, e.g. symmetric geometries or wetting of inhomogeneous surfaces.

Using analytic reference solutions, the implemented boundary conditions have been shown to be second order convergent in space. The implementation of contact angle models has been verified by comparison to available data from literature and detailed numerical results, showing excellent agreement with the references. Since most available verification cases consider stationary states, an extended model for the rise of a liquid in a capillary has been derived, starting from the free surface continuum mechanical description.

Based on the in depth understanding of the capillary rise model, four fundamentally different approaches have been compared in collaborative effort: an ALE approach, a level-set based XDG method and an algebraic as well as a geometric VOF implementation. The analysis shows good qualitative but only reasonable quantitative agreement with available rise models, which decreases for an increasing influence of inertia. However, the cross code verification shows excellent concordance between the different numerical implementations, with only minor deviations for the algebraic VOF method, which does not provide mesh convergent solutions in general. Moreover, the results demonstrate that the ad-hoc movement of the contact line using a no slip boundary condition may not only quantitatively but also qualitatively change simulation results. Hence, this approach is not a viable model for the simulation of wetting processes.

First comparisons to experimental results show include surface shapes within complex geometries and a promising application for the implemented approach. To allow for a maintainable, flexible, and tested framework for future investigations, all implementations have been developed using the version control system git in combination with Bitbucket.

9.2 OUTLOOK

Aiming at the investigation of additional physical influences on the wetting process and to cover technically relevant applications, the following points offer several interesting research questions.

MODEL VALIDATION The provided method is capable to cover 3D experimental geometries, e.g. for capillaries or growing droplets. This allows for experimental validation of the available wetting models and a detailed comparison of local velocity fields. However, for the oscillating capillary rise regime, more detailed measurements than currently available are required. In this case, a combination with sub-scale models based on available asymptotic expansions may offer a compromise between the required simulation resolution and a stability restriction for the time step.

NUMERICAL METHODS In comparison to single phase flows, stability problems are often more prominent in multiphase flows due to the non-linear properties of the interface curvature. Hence, a more detailed understanding of these stability properties are also beneficial for the simulation of wetting processes. Such an analysis could provide corresponding stability restrictions for the control point algorithm. Moreover, to simulate stronger deformations, a smoothing of the surface mesh combined with a conservative remeshing of the bulk mesh are promising improvements for the developed approach.

SURFACE ROUGHNESS Future investigations may incorporate the influence of surface roughness. In this context, the question arises of how a slip length on the nano-meter scale (typically obtained from MD simulations on a perfectly flat surface down to the atomic scale) can predict the movement of the contact line. Otherwise, the slip length may not be more than a parameter used to quantify the dissipation during the contact line movement.

SURFACTANTS The influence of surfactants is known to change the velocity in experimental observations field close to the contact line. In this context, surfactants are transported towards the contact line and may be adsorped onto the solid surface. To account for such processes, a model that allows for rolling motion becomes essential. While slip and scale models can mostly not provide this kinematic property, the IFM might offer an alternative to investigate such processes.

A

INCONSISTENCIES

Errors do exist. They are nothing less but part of human nature. They do exist in scientific publications and despite my outmost effort, they have to be expected within this thesis. During the work of this thesis, certain arguments in literature seemed inconsistent. May they be typos or logical errors I can not judge. Let the following list be witness that I have not quickly skimmed through them, but given them the appropriate attention they deserve. I hope these notes can be of use to anyone referring to these references.

- [92]: The first equation that gives the general solution for the Bi-Laplace equation is incorrect, as well as the stream function solution for the flow field in the wedge with no-slip boundary conditions on both sides of the wedge
- [32, p.679]: The slip length should become positive at 0.3 and not at 3 as written in the text.
- [82]: The approximation of the normal is only possible in cases for small interface curvatures, yet it is used as a general approach
- [108]: Equation (2) has an R too much in the viscous term on the left hand side. The estimate for the occurrence of height oscillations does not seem to be affected.
- [108] and [109]: Both references seemingly use the same data on the capillary rise of ether, but different stationary rise heights. While these have possibly been obtained from experiments, neither of them agrees with the value computed using Jurin's height.
- [121]: Equation (2) can not be cast into equation (6) in contrast to what is stated on page 759. In addition, the analytic solution to the perturbed problem is incomplete, see Appendix B for a full solution.
- [140]: The stability criteria does no agree with what is computed in the available implementation, where the surface Courant number contains L^3_{PeN} instead as the plain L_{PeN} contribution given in [140]. Furthermore, the dimensions of the equation that has been derived for the pressure

velocity coupling do not agree. In addition, concerning Figure 8, the formulas for the computation of the error are missing and the average face area has the dimension m^{-1}.

- [132]: A minus sign seems to be missing in equation (10) in front of the pressure. While this seems to be a typo, the definition of the discrete pressure might compensate for this change in sign in comparison to equation (2).
- [42, p.516]: This reference gives $h_0 = 0$ as initial condition for the Runge-Kutta approach, which is used for the solution of the scaled classical rise model. This is surprising as the considered ODE becomes singular in this case.

B

CAPILLARY RISE

This section provides the derivation of the pertubation solution for the capillary rise equation for small Ω, which corresponds to the oscillation limit. Using the general solution of (181) for $\zeta < 1$ or $\Omega < 2$, respectively, gives

$$\epsilon(t) \approx A \exp(-\zeta\omega_0 t)\cos(\sqrt{1-\zeta^2}\omega_0 t + \varphi) \tag{227}$$

with

$$A = \epsilon_0 \exp(\zeta\omega_0 t_0)\sqrt{1 + \frac{(\dot{\epsilon}_0 + \zeta\omega_0\epsilon_0)^2}{\epsilon_0^2(1-\zeta)\omega_0^2}} \tag{228}$$

$$\varphi = \tan^{-1}\left(\frac{-(\dot{\epsilon}_0 + \zeta\omega_0\epsilon_0)}{\omega_0\epsilon_0\sqrt{1-\zeta^2}}\right) - \sqrt{1-\zeta^2}\omega_0 t_0, \tag{229}$$

where $\epsilon(t_0) = \epsilon_0$, and $\dot{\epsilon}(t_0) = \dot{\epsilon}_0$. Transforming back to z with $z = z_{Jur} + \epsilon(t)$ gives

$$z(t) \approx z_{Jur} + A \exp(-\zeta\omega_0 t)\cos(\sqrt{1-\zeta^2}\omega_0 t + \varphi) \tag{230}$$

with

$$A = (h_0^2 - z_{Jur})\exp(\zeta\omega_0 t_0)\sqrt{1 + \frac{(2h_0\dot{h}_0 + \zeta\omega_0(h_0^2 - z_{Jur}))^2}{(h_0^2 - z_{Jur})^2(1-\zeta)\omega_0^2}} \tag{231}$$

$$\varphi = \tan^{-1}\left(\frac{-(2h_0\dot{h}_0 + \zeta\omega_0(h_0^2 - z_{Jur}))}{\omega_0(h_0^2 - z_{Jur})\sqrt{1-\zeta^2}}\right) - \sqrt{1-\zeta^2}\omega_0 t_0 \tag{232}$$

To obtain the solution for h, the transformation $h = \sqrt{z}$ is applied, yielding

$$h(t) \approx \sqrt{h_{Jur}^2 + A \exp(-\zeta\omega_0 t)\cos(\sqrt{1-\zeta^2}\omega_0 t + \varphi)} \tag{233}$$

with

$$A = (h_0^2 - h_{Jur}^2)\exp(\zeta\omega_0 t_0)\sqrt{1 + \frac{(2h_0\dot{h}_0 + \zeta\omega_0(h_0^2 - h_{Jur}^2))^2}{(h_0^2 - h_{Jur}^2)^2(1-\zeta)\omega_0^2}} \tag{234}$$

$$\varphi = \tan^{-1}\left(\frac{-(2h_0\dot{h}_0 + \zeta\omega_0(h_0^2 - h_{Jur}^2))}{\omega_0(h_0^2 - h_{Jur}^2)\sqrt{1-\zeta^2}}\right) - \sqrt{1-\zeta^2}\omega_0 t_0. \tag{235}$$

Note that this transformation applies for $h_0 > 0$. For $t_0 = \dot{h}_0 = 0$ the general solution (233) from above reduces to

$$h(t) \approx \sqrt{h_{jur}^2 + A \exp(-\zeta\omega_0 t) \cos(\sqrt{1-\zeta^2}\omega_0 t + \varphi)} \tag{236}$$

$$A = (h_0^2 - h_{jur}^2)\sqrt{1 + \frac{\zeta^2}{1-\zeta}}, \quad \varphi = \tan^{-1}\left(\frac{-\zeta}{\sqrt{1-\zeta^2}}\right). \tag{237}$$

C

CAPILLARY RISE - BENCHMARK

In Chapter 7 the results from four different numerical methods and two reference solutions have been presented, using scaling II from Table 9. Two additional scalings are possible, for which the results are presented here.

SCALING I - THE INFLUENCE OF INERTIA Among the different scalings given in Table 9, scaling I emphasizes the influence of inertia. The results for this scaling, applied to the data of the classical, and the extended 1D models from the capillary rise test case in Chapter 7 are displayed in Figures 69 and 70. The dotted line marks the corrected stationary height based on (137). The h-axis of both plots is scaled equally to allow for a direct comparison. The result of scaling I for the case $\Omega = 0.1$ are such that the oscillation has not yet started. However, overall results show that the order of increasing dynamics with decreasing values of Ω is the same as for the other two scalings. As a general tendency the classical model is underestimating the results, while the extended model is overestimating them in terms of the dynamics of the solution.

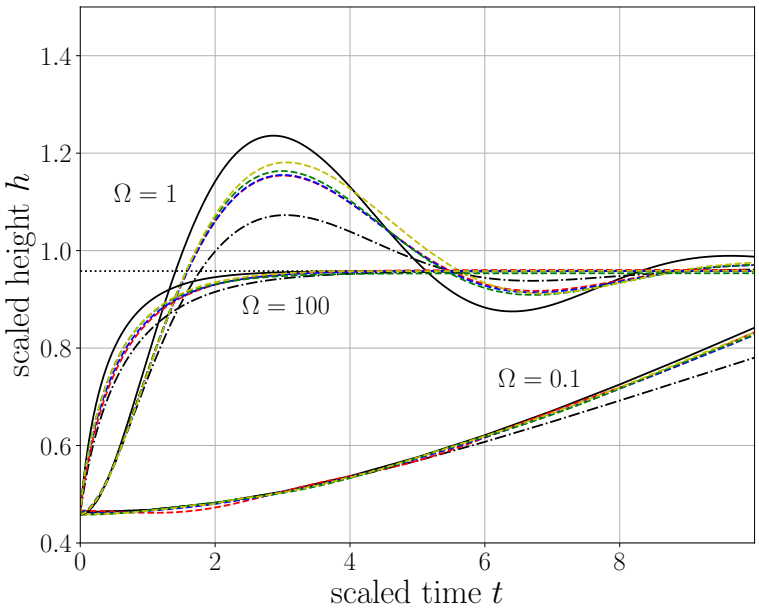

Figure 69: Comparison of benchmark results for $\Omega = 0.1, 1, 100$ using scaling I.

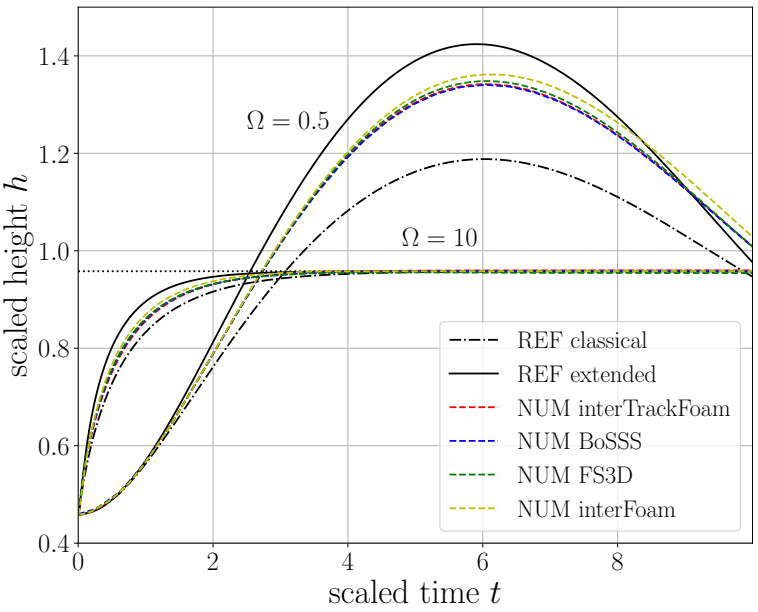

Figure 70: Comparison of benchmark results for $\Omega = 0.5, 10$ using scaling I.

SCALING III - THE INFLUENCE OF GRAVITY Applying scaling III from Table 9 emphasizes the influence of gravity. The corresponding results are shown in Figures 71 and 72. The most significant observation for this scaling is that the initial height is emphasized as can be seen by comparison to the results for scaling I and II in Figures 71 and 63, and 64, respectively. This feature is different from the results in Ref. [42]. It is reported that $h_0 = 0$ has been used. However, since the considered model becomes singular for vanishing initial conditions, it is more likely that a small value larger than zero has been used. For the simulations conducted within this benchmark study, a significant initial height is required for all solvers. Hence, the initial heights for this scaling differ significantly. Besides, for $\Omega \leqslant 1$ this scaling shows the long time oscillation behavior in Figure 71. It can be seen that with increasing Ω, the oscillation time scale reduces.

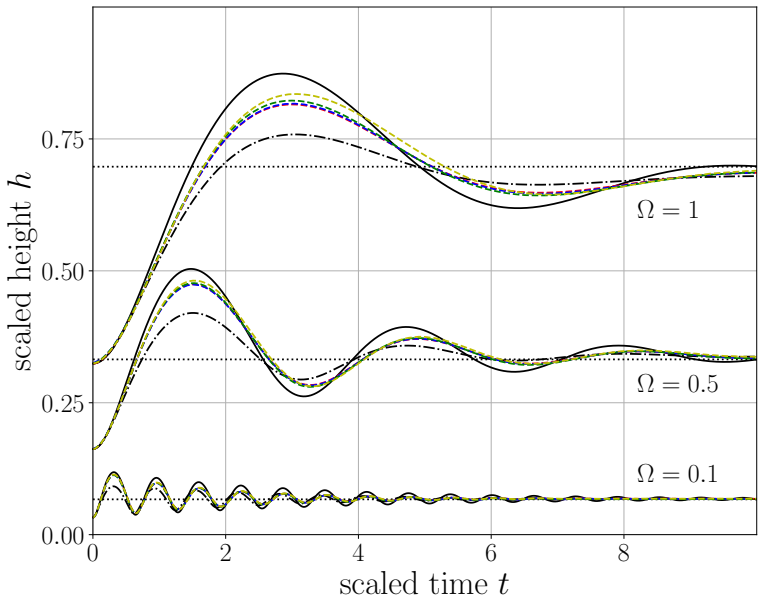

Figure 71: Comparison of benchmark results for $\Omega = 0.1, 0.5, 1$ using scaling III.

For completeness, the results for $\Omega = 10$ and $\Omega = 100$ are illustrated in Figure 72. The scaling yields basically horizontal curves at the level of the scaled initial height. The data has been scaled such that only a short period of time at the initial rise of the curves is shown, i.e. the liquid has barely moved from its initial condition. This scaling enlarges the differences between the initial conditions. This shows that the initial mesh for the ALE-method has a slightly different initial height in comparison to the other approaches. As this error is below 1 % it is considered negligible.

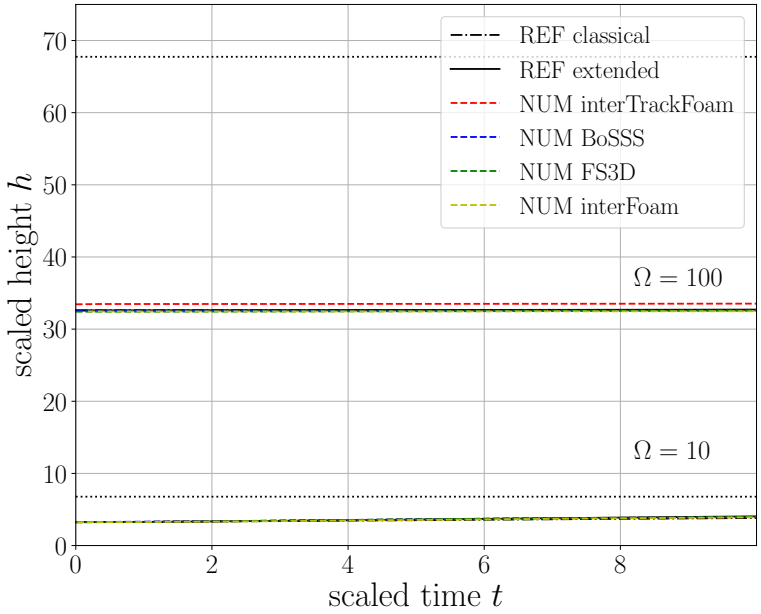

Figure 72: Comparison of benchmark results for $\Omega = 10, 100$ using scaling III.

D

EXACT STATIONARY DROPLET SHAPES

This chapter describes an algorithm for the computation of the free surface shape of 2D liquid drops of a given area under the influence of gravity for contact angles $\theta < 90°$. The solution is used in Figure 41 as reference solution for the ALE-method presented in Chapter 4.

If the interface is given as a graph, then $\Sigma = \{(r, h(r)) \in \mathbb{R}^2 : r \in (0, 2r_{cl})\}$, where r_{cl} is the distance between the symmetry plane of the drop and the contact line. Let σ be the surface tension coefficient, ρ the liquid density, g the gravitational acceleration, and θ the static contact angle. Then, using the above graph representation, the interface shape is the solution of the boundary value problem

$$\sigma h'' = (1 + h'^2)^{3/2}(\rho g h - p_0) \qquad \text{in } (0, 2r_{cl}), \tag{238}$$

$$h(0) = 0, \quad h'(0) = \tan\theta, \tag{239}$$

where the interface height h needs to satisfy the integral condition

$$A = \int_0^{2r_{cl}} h \, d\xi. \tag{240}$$

The above problem is an integro-differential equation for the interface shape h in combination with finding the corresponding pressure is an inverse problem for identifying p_0. The goal is now, given σ, ρ, g, θ, and a drop area A, to find a pressure p_0 and a surface height h, satisfying eqs. (238) and (239) as well as the integral condition (240).

The inverse problem eqs. (238)–(240) is solved by integrating the ODE (238), using an ODE-integrator for initial value problems, while adjusting the pressure value p_0 to satisfy (240). This approach is similar to a shooting method, though in this case the parameter p_0 is changed instead of subsequently adjusting an initial condition. As ODE-integrator, the `odeint` function from the `numpy` package version 1.17.2 with python version 3.7.4 is used to integrate (238) with (239) as initial conditions. For all cases, $N_x = 10000$ integration steps with a length $\Delta x = 4r_{max}/N_x$ are used (for definition of r_{max} see below).

As the radius r_{cl} is not known a priori, the integration domain is chosen such that it is much larger than the expected wetted radius. For this purpose, the radius of the wetted area is estimated using the radius of the wetted area

in the large and small Eötvös number limits. In the small Eötvös number limit, the drop forms a circular section, while in the large Eötvös number limit the drop has the shape of a puddle. The latter drop shape is estimated by two quarter circles with the radius L_{cap} at the left and right side of the drop and a square region with height L_{cap} in-between. This leads to

$$r_{\text{small Eo}} = \sin\theta\sqrt{2A/(2\theta - \sin(2\theta))}, \tag{241}$$

$$r_{\text{large Eo}} = L_{cap} + A/(2L_{cap}) \tag{242}$$

as estimates for the wetted radius of the different drop shapes, where the Capillary length is $L_{cap} = \sqrt{\sigma/(\rho g)}$. Based on these estimates, the integration domain for the ODE-integrator is set to $4r_{max}$, where

$$r_{max} = \max\{r_{\text{large Eo}}, r_{\text{small Eo}}\}. \tag{243}$$

If the solution does not have a zero while being convex, then the integration interval is simply doubled. During the integration of (238), the local curvature is evaluated to ensure a convex drop shape. If $\rho g h_i > p_0^n$ for the interface height h_i at a position $i\Delta x$, then the current droplet shape is rejected (the height h diverges) and the pressure guess is adapted as described below. The iteration index for the subsequent iterations of the pressure estimates is a superscript n.

The integral condition (240) is discretized for a discrete drop shape h^n, using the trapezoidal rule. Let N be such that $h_{N+1}^n \geqslant 0$ and $h_{N+2}^n < 0$, then the drop area is computed by

$$A^n := \sum_{i=0}^{N} \frac{h_i^n + h_{i+1}^n}{2}\Delta x. \tag{244}$$

Overall Algorithm The algorithm requires θ, ρ, g, σ and the drop area A as input parameters. The main idea of the algorithm is to improve the current pressure iterate by subsequently narrowing a pressure interval - a method also known as *nested intervals*. This interval is bounded by a lower pressure bound p_- and an upper pressure bound p_+, that are subsequently increased and decreased, respectively. The lower pressure bound p_- is always increased, when it was not possible to find a convex solution for the current pressure iterate as described above, or, if a convex solution was found, then the corresponding area is larger than A. In the former case, the pressure is to be increased in order to find a convex drop shape, while in the latter case, the pressure has to be increased in order to decrease the corresponding drop area. The upper pressure bound is always set to a pressure value for which a convex interface shape with an area that is smaller than A. In this case, the current pressure value has to be decreased to increase the drop area.

The following algorithm consists of two steps. In the first step the next pressure iterate is estimated. In the second step the pressure is increased (in

both cases) until a convex drop shape (that may have a too large or too small area) is obtained. The second step is executed while updating the pressure bounds. These steps are repeated until the relative error of the drop area is decreased below 10^{-5}.

Estimating the Next Pressure Value As initial pressure bounds $p_-^{n=0} = 0$ and $p_+^{n=0} = \texttt{MAX}$ are used, where MAX is the representation of infinity in the IEEE 754 floating point standard. Obviously, $\tilde{p}_0 \in [p_-^{n=0}, p_+^{n=0}]$.

Each iteration starts by computing a new pressure estimate between the lower and upper pressure bounds. The pressure is initialized with $\tilde{p}_0^{n=0} = \sigma/\tilde{r}$, where $\tilde{r}$ is the radius of curvature of an area equivalent circular section with contact angle θ. Each subsequent ($n > 0$) pressure iterate is computed as follows. A first estimate is obtained by

$$p_0^{*\,n+1} = p_0^n \sqrt{A^n/A}. \tag{245}$$

This equation is based on the area $A = \pi\tilde{r}^2$ of a circular 2D drop, and the pressure $p = \sigma/\tilde{r}$ inside the drop, which yields in combination $A = \pi(\sigma/p)^2$. Dividing $A^n = \pi(\sigma/p_0^n)^2$ by $A = \pi(\sigma/p_0^{n+1})^2$ yields (245).

If the pressure estimate (245) yields a value outside the pressure interval, i.e. $p_0^{*\,n+1} \notin [p_-^{n+1}, p_+^{n+1}]$ then the pressure estimate is chosen as

$$p_0^{*\,n+1} = \frac{p_-^{n+1} + p_+^{n+1}}{2} \tag{246}$$

instead of (245). This step corresponds to a bisection method.

Obtaining a Convex Solution Either the current pressure estimate is the initial pressure estimate $\tilde{p}_0$ or it is $p_0^{*\,n+1}$. In both cases, the python ODE-integrator is used to solve the differential equation eqs. (238) and (239). If the ODE-integrator yields a convex surface shape as described above, the pressure value is accepted and the pressure bounds are adjusted as described below. Otherwise, the pressure is increased until a convex drop shape is found as follows.

If, on the one hand, the current pressure estimate is $\tilde{p}_0$, then the pressure estimate is doubled until a convex drop shape is found. Then, this pressure is accepted as the current pressure iterate and the algorithm continues by setting the pressure bounds as described below. If, on the other hand, the current pressure estimate is $p_0^{*\,n+1}$, the pressure is increased iteratively by taking the next pressure guess $p_0^{**\,n+1} := (p^{*\,n+1} + p_+^{n+1})/2$. If $p_0^{**\,n+1}$ does not yield a convex drop shape, the pressure is further increased by $p_0^{***\,n+1} := (p^{**\,n+1} + p_+^{n+1})/2$ etc., until a sufficiently large pressure value is found which yields a convex drop shape. In both cases, the lower pressure bound is increased to the pressure value for which no convex surface could be found. The resulting pressure value is then accepted as the next pressure iterate p_0^{n+1}.

Updating the pressure bounds For $n \geqslant 0$, the pressure bounds are set as follows:

$$A^n \geqslant A, \quad \text{then} \quad p_-^{n+1} = p_0^n, \quad p_+^{n+1} = p_+^n \tag{247}$$

$$A^n < A, \quad \text{then} \quad p_-^{n+1} = p_-^n, \quad p_+^{n+1} = p_0^n, \tag{248}$$

which corresponds to the method of nested intervals outlined above.

Convergence Condition The pressure value p_0^{n+1} is obtained as described above. The corresponding h^{n+1} yields the area A^{n+1} by applying (244). If A^{n+1} satisfies the condition

$$\frac{A^{n+1} - A}{A} \leqslant 10^{-5}, \tag{249}$$

then the algorithm is considered converged. Otherwise, the algorithm starts a new iteration by estimating the next pressure value.

With the algorithm described above, the surface shapes for different Eötvös numbers in Figure 73 have been computed. The figure shows drop shapes for a contact angle of $\theta = 45°$ and Eötvös numbers between the spherical cap shape at $Eo \approx 10^{-3}$ and the puddle shape with $Eo \approx 10$. All interface shapes enclose the same area with the x-axis.

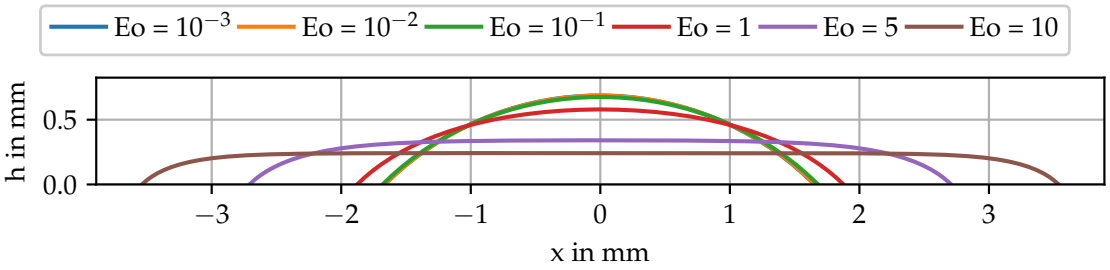

Figure 73: Two dimensional drop shapes for a contact angle of $\theta = 45°$, a drop area of $A = 1.57 \times 10^{-6}\,m^2$, and various Eötvös numbers.

BIBLIOGRAPHY

[1] Ablett, R. „XXV. An investigation of the angle of contact between paraffin wax and water.“ In: *The London, Edinburgh, and Dublin Philosophical Magazine and Journal of Science* 46.272 (1923), pp. 244–256.

[2] Aubram, D. *Differential geometry applied to continuum mechanics*. Ed. by S. A. Savidis. Veröffentlichungen des Grundbauinstitutes der Technischen Universität Berlin. 2009.

[3] Bascom, W. D., Conttington, R., and Singleterry, C. „Dynamic Surface Phenomena in the Spontaneous Spreading of Oils on Solids.“ In: *Advances in Chemistry* 43 (1964).

[4] Basting, S., Quaini, A., Čanić, S., and Glowinski, R. „Extended ALE Method for fluid–structure interaction problems with large structural displacements.“ In: *Journal of Computational Physics* 331 (2017), pp. 312 –336.

[5] Batchelor, G. K. *An Introduction to Fluid Dynamics*. Cambridge Mathematical Library. Cambridge University Press, 2000.

[6] Bazhlekov, I. B. and Chesters, A. K. „Numerical investigation of the dynamic influence of the contact line region on the macroscopic meniscus shape.“ In: *Journal of Fluid Mechanics* 329 (1996), 137–146.

[7] Beaglehole, D. „Profiles of the precursor of spreading drops of siloxane oil on glass, fused silica, and mica.“ In: *The Journal of Physical Chemistry* 93.2 (1989), pp. 893–899.

[8] Benson, D. J. „An efficient, accurate, simple ale method for nonlinear finite element programs.“ In: *Computer Methods in Applied Mechanics and Engineering* 72.3 (1989), pp. 305 –350.

[9] Blake, T. „Dynamic Contact Angle and Wetting Kinetics.“ In: *Wettability*. Ed. by J. Berg. Vol. 49. surfactant science series. Dekker, 1993.

[10] Blake, T. and Shikhmurzaev, Y. „Dynamic Wetting by Liquids of Different Viscosity.“ In: *Journal of Colloid and Interface Science* 253.1 (2002), pp. 196 –202.

[11] Blake, T. D. „The physics of moving wetting lines.“ In: *Journal of Colloid and Interface Science* 299.1 (2006), pp. 1–13.

[12] Blake, T. D., Clarke, A., and Ruschak, K. J. „Hydrodynamic assist of dynamic wetting.“ In: *AIChE Journal* 40.2 (1994), pp. 229–242.

[13] Bonn, D., Eggers, J., Indekeu, J., Meunier, J., and Rolley, E. „Wetting and spreading.“ In: *Rev. Mod. Phys.* 81.2 (2009), pp. 739–805.

[14] Bosanquet, C. „On the flow of liquids into capillary tubes.“ In: *Philosophical Magazine Series 6* 45.267 (1923), pp. 525–531.

[15] Bothe, D. *Mathematical Modeling of Fluid Interfaces*. Lecture notes. 2016.

[16] Brackbill, J., Kothe, D., and Zemach, C. „A continuum method for modeling surface tension.“ In: *Journal of Computational Physics* 100.2 (1992), pp. 335–354.

[17] Bracke, M., Voeght, F., and Joos, P. „The kinetics of wetting: the dynamic contact angle.“ In: *Trends in Colloid and Interface Science III* (1989), pp. 142–149.

[18] Brittin, W. E. „Liquid Rise in a Capillary Tube.“ In: *Journal of Applied Physics* 17.1 (1946), pp. 37–44.

[19] Bänsch, E. *Mesh moving methods for multiphase problems*. 2014.

[20] Chen, K. P., Saric, W., and Stone, H. A. „On the deviatoric normal stress on a slip surface.“ In: *Phys. Fluids* 12.12 (2000), p. 3280.

[21] Chen, L., Yu, J., and Wang, H. „Convex Nanobending at a Moving Contact Line: The Missing Mesoscopic Link in Dynamic Wetting.“ In: *ACS Nano* 8.11 (2014). PMID: 25337962, pp. 11493–11498.

[22] Chen, Q., Ramé, E., and Garoff, S. „Experimental studies on the parametrization of liquid spreading and dynamic contact angles.“ In: *Colloids and Surfaces A: Physicochemical and Engineering Aspects* 116.1 (1996), pp. 115 –124.

[23] Concus, P. „Static menisci in a vertical right circular cylinder.“ In: *Journal of Fluid Mechanics* 34.3 (1968), pp. 481–495.

[24] Demirdžić, I. „On the Discretization of the Diffusion Term in Finite-Volume Continuum Mechanics.“ In: *Numerical Heat Transfer, Part B: Fundamentals* 68.1 (2015), pp. 1–10.

[25] Demirdžić, I. and Perić, M. „Space conservation law in finite volume calculations of fluid flow.“ In: *Int. J. Numer. Meth. Fluids* 8.9 (1988), pp. 1037–1050.

[26] Dettre, R. H. and E., J. J. R. „Contact Angle Measurements on Rought Surfaces.“ In: ed. by F. Fowkes. 1964. Chap. 8, pp. 136–144.

[27] Donea, J., Huerta, A., Ponthot, J.-P., and Rodríguez-Ferran, A. „Arbitrary Lagrangian-Eulerian Methods.“ In: Wiley-Blackwell, 2004. Chap. 14.

[28] Dreyer, M., Delgado, A., and Path, H.-J. „Capillary Rise of Liquid between Parallel Plates under Microgravity.“ In: *Journal of Colloid and Interface Science* 163.1 (1994), pp. 158–168.

[29] Dupont, J.-B. and Legendre, D. „Numerical simulation of static and sliding drop with contact angle hysteresis.“ In: *Journal of Computational Physics* 229.7 (2010), pp. 2453–2478.

[30] Dupré, A. M. and Dupré, P. *Théorie mécanique de la chaleur*. Gauthier-Villars, 1869.

[31] Durst, F. *Grundlagen der Strömungsmechanik*. Springer-Verlag Berlin Heidelberg, 2006.

[32] Dussan V., E. B. „The moving contact line: the slip boundary condition.“ In: *Journal of Fluid Mechanics* 77.04 (1976), pp. 665–684.

[33] Dussan, V. E. B. and Davis, S. H. „On the motion of a fluid-fluid interface along a solid surface.“ In: *Journal of Fluid Mechanics* 65.1 (1974), pp. 71–95.

[34] Edwards, D., Brenner, H., and Wasan, D. *Interfacial Transport Processes and Rheology*. Ed. by H. Brenner. Butterworth-Heinemann, 1991.

[35] Eggers, J. and Evans, R. „Comment on “Dynamic wetting by liquids of different viscosity,” by T.D. Blake and Y.D. Shikhmurzaev.“ In: *Journal of Colloid and Interface Science* 280.2 (2004), pp. 537 –538.

[36] Elliott, G. and Riddiford, A. „Dynamic contact angles: I. The effect of impressed motion.“ In: *Journal of Colloid and Interface Science* 23.3 (1967), pp. 389 –398.

[37] Ferziger, J. H. and Perić, M. *Numerische Strömungsmechanik*. Vol. 1. Springer-Verlag Berlin Heidelberg, 2008.

[38] Fressmann, D. and Wriggers, P. „Advection approaches for single- and multi-material arbitrary Lagrangian–Eulerian finite element procedures.“ In: *Computational Mechanics* 39.2 (2007), pp. 153–190.

[39] Fricke, M., Köhne, M., and Bothe, D. „A kinematic evolution equation for the dynamic contact angle and some consequences.“ In: *Physica D: Nonlinear Phenomena* 394 (2019), pp. 26 –43.

[40] Fricke, M., Marić, T., and Bothe, D. „Contact Line Advection using the Level Set Method.“ In: *Proc. in Appl. Math. and Mech.* (2019).

[41] Fries, N. and Dreyer, M. „An analytic solution of capillary rise restrained by gravity.“ In: *Journal of Colloid and Interface Science* 320.1 (2008), pp. 259–263.

[42] Fries, N. and Dreyer, M. „Dimensionless scaling methods for capillary rise.“ In: *Journal of Colloid and Interface Science* 338.2 (2009), pp. 514–518.

[43] Gennes, P. G. de. „Wetting: statics and dynamics.“ In: *Reviews of Modern Physics* 57.3 (1985), pp. 827–863.

[44] Gerbeau, J.-F. and Lelièvre, T. „Generalized Navier boundary condition and geometric conservation law for surface tension.“ In: *Computer Methods in Applied Mechanics and Engineering* 198.5 (2009), pp. 644 –656.

[45] Gerbeau, J.-F., Lelièvre, T., and Le Bris, C. „Simulations of MHD flows with moving interfaces.“ In: *Journal of Computational Physics* 184.1 (2003), pp. 163 –191.

[46] Gerbeau, J.-F., Le Bris, C., and Lelièvre, T. *Mathematical methods for the Magnetohydrodynamics of Liquid Metals*. Ed. by G. Golub, A. Greenbaum, A. Stuart, and E. Süli. Oxford Science Publications, 2006.

[47] Giacomello, A., Schimmele, L., and Dietrich, S. „Wetting hysteresis induced by nanodefects." In: *Proceedings of the National Academy of Sciences* 113.3 (2016), E262–E271.

[48] Greenshields, C. J. *OpenFOAM Programmer's Guide*. Tech. rep. OpenFOAM Foundation Ltd., 2015.

[49] Gründing, D., Smuda, M., Antritter, T., Fricke, M., Rettenmaier, D., Kummer, F., Stephan, P., Marschall, H., and Bothe, D. „A comparative study of transient capillary rise using direct numerical simulations." In: (2019). Submitted.

[50] Gründing, D. „An enhanced model for the capillary rise problem." In: *International Journal of Multiphase Flows* (2019). doi: 10.1016/j.ijmultiphaseflow.2020.103210.

[51] Gründing, D., Bothe, D., and Marschall, H. „Wetting phenomena with ALE interface tracking." In: *Proc. in Appl. Math. and Mech.* 18.1 (2018). doi: 10.1002/pamm.201800430, e201800430.

[52] Gründing, D., Fleckenstein, S., and Bothe, D. „A subgrid-scale model for reactive concentration boundary layers for 3D mass transfer simulations with deformable fluid interfaces." In: *International Journal of Heat and Mass Transfer* 101 (Oct. 2016). doi: 10.1016/j.ijheatmasstransfer.2016.04.119, pp. 476–487.

[53] Gründing, D., Fricke, M., and Bothe, D. „Capillary Rise - Jurin's Height vs Spherical Cap." In: *PAMM* 19.1 (2019). doi: 10.1002/pamm.201900336, e201900336.

[54] Gurumurthy, V. „Dynamics of corner flows driven by wettability." PhD thesis. TU Darmstadt, 2018.

[55] Hadamard, M. „Mouvement permanent lent d'une sphère liquide et visqueuse dans un liquide visqueux." In: *C.R. Acad. Sci. Paris* 152 (1911), pp. 1735–1738.

[56] Hartmann, M., Fricke, M., Weimar, L., Gründing, D., Marić, T., Bothe, D., and Hardt, S. „Breakup Dynamics of Capillary Bridges on Hydrophobic Stripes." In: (2019). Submitted.

[57] Hauksbee, F. *Physico Mechanical Experiments*. London: Printed by R. Brugis, 1709.

[58] Hirsch, C. *Numerical Computation of Internal and External Flows*. Butterworth-Heinemann, 2007.

[59] Hirt, C., Amsden, A. A., and Cook, J. „An arbitrary Lagrangian-Eulerian computing method for all flow speeds.“ In: *Journal of Computational Physics* 14.3 (1974), pp. 227–253.

[60] Hoffman, R. L. „A Study of the Advancing Interface. I. Interface Shape in Liquid-Gas Systems.“ In: *Journal of Colloid and Interface Science* 50.2 (Feb. 1975), pp. 228–241.

[61] Huh, C. and Mason, S. G. „The steady movement of a liquid meniscus in a capillary tube.“ In: *Journal of Fluid Mechanics* 81.03 (1977), p. 401.

[62] Huh, C. and Scriven, L. „Hydrodynamic model of steady movement of a solid/liquid/fluid contact line.“ In: *Journal of Colloid and Interface Science* 35.1 (1971), pp. 85–101.

[63] Ishii, M. and Hibiki, T. *Thermo-Fluid Dynamics of Two-Phase Flow*. 2nd ed. Springer-Verlag New York, 2011.

[64] Issa, R. „Solution of the implicitly discretised fluid flow equations by operator-splitting.“ In: *Journal of Computational Physics* 62.1 (1986). Idea how the piso loop in OpenFOAM is implemented, pp. 40–65.

[65] Jiang, T.-S., Soo-Gun, O., and Slattery, J. C. „Correlation for dynamic contact angle.“ In: *Journal of Colloid and Interface Science* 69.1 (1979), pp. 74–77.

[66] Joos, P, Remoortere, P. V., and Bracke, M. „The kinetics of wetting in a capillary.“ In: *Journal of Colloid and Interface Science* 136.1 (1990), pp. 189–197.

[67] Jurin, J. „II. An account of some experiments shown before the Royal Society; with an enquiry into the cause of the ascent and suspension of water in capillary tubes.“ In: *Philosophical Transactions* 30.355 (1719), pp. 739–747.

[68] Jurin, J. „II. An account of some new experiments, relating to the action of glass tubes upon water and quicksilver.“ In: *Philosophical Transactions of the Royal Society of London* 30.363 (1719), pp. 1083–1096.

[69] Kistler, S. „Hydrodynamics of Wetting.“ In: *Wettability*. Ed. by J. Berg. Vol. 49. surfactant science series. Dekker, M., 1993.

[70] Klitz, M. „Numerical Simulation of Droplets with Dynamic Contact Angles.“ PhD thesis. Rheinische Friedrich-Wilhelms-Universität Bonn, 2014.

[71] Kummer, F. „The BoSSS Discontinuous Galerkin solver for incompressible fluid dynamics and an extension to singular equations.“ PhD thesis. Technische Universität Darmstadt, 2012.

[72] Lamb, H. *Hydrodynamics*. 4th ed. Cambridge university press, 1916.

[73] Laplace, P. S. *Theori'e de la m'ecanique c'eleste*. 1839.

[74] Leal, L. G. *Advanced Transport Phenomena: Fluid Mechanics and Convective Transport Processes*. Cambridge Series in Chemical Engineering. Cambridge University Press, 2007.

[75] Legendre, D. and Maglio, M. „Numerical simulation of spreading drops.“ In: *Colloids and Surfaces A: Physicochemical and Engineering Aspects* (2013).

[76] Levine, S., Reed, P., Watson, E., and Neale, G. „A Theory of the Rate of Rise of a Liquid in a Capillary.“ In: *Colloid and Interface Science*. Ed. by M. Kerker. Academic Press, 1976, pp. 403 –419.

[77] Levine, S., Lowndes, J., Watson, E. J., and Neale, G. „A theory of capillary rise of a liquid in a vertical cylindrical tube and in a parallel-plate channel.“ In: *Journal of Colloid and Interface Science* 73.1 (1980), pp. 136–151.

[78] Lippert, A. „Direct Numerical Simulations of Thermocapillary Driven Motions in Two-Phase Flows.“ PhD thesis. Technische Universität Darmstadt, 2016.

[79] Lohse, D. „Beständige Bläschen.“ In: *Physical Journal* (2017).

[80] Lopez, J., Miller, C. A., and Ruckenstein, E. „Spreading kinetics of liquid drops on solids.“ In: *Journal of Colloid and Interface Science* 56.3 (1976), pp. 460 –468.

[81] Lorenceau, É., Quéré, D., Ollitrault, J.-Y., and Clanet, C. „Gravitational oscillations of a liquid column in a pipe.“ In: *Physics of Fluids* 14.6 (2002), pp. 1985–1992.

[82] Lowndes, J. „The numerical simulation of the steady movement of a fluid meniscus in a capillary tube.“ In: *Journal of Fluid Mechanics* 101.3 (1980), 631–646.

[83] Lucas, R. „Ueber das Zeitgesetz des kapillaren Aufstiegs von Flüssigkeiten.“ In: *Kolloid-Zeitschrift* 23.1 (1918), pp. 15–22.

[84] Ludviksson, V. and Lightfoot, E. N. „Deformation of advancing menisci.“ In: *AIChE Journal* 14.4 (1968), pp. 674–677.

[85] Lukyanov, A. V. and Pryer, T. „Hydrodynamics of Moving Contact Lines: Macroscopic versus Microscopic.“ In: *Langmuir* 33.34 (2017). PMID: 28783342, pp. 8582–8590.

[86] Maggi, F. and Alonso-Marroquin, F. „Multiphase capillary flows.“ In: *International Journal of Multiphase Flow* 42 (2012), pp. 62 –73.

[87] Marić, T., Marschall, H., and Bothe, D. „lentFoam – A hybrid Level Set/Front Tracking method on unstructured meshes.“ In: *Computers & Fluids* 113 (2015). Small scale simulation of multiphase flows, pp. 20 –31.

[88] Massoudi, R. and King, A. D. „Effect of pressure on the surface tension of water. Adsorption of low molecular weight gases on water at 25°." In: *The Journal of Physical Chemistry* 78.22 (1974), pp. 2262–2266.

[89] Mathieu, B. „Études physique, expérimentale et numérique des mécanismes de bas intervenant dans les écoulements diphasiques." PhD thesis. Polytech Marseille, Université de Provence, 2003.

[90] Max, N. „Weights for Computing Vertex Normals from Facet Normals." In: *Journal of Graphics Tools* 4.2 (1999), pp. 1–6.

[91] Michaelis, M. and Dreyer, M. E. „Test-Case No 31: Reorientation of a Free Liquid Interface in a Partly Filled Right Circular Cylinder Upon Gravity Step Reduction (PE)." In: *Multiphase Science and Technology* 16.1-3 (2004), pp. 219–238.

[92] Moffatt, H. K. „Viscous and resistive eddies near a sharp corner." In: *Journal of Fluid Mechanics* 18.1 (Jan. 1964), pp. 1–18.

[93] Moukalled, F., Mangani, L., and Darwish, M. *The Finite Volume Method in Computational Fluid Dynamics*. 1st ed. Springer International Publishing, 2016.

[94] Muzaferija, S. and Perić, M. „Computation of free-surface flows using the finite-volume method and moving grids." In: *Numerical Heat Transfer, Part B: Fundamentals* 32.4 (1997), pp. 369–384.

[95] Navier, C. L.M. H. „Mémoire sur les lois du mouvement des fluids." In: *Mem. Acad. Sci. Inst. Fr.* 6 (1823), pp. 389–416.

[96] Ngan, C. G. and Dussan V., E. B. „On the nature of the dynamic contact angle: an experimental study." In: *Journal of Fluid Mechanics* 118 (1982), 27–40.

[97] Noh, W. *CEL: A Time-Dependent, Two-Space-Dimensional, Coupled Eulerian-Lagrange Code*. Tech. rep. 1963.

[98] Osher, S. and Fedkiw, R. P. „Level Set Methods: An Overview and Some Recent Results." In: *Journal of Computational Physics* 169.2 (2001), pp. 463 –502.

[99] Park, J. K. and Kang, K. H. „Numerical analysis of moving contact line with contact angle hysteresis using feedback deceleration technique." In: *Physics of Fluids* 24.4 (2012), p. 042105.

[100] Parmitano, L. *Post on the ESA-blog of astronaut Luca Parmitano entitled EVA 23: exploring the frontier, from 20th August 2013*. http://blogs.esa.int/luca-parmitano/2013/08/20/eva-23-exploring-the-frontier/. Blog post by profile RAFFAELLA. 2013.

[101] Patankar, S. V. *Numerical heat transfer and fluid flow*. Series on Computational Methods in Mechanics and Thermal Science. Hemisphere Publishing Corporation (CRC Press, Taylor & Francis Group), 1980.

[102] Pesci, C., Marschall, H., Ulaganathan, V., Kairaliyeva, T., Miller, R., and Bothe, D. „Experimental and Computational Analysis of Fluid Interfaces Influenced by Soluble Surfactant.“ In: *Transport Processes at Fluidic Interfaces*. Ed. by D. Bothe and A. Reusken. Advances in Mathematical Fluid Mechanics. Springer International Publishing, AG Cham, 2017. Chap. 15.

[103] Pesci, C., Weiner, A., Marschall, H., and Bothe, D. „Computational analysis of single rising bubbles influenced by soluble surfactant.“ In: *Journal of Fluid Mechanics* 856 (2018), 709–763.

[104] Phuc, P., Chiba, S., and Kazuo, M. *Large Scale Transient CFD Simulations for Buildings using OpenFOAM on a World's Top-class Supercomputer*. The 4th Annual OpenFOAM User Conference 2016, 2016.

[105] Popinet, S. „An accurate adaptive solver for surface-tension-driven interfacial flows.“ In: *Journal of Computational Physics* 228.16 (2009), pp. 5838–5866.

[106] Pr"uss, J. and Simonett, G. *Moving Interfaces and Quasilinear Parabolic Evolution Equations*. Vol. 105. Birkhäuser Basel, Jan. 2016.

[107] Qian, T., Sheng, P., and Wang, X.-P. „Generalized Navier Boundary Condition for the Moving Contact Line.“ In: *Communications in Mathematical Sciences* 1.2 (2003), pp. 333–341.

[108] Quéré, D. „Inertial capillarity.“ In: *Europhysics Letters (EPL)* 39.5 (1997), pp. 533–538.

[109] Quéré, D. „Fluid Coating on a Fiber.“ In: *Annual Review of Fluid Mechanics* 31.1 (1999), pp. 347–384.

[110] Quéré, D., Raphaël, É., and Ollitrault, J.-Y. „Rebounds in a Capillary Tube.“ In: *Langmuir* 15.10 (1999), pp. 3679–3682.

[111] Ramé, E. and Garoff, S. „Microscopic and Macroscopic Dynamic Interface Shapes and the Interpretation of Dynamic Contact Angles.“ In: *Journal of Colloid and Interface Science* 177.1 (1996), pp. 234 –244.

[112] Rettenmaier, D. „Numerical Simulation of Shear Driven Wetting.“ PhD thesis. TU Darmstadt, 2019.

[113] Rieber, M. „Numerische Modellierung der Dynamik freier Grenzflächen in Zweiphasenströmungen.“ PhD thesis. University of Stuttgart, 2004.

[114] Rose, W. and Heins, R. „Moving interfaces and contact angle rate-dependency.“ In: *Journal of Colloid Science* 17.1 (1962), pp. 39 –48.

[115] Ryskin, G. and Leal, L. G. „Numerical solution of free-boundary problems in fluid mechanics. Part 1. The finite-difference technique.“ In: *Journal of Fluid Mechanics* 148 (1984), 1–17.

[116] Ryskin, G. and Leal, L. G. „Numerical solution of free-boundary problems in fluid mechanics. Part 2. Buoyancy-driven motion of a gas bubble through a quiescent liquid.“ In: *Journal of Fluid Mechanics* 148 (1984), 19–35.

[117] Ryskin, G. and Leal, L. G. „Numerical solution of free-boundary problems in fluid mechanics. Part 3. Bubble deformation in an axisymmetric straining flow.“ In: *Journal of Fluid Mechanics* 148 (1984), 37–43.

[118] Savidis, S. A., Aubram, D., and Rackwitz, F. „Arbitrary Lagrangian-Eulerian Finite Element Formulation for Geotechnical Construction Processes.“ In: *Journal of Theoretical and Applied Mechanics* (2008).

[119] Schonhorn, H., Frisch, H. L., and Kwei, T. K. „Kinetics of Wetting of Surfaces by Polymer Melts.“ In: *Journal of Applied Physics* 37.13 (1966), pp. 4967–4973.

[120] Schwartz, A. M. and Tejada, S. B. „Studies of dynamic contact angles on solids.“ In: *Journal of Colloid and Interface Science* 38.2 (1972), pp. 359 –375.

[121] Schönfeld, F. and Hardt, S. „Dynamic contact angles in CFD simulations.“ In: *Computers & Fluids* 38.4 (2009), pp. 757 –764.

[122] Shikhmurzaev, Y. „The moving contact line on a smooth solid surface.“ In: *International Journal of Multiphase Flow* 19.4 (1993), pp. 589–610.

[123] Shikhmurzaev, Y. D. „Singularities at the moving contact line. Mathematical, physical and computational aspects.“ In: *Physica D: Nonlinear Phenomena* 217.2 (2006), pp. 121–133.

[124] Shikhmurzaev, Y. D. *Capillary Flows with Forming Interfaces*. 1st ed. 2008.

[125] Shikhmurzaev, Y. D. and Blake, T. D. „Response to the comment on J. Colloid Interface Sci. 253 (2002) 196 by J. Eggers and R. Evans.“ In: *Journal of Colloid and Interface Science* 280.2 (2004), pp. 539 –541.

[126] Shin, S., Chergui, J., and Juric, D. „Direct simulation of multiphase flows with modeling of dynamic interface contact angle.“ In: *Theoretical and Computational Fluid Dynamics* 32.5 (2018), pp. 655–687.

[127] Slattery, J. C., Sagis, L., and Oh, E. S. *Interfacial Transport Phenomena*. Second Edition. Springer Science Business Media, 2007.

[128] Snoeijer, J. H. and Andreotti, B. „Moving Contact Lines: Scales, Regimes, and Dynamical Transitions.“ In: *Annual Review of Fluid Mechanics* 45.1 (2013), pp. 269–292.

[129] Soulaimani, A. and Saad, Y. „An Arbitrary Lagrangian-Eulerian finite element method for solving three-dimensional free surface flows.“ In: *Computer Methods in Applied Mechanics and Engineering* 162.1 (1998), pp. 79 –106.

[130] M. Souli and D. J. Benson, eds. *Arbitrary Lagrangian-Eulerian and Fluid–Structure Interaction*. John Wiley & Sons, Inc., 2010.

[131] Spelt, P. D. „A level-set approach for simulations of flows with multiple moving contact lines with hysteresis.“ In: *Journal of Computational Physics* 207.2 (2005), pp. 389–404.

[132] Sprittles, J. E. and Shikhmurzaev, Y. D. „Finite element framework for describing dynamic wetting phenomena.“ In: *International Journal for Numerical Methods in Fluids* 68.10 (Apr. 2012), pp. 1257–1298.

[133] Sprittles, J. and Shikhmurzaev, Y. „Finite element simulation of dynamic wetting flows as an interface formation process.“ In: *Journal of Computational Physics* 233 (2013), pp. 34–65.

[134] Stange, M., Dreyer, M. E., and Rath, H. J. „Capillary driven flow in circular cylindrical tubes.“ In: *Physics of Fluids* 15.9 (2003), pp. 2587–2601.

[135] Sui, Y. and Spelt, P. „Sustained inertial-capillary oscillations and jet formation in displacement flow in a tube.“ In: *Physics of Fluids* 23.12 (2011), p. 122104.

[136] Sussman, M., Smereka, P., and Osher, S. „A Level Set Approach for Computing Solutions to Incompressible Two-Phase Flow.“ In: *Journal of Computational Physics* 114.1 (1994), pp. 146 –159.

[137] Szekely, J., Neumann, A., and Chuang, Y. „The rate of capillary penetration and the applicability of the Washburn equation.“ In: *Journal of Colloid and Interface Science* 35.2 (1971), pp. 273–278.

[138] Tanner, L. H. „The spreading of silicone oil drops on horizontal surfaces.“ In: *Journal of Physics D: Applied Physics* 12.9 (1979), pp. 1473–1484.

[139] Thomas, P. D. and Lombard, C. K. „Geometric Conservation Law and Its Application to Flow Computations on Moving Grids.“ In: *American Institute of Aeronautics and Astronautics* 17.10 (1979), pp. 1030–1037.

[140] Tuković, Ž. and Jasak, H. „A moving mesh finite volume interface tracking method for surface tension dominated interfacial fluid flow.“ In: *Computers & Fluids* 55 (2012), pp. 70–84.

[141] Tuković, Ž. „Metoda kontrolnih volumena na domenama promjenjivog oblika.“ PhD thesis. University of Zagreb, 2005.

[142] Ubbink, O. „Numerical prediction of two fluid systems with sharp interfaces.“ PhD thesis. Imperial College of Science, Technology and Medicine, 1997.

[143] Voinov, O. V. „Hydrodynamics of wetting.“ In: *Fluid Dynamics* 11.5 (1976), pp. 714–721.

[144] Waid, J. „Direct Numerical Simulation of Dynamic Wetting Processes by means of Arbitrary Lagrangian-Eulerian Interface-Tracking using OpenFOAM.“ MA thesis. TU Darmstadt, 2017.

[145] Washburn, E. W. „The Dynamics of Capillary Flow.“ In: *Phys. Rev.* 17 (3 1921), pp. 273–283.

[146] Weatherburn, C. *Differentialgeometry of Three Dimensions*. Vol. I. Reprint. The Syndics of the Cambridge University Press, 1955.

[147] Weber, P. S., Marschall, H., and Bothe, D. „Highly accurate two-phase species transfer based on ALE Interface Tracking.“ In: *International Journal of Heat and Mass Transfer* 104 (2017), pp. 759 –773.

[148] Williams, R. „The advancing front of a spreading liquid.“ In: *Nature* (1977).

[149] Yarnold, G. D. and Mason, B. J. „The Angle of Contact Between Water and Wax.“ In: *Proceedings of the Physical Society. Section B* 62.2 (1949), pp. 125–128.

[150] Young, T. „III. An essay on the cohesion of fluids.“ In: *Philosophical Transactions of the Royal Society of London* 95 (1805), pp. 65–87.

[151] Zhang, J., Borg, M., and Reese, J. „Multiscale simulation of dynamic wetting.“ In: *Journal of Heat and Mass Transfer* (2017).

[152] Zhmud, B., Tiberg, F., and Hallstensson, K. „Dynamics of Capillary Rise.“ In: *Journal of Colloid and Interface Science* 228.2 (2000), pp. 263–269.

[153] dataphysics. *OCA product series*. Tech. rep. dataphysics, 2018.